Development of the surface-enhanced infrared spectroscopic approach and surface-enhanced Raman spectroscopy coupled with electrochemistry to study reaction mechanism of membrane proteins

Natalia Grytsyk

UNIVERSITÉ DE STRASBOURG

ÉCOLE DOCTORALE DES SCIENCES CHIMIQUES

UMR 7140 – Chimie de la matière complexe

THÈSE présentée par :

Natalia GRYTSYK

soutenue le : **1 décembre 2017**

pour obtenir le grade de : **Docteur de l'université de Strasbourg**

Discipline/ Spécialité : Chimie

Développement d'approches spectroscopiques infrarouge exaltées de surface et Raman couplée à l'électrochimie pour l'étude du mécanisme réactionnel des protéines membranaires

THÈSE dirigée par :
Pr. Dr. HELLWIG Petra Professeur, université de Strasbourg

RAPPORTEURS :
Pr. SZUNERITS Sabine Professeur, université de Lille
Dr. GASNIER Bruno Directeur de recherche, université Paris Descartes CNRS

AUTRES MEMBRES DU JURY :
Dr. SCHALK Isabelle Directrice de recherche, université de Strasbourg CNRS

ACKNOWLEDGMENTS

First of all I would like to express my sincere respect to my thesis director Pr. Petra Hellwig for the opportunity to realize this thesis, for the interesting subjects, supervision and important suggestions.

I would also like to thank Pr. Sabine Szunerits, research directors Bruno Gasnier and Isabelle Schalk for accepting to be my committee members.

I am grateful to Pr. Thorsten Friedrich and his team for the collaboration and for the opportunity to work in his laboratory in Freiburg. I would especially thank Johannes for his supervision, kindness and help to purify complex I.

I am also grateful to Pr. Ronald Kaback for collaboration, important advices, enormous energy, enthusiasm and optimism.

I am deeply indebted to Pr. Olga A. Zaporozhets and Pr. Yves Mely for their opportunity to go to Strasbourg and subsequent meeting with Pr. Petra Hellwig that resulted in this PhD thesis. And also thanks to Dr. Tetiana Keda for her humanity and enormous kindness. I would especially thank my first school teacher in chemistry Oksana A. Usata for the interesting lessons and for giving the inspiration to continue studying chemistry at the University.

I want to express my sincere appreciation to Dr. Zahia Boubegtiten for the continuous help and important advices. I am very grateful to all my past and present colleagues: to Frederic, Youssef, Filipa, Sinan, Alicia, Batoul and to all internship students. Thanks Anton for your special humor and help in solving my technical problems. I am also grateful to all my compatriots from Illkirch, Strasbourg and Cronenbourg for their great help in the integration in French system and French society during my Master 2.

I would especially thank my close friend Mireille Khalil. Thank you for your encouragement, enormous kindness, great help in the administrative questions, for listening and being my support all the time. I would like to thank Soumia for the great help in administrative tasks and Martine for the kindness, humanity and good moments during these years. Special thanks to Pr. Alexandre Varnek and Dr. Olga Klimchuk for good advices and support. And thanks to Timur from Pr. Varnek's group for spent good times, for being always very friendly and kind.

My deepest thanks go to my good friend Waêl. I am very grateful for your help, support, for great moments and wonderful sense of humor.

Finally, I dedicate this thesis to my parents, Tetiana and Oleksii, and to my brother Vyacheslav. Thank you for your love, enormous encouragement and believing in me all the time.

List of Abbreviations

ν_s: symmetric stretching vibration

ν_{as}: asymmetric stretching vibration

δ: deformation vibration

ε: molar extinction coefficient

AESF: American Electroplaters' and Surface Finishers' Society

ANTA: amino-nitrilotriacetic acid

ATP: Adenosine triphosphate

ATR: attenuated total reflection

CAPS: N-cyclohexyl-3-aminopropanesulfonic acid

CCD: charged couple device

CE: chemical enhancement

CT: charge transfer

Cyt *c*: cytochrome *c*

DDM: n-dodecyl-β-D-maltoside

DEER: double electron-electron resonance

DFT: density functional theory

DMSO: dimethyl sulfoxide

DNA: deoxyribonucleic acid

DTGS: deuterated triglycine sulfate

DTSP: 3,3′-dithiodipropionic acid di(N-hydroxysuccinimide ester)

EC-SERS: electrochemical surface-enhanced Raman spectroscopy

EDC: 1-Ethyl-3-(3-dimethylaminopropyl)carbodiimide

EM: electromagnetic

EOT: extraordinary optical transmission

ETC: electron transport chain

FIB: focused ion beam

FIR: far infrared

FMN: flavin mononucleotide

FON: film-over-nanospheres

FTIR: Fourier transform infrared spectroscopy

GPCR: G-protein-coupled receptor

Hb: hemoglobin

HEPES: 4-(2-hydroxyethyl)-1-piperazineethanesulfonic acid

HIV: human immunodeficiency virus

IR: infrared

IRE: internal reflection element

ITO: indium tin oxide

LacY: Lactose Permease

LN-MCT: liquid nitrogen cooled Mercury-Cadmium-Telluride

LSPR: localized surface plasmon resonance

Mb: myoglobin

MES: 2-(N-morpholino)ethanesulfonic acid

MFS: major facilitator superfamily

MIR: mid infrared

MUA: mercaptoundecanoic acid

MW: molecular weight

MWCO: molecular weight cut-off

NAD^+: nicotinamide adenine dinucleotide (oxidized)

NADH: nicotinamide adenine dinucleotide (reduced)

NIR: near infrared

NMR: nuclear magnetic resonance

NP: nanoparticles

NPG: *p*-nitrophenyl-α-D-galactopyranoside

NSL: nanosphere lithography

NTA: nitrilo-triacetic acid

OD: optical density

OG: octyl-β-D-glucoside

ORC: oxidation and reduction cycles

PDB: protein data bank

PMSF: phenylmethylsulfonyl fluoride

POPE: 1-palmitoyl-2-oleoyl-sn-glycero-3-phosphoethanolamine

POPG: 1-palmitoyl-2-oleoyl-sn-glycero-3-phospho-(1-rac-glycerol)

PVC: polyvinyl chloride

RF: radiofrequency

PS: *Pseudomonas stutzeri*

RR: resonance Raman

RRS: resonance Raman scattering

SAM: self-assembled monolayer

SCE: saturated calomel electrode

SDA: site-directed alkylation

SDS-PAGE: sodium dodecyl sulfate polyacrylamide gel electrophoresis

SEIRAS: surface-enhanced infrared spectroscopy

SERS: surface-enhanced Raman spectroscopy

SHE: standard hydrogen electrode

SHINERS: shell-isolated nanoparticle-enhanced Raman spectroscopy

sm-FRET: single molecule fluorescence resonance energy transfer

SSV: segment sphere voids

TCA: trichloroacetic acid

TDG: β-D-galactopyranosyl-1-thio-β-D-galactopyranoside

TM: trans-membrane

UQ: ubiquinone

UV: ultraviolet

WE: working electrode

WT: wild-type

List of publications

Published articles

1. *pKa of Glu325 in LacY*. Grytsyk, N., Sugihara, J., Kaback, H. R., and Hellwig, P. Proceedings of the National Academy of Sciences (PNAS). Volume 114, 2017, pages 1530-1535. (doi: 10.1073/pnas.1621431114)

Articles in preparation

1. *Identification of residues ruling the apparent pK of Glu325 up to 10.5 in LacY: an infrared spectroscopic study.* Grytsyk, N., Sugihara, J., Kaback, H. R., and Hellwig, P.

2. *Probing gold grids for a combined electrochemical and surface-enhanced Raman spectroscopic approach*. Grytsyk, N., Boubegtiten-Fezoua, Z., and Hellwig P.

3. *Mg^{2+}-binding triggers rearrangement of the IM30 ring structure, resulting in augmented exposure of hydrophobic surfaces competent for membrane binding.* Jennifer Heidrich, Benedikt Junglas, Natalia Grytsyk, Nadja Hellman, Kristiane Rusitzka, Wolfgang Gebauer, Jürgen Markl, Petra Hellwig and Dirk Schneider

TWENTY-ONE AMINO ACIDS

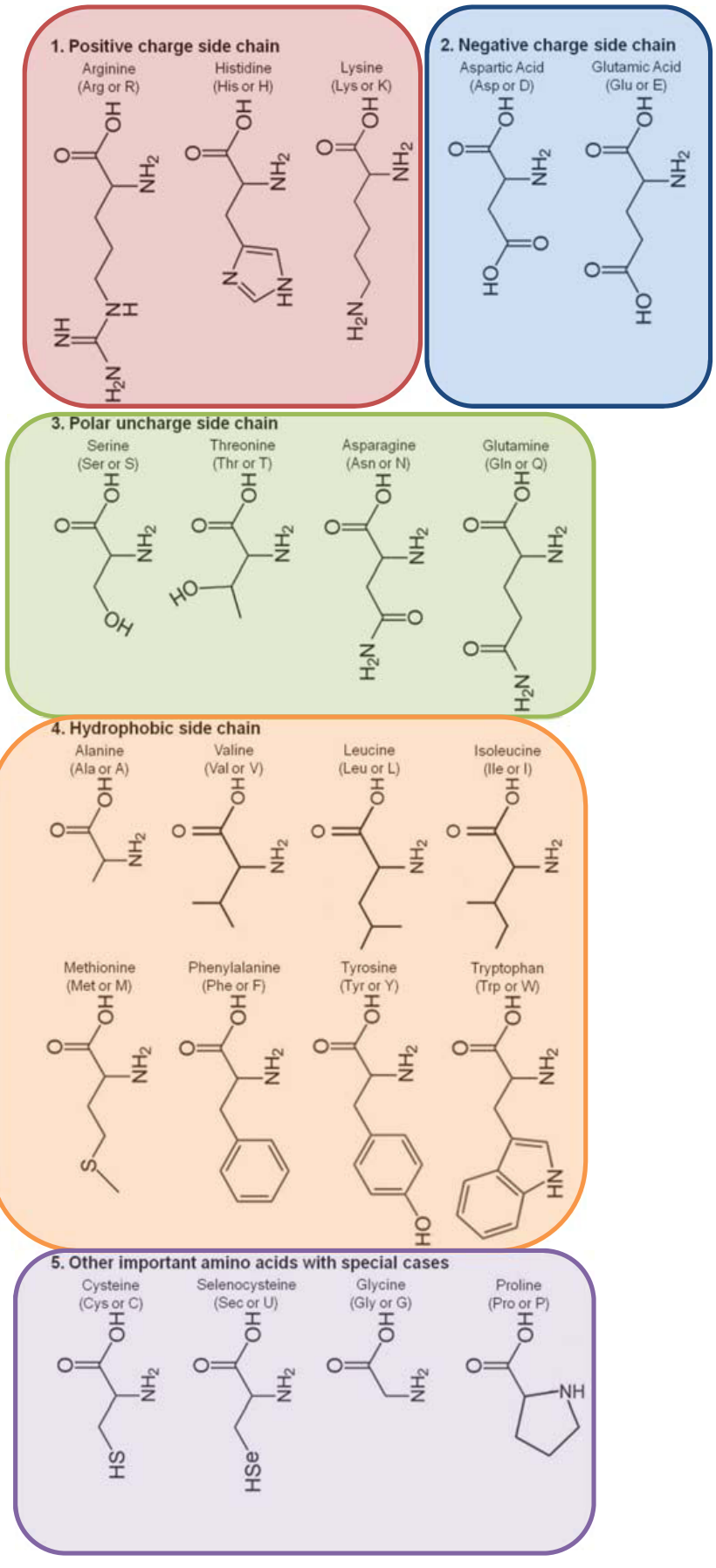

Table of contents

Chapter 2 – MATERIALS AND METHODS

Chapter 3 - COMBINED PERFUSION AND SEIRAS APPROACH TO DETERMINE THE PKA OF AN ACIDIC RESIDUE IN LACTOSE PERMEASE

Chapter 4 - THE STUDY OF COMPLEX I BY PERFUSION-SEIRAS APPROACH

Chapter 5 - PROBING GOLD GRIDS FOR A COMBINED ELECTROCHEMICAL AND SURFACE-ENHANCED RAMAN SPECTROSCOPIC APPROACH

RESUME

1. Introduction

Mon travail de thèse s'articule autour des développements des approches infrarouge exaltée de surface et Raman couplée à l'électrochimie pour l'étude du mécanisme de réaction des protéines membranaires. Cette thèse est composée de deux parties principales: la première est axée sur le développement de la spectroscopie infrarouge exaltée de surface (SEIRAS) combinée avec une cellule de perfusion et la deuxième est focalisée sur le développement de l'approche électrochimique combinée avec la spectroscopie Raman exaltée de surface (SERS) pour l'étude des protéines redox actives.

Les deux parties principales de cette thèse seront développées et détaillées dans la suite de ce résumé.

2. SEIRAS combinée avec la cellule de perfusion

Concernant la première partie, la monocouche de protéine a été immobilisée sur la surface du cristal ATR (réflexion totale atténuée) qui a été modifiée avec une couche d'or nanostructurée. Ce cristal ATR a été couplé avec une cellule de perfusion illustrée schématiquement sur la Figure 1.

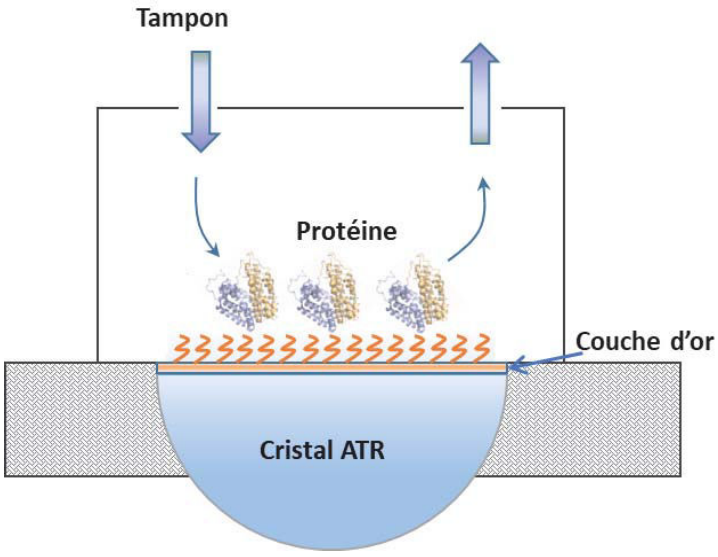

Figure 1: Représentation de la configuration expérimentale SEIRAS-perfusion

Concernant la première partie, nous nous sommes intéressés à la détermination de la valeur pKa de l'acide aminé Glu325 dans la protéine membranaire Lactose Permease (LacY) et ses mutants. LacY est une protéine de transport membranaire. Cette protéine catalyse la translocation couplée d'un galactoside et d'un H^+ à travers la membrane cellulaire. LacY couple l'énergie libre libérée lors de la translocation de H^+ en réponse au gradient électrochimique H^+ ($\Delta\mu_H{}^+$) pour entraîner l'accumulation des galactopyranosides contre un gradient de concentration. La cristallographie aux rayons X a révélé la structure cristalline de LacY (Figure 2).

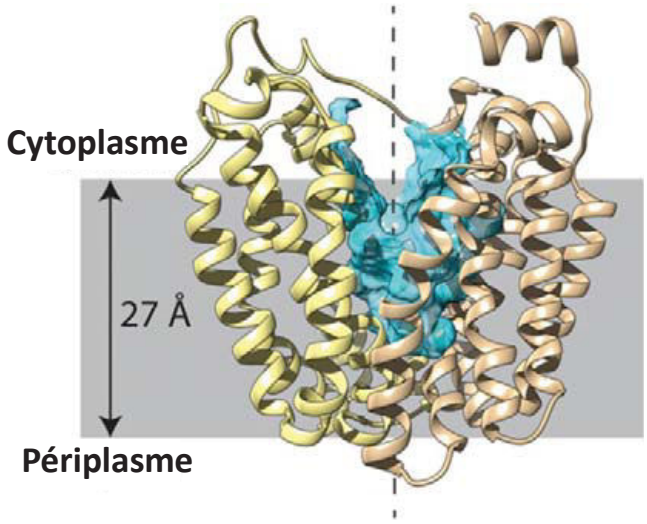

Figure 2: Structure de la protéine Lactose Permease (code PDB 2V8N)

La structure présente deux faisceaux (de 6 hélices chacun) qui sont liés par une longue boucle cytoplasmique entre les hélices VI et VII. LacY a une cavité hydrophile profonde qui est entourée par les deux faisceaux à 6 hélices.

Le mécanisme de symport commence par la protonation de LacY (étape 1 ou 6 pour l'afflux ou l'efflux, respectivement). Le sucre (S) interagit avec LacY protonée (étape 2 ou 5) et induit un changement conformationnel vers une conformation occluse (étape 3 ou 4), qui peut ensuite se relaxer à une autre conformation où le sucre se dissocie d'abord (étape 2 ou 5), suivi d'une déprotonation (étape 1 ou 6) et la régénération de LacY non liée (étapes 7 et 8) (Figure 3).

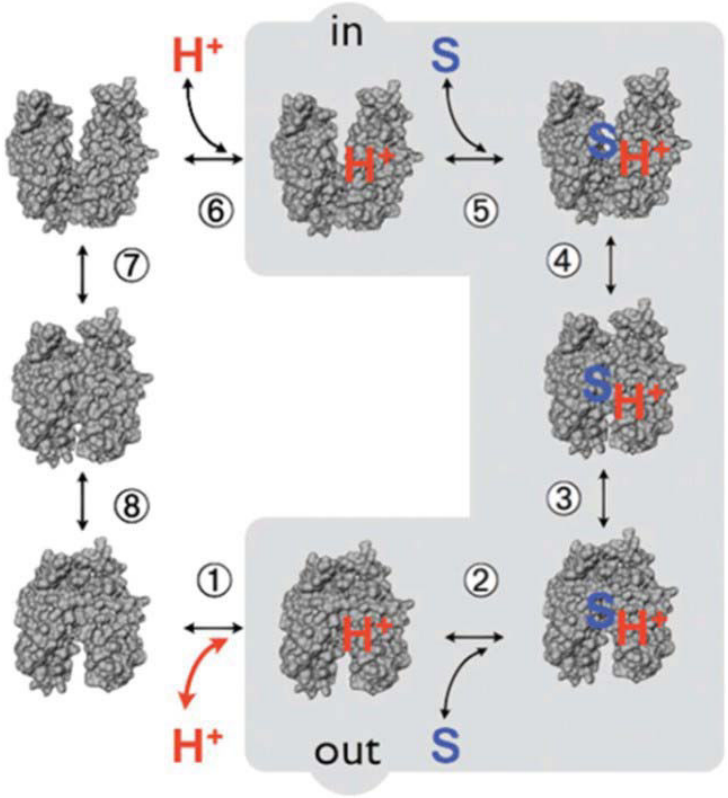

Figure 3: Schéma cinétique pour le symport de galactoside/H^+, échange et contre-courant

Cependant, il y a encore beaucoup de questions concernant le fonctionnement de LacY qui doivent être clarifiées. Par exemple, quel(s) résidu(s) est (sont) responsable(s) d'un pK élevé d'interaction de la protéine avec le sucre? Y a t'il un résidu spécial qui joue un rôle central dans le mécanisme «de couplage» de symport? Pour répondre à ces questions, nous avons développé une nouvelle approche. Cette approche qui combine la spectroscopie infrarouge exaltée de surface avec une cellule de perfusion nous permet d'enregistrer les spectres différentiels pour identifier et déterminer la valeur de pK_a d'un résidu dans LacY sauvage et dans différents mutants. Les mutations ont été effectuées dans le centre actif de la protéine.

Tout d'abord, nous avons enregistré des spectres infrarouges différentiels de LacY G46W/G262W (mutant qui contient Glu325 et qui est stable à des pH élevés) (Figure 4).

La bande à 1742 cm^{-1} correspond à la déprotonation d'un acide aminé. Pour identifier cet acide aminé, nous avons effectué la même expérience avec le mutant LacY G46W/G262W/E325A pour lequel il manque Glu325 (Figure 5).

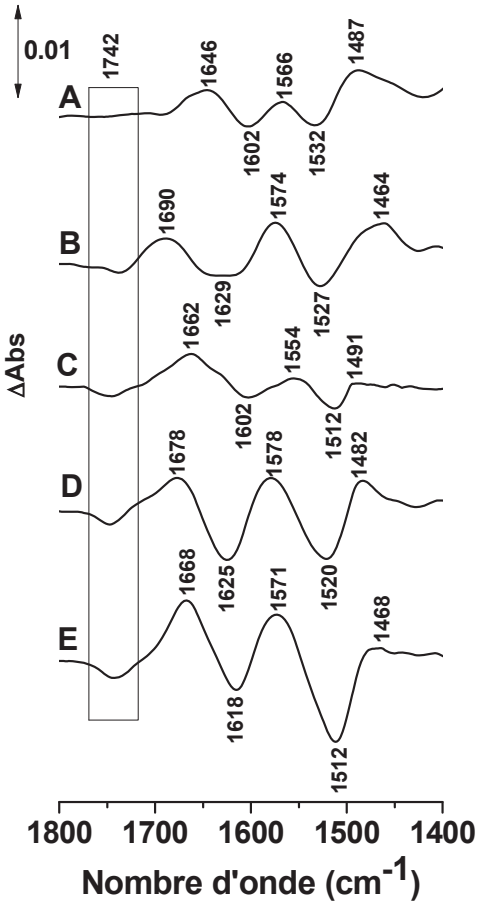

Figure 4: Les spectres différentiels de LacY G46W/G262W en présence de 80 µM NPG dans les deux solutions de perfusion. Le spectre correspondant à l'échantillon équilibré à pH 7.0 a été soustrait de celui de l'échantillon équilibré à 9.0 (A), 10.0 (B), 10.5 (C), 10.9 (D) et 11.5 (E), respectivement

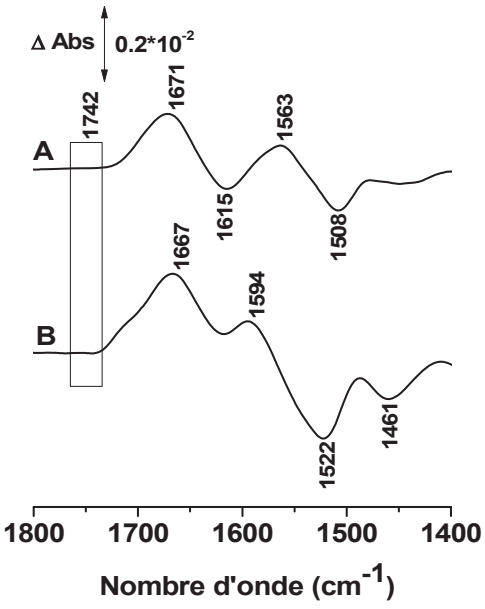

Figure 5: Spectres differentiels de LacY G46W/G262W/E325A pH 11.5 – pH 7 (A) et pH 10.9 – pH 7 (B)

L'absence de signal à 1742 cm^{-1} dans la Figure 5 confirme que c'était Glu325 qui a été déprotoné à haute valeur de pH (à partir de pH 10) dans l'expérience de la Figure 4.

Le pK_a de Glu325 a été déterminé en traçant Δ Absorbance à 1742 cm^{-1} par rapport au pH (Figure 6).

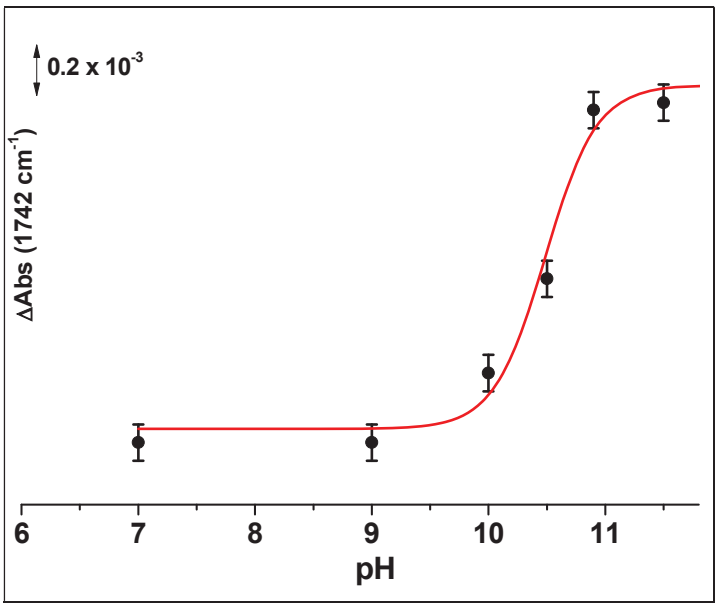

Figure 6: Dépendance de Δ Absorbance à 1742 cm^{-1} en fonction du pH

Donc, Glu325 a un pK_a de 10.5 ± 0.1, une valeur qui s'accorde remarquablement bien avec les pK^{app}s obtenus précédemment pour WT LacY ou mutant LacY G46W/G262W.

Ensuite, de la même manière nous avons déterminé les pKa de Glu325 dans les mutants: LacY E325D, LacY H322Q, LacY R302K, $LacY_{ww}$ R302K, LacY R302A et $LacY_{ww}$ R302A. Les résultats sont résumés dans la Figure 7 et dans le Tableau **1**.

Tableau 1: Corrélation entre pKa de Glu325 et activité

Mutant	Activité	pK_a	Position de bande/cm^{-1}
LacY WT	transport actif	10.5	1742
$LacY_{ww}$	pas de transport actif	10.5	1742
$LacY_{ww}$ E325A/LacY E325A	pas de transport actif	titrage supprimé	
LacY E325D	transport actif à faible taux (15% de LacY WT)	8.3	1728
LacY H322Q	pas de transport actif	10.1	1737
$LacY_{ww}$ R302K	pas de transport actif	8.4	1745
$LacY_{ww}$ R302A		10.3	1742

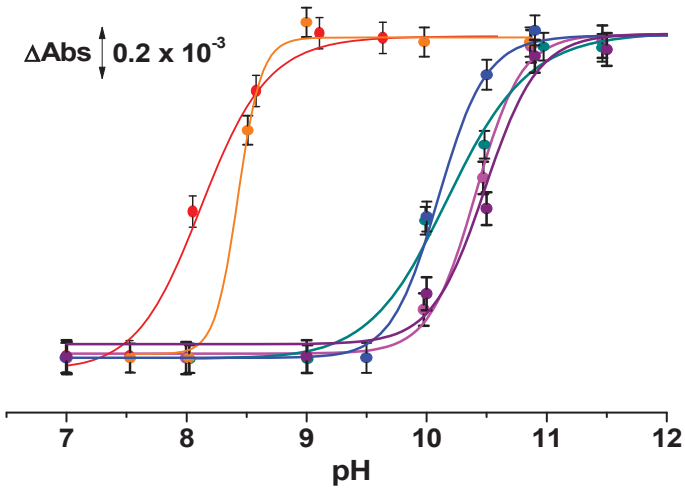

Figure 7: Dépendance de Δ Absorbance en fonction du pH mesurée avec LacY G46W/G262W en l'absence (magenta) et présence (violet) de sucre, LacY E325D (rouge), LacY H322Q (bleu), $LacY_{ww}$ R302K (orange) et $LacY_{ww}$ R302A (cyan)

En conclusion, les résultats fournissent des preuves expérimentales directes que Glu325 dans LacY sauvage a un pK_a de 10.5, une valeur qui coïncide précisément avec la variation de l'affinité de LacY pour le galactoside en fonction du pH. Il est possible de conclure qu'il n'y a pas de corrélation directe entre l'activité de transport et la valeur pKa de Glu325.

Les mutations des résidus impliqués dans la translocation de H^+ modifient la valeur pK_a du groupe carboxylique en position 325 indiquant une perturbation de la liaison hydrogène.

Ensuite, l'approche SEIRAS-perfusion a été appliquée pour les études d'une grande protéine membranaire de la chaîne respiratoire - complexe I.

Le complexe I (NADH: ubiquinone oxydoréductase) joue un rôle important dans la chaîne de transport d'électrons dans les mitochondries et bactéries. Il fournit environ 40% du flux de protons lors de la génération de force motrice de protons qui est nécessaire pour la synthèse de l'ATP. Le complexe I catalyse le transfert de deux électrons du nicotinamide adénine dinucléotide réduit (NADH) à l'ubiquinone qui est couplé à la translocation de quatre protons à travers la membrane mitochondriale interne. Le complexe I bactérien est un mini modèle de l'enzyme mitochondriale. C'est l'ensemble en forme de L qui comprend 14 sous-unités "noyau" (7 hydrophiles et 7 hydrophobes, ~ 550 kDa de masse combinée) et qui est conservé des bactéries aux humains (Figure 8).

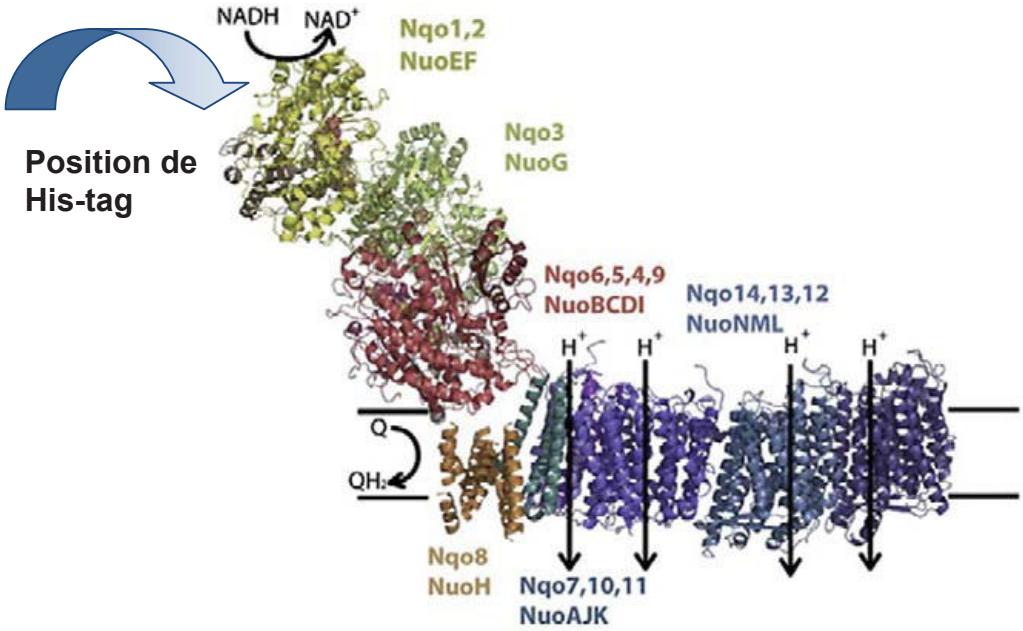

Figure 8: Structure de l'ensemble du complexe I de *Thermus thermophilus* (code PDB 3M9S)

Pour le moment, il existe encore beaucoup de questions liées au mécanisme moléculaire de fonctionnement du complexe I. Par exemple, les détails du transport des ions à travers les membranes et le transport d'électrons par des groupes prothétiques métalliques sont bien compris mais la conversion d'énergie de la reaction redox en mouvement mécanique n'est toujours pas comprise dans le complexe I. C'est pourquoi le développement de nouvelles approches qui

peuvent donner une idée du mécanisme moléculaire du fonctionnement des protéines membranaires est important.

L'approche SEIRAS-perfusion a été utilisée pour étudier les changements conformationnels dans le complexe I immobilisé lors de l'oxydation et de la réduction. La Figure 9 montre les spectres IR obtenus à partir des échantillons équilibrés avec différents agents oxydants (ubiquinone-2 (Q-2), ubiquinone-10 (Q-10), hexacyanoferrate de potassium (III) ($K_3[Fe(CN)_6]$) ou avec un tampon MES contenant de l'oxygène solubilisé) et soustraits de celui de l'échantillon équilibré avec l'agent réducteur NADH.

Les différences dans les spectres (Figure 9A-D) peuvent être expliquées par des degrés d'oxydation du complexe I différents lors de l'utilisation des différents agents oxydants. Par exemple, il est prévu que le degré d'oxydation du complexe I est plus important lors de l'utilisation d'ubiquinone-2 (Figure 9A) par rapport à l'ubiquinone-10 (Figure 9B). Ceci peut être expliqué par le fait que Q-2 n'a que deux sous-unités isoprényles tandis que Q-10 a dix sous-unités et donc Q-2 peut facilement entrer dans le site de liaison de quinone du complexe I et l'oxyder. Quoi qu'il en soit, les transferts d'électrons et de protons par le complexe I sont attendus lors de l'utilisation de Q-2 ou Q-10.

Le profil du spectre oxydé moins réduit de la Figure 9C obtenu lors de l'utilisation de $K_3[Fe(CN)_6]$ en tant qu'agent oxydant est presque identique à ceux illustrés sur la Figure 9A-B lors de l'utilisation de Q-2 et Q-10, respectivement, dans la région spectrale entre 1800 cm^{-1} et 1638 cm^{-1}. Dans la région entre 1638 cm^{-1} et 1200 cm^{-1}, le spectre de la Figure 9C est assez différent comparé à ceux de la Figure 9A-B. Cette observation pourrait être expliquée par le fait que seul le transfert d'électrons est possible lors de l'utilisation $K_3[Fe(CN)_6]$. Par conséquent, les changements conformationnels correspondants seront différents. Cette observation est importante puisque cette approche SEIRAS- perfusion peut encore être utilisée pour étudier le couplage H^+/e.
Le décalage du spectre de la Figure 9D vers les nombres d'onde inférieurs peut être expliqué par le fait que le complexe I n'est pas complètement mais partiellement oxydé par l'oxygène dissous dans la solution du tampon MES.

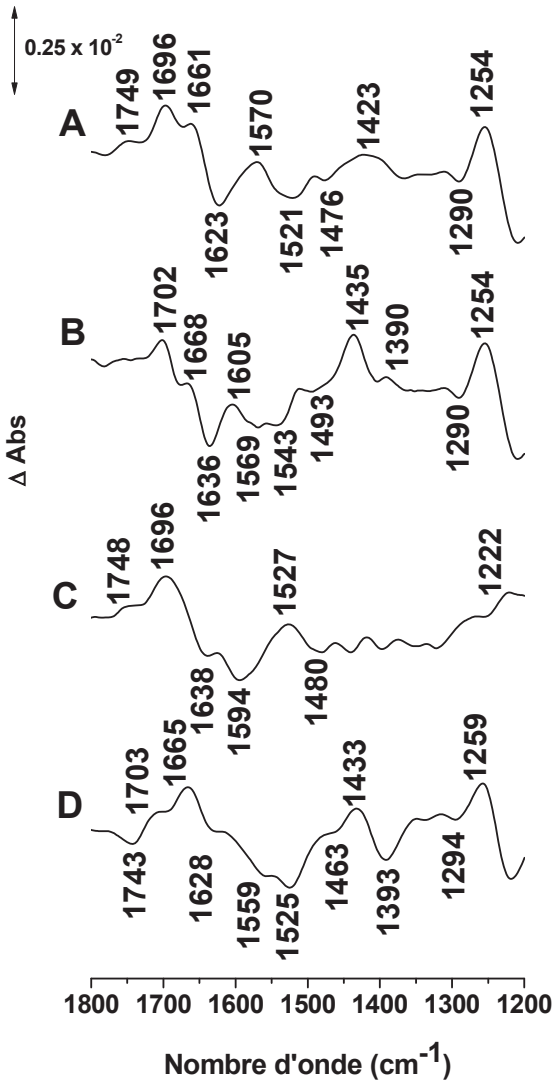

Figure 9: Les spectres FTIR du complexe I obtenus à partir de l'échantillon équilibré avec l'agent oxydant: ubiquinone-2 (A), ubiquinone-10 (B), $K_3[Fe(CN)_6]$ (C) ou avec un tampon MES (D), respectivement, et soustraits de ceux de l'échantillon équilibré avec NADH

Les résultats présentés confirment que l'oxydation et la réduction du complexe I induisent des changements conformationnels globaux qui sont liés au mécanisme du fonctionnement de la protéine. Il est largement admis que l'énergie libérée par la réaction redox est convertie en changements conformationnels globaux de la protéine permettant la translocation des protons.

L'approche SEIRAS-perfusion a été également utilisée pour étudier les changements conformationnels dans la protéine IM30 lors de l'interaction avec Mg^{2+}.

3. SERS combinée avec la cellule électrochimique

La deuxième partie concerne le développement d'une approche combinée spectroscopie Raman exaltée de surface – électrochimie. La cellule spectroélectrochimique comporte une grille d'or. Cette grille d'or sert comme substrat SERS et comme l'électrode de travail. L'approche a été appliquée à l'oxydation et la réduction des protéines d'hème immobilisées.
L'adsorption des protéines sur la grille d'or modifiée n'affecte pas la stabilité des structures protéiques. La rugosité de la grille d'or est à l'origine de l'exaltation de surface. Dans les spectres SERS du cytochrome *c* (Cyt *c*), de l'hémoglobine (Hb), de la myoglobine (Mb) et de la protéine membranaire cytochrome cbb_3 oxydase (cbb_3), les bandes caractéristiques des formes oxydées et réduites sont totalement réversibles.

La chimisorption des alcanethiols est la méthode la plus efficace pour la fonctionnalisation des surfaces d'or. Trois types de thiols ont été testés pour l'adsorption de Cyt *c* sur deux grilles d'or (taille du trou de 35 μm et 8 μm): l'acide 11-mercaptoundecanoïque chargé négativement (11-MUA), la cystéamine chargée positivement et le mélange neutre de 6-mercapto-1-hexanol avec 1-hexanethiol (Figure 10).

La Figure 10 illustre que les spectres du Cyt *c* adsorbé sur les surfaces modifiées avec différents thiols sont très comparables. Le Cyt *c* adsorbé sur la grille d'or modifiée avec 11-MUA a montré l'exaltation du signal la plus élevée. Ce thiol a donc été utilisé pour les modifications lors des expériences présentées ci-après.

Pour étudier si les signaux peuvent être encore plus exaltés, l'effet de l'ajout des nanoparticules d'or (Au NPs) sur une grille d'or a été examiné. Mais dans ce cas, les intensités des signaux étaient moins intenses comparé aux intensités des signaux du Cyt *c* adsorbé sur la grille d'or sans nanoparticules. Ainsi, l'électrode idéale pour les expériences SERS est la grille d'or modifiée avec 11-MUA sans Au NPs.

La Figure 11A-C représente les spectres Raman des Cyt *c*, Hb et Mb mesurés avec une cellule électrochimique en présence de la grille d'or.

Les processus d'oxydation et de réduction de ces protéines peuvent être contrôlés à partir des fréquences des modes de vibration caractéristiques ν_4, ν_{10} et ν_{19}. Après réduction complète du Cyt *c* en utilisant la cellule spectroélectrochimique, la fréquence de le mode ν_{19} est décalée de 1562 à

1582 cm^{-1} et les fréquences des modes ν_4 et ν_{10} sont décalées de 1369 et 1635 cm^{-1} à 1361 et 1621 cm^{-1}, respectivement (Figure 11A). Lors de la réduction de l'Hb (Figure 11B), les bandes à 1376 (ν_4), 1586 (ν_{19}) et 1640 (ν_{10}) cm^{-1} sont entièrement décalées vers 1355, 1547 et 1605 cm^{-1}, respectivement. Pour le Mb réduit, les bandes marqueurs, ν_4 et ν_{10} sont également décalées (Figure 11C).

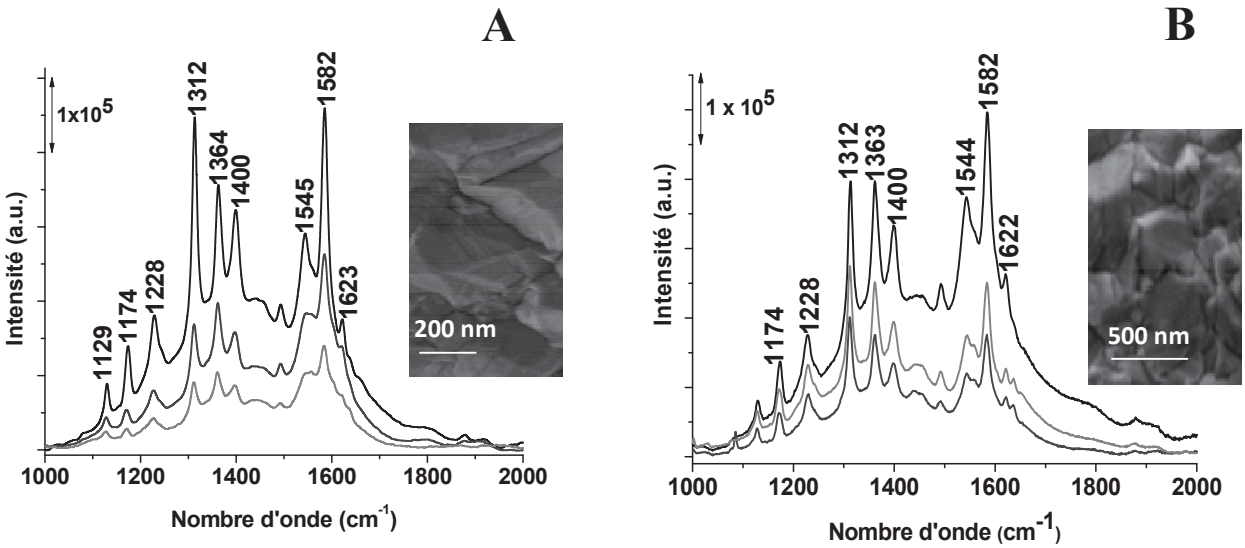

Figure 10: Les spectres SERS du Cyt *c* adsorbé sur les surfaces des grilles avec une taille de trou de 35 µm (A) et de 8 µm (B) modifiées avec différents thiols: acide 11-mercaptoundecanoïque (noir), cysteamine (gris foncé) et mélange de 6-mercapto-1-hexanol avec 1-hexanethiol (gris)

Les spectres SERS de la cytochrome *cbb_3* oxydase dans les formes oxydées et réduites ont également été obtenus en utilisant cette cellule.

En conclusion, la cellule spectroélectrochimique adaptée ici pour le SERS nous a permis d'obtenir des spectres complètement et réversiblement oxydés et réduits des protéines (Cyt *c*, Hb, Mb, *cbb_3* oxydase). De plus, la bonne qualité des données et leur reproductibilité démontrent que cette cellule peut être utilisée avec succès pour les études électrochimiques de diverses protéines redox.

Ainsi donc, deux approches ont été développées et appliquées avec succès pour les études des protéines.

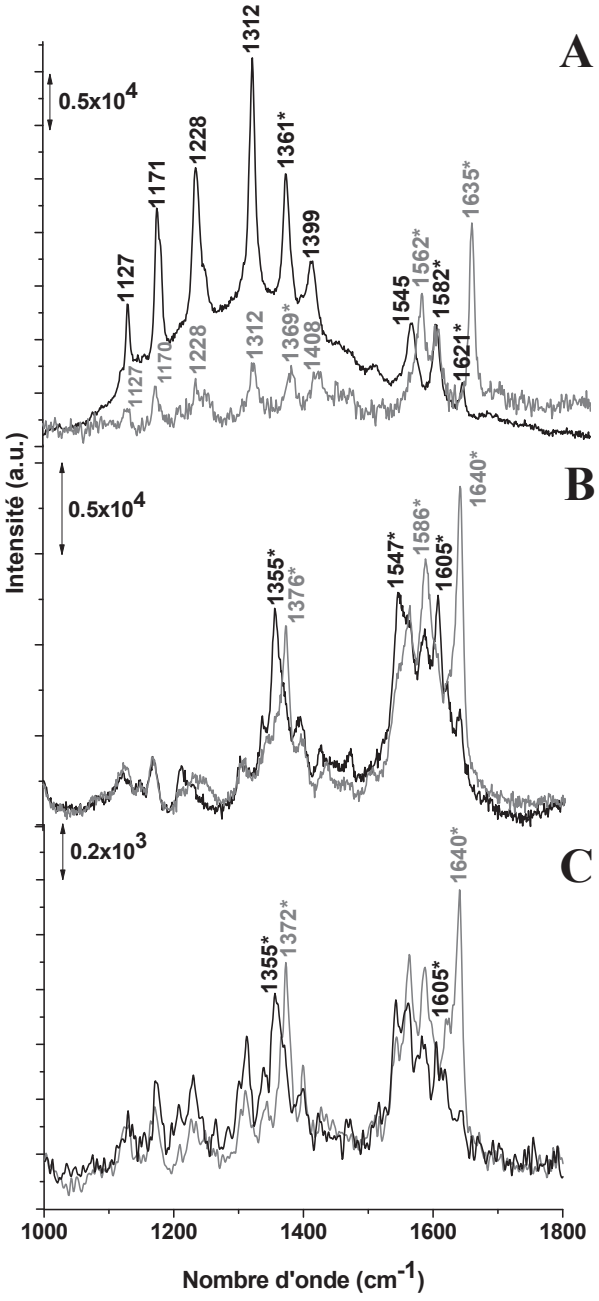

Figure 11: Spectres SERS des formes réduites (noires) et oxydées (gris) des Cyt *c* (A), Hb (B) et Mb (C) dans 10 mM KPi, 50 mM KCl à pH 8.0

I. INTRODUCTION

List of figures in chapter 1

1. Characterization of protein structure and function

Proteins play important roles in the living systems. They function like structural components of cells and cellular organelles, catalyze biochemical reactions, serve as signaling molecules, receive and respond to stimulus or function as one of the most important components of immune system in form of antibodies.[1] Membrane proteins are a special class of the proteins. They perform most of the specific functions in the biological membranes. Characteristic functional properties of the cell membranes are provided by these proteins.[2] Even small changes in the protein sequence or structure can change their functions. Certain living systems circumvent hostile atmospheres by changing or shuffling composition of their proteins. For example, the human immunodeficiency virus (HIV) evades host immune system by mutation of its own envelope protein. Thus, the proteins act as harbinger of life.[1]

Since the proteins play important roles in living systems it is of great interest to explore their structure, function, working mechanisms and other aspects. Moreover, in almost all cases of disease and disorder proteins are targets for different therapies and interventions. That is why protein studies are important. Thus, the methods and approaches to study the proteins become more diverse in terms of multitude of applied techniques and in terms of improving approaches within individual techniques. Proteins can be characterized by investigation of the structural, biochemical, electromagnetic, spectroscopic and thermodynamic properties.[3]

Some methods widely used to characterize protein structure and functions are briefly described below.

1.1 Methods to characterize protein structure and functions

The diffraction of X-rays by protein crystals. X-ray crystallography at atomic resolution is the main technique to solve the three-dimensional structure of molecules.

X-rays are electromagnetic radiation with a wavelength of around 0.1 nm. A small fraction of x-ray beam focused at the sample is scattered by the atoms in this sample. In the case of well-ordered crystal, the scattered waves reinforce one another at certain points and appear as diffraction spots when the x-rays are recorded (Figure 1).

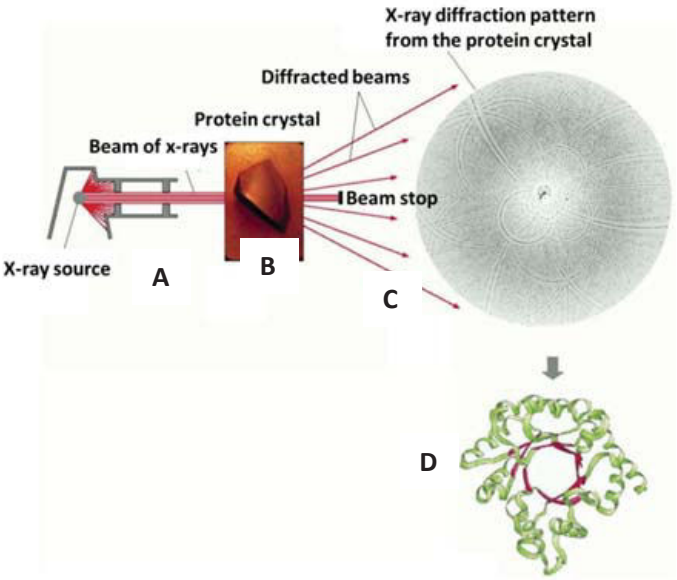

Figure 1: X-ray crystallography. (A) A narrow parallel beam of x-rays is directed at a well-ordered crystal (B). Shown here is a protein crystal of ribulose bisphosphate carboxylase, an enzyme with a central role in CO_2 fixation during photosynthesis. Some of the beam is scattered by the atoms in the crystal. The scattered waves reinforce one another at certain points and appear as a pattern of diffraction spots (C). This diffraction pattern, together with the amino acid sequence of the protein, can be used to produce an atomic model (D). The complete atomic model is hard to interpret, but this simplified version, derived from the x-ray diffraction data, shows the protein's structural features clearly (α helices, *green*; β strands, *red*)[4]

Information about the locations of the atoms in the crystal can be obtained from the position and intensity of each spot in the x-ray diffraction pattern. Nowadays, x-ray diffraction analysis becomes automated and the limit step is generation of suitable protein crystals.

The three-dimensional structures of about 10000 different proteins have now been determined by x-ray crystallography or by nuclear magnetic resonance (NMR) spectroscopy (see below).

Molecular structure determination using nuclear magnetic resonance spectroscopy. Nuclear magnetic resonance (NMR) spectroscopy is the technique widely used to analyze the structure of small molecules. Nowadays, it is also applied to study small proteins or protein domains. NMR requires a small volume of concentrated protein solution that is placed in a strong magnetic field.

Certain atomic nuclei, like those of hydrogen, have a magnetic moment or spin. In the strong magnetic field spins of the atoms are aligned but they can be misaligned in response to applied radiofrequency (RF) pulses of electromagnetic radiation. Upon relaxation of the excited hydrogen

nuclei they emit RF radiation, which can be measured and displayed as a spectrum. Emitted radiation depends on the environment of each hydrogen nucleus. The spectral shifts reveal the distance between the interacting pair of hydrogen atoms. Thus, NMR can provide the information about the distances between the parts of the protein molecule.

NMR spectroscopy can readily determine the structure of small proteins of about 20000 Da or less because of the technical reasons (loss of resolution). Nevertheless, now the technical advances have changed the limit to 100000 Da.

Sequence similarity can provide clues about protein function. Owing to the proliferation of protein and nucleic acid sequences which are catalogued in genome databases, the function of a gene – and subsequently its encoded protein – can often be predicted by simply comparing its sequence with the sequence of previously characterized genes. Since amino acid sequence determines protein structure and structure defines the biochemical function, proteins with a similar amino acid sequence often perform similar biochemical functions, even when they are found in distantly related organisms.

The most popular sequence alignment programs are BLAST and FASTA. They scan the database for similar sequences until a cluster of residues falls into full or partial alignment. These comparisons allow prediction the functions of individual proteins, families of proteins, or even the entire protein complement of a newly sequenced organism. But the predictions on the basis of sequence analysis are often only a tool to direct further experimental investigations.[4]

1.2 Vibrational spectroscopy as a valuable tool for the investigation of protein structure and functions

Vibrational spectroscopy has significant potential as an analytical technique to study proteins at the molecular level because vibrations are reporters of group structure and group environment. Because of the large number of normal modes, the vibrational spectrum is complex with many of the overlapping vibrational bands. Therefore, attempts to extract important information from the spectrum may appear complicated. However, this is not the case. On the one hand it is often possible to choose a spectral region that gives answers to specific questions. On the other hand, using special difference techniques it is possible to observe only those groups that actively participate in a catalytic reaction.

The vibrational spectrum of biomolecules can be registered using Raman scattering and the absorption of infrared (IR) light. A change of 0.02% of the bond strength can be easily detected by vibrational spectroscopy. Since the bond energy and bond length are directly related, bond distortions during the reaction can be monitored with a good accuracy.[5] It was concluded: "although an oversimplification, it can be said that the resolution of vibrational spectroscopy picks up where diffraction and multidimensional NMR techniques leave off, at approximately 0.2 Å, and extends down to much lower lengths".

Thus, a wealth of information about structure and environment of amino-acid side-chains, the protein backbone, about bound ligands or cofactors can be extracted from the spectral parameters: band position, bandwidth and absorption coefficient. Therefore, vibrational spectroscopy is a valuable tool for the investigation of protein structure, of the molecular mechanism of protein reactions and of protein folding, unfolding and misfolding.[6]

Recent progress in the area of Surface enhanced infrared absorption spectroscopy (SEIRAS) and Surface enhanced Raman spectroscopy (SERS) overcome some of the limitations of sensitivity of detection when using traditional IR and Raman spectroscopies to study proteins.
Despite the exciting advances and the growing use of SEIRAS and SERS in the protein studies, there is still a great potential for further development of these techniques. This mainly concerns the development of a reproducible method for surface preparation. Once this has been achieved, SEIRAS and SERS could have a much greater impact within protein studies and could be used more reliably within medical diagnostics.[7]

In this PhD work two approaches to study the proteins were developed: SEIRAS coupled to perfusion cell and surface enhanced Raman spectroscopy combined to electrochemistry.

In the section 2 some experimental approaches related to the SEIRAS studies will be described first and then in the section 3 some important experimental aspects for the studies by means of electrochemical SERS will be presented.

2. Study of the protein structure and functions by SEIRAS

2.1 Immobilization of proteins to solid surfaces

An appropriate immobilization of the proteins to the solid surfaces is an important step to form a stable membrane protein monolayer for the further studies with SEIRAS. The amphiphilic character of membrane proteins and their low conformational stability affect their properties through the interaction with the solid surface. Proteins can be adsorbed to surfaces by different interactions such as electrostatic attraction, hydrogen bonding, hydrophobic interaction, etc. Since the energies are weak, the diversity of these interactions often results in the non-specific binding which is unfavorable for functional studies. One of the major challenges in protein immobilization is to control the protein orientation and retain biological activity at the same time (see also section 3.3).[8] Some examples of immobilization of the proteins to solid surfaces are described below.

2.1.1 Surface-tethering of membrane proteins with histidine tags

Chelator-based immobilization is widely used in chromatographic protein purification[9] where the interaction of oligo-histidine tags (His-tag) with di-valent metal ions immobilized *via* chelators such as nitrilo-triacetic acid (NTA) is used. His-tags contain a sequence of six to twelve histidine residues that specifically bind to transition metals like Cu(II), Co(II), Zn(II), or Ni(II).[10] The proteins that carry a His-tag, are normally generated by genetic engineering. The localization of the His-tag in the protein can be arbitrary chosen. The interaction between His-tag and Ni-NTA is much more specific comparing to electrostatic interactions between protein and SAM surfaces.

After the immobilization of the protein *via* the His-tag to the surface the bio-beads can be added to the bulk solution to remove the detergent from the protein.[11] Lipids can be supplied in order to replace the detergent and form a lipid layer surrounding the protein molecules.[12] The reconstitution of membrane proteins into lipid layers provides the long-term stability of protein films.

This method of immobilization is widely used in the present PhD work for the development of a combined SEIRAS-perfusion approach that can be used to study the proteins such as Lactose Permease (LacY) and complex I.

2.1.2 Streptavidin/biotin interaction as an alternative to the His-tag/NTA approach

The streptavidin/biotin interaction is an alternative to the His-tag/NTA approach. Biotin (Figure 2) has an extremely high binding affinity to tetrameric streptavidin (K_d of 10^{-15} M). This is considered to be the strongest non-covalent binding entity in nature.[13]

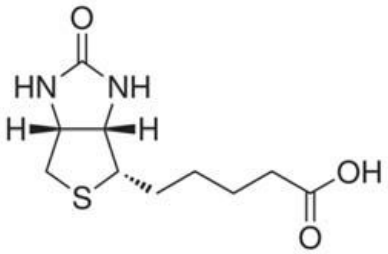

Figure 2: Structural formula of biotin

After the preparation of a biotin modified gold surface by 1-Ethyl-3-(3-dimethylaminopropyl)carbodiimide (EDC) catalyzed reaction with cysteamine, two of the four binding sites of streptavidin interact with immobilized biotins while the other two are exposed to the bulk solution. The latter sites are available to bind the strep-tagged proteins. The strep-tag is a peptide that binds to streptavidin at the same binding site as biotin. It was reported previously that this approach was successfully used for the immobilization of the glutamate transporter *ecgltP* from *Escherichia coli*.[14] The streptavidin/biotin method is superior to the His-NTA approach because it is more selective. But the streptavidin tetramer has a high molecular weight (4 × 13 kDa) and it forms a bulky layer along the plasmonic surface. Thus, this protein layer decreases the effective amount of photons due to absorption in the fingerprint region. Moreover, it forms a physical spacer on top of which bound species might not be probed with high sensitivity anymore. From this point of view, the His-tag immobilization technique is advantageous.

2.1.3 Nanodiscs: a variation of His-tag/Ni-NTA immobilization

Membrane proteins must be folded into the stable three-dimensional structures in order to accomplish their function. Living cells use a complex apparatus to control protein folding and membrane insertion. Sligar and coworkers[15] introduced the so-called nanodiscs in order to study the folding process under controlled conditions. Nanodiscs consist of small patches of lipid bilayer

(10 – 20 nm in diameter) surrounded by an amphiphilic scaffold protein. This protein shields the hydrophobic fatty acid chains from the aqueous buffer solution and inhibits spontaneous vesicle formation (Figure 3). Nanodiscs are used as the water-soluble carriers and provide a native environment for the proteins. Oriented binding can be achieved due to the His-tag modified scaffold protein. It is important that the scaffold protein necessarily carries a His-tag but the target membrane protein is studied in its wild-type form.

Up to now only Vogel and coworkers reported a SEIRAS application of nanodiscs to study G-protein-coupled receptor (GPCR) rhodopsin.[16]

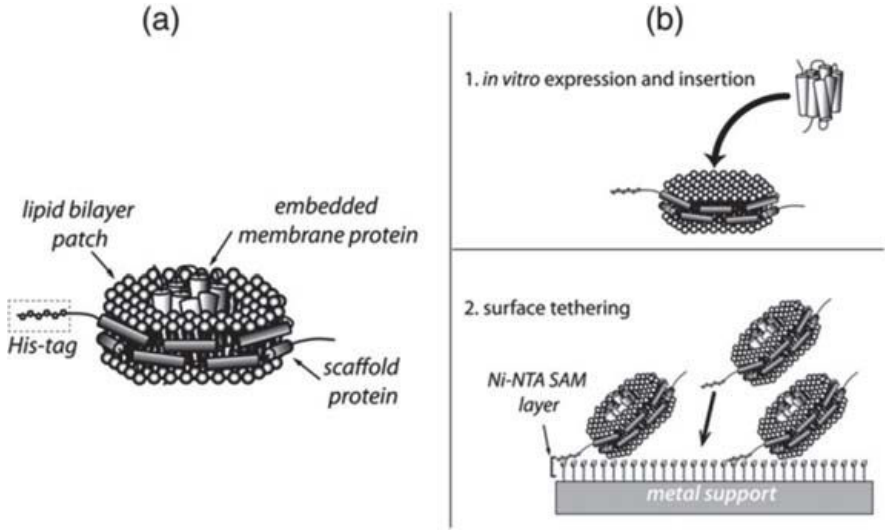

Figure 3: (a) Membrane protein embedded in a nanodisc composed of lipid bilayer and membrane scaffold protein. (b) The membrane protein folds into the nanodisc during or after *in vitro* expression. Afterwards the protein/nanodisc is tethered to the Ni-NTA SAM modified surface via the His-tag at the terminus of the scaffold protein[8]

Once immobilized, the protein studies can be performed.
Conformational changes of the proteins are crucial for their functioning. Thus, in order to understand protein functions it is also important to know about their conformational changes. Therefore, general information on the conformational changes of the proteins is given below.

2.2 Conformational changes in proteins

Overview of conformational changes. Protein conformation is very important in the understanding biomolecular interactions. In the simplest case, two molecules may interact with no change in their conformation, as the key-and-lock model. Interactions between the molecules that involve their

conformational changes are more versatile. In the induced-fit model, first two molecules undergo conformational changes at their interface and only after they interact optimally with each other.

Conformational changes in proteins are possible due to their intrinsic flexibility. These changes may occur with only relatively small consumption of energy. Conformational changes in single polypeptides at the molecular structural level are the result of changes in main chain torsional angles and side chain orientations. The overall effect of these changes may be the reorientations of few residues and small torsional changes. On the other hand, torsional changes localized at few critically placed residues may result in the large changes in tertiary structure. The later type of conformational changes is described below and it is known as domain motions.

Domain motions. Domain motions comprise two basic components: hinge and shear motions. Hinge motions may occur within alpha-helices, beta-sheets and strands that are not constrained by tertiary packing forces. In order to undergo the hinge-motion, residue must bear little tertiary structure packing constraints on its main chain. The hinge lies outside the interface between the two domains connected by this hinge. A bound ligand usually stabilizes the closed conformation of the protein. If the closed conformation is strongly held together without a ligand, then the hinge opening will have to overcome a high energy barrier.

Another type of motions – shear motions – occur parallel to the interface between closely packed segments of polypeptides. This type of motion is more severely constrained comparing to the hinge one due to interdigitating side chains. Combination of a number of shear motions results in a large enough sheared domain motion. Proteins that undergo shear movements often have layered architecture. The shearing may occur across helix-helix, helix-sheet, helix-loop and sheet-loop interfaces.

Shear motion occurs at the level of tertiary structure interactions. Small shear movements not requiring the interdigitating repacking are common in domain motions. These shear movements are normally accommodated by the small changes in side chain torsional. Thus, the shear-motion causes the segments to shift and rotate relative to each other for up to 2 Å and 15°, respectively.[17-19]

Schematic representation of hinged and shear mechanisms for domain closure is shown in Figure 4.

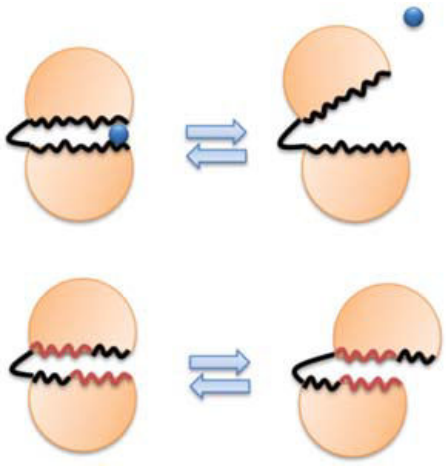

Figure 4: Hinged (top) and shear (bottom) mechanisms for domain closure. Ligand is represented as blue circle[18]

In the next sections widely used methods to induce changes in the immobilized proteins for the SEIRAS studies are described.

2.3 Methods to induce changes in immobilized proteins during SEIRAS studies

Subtraction of the absorption spectrum of the protein in one substate from the absorption spectrum of the same protein in another substate gives the difference spectrum. Acquisition of mid-IR difference spectra with sufficiently high resolution between two protein substates depends on the ability to manipulate the sample in a quantifiable way between the two substates.

In the ideal case the transition should occur in a manner that minimally perturbs other aspects of the protein. These transitions normally should be repeated many times with the same sample.

These conditions are critical since, typically, a change of the single normal mode that appears as a component of an IR difference spectrum can be as small as 10^{-5} OD of the underlying absolute IR absorbance of the protein itself.[20]

Four methods widely used to induce changes in the immobilized proteins during SEIRAS analyses are described briefly below.

2.3.1 Photochemistry

Light-induced infrared difference spectroscopy was the first technique that has been applied to study proteins from the early 1980s. Reactions in photosensitive proteins like bacteriorhodopsin[21-24] or in photosynthetic reaction centers[25-27] can be induced by continuous illumination or by a light flash. Light-induced difference spectra can be calculated from the spectra recorded before and during/after illumination.

In the case of photochemically-active systems, transitions are usually induced with light of an appropriate wavelength. This can minimally perturb the rest of the system, provided that the thermostatting is used, and changes can be induced rapidly to minimize the IR baseline drifts between states. This technique was first successfully applied for transmission FTIR spectroscopy[28, 29] and it can be used either with a pulsed actinic source to initiate fast transient reactions or with continuous illumination to induce a photostationary state[30, 31]. Non-photochemically-active electron transfer proteins can be also studied with this technique by addition of appropriate light-activated chemicals.[32] Photochemistry can be also applicable to samples measured in attenuated total reflection (ATR) mode.[33]

In this case, it is possible to change conditions, such as pH, ionic strength or specific reagents during the acquisition of photo-induced spectra of the same stable protein layer.[34]

2.3.2 Electrochemistry

Electrochemical control of the redox states of the electron transfer proteins was developed for the transmission mode by utilization of an optically transparent working electrode in combination with redox mediators to equilibrate the potential applied to the working electrode with the protein.[35] It is important that the same principle can be used with the ATR configuration.

Applied potential can be controlled manually or automatically *via* a conventional three-electrode potentiostat. Switch between several potentials or even full redox titration can be used to separate spectroscopic characteristics of individual redox centers in complex systems.[36, 37]

2.3.3 Dialysis

Dialysis manipulation method involves a microdialysis cell assembled above an internal reflection element (IRE) prism.

The perfusion ATR-unit is separated into two compartments (one for the sample and one for effector molecules) by a dialysis membrane (Figure 5). The membrane of a certain molecular weight cut-off (MWCO) is mounted 350 µm above the ATR crystal using a silicon O-ring (Figure 5B). The solution with the studied protein in the first compartment with a sample volume of below 5 µL is in contact with the ATR plate (Figure 5C). The upper flow compartment has a volume of approximately 100 µL (Figure 5A). ZnSe prism with diamond ATR plate for IR beam guide is illustrated in Figure 5D. A peristaltic pump is used to obtain pulsation-free flow.

The ultrasound head of an ultrasonic scaler can be coupled into the perfusion tube to provide the stirring since mechanical stirring in the micro volumes is impossible. The intensity of the ultrasound waves is adjusted strong enough to achieve faster equilibration in the dialysis chamber but low enough to keep the protein intact.

The perfusion-ATR unit is characterized by small volumes of the order of microliters for both the solution of the target protein and effector molecules, by high stability, fast response at high sensitivity for the detection of binding-induced conformational changes and reactions.[38]

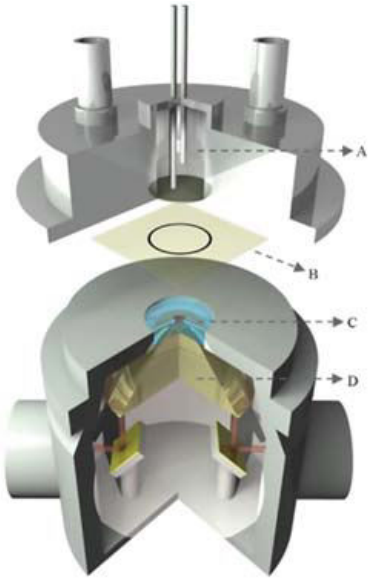

Figure 5: ATR–IR microdialysis cell: (A) compartment for continuous perfusion of solutions; (B) dialysis membrane with silicon O-ring; (C) compartment for target proteins; (D) ZnSe prism with diamond ATR plate for IR beam guide[38]

2.3.4 Perfusion

In the perfusion method, a buffer whose chemical composition can be changed by automated switching between two different buffer reservoirs is pumped over the protein film surface (Figure 6). At present, this method can be applied to stable hydrophobic protein layers adhered to the IRE in ATR mode, either as detergent-free hydrophobic protein or one that has been reconstituted into lipids. This method provides particular flexibility for the studies of ligand binding, redox changes or transitions between the intermediates. Difference spectra can be automatically recorded over many cycles by using programmable computer-controlled valves provided that the reaction can be made to be reversible.

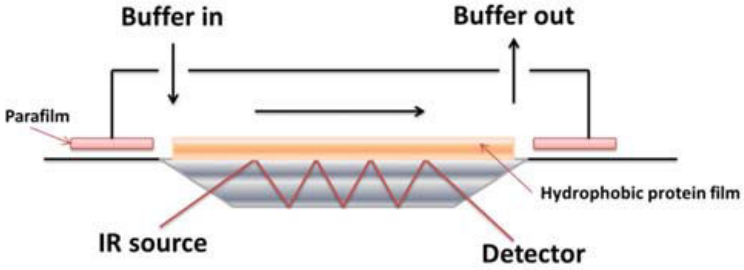

Figure 6: Schematic representation of perfusion cell[20]

This buffer exchange method in ATR mode was first applied to study the changes induced by ligand binding to the nicotinic acetylcholine receptor.[39] Afterwards, perfusion has been extended with more modern microprism IREs to monitor a wide range of changes induced by redox-state changes,[33, 40] ligand binding[41, 42] or interconversions between reaction intermediates.[43, 44]

In this PhD study a new combined perfusion-SEIRAS approach is developed and applied to investigate the transport proteins as well as the protein from respiratory chain. These proteins are described below in the next sections.

2.4 Lactose permease

A membrane transport protein is a membrane protein involved in the transport of ions, small molecules or macromolecules across the biological membranes.

Transporters are a class of membrane transport proteins that move different ions and molecules across cell membranes. These proteins undergo conformational changes after substrate binding and only bound molecules are transported across the membrane.[2]

Lactose permease (LacY) belongs to the membrane transport proteins and consists of 417 amino acid residues. It catalyzes the coupled translocation of a galactoside and an H^+ across the cell membrane (so called galactoside/H^+ symport).[45] LacY as well as many major facilitator superfamily (MFS) members couples the free energy that releases from the downhill translocation of H^+ in response to the H^+ electrochemical gradient ($\Delta\mu_{H}^{+}$) to drive accumulation of galactopyranosides against a concentration gradient. Even in the absence of $\Delta\mu_{H}^{+}$ LacY can transduce the energy released from the downhill transport of sugar to drive uphill H^+ transport generating $\Delta\mu_{H}^{+}$.[46]

X-ray crystallography revealed the crystal structure of LacY. It has N- and C-terminal domains, each one with six largely irregular transmembrane helices that surround an aqueous cavity open to the cytoplasm. Another structure with a narrow periplasmic opening and an occluded galactoside was obtained as well. This structure confirmed many observations indicating that binding of sugar involves induced fit.

The crystal structure of inward-facing conformation of LacY is depicted in Figure 7. The structure represents two 6-helix bundles that are related by a quasi-twofold symmetry axis perpendicular to the membrane plane and are linked by a long cytoplasmic loop between helices VI and VII. Moreover, each six-helix bundle contains two 3-helix bundles with inverted symmetry. LacY has a deep hydrophilic cavity that is surrounded by the two 6-helix bundles. This cavity is tightly sealed on the periplasmic face and open to the cytoplasmic side only (so called an inward-open conformation).

The initial structures led to the alternating access model for transport in which the substrate-binding site is alternatively exposed to either side of the membrane due to the rotation of two 6-helix bundles against each other.[47, 48]

Figure 7: Ribbon presentation of LacY in an inward-open conformation. (Left) N-terminal helix bundle (light yellow). (Right) C-terminal helix bundle (tan). The cytoplasmic side is shown at the top. Bound β-D-galactopyranosyl-1-thio-β-D-galactopyranoside (TDG) is represented in magenta (PDB 1PV7)

Binding of sugar to the purified LacY in detergent does not change an ambient pH.[49] This indicates that LacY is protonated over the physiological range of pH. Many observations suggest that protonation precedes galactoside binding on one side of the membrane and follows sugar release on the other side (Figure 8).[45, 50]

Symport mechanism starts with protonation of LacY (step 1 or 6 for influx or efflux, respectively). Sugar (S) binding to protonated LacY (step 2 or 5) induces a conformational change to an occluded conformation (step 3 or 4), which afterwards can relax to either side where sugar dissociates first (step 2 or 5), followed by deprotonation (step 1 or 6) and relaxation to the not bound LacY *via* an apo occluded intermediate (steps 7 and 8). When symport is in the influx direction (step 1, protonation), the pK is very alkaline (~10.5), and step 6 (deprotonation) normally should have much lower pK value for deprotonation to occur (i.e., Arg302 approximates protonated Glu325).[46]

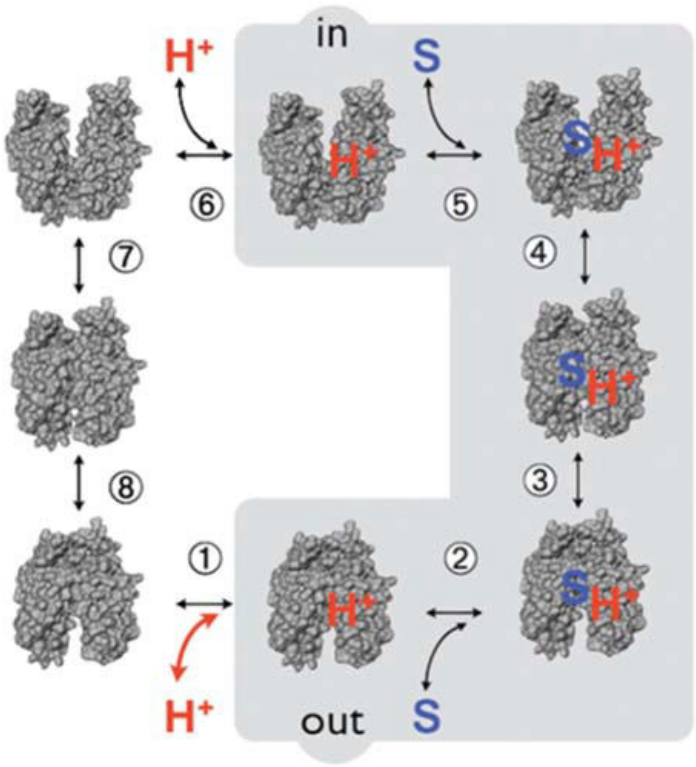

Figure 8: Kinetic scheme for galactoside/H^+ symport, exchange, and counterflow[46]

It is very probable that the rate-limiting step for lactose/H^+ symport in the absence of $\Delta\mu_H^+$ is deprotonation, whereas in the presence of $\Delta\mu_H^+$ the rate-limiting step is opening of apo LacY on the other side of the membrane.[51, 52]

2.4.1 Experimental approaches used to study LacY

Different experimental approaches provided a strong evidence of the alternating access mechanism in LacY.

Site-directed alkylation (SDA) data provided evidence that binding of sugar markedly increases the probability of opening on the periplasmic side, but that binding of sugar also increases the probability of closing on the inside. This implicates that opening and closing may be reciprocal.[53-55]

Single molecule fluorescence resonance energy transfer (sm-FRET) was used to study ligand-induced distance changes on the cytoplasmic and periplasmic sides of LacY. It was shown that addition of a sugar results in a decrease of the distance on the cytoplasmic side and in distance distribution on the periplasmic side. The results support the alternating access model.[56]

The double electron-electron resonance (DEER) measurements also provided strong confirmation of the alternating access model. Moreover, multiple distance distributions that have been typically observed for the WT symporter with or without bound sugar may implicate the presence of intermediate conformation(s) in LacY.[57-59]

Site-directed cross-linking provided the information that 17 Å is the minimum length of cross-linker which is necessary for maximum transport activity. The distance is similar to that obtained from DEER measurements for opening of periplasmic side in the presence of sugar.[60]

Fluorescence of intrinsic Trp151 residue in LacY is a sensitive tool for functional studies. This approach allows direct measurement of sugar binding and global conformational changes in LacY. The results provided yet another strong confirmation of the alternating access mechanism.[61-63]

However, there are still many questions concerning the functioning of LacY that must be clarified. For example, which residue(s) is/are responsible for such a high pK of sugar binding? Is there a special residue that plays a central role in the "coupling" mechanism of symport?

To give the insight on these and many other questions the new sensitive approaches must be developed.

2.5 Complex I

As was mentioned above in the section 2.3.4 developed perfusion-SEIRAS approach would be also interesting to apply to study the protein from the electron transport chain (ETC). ETC comprises complexes transferring electrons from electron donors to electron acceptors *via* redox reactions. The electron transfer is coupled with the transfer of protons across a membrane.

Complex I (NADH:ubiquinone oxidoreductase) plays an important role in the electron transport chain in mitochondria and many bacteria. It provides about 40% of the proton flux during proton-motive force generation which is necessary for the synthesis of ATP (adenosine triphosphate).[64-69] Complex I catalyzes the transfer of two electrons from reduced nicotinamide adenine dinucleotide (NADH) to ubiquinone which is coupled to the translocation of four protons across the inner mitochondrial membrane.[70] Complex I is a reversible machine that can utilize the trans-membrane (TM) potential to reduce NAD^+ by ubiquinol.[71]

Complex I belongs to the family of membrane-residing oxidoreductases that are found in all kingdoms of life. The members of this family couple oxidation of different soluble electron donors and reduction of membrane bound quinone analogues to the translocation of ions against TM potential.[72]

Bacterial complex I is a mini model of the mitochondrial enzyme.[73] It is the L-shaped assembly that comprises 14 "core" subunits (7 hydrophilic and 7 hydrophobic, ~550 kDa combined mass) conserved from bacteria to humans (Figure 9).[64, 65, 68]

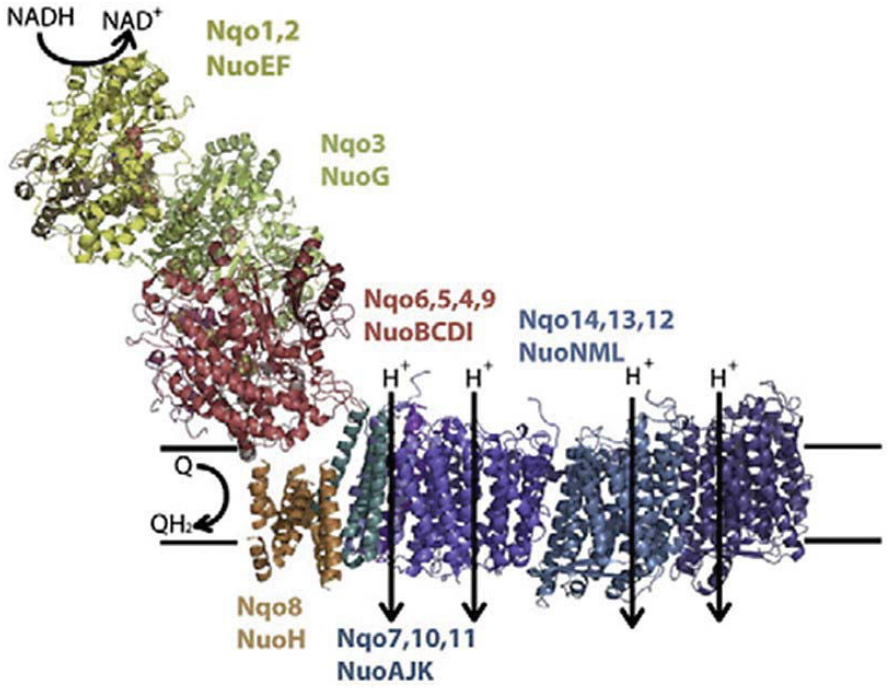

Figure 9: Structure of the entire *Thermus thermophilus* complex I (PDB 3M9S)[74]

Different modules of complex I are presented in Figure 9: the NADH oxidizing or N-module (subunits NuoEFG) which is necessary for electron input from NADH into the chain of iron–sulfur clusters (Figure 10), the Q-module, which contains subunits NuoBCDI that conduct electrons to quinone binding site and proton translocating P-module (subunits NuoLMNKAJ) necessary for the pumping of the protons across the membrane.[66]

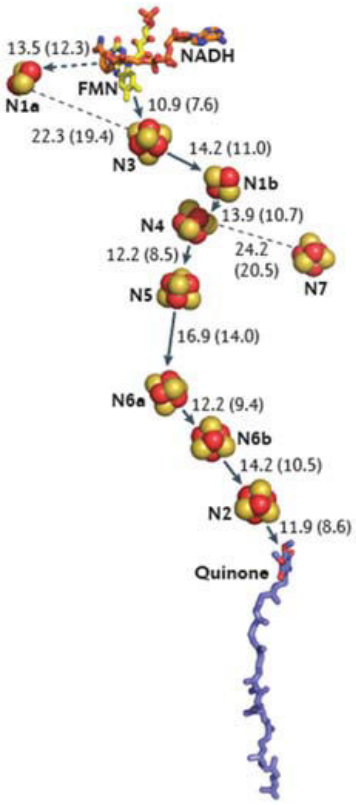

Figure 10: Electron transfer chain in *T. thermophilus*. Crystallographic positions of all electron carriers are shown, except ubiquinone, which was placed manually in the predicted Q-site[74]

First, NADH (electron donor) binds to the binding pocket in the NouE subunit of the peripheral arm enabling effective hydride transfer to flavin mononucleotide (FMN).[75] Suggested electron transfer pathway on the basis of distance analysis between redox centers is: NADH→FMN→N3 →N1b→N4→N5→N6a→N6b→N2→Q. Transfer of two electrons at the first step (FMN reduction) and last step (quinone reduction) in the chain is involved but Fe–S clusters transfer only one electron at a time. It was suggested that the limiting step of overall rate of electron transfer is quinone binding and release.[76] As can be expected for the terminal cluster in the redox chain N2 has the highest potential (–100 mV to –150 mV) whereas N3, N4 and N6a are equipotential at about –250 mV.

In opposite, the intermediate clusters N1b, N5 and N6b have lower potentials, in part due to the electrostatic interactions with reduced clusters nearby resulting in alternating high and low potentials, or a "roller-coaster" redox profile along the chain.[77]

It was suggested previously that in complex I electrons may be delivered through the remote cluster N7 in subunit NuoG (Figure 10).[68] Cluster N7 in complex I from *Thermus thermophilus* is 20.5 Å away from cluster N4 which is the nearest cluster of the chain. Since a cut off distance is ~14 Å such a distance is incompatible with physiological electron transfer.[78] Thus cluster N7 was thought to be an evolutionary remnant.[79] However, in the 12 subunit (missing subunits NuoF, E) analogues of complex I from microaerobes *Campylobacter jejuni* and *Helicobacter pylori*, it was revealed that NuoG contains additional conserved cysteines in the N-terminal part which were suggested to ligate an additional Fe_4S_4 cluster.[80]

P-module comprises six membrane embedded subunits. The three largest subunits, NuoL, M and N, are homologous to each other. A structural motif of 14 TM helices common between these subunits was revealed by the crystallographic structure .[81] Ten helices constitute a conserved functional core which is divided into two five-helical bundles that are related to each other by internal symmetry. This ten-helical core comprises charged, membrane embedded, conserved and functionally important amino acids that are found on flexible TM helices,[82] suggesting that these subunits might actively translocate the protons across the membrane.

Crystallographic structures of complex I determined the positions of all subunits. Complex I operates by a conformation driven mechanism[81, 82] that is why the energy of electrons fed from NADH must be converted into the conformational changes in the membrane domain driving proton translocation across the biological membrane.

Reaction that is catalyzed in the coupling site of complex I:

$$Q + 2e^- + 2H^+ \leftrightarrow QH_2$$

Two protons must be delivered to the catalytic sites for H_2 and ubiquinone reduction. It was suggested previously that the protons might be delivered either from bulk solvent directly or the proton translocation pathway may be present, either within subunit NuoH or, as was supposed, in the subunit NuoD.[75]

A cyclic scheme in Figure 11 represents the suggested cycle and mechanism of conformational changes in complex I. In the suggested model protein conformation determines affinity of quinone and quinol to the coupling site. The mechanism is fully reversible.

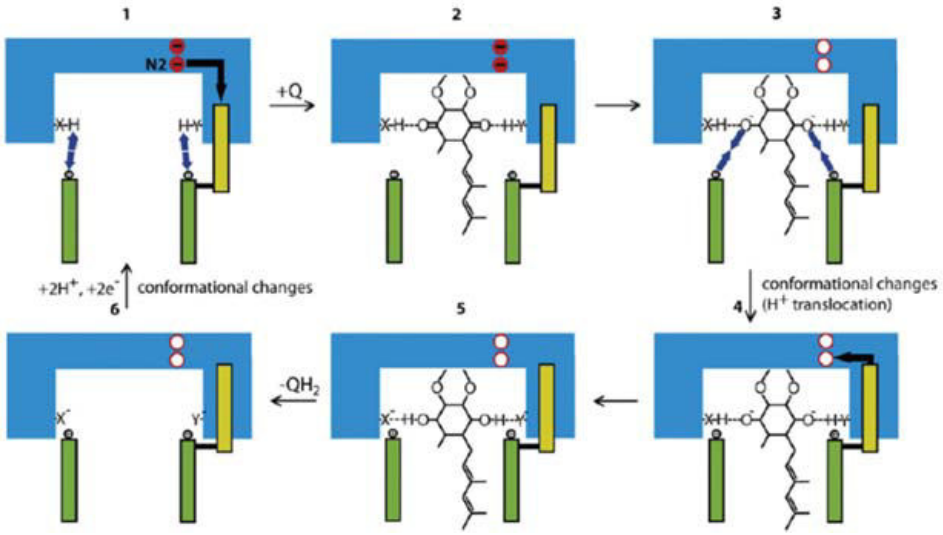

Figure 11: Representation of the proposed model of conformational coupling in complex I. Cluster N2 and the adjacent reducible cluster (most probably N6a[(83)]) are shown as red circles empty when oxidized and filled when reduced[(74)]

Direct cycle: first, ubiquinone binds (state 1→state 2) to the Q-site where ionisable amino acid residues with high pK_a values form hydrogen bonds to quinone's keto groups. Ubiquinol ion is formed upon transfer of two electrons (state 3). Conformational changes driving proton translocation are induced by the electrostatic interaction (blue arrows) between negatively charged quinol and positively charged groups on movable structural elements (green cylinders) (state 3→state 4). Oxidation of cluster N2 results in the shifts (black arrow) of nearby hydrophilic helices (yellow cylinder),[(84)] assisting conformational changes. As a result of approach of positively charged groups, pK_a value of quinol coordinating groups is reduced, leading to protonation of ubiquinol (state 5). Re-protonation of negatively charged groups X and Y is allowed after dissociation of ubiquinol (state 6). Protein charge distribution is returned to initial state and this leads to relaxation of the structure into the initial conformation (state 1). Reverse shifts of helices (black arrow) assisting this conformational change occurs after reduction of cluster N2 and adjacent cluster.

It is important to note that state 1 is the lowest energy state in the absence of TM potential, while in the presence of high trans-membrane potential state 6 is the lowest energy state.

However, there are still many questions related to the molecular mechanism of functioning. For example, the details of oxidoreduction catalysis for NADH and quinones,[(71, 85, 86)] directed ion

transport across membranes[82, 87] and electron transport by metal prosthetic groups[88] are well understood but the energy transformation from the transfer of electrons into mechanical movement is still not understood in complex I.

That is why development of the new approaches that can give insight onto the molecular mechanism of membrane protein functioning is of a great importance.

In the following sections another part of the PhD work related to the development of a combined electrochemical-SERS approach will be presented.

3. Development of a combined electrochemical and surface enhanced Raman spectroscopic approach

3.1 History of electrochemical surface-enhanced Raman spectroscopy

The surface-enhanced Raman scattering (SERS) spectra were first obtained from an electrochemical cell leading to the discovery of the SERS effect in mid-1970s.

The first vibrational spectroscopy that was employed to characterize species on electrode surfaces was Raman spectroscopy. However, the intrinsic disadvantage of Raman process is its very low detection sensitivity. Thus, performing of electrochemical Raman experiments without enhancement was not possible.[89]

Therefore, Fleischmann, Hendra and McQuillan of University of Southampton developed an approach to increase the number of adsorbed molecules (they chose pyridine, Py). They increased the surface area of the Ag electrode using electrochemical roughening method by applying about 450 potential oxidation and reduction cycles (ORC) to the Ag electrode. It was unexpected but obtained Raman spectrum was of a high quality.[90] First it was supposed that the high quality spectra were obtained due to the large number of Py molecules adsorbed on the significantly increased surface area of the electrode. In fact, this was the first SERS measurement and the roughened electrode was the first nanostructure exhibiting the SERS activity. Nevertheless this SERS effect was recognized only in 1974.

Jeanmaire and Van Duyne of Northwestern University surprisingly revealed that, starting from the degree of the roughness used by Fleischmann *et al.*,[90] Raman signals increased as the surface roughness decreased. In fact, this was the first demonstration that the SERS effect depends on the

size of nanostructures. Albrecht and Creighton of University of Kent reported independently a similar result in the same year.[91] These two groups provided the strong evidences that the enormously strong surface Raman signal is caused by the surface-enhanced Raman scattering (SERS). These findings opened up a great opportunity to design highly sensitive surface diagnostic techniques that can be applicable to not only electrochemical but also biological and other ambient interfaces.

An important progress in electrochemical surface-enhanced Raman spectroscopy was made in the mid-1990s. VIIIB transition metals that are of a great importance for electrochemistry and catalysis were used for the substantial surface Raman enhancements. Since the early-2000s, well-controlled nanostructures of both coinage (e.g., Au, Ag and Cu) and transition metals replaced randomly roughened surfaces. These nanostructures were introduced as a very promising class of highly SERS-active substrates.[92] Until now, many molecular-level investigations by Raman spectroscopy of different adsorbates at different material electrodes have been successfully performed. Thus, Raman spectroscopy became a widely used method in electrochemistry. Moreover, a systematic study on electrochemical-SERS (EC-SERS) processes could be useful to give insight on the SERS mechanisms.[89]

Thus, fabrication of the appropriate SERS active electrode surfaces is an important step for the subsequent successful EC-SERS studies. Some widely used approaches are reviewed below.

3.2 Preparation of SERS-active electrode surfaces

From the previous SERS studies of Au, Ag and Cu it is well-known that for a large surface enhancement some form of surface roughness is a necessary, but not sufficient, requirement.

With the progress in nanoscience and nanotechnology, the SERS active substrates have been expanded from massive metal electrodes to nanoparticle assembled electrodes and template fabricated substrates for the larger enhancement.[89]

3.2.1 Electrochemical oxidation and reduction cycle(s)

The electrodes for the EC-SERS studies are normally made by sealing a metal rod into an inert Teflon® sheath.

Reproducibility of the experiments can be improved by the mechanical polishing of the electrode surface with alumina powders down to 0.3 μm, rinsing with ultra pure water and sonication in order to remove any adhering alumina. Surface impurities can be also removed by electrochemical cleaning. Afterwards, the electrode surface can be activated by electrochemical oxidation and reduction cycles (ORC). Different ORC conditions can be used depending on the used electrode material. Different parameters can vary during the ORC roughing process: oxidation and reduction potentials, the type of potential-time function and the amount of charge passed during the oxidation step. The choice of the applied potential is dictated by the used electrode material and electrolyte.[89]

3.2.2 The use of metal nanoparticles

The SERS substrates fabricated by electrochemical roughening process have a rather broad distribution of roughness. Alternatively, nowadays with the development of nanotechnology it is possible to synthesize or fabricate metal nanostructures with shape and size with a narrow size distribution. The surface uniformity of the EC-SERS substrate can be significantly improved by the nanoparticles assembled on an electric conductive substrate. Thus, assembled nanoparticles or nanoparticle sols are widely used in recent years as SERS active substrates.[89]

Figure 12 represents different ways of plasmon-assisted Raman scattering. Bare Au nanospheres are deposited as a film on a solid support and the studied molecules (blue dots in Figure 12A) are in direct contact with the surface of Au nanospheres. The same contact mode can be applied to the transition-metal-coated nanoparticles (NPs) (Figure 12B). This can extend the application of SERS to other wavelength regions and transition-metal-catalyzed reactions.

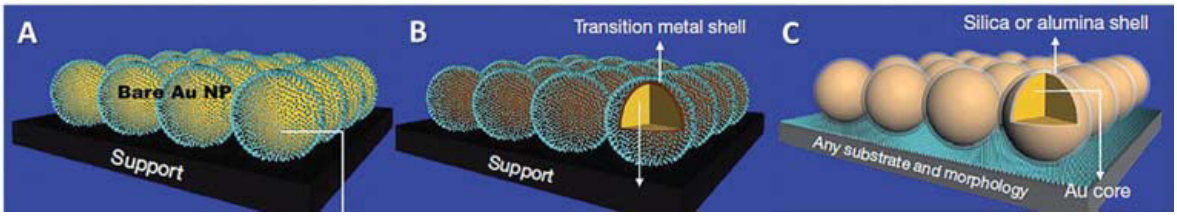

Figure 12: Different modalities of SERS[93]

In the shell-isolated nanoparticle-enhanced Raman spectroscopy (SHINERS)[94, 95] the Au nanospheres are protected by a 2 nm ultrathin glass shell (Figure 12C). This shell isolates the gold surface from the probed molecules and therefore prevents the possible disturbing interactions. On the other hand, significant NP-enhanced Raman signal still can be achieved at the metal–molecule

separation of 2 nm. A very large number of "tips" are simultaneously probing the underlying molecules because a "smart dust" of Au/SiO_2 particles is covering the entire surface. The thickness of the glass shell can be controlled. A very thin aluminum oxide shell can be also prepared in addition to encapsulation by silica.[93]

Thus, the synthesized metal nanoparticles can then be deposited on the conductive solid electrode surface, for example on Au, Pt, or Pd surface, glassy carbon, indium tin oxide (ITO) and used for EC-SERS studies. Before the assembly a solid electrode surface must be thoroughly polished or cleaned. Afterwards, solution containing nanoparticles are deposited on the electrode surface and left for drying in air or under vacuum.[89]

This approach is very flexible and can be applied to probably any surface.[93]

3.2.3 Fabrication of ordered SERS substrates by template method

Very ordered substrates with controlled inter-particle spacing can be fabricated by the promising template methods. Nanosphere lithography (NSL) is a widely method used for the preparation of SERS-active substrates.[89] Outstanding control over NP size, shape and interparticle spacing can be provided by this very powerful and highly flexible nanofabrication approach.

The following description of NSL refers to the single-layer periodic particle array which is the simplest configuration.[89, 96-98] The surface of a substrate is covered by a self-assembled monolayer of hexagonally close-packed nanospheres (Figure 13 top).

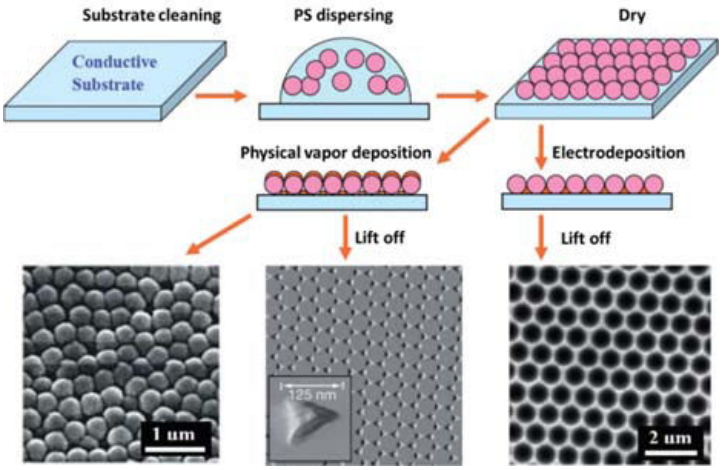

Figure 13: Nanosphere lithography for the fabrication of nanostructured SERS substrates[89]

The nanospheres are drawn together by capillary forces upon solvent evaporation. Afterwards the resulting self-assembled 2D monolayer of hexagonally packed nanospheres can be used as a colloidal crystal mask (side view: Figure 13 top right; top view: Figure 14) for the following deposition of metal onto this mask, either by physical vapor or electrochemical deposition (Figure 13 middle).[89]

Metal can reach the substrate through the C_3-symmetric interstices (Figure 14) while all other regions on the substrates are hidden by the colloidal crystal mask.

Depending on the thickness of the deposited metal layer three types of nanostructured SERS substrates can be prepared (see Figure 13 bottom). Film-over-nanospheres (FON) surface (Figure 13 bottom left) can be fabricated by the physical vapor deposition on the crystal mask.

Sonication of the sample results in the removal of the nanospheres and leads to triangular-shaped Ag nanoparticles (Figure 13 bottom middle and Figure 14).

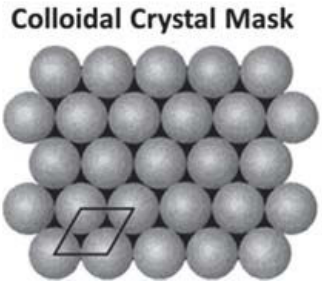

Figure 14: Colloidal crystal mask used as a template[97]

High field enhancements upon resonant plasmon excitation can be achieved due to the sharp tips. A thin structured film comprising a regular hexagonal array of uniform segment sphere voids (SSV), (Figure 13 bottom right) can be fabricated by the electrochemical deposition with subsequent removal of the spheres.

3.2.4 Fabrication of gold grids by means of electroforming

Electroforming was first observed by Jacobi during the electrodeposition of copper onto a printing plate in 1837.[99] The American Electroplaters' and Surface Finishers' Society (AESF) defines electroforming as "the production or reproduction of an article by electrodeposition upon a mandrel or mould that is subsequently separated from the deposit". Electroforming is a competitive process

in precision manufacturing since it is able to produce/reproduce shapes to close dimensional tolerances with good surface and superior metallurgical properties.

Basically, electroforming is a special form of electroplating. The basic principles of electroforming are represented in Figure 15. In electroplating, metal is dissolved electrolytically at an anode.

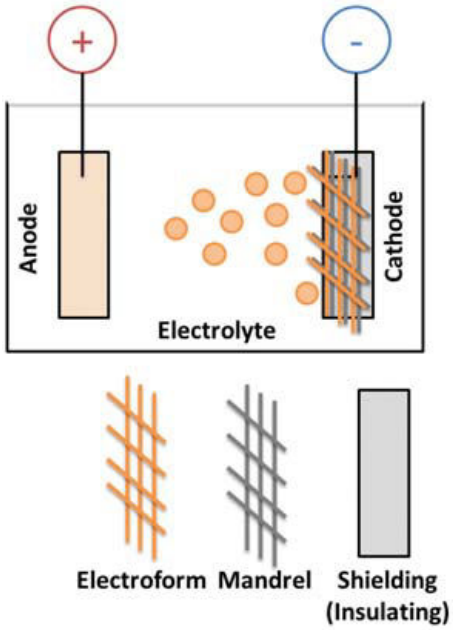

Figure 15: The principles of electroforming[(100)]

The purpose of use of the deposited metal makes the difference between electroforming and electroplating. In electroplating an existing article is covered by a metallic coating to provide decorative and/or protective surfaces. However, electroform is a metallic object that was fabricated by utilizing the electroplating process to deposit a metal on the mandrel. The purpose of electroform is to serve functionally or decoratively as a separate entity.
In practice, the mandrel (cathode) has the desired shape prior to electrodeposition. An exact replica of the mandrel surface is produced due to the ionic action of the process. The original (positive) form can be regenerated from the fabricated (negative) replica. Thus, many identical forms can be produced from a single mandrel.[(100)]

The side of electroform that was in contact with the plating solution and the one that was in the intimate contact with the mandrel have different surface morphology. The first side represents a rough surface with sharp edges and corners that can be thus a promising substrate for the surface

enhanced Raman spectroscopy.[101] Thus, gold grids fabricated by means of electroforming would be very promising for the coupled EC-SERS approach since they can serve as working electrodes and as SERS active substrates.

Covering the metal surface with biocompatible coatings can prevent irreversible structural changes of the proteins due to the electric field or the attack of metal ions. Therefore, general information about biocompatible surface modification of the electrodes is given below.

3.3 Biocompatible surface modification of the electrodes

The biocompatible coatings interact with the biomolecules in a way which is more closely related to their natural environment. Self-assembly of amphiphiles carrying a thiol function is the most versatile and simple coatings. The alkanethiol derivatives bind to Ag or Au due to the formation of a covalent metal-sulfur bond and afterwards they form the densely packed monolayers (self-assembled monolayers, SAMs) due to the hydrophobic interactions between the aliphatic chains.[102] The SAMs may be appropriately functionalized to allow for electrostatic, hydrophobic or covalent binding of the biomolecules. Thus, positively charged proteins can be immobilized on the SAMs made of carboxyl-terminated thiols *via* electrostatic interactions. The pK_a of the carboxylate group in the layer is distinctly higher compared to that of the molecule in solution. This pK_a shift depends on the electrode potential, the ionic strength, and the distance from the electrode.

The electrostatic binding of proteins can be also a first step toward covalent cross-linking. Thus, to form, for example, a cross-link between amino and carboxyl groups the last ones can be activated by 1-ethyl-3-[3-(dimethylamino) propyl] carbodiimide hydrochloride (EDC).

Nevertheless, since the surface enhancement decays with the distance from the electrode not all of the biocompatible coatings are suitable for SERS. Thus, the enhancement of the SERS signal at a distance of 3.5 nm from the surface is decreased by a factor of ca. 2.5 for a surface roughness of ca. 20 nm. Nevertheless, still this loss of intensity may be acceptable because the enhancement may still be sufficient for studying of bound proteins.

An alternative simpler approach is based on the direct adsorption of the solubilized proteins since the detergent molecules may provide a sort of ”protecting” surface coating.[103]

In order to study the proteins by means of EC-SERS they must be adsorbed on the working electrodes modified with the appropriate biocompatible SAMs.

The general description of an experimental setup normally used in the EC-SERS studies is given below.

3.4 Experimental setup used in electrochemical surface-enhanced Raman spectroscopy

In a typical electrochemical-SERS study, the electrochemical system is investigated upon changing of the electrode potential and recording the spectral response such as change of intensity and frequency or even the appearance of new bands. Normally, the experimental data is interpreted by analyzing the changes in intensity or frequency of some characteristic marker bands that can be directly related to a change in the structure, composition, morphology, surface coverage, orientation.

The core component of the EC-SERS experimental setup is the EC-SERS cell. Typically, the cell configuration comprises a conductive SERS-active working electrode, an inert counter electrode (it can be Pt wire ring) to form a closed circuit and a reference electrode (usually saturated calomel electrode, SCE, or a Ag/AgCl electrode) to indicate the potential of the working electrode. Schematic representation of the EC-SERS cell can be seen in Figure 16.

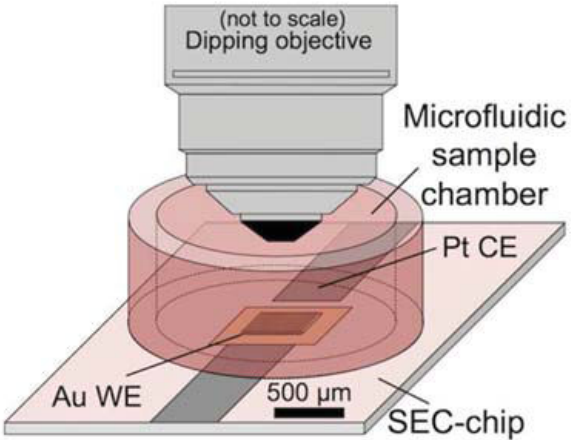

Figure 16: Schematic representation of the Raman spectroelectrochemical cell[104]

In order to allow both efficient Raman and accurate electrochemical measurements the three electrodes should be assembled in a good relative geometric position. For example, to ensure an accurate control of the applied potential the reference electrode should be placed very close to the

working electrode. To protect the solution or electrode from the contaminations an optically transparent quartz or glass window may be used.[89]

Some redox active proteins that can be studied by a combined EC-SERS approach are described in the following sections.

3.5 Heme proteins

Heme proteins, i.e., iron porphyrins, are ubiquitous protein cofactors and crucial elements which are necessary for the different biological functions of proteins and enzymes.[105]

These functions comprise the transport of molecular oxygen (hemoglobin), the transfer of electrons (cytochromes) and the metabolism of substrates (heme enzymes). It was reported as well that heme proteins may act as sensors or signal transducers.[106, 107] Hemes are cyclic methine-bridged tetrapyrroles with the four pyrrole nitrogens that coordinate the central iron (Figure 17).

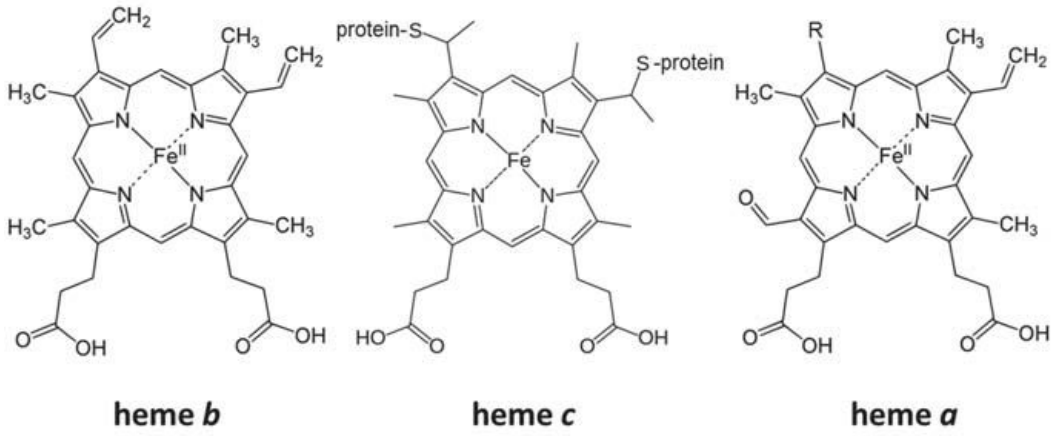

Figure 17: Structural formulas of heme *b*, heme *c*, and heme *a*. The substituent R in heme *a* is a long-chain aliphatic substituent[108]

At least one remaining coordination site is usually occupied by an amino acid side chain. The sixth coordination site can be vacant (five-coordinated – 5c) or occupied by some amino acid side chain or a small ligand, for example water or oxygen (six-coordinated – 6c). Most of the natural occurring hemes can be sorted into three groups, type-*a*, -*b*, and -*c* depending on the substitution pattern of the porphyrin macrocycles. Type-*b* hemes have two vinyl substituents whereas type-*a* hemes carry a vinyl and a formyl function. Moreover, a long-chain aliphatic substituent with the specific

constitution depending on the organism is included in the type-*a* hemes. In the type-*c* hemes two vinyl substituents are used to form covalent linkages to the protein by means of addition of the thiol functions of cysteine residues, such that two thioether bridges are formed.[108]

3.5.1 Cytochrome *c*

Cytochrome *c* (Cyt *c*) is a small (*ca*. 12 kDa) soluble protein that is found in plants, bacteria, fungi and higher organisms.[109] It has a covalently-bound heme type-*c* anchored to two cysteine (Cys) side chains by interaction of the thiol groups with the vinyl substituents. A histidine (His) and a methionine (Met) side chains are the axial ligands in both the reduced and the oxidized form of Cyt *c* (Figure 18).

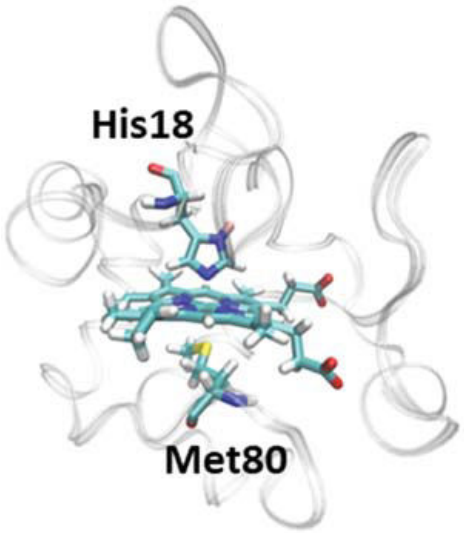

Figure 18: Structure of ferric horse heart Cyt *c* (PDB 1AKK). The picture represents the heme and the native axial Met80 and His18 ligands (licorice)

Cyt *c* functions as an electron carrier in energy transduction by switching between both oxidation states. It transfers electrons between cytochrome *c* reductase and cytochrome *c* oxidase where four electrons are used to reduce oxygen to water. Cyt *c* is supposed to diffuse along the membrane surface from the electron donors to the electron acceptors embedded in the mitochondrial membrane.[108]

By varying external parameters such as pH or temperature, or by binding to denaturants, amphiphiles or anionic surfaces Cyt *c* can be stabilized in different conformational state.[110] Most of the underlying conformational transitions include structural changes in the heme pocket and on the

level of the protein tertiary and secondary structure. These conformational changes are usually reversible.

Ferri-Cyt *c* exists in different conformational states probably due to the relatively weak Fe-S(Met80) bond in the oxidized state of the heme. The reduced form of Cyt *c* is significantly more stable comparing to ferri-Cyt *c* and unfolding requires much harsher conditions, i.e., more extreme pH values, higher temperatures and higher denaturant concentrations.

Enormous number of vibrational spectroscopic studies on Cyt *c* is not just motivated by its central role in bioenergetics. This well-characterized protein is particularly suited as a model system to understand the fundamental issues in protein-membrane interactions, protein folding, in biological electron transfer as well as to test, develop and validate the novel experimental approaches.[108]

3.5.2 Hemoglobin and Myoglobin

In aerobic organisms myoglobin (Mb) and hemoglobin (Hb) play role in oxygen transport and storage.[105] The oxygen-binding unit is a *b*-type heme (iron protoporphyrin IX) in both proteins. In this heme *b* only one axial coordination site is occupied by a histidine (proximal site). Molecular oxygen can reversibly bind to the second (distal) site. Crystal structures of Hb and Mb are represented in Figure 19.

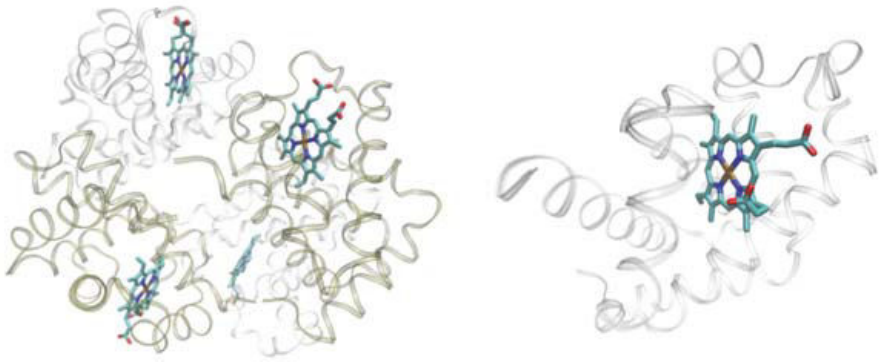

Figure 19: Crystal structures of hemoglobin (PDB 1GZX) (left) consisting of two pairs of two subunits ($\alpha_2\beta_2$) and myoglobin (PDB 3RGK) (right). On the both structures hemes are presented in licorice

Redox state of the heme does not change upon oxygen binding and release; it always remains in the reduced form. Myoglobin is a single peptide chain of *ca.* 18 kDa, whose function is oxygen storage in muscle tissue.[108]

Hemoglobin consists of two pairs of two subunits ($\alpha_2\beta_2$) that form a complex quaternary structure. Four subunits of Hb modulate the oxygen binding affinity of the fours hemes. Hb can undergo conformational transition between a relaxed state *R* (low oxygen affinity) and a tense state *T* (high oxygen affinity). Thus, Hb can release oxygen at low oxygen partial pressure in the cells where oxygen is used for energy conversion and it can efficiently bind oxygen at high oxygen partial pressure in lung tissue.[111]

The cofactors of Mb and Hb are not covalently bound to the protein matrix. That is why they can readily be removed and replaced by synthetic protoporphyrin isotopomers for the subsequent studies.

Mb and Hb exist in three stable states.[112-114] The heme iron in the met-myoglobin (met-Mb) is in the ferric (inactive) form and coordinated by a His and a water molecule. Reduction of the heme is followed by the loss of the aqua-ligand. In the deoxy-myoglobin (deoxy-Mb), the heme iron moves slightly out of the porphyrin plane. Deoxy-Mb can bind molecular oxygen at the vacant coordination site (oxy-myoglobin, oxy-Mb). Oxygen binding results in the movement of the iron back into the heme plane.

Mb and Hb are two of the first proteins whose high-resolution crystal structures were obtained. Many structural details related to the functioning of these proteins have subsequently been revealed by spectroscopic techniques, among which RR and IR spectroscopy played a very important role.[108]

3.5.3 Cytochrome cbb_3 oxidase

The membrane protein cbb_3 oxidase is an example of the heme protein comprising more than one heme in its structure. Therefore validation of the new developed approaches using this more complex protein comparing to Cyt *c*, Hb and Mb would be important.

In aerobic respiration heme- and copper-containing terminal oxidases (CcO) reduce molecular oxygen to water and play role of either cytochrome *c* oxidases or quinol oxidases. On the basis of structural analyses, genomic and phylogenetic CcO were classified in three families: A (mitochondrial-like oxidases), B (ba_3-like oxidases), and C type (cbb_3-type oxidases).[115]

The C-family (cbb_3 oxidases) is an abundant oxygen reductase family after the A-family. The enzymes of this family consist of at least three subunits (CcoN, CcoO and CcoP).[116]

CcoN subunit comprises a low-spin heme *b* and a binuclear active site containing a high-spin heme *b* and an adjacent copper ion Cu_B. CcoO and CcoP comprise one and two low-spin hemes *c*, respectively.[117]

Crystal structure of *P. Stutzeri cbb₃* oxidase is displayed in Figure 20.

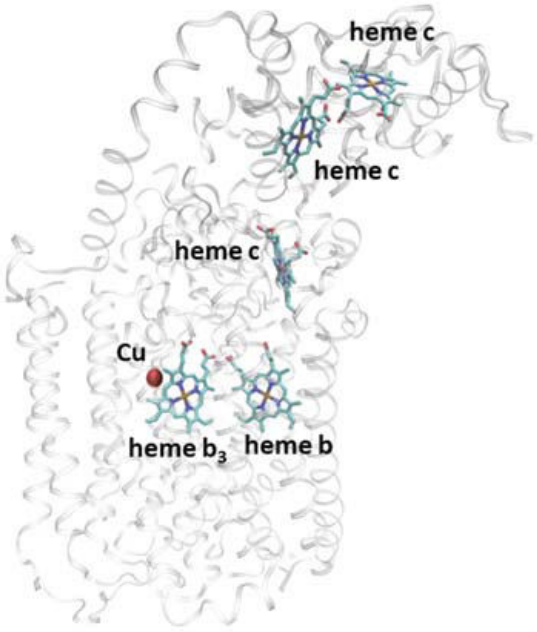

Figure 20: Representation of crystal structure of *P. Stutzeri cbb₃* oxidase (PDB 5DJQ). Hemes are presented in sticks

Fully-reduced enzyme is able to deliver four electrons to oxygen through the multiphasic process that was studied in detail for the mitochondrial CcO and other members of A family.[118-123]

Thus, during electron transfer both hemes are oxidized by the electron transfer to the bound oxygen. Electron redistribution from Cu_A results in the subsequent re-reduction of low-spin heme. Both low-spin heme and Cu_A become fully-oxidized after complete reduction of O_2 to water.

Two processes with respective kinetic constant values of 11000 and 1300 s^{-1} were observed upon the reaction of the detergent-solubilized *cbb₃* oxidase from *Rhodobacter sphaeroides* with O_2.[124] It was suggested that the faster process corresponds to the oxygen binding to heme b_3 and slower one likely is related to the oxidation of the heme groups. An uptake of protons from the solution is accompanied the latter phase.

Objectives of the thesis

The main aim of his study is to develop sensitive combined approaches to explore protein functions, conformational changes and other aspects since these biomolecules play important roles in the living systems. Two approaches will be developed: SEIRAS combined with perfusion cell and SERS combined with electrochemistry.

The first approach will be applied to study transporter protein Lactose Permease, the protein from the respiratory chain complex I and another protein involved in thylakoid membrane (TM) biogenesis and/or maintenance – IM30. The second approach will be first validated using well characterized small heme proteins such as cytochrome *c*, hemoglobin and myoglobin and afterwards the applicability of the approach will be extended to study redox-induced changes in the membrane heme protein cytochrome cbb_3 oxidase.

- ✓ **Determination of the pK_a of an acidic residue in Lactose Permease**

Many different methods were already applied to give insight into the structure and mechanistic details of the function of Lactose Permease. Thus, different proofs of the alternating access mechanism were already provided. However, there are still many questions related to the functioning of this protein. For instance, which residue(s) is/are responsible for a high pK of sugar binding? Is there a special residue playing a central role in the "coupling" mechanism of symport? To answer some questions perfusion-SEIRAS approach will be used. Here, LacY WT and different mutants ($LacY_{ww}$, $LacY_{ww}$ E325A, LacY E325A, LacY E325D, LacY H322Q, LacY R302K, $LacY_{ww}$ R302K, LacY R302A and $LacY_{ww}$ R302A) will be studied in order to determine the pK_a value of an acidic residue and to identify this residue.

- ✓ **Redox-induced conformational changes in complex I**

Complex I is an intensively studied membrane protein. Until now many techniques were used to understand different aspects of molecular mechanism of functioning such as for example ion transport across membranes and electron transport by metal prosthetic groups. However, little is known about the energy transformation from the transfer of electrons into mechanical movement. IR spectroscopy is a powerful tool to visualize conformational changes of proteins during their interactions with different substrates and during induced reactions such as electron transfer.

Therefore, to give insight into the redox-induced conformational changes in complex I perfusion-SEIRAS approach will be used. Complex I will be oxidized by different oxidizing agents such as Q-2, Q-10, $K_3[Fe(CN)_6]$ and naturally dissolved O_2 in the buffer under atmospheric conditions and reduced by NADH.

- ✓ **Substrate-induced conformational changes in IM30**

Until now little is known about the molecular mechanism of functioning of IM30. Nevertheless, the evidence was given that this protein is active in the presence of Mg^{2+} ions. Perfusion-SEIRAS approach will be applied to give the insight into the Mg^{2+}-induced conformational changes in IM30. Different concentrations of Mg^{2+} ions will be tested.

- ✓ **Development of SERS-electrochemical approach**

In this PhD thesis attention will be also focused on the adapting of the electrochemical cell for the studies by means of Raman spectroscopy. In this cell gold grid can serve both as working electrode and probably as SERS active substrate. First, FIB (focused ion beam) images must be recorded in order to have an idea about the surface morphology of the gold grids. Afterwards, it is important to monitor the signal intensities of the proteins adsorbed on the gold grid modified with different SAMs of thiols. Finally, gold nanoparticles will be deposited on the surface of grids to check if they can enhance the signals of the adsorbates. The experimental setup will be validated using well-characterized small heme proteins Cyt *c*, Hb, Mb and then this approach will be extended to test larger membrane protein cbb_3 containing few hemes in its structure.

4. References

1. Tanford, C., and Reynolds, J. (2003) *Nature's robots: a history of proteins*, OUP Oxford.

2. Lodish, H., Berk, A., Zipursky, S. L., Matsudaira, P., Baltimore, D., and Darnell, J. (2000) Molecular cell biology 4th edition, *National Center for Biotechnology InformationÕs Bookshelf*.

3. Malik, S., and Shrivastava, T. (2013) Protein characterization using modern biophysical techniques, *Advances in Protein Chemistry, ed by Ashraf GM and Sheikh IA. OMICS Group eBooks, Foster City*, 4-18.

4. Alberts, B., Johnson, A., Lewis, J., Walter, P., Raff, M., and Roberts, K. (2002) Molecular Biology of the Cell 4th Edition: International Student Edition, Routledge.

5. Deng, H., and Callender, R. (1999) [8] Raman spectroscopic studies of the structures, energetics and bond distortions of substrates bound to enzymes, *Methods in enzymology 308*, 176-201.

6. Barth, A., and Zscherp, C. (2002) What vibrations tell about proteins, *Quarterly reviews of biophysics 35*, 369-430.

7. Li-Xu, W., and Jiang, X.-E. (2012) Bioanalytical applications of surface-enhanced infrared absorption spectroscopy, *Chinese Journal of Analytical Chemistry 40*, 975-982.

8. Ataka, K., Stripp, S. T., and Heberle, J. (2013) Surface-enhanced infrared absorption spectroscopy (SEIRAS) to probe monolayers of membrane proteins, *Biochimica et Biophysica Acta (BBA)-Biomembranes 1828*, 2283-2293.

9. Block, H., Maertens, B., Spriestersbach, A., Brinker, N., Kubicek, J., Fabis, R., Labahn, J., and Schäfer, F. (2009) Immobilized-metal affinity chromatography (IMAC): a review, *Methods in enzymology 463*, 439-473.

10. Gaberc-Porekar, V., and Menart, V. (2005) Potential for using histidine tags in purification of proteins at large scale, *Chemical engineering & technology 28*, 1306-1314.

11. Rigaud, J.-L., Levy, D., Mosser, G., and Lambert, O. (1998) Detergent removal by non-polar polystyrene beads, *European Biophysics Journal 27*, 305-319.

12. Ataka, K., Giess, F., Knoll, W., Naumann, R., Haber-Pohlmeier, S., Richter, B., and Heberle, J. (2004) Oriented attachment and membrane reconstitution of His-tagged cytochrome c oxidase to a gold electrode: in situ monitoring by surface-enhanced infrared absorption spectroscopy, *Journal of the American Chemical Society 126*, 16199-16206.

13. Green, N. (1963) Avidin. 3. The nature of the biotin-binding site, *Biochemical Journal 89*, 599.

14. Jiang, X., Zuber, A., Heberle, J., and Ataka, K. (2008) In situ monitoring of the orientated assembly of strep-tagged membrane proteins on the gold surface by surface enhanced infrared absorption spectroscopy, *Physical Chemistry Chemical Physics 10*, 6381-6387.

15. Bayburt, T. H., Grinkova, Y. V., and Sligar, S. G. (2002) Self-assembly of discoidal phospholipid bilayer nanoparticles with membrane scaffold proteins, *Nano Letters 2*, 853-856.

16. Zaitseva, E., Saavedra, M., Banerjee, S., Sakmar, T. P., and Vogel, R. (2010) SEIRA spectroscopy on a membrane receptor monolayer using lipoprotein particles as carriers, *Biophysical journal 99*, 2327-2335.

17. Perutz, M. F. (1989) Mechanisms of cooperativity and allosteric regulation in proteins, *Quarterly reviews of biophysics 22*, 139-237.

18. Gerstein, M., Lesk, A. M., and Chothia, C. (1994) Structural mechanisms for domain movements in proteins, *Biochemistry 33*, 6739-6749.

19. Janin, J., and Wodak, S. J. (1983) Structural domains in proteins and their role in the dynamics of protein function, *Progress in biophysics and molecular biology 42*, 21-78.

20. Rich, P. R., and Iwaki, M. (2007) Methods to probe protein transitions with ATR infrared spectroscopy, *Molecular BioSystems 3*, 398-407.

21. Gerwert, K. (1999) Molecular reaction mechanisms of proteins monitored by time-resolved FTIR-spectroscopy, *Biological chemistry 380*, 931-935.

22. Heberle, J. (1999) Time-resolved ATR/FT-IR spectroscopy of membrane proteins, *Recent Res. devel. Appl. Spectr 2*, 147-159.

23. Maeda, A. (1995) Application of FTIR spectroscopy to the structural study on the function of bacteriorhodopsin, *Israel journal of chemistry 35*, 387-400.

24. Rothschild, K. J. (1992) FTIR difference spectroscopy of bacteriorhodopsin: toward a molecular model, *Journal of bioenergetics and biomembranes 24*, 147-167.

25. Mäntele, W. (1995) Infrared vibrational spectroscopy of reaction centers, In *Anoxygenic Photosynthetic Bacteria*, pp 627-647, Springer.

26. Breton, J. (2001) Fourier transform infrared spectroscopy of primary electron donors in type I photosynthetic reaction centers, *Biochimica et Biophysica Acta (BBA)-Bioenergetics 1507*, 180-193.

27. Nabedryk, E. (1996) Light-induced Fourier transform infrared difference spectroscopy of the primary electron donor in photosynthetic reaction centers, *Infrared spectroscopy of biomolecules*, 39-81.

28. Rothschild, K. J., Zagaeski, M., and Cantore, W. A. (1981) Conformational changes of bacteriorhodopsin detected by Fourier transform infrared difference spectroscopy, *Biochemical and biophysical research communications 103*, 483-489.

29. Mäntele, W., Nabedryk, E., Tavitian, B., Kreutz, W., and Breton, J. (1985) Light-induced Fourier transform infrared (FTIR) spectroscopic investigations of the primary donor oxidation in bacterial photosynthesis, *FEBS letters 187*, 227-232.

30. Uhmann, W., Becker, A., Taran, C., and Siebert, F. (1991) Time-resolved FT-IR absorption spectroscopy using a step-scan interferometer, *Applied Spectroscopy 45*, 390-397.

31. Dyer, R. B., Peterson, K. A., Stoutland, P. O., and Woodruff, W. H. (1994) Picosecond infrared study of the photodynamics of carbonmonoxy-cytochrome c oxidase, *Biochemistry 33*, 500-507.

32. Lübben, M., and Gerwert, K. (1996) Redox FTIR difference spectroscopy using caged electrons reveals contributions of carboxyl groups to the catalytic mechanism of haemcopper oxidases, *FEBS letters 397*, 303-307.

33. Iwaki, M., Andrianambinintsoa, S., Rich, P., and Breton, J. (2002) Attenuated total reflection Fourier transform infrared spectroscopy of redox transitions in photosynthetic reaction centers: comparison of perfusion-and light-induced difference spectra, *Spectrochimica Acta Part A: Molecular and Biomolecular Spectroscopy 58*, 1523-1533.

34. Okubo, T., and Noguchi, T. (2007) Selective detection of the structural changes upon photoreactions of several redox cofactors in photosystem II by means of light-induced ATR-FTIR difference spectroscopy, *Spectrochimica Acta Part A: Molecular and Biomolecular Spectroscopy 66*, 863-868.

35. Moss, D., Nabedryk, E., Breton, J., and Mantele, W. (1990) Redox-linked conformational changes in proteins detected by a combination of infrared spectroscopy and protein electrochemistry, *European Journal of Biochemistry 187*, 565-572.

36. Marshall, D., Fisher, N., Grigic, L., Zickermann, V., Brandt, U., Shannon, R. J., Hirst, J., Lawrence, R., and Rich, P. R. (2006) ATR-FTIR redox difference spectroscopy of Yarrowia lipolytica and bovine complex I, *Biochemistry 45*, 5458-5467.

37. Osyczka, A., Zhang, H., Mathé, C., Rich, P. R., Moser, C. C., and Dutton, P. L. (2006) Role of the PEWY Glutamate in Hydroquinone− Quinone Oxidation− Reduction Catalysis in the Qo Site of Cytochrome bc 1, *Biochemistry 45*, 10492-10503.

38. Džafić, E., Klein, O., Screpanti, E., Hunte, C., and Mäntele, W. (2009) Flexibility and dynamics of NhaA Na+/H+-antiporter of Escherichia coli studied by Fourier transform infrared spectroscopy, *Spectrochimica Acta Part A: Molecular and Biomolecular Spectroscopy 72*, 102-109.

39. Baenziger, J. E., Miller, K. W., and Rothschild, K. J. (1993) Fourier transform infrared difference spectroscopy of the nicotinic acetylcholine receptor: evidence for specific protein structural changes upon desensitization, *Biochemistry 32*, 5448-5454.

40. Iwaki, M., Giotta, L., Akinsiku, A. O., Schägger, H., Fisher, N., Breton, J., and Rich, P. R. (2003) Redox-induced transitions in bovine cytochrome bc 1 complex studied by perfusion-induced ATR-FTIR spectroscopy, *Biochemistry 42*, 11109-11119.

41. Iwaki, M., and Rich, P. R. (2004) Direct detection of formate ligation in cytochrome c oxidase by ATR-FTIR spectroscopy, *Journal of the American Chemical Society 126*, 2386-2389.

42. Iwaki, M., Cotton, N. P., Quirk, P. G., Rich, P. R., and Jackson, J. B. (2006) Molecular recognition between protein and nicotinamide dinucleotide in intact, proton-translocating transhydrogenase studied by ATR-FTIR spectroscopy, *Journal of the American Chemical Society 128*, 2621-2629.

43. Nyquist, R. M., Heitbrink, D., Bolwien, C., Gennis, R. B., and Heberle, J. (2003) Direct observation of protonation reactions during the catalytic cycle of cytochrome c oxidase, *Proceedings of the National Academy of Sciences 100*, 8715-8720.

44. Iwaki, M., Puustinen, A., Wikström, M., and Rich, P. R. (2006) Structural and chemical changes of the PM intermediate of Paracoccus denitrificans cytochrome c oxidase revealed by IR spectroscopy with labeled tyrosines and histidine, *Biochemistry 45*, 10873-10885.

45. Guan, L., and Kaback, H. R. (2006) Lessons from lactose permease, *Annu. Rev. Biophys. Biomol. Struct. 35*, 67-91.

46. Kaback, H. R. (2015) A chemiosmotic mechanism of symport, *Proceedings of the National Academy of Sciences 112*, 1259-1264.

47. Abramson, J., Smirnova, I., Kasho, V., Verner, G., Kaback, H. R., and Iwata, S. (2003) Structure and mechanism of the lactose permease of Escherichia coli, *Science 301*, 610-615.

48. Guan, L., Mirza, O., Verner, G., Iwata, S., and Kaback, H. R. (2007) Structural determination of wild-type lactose permease, *Proceedings of the National Academy of Sciences 104*, 15294-15298.

49. Smirnova, I., Kasho, V., Sugihara, J., Vázquez-Ibar, J. L., and Kaback, H. R. (2012) Role of protons in sugar binding to LacY, *Proceedings of the National Academy of Sciences 109*, 16835-16840.

50. Madej, M. G., and Kaback, H. R. (2014) The life and times of Lac permease: Crystals ain't everything, but they certainly do help, In *Membrane Transport Mechanism*, pp 121-158, Springer.

51. Garcia-Celma, J. J., Smirnova, I. N., Kaback, H. R., and Fendler, K. (2009) Electrophysiological characterization of LacY, *Proceedings of the National Academy of Sciences 106*, 7373-7378.

52. Garcia-Celma, J. J., Ploch, J., Smirnova, I., Kaback, H. R., and Fendler, K. (2010) Delineating electrogenic reactions during lactose/H+ symport, *Biochemistry 49*, 6115-6121.

53. Kaback, H. R., Dunten, R., Frillingos, S., Venkatesan, P., Kwaw, I., Zhang, W., and Ermolova, N. (2007) Site-directed alkylation and the alternating access model for LacY, *Proceedings of the National Academy of Sciences 104*, 491-494.

54. Nie, Y., Ermolova, N., and Kaback, H. R. (2007) Site-directed alkylation of LacY: effect of the proton electrochemical gradient, *Journal of molecular biology 374*, 356-364.

55. Nie, Y., Sabetfard, F. E., and Kaback, H. R. (2008) The Cys154→ Gly mutation in LacY causes constitutive opening of the hydrophilic periplasmic pathway, *Journal of molecular biology 379*, 695-703.

56. Majumdar, D. S., Smirnova, I., Kasho, V., Nir, E., Kong, X., Weiss, S., and Kaback, H. R. (2007) Single-molecule FRET reveals sugar-induced conformational dynamics in LacY, *Proceedings of the National Academy of Sciences 104*, 12640-12645.

57. Pannier, M., Veit, S., Godt, A., Jeschke, G., and Spiess, H. W. (2011) Dead-time free measurement of dipole–dipole interactions between electron spins, *Journal of Magnetic Resonance 213*, 316-325.

58. Smirnova, I., Kasho, V., Choe, J.-Y., Altenbach, C., Hubbell, W. L., and Kaback, H. R. (2007) Sugar binding induces an outward facing conformation of LacY, *Proceedings of the National Academy of Sciences 104*, 16504-16509.

59. Radestock, S., and Forrest, L. R. (2011) The alternating-access mechanism of MFS transporters arises from inverted-topology repeats, *Journal of molecular biology 407*, 698-715.

60. Zhou, Y., Guan, L., Freites, J. A., and Kaback, H. R. (2008) Opening and closing of the periplasmic gate in lactose permease, *Proceedings of the National Academy of Sciences 105*, 3774-3778.

61. Smirnova, I. N., Kasho, V. N., and Kaback, H. R. (2006) Direct sugar binding to LacY measured by resonance energy transfer, *Biochemistry 45*, 15279-15287.

62. Smirnova, I., Kasho, V., Sugihara, J., and Kaback, H. R. (2009) Probing of the rates of alternating access in LacY with Trp fluorescence, *Proceedings of the National Academy of Sciences 106*, 21561-21566.

63. Smirnova, I., Kasho, V., Sugihara, J., and Kaback, H. R. (2011) Opening the periplasmic cavity in lactose permease is the limiting step for sugar binding, *Proceedings of the National Academy of Sciences 108*, 15147-15151.

64. Walker, J. E. (1992) The NADH: ubiquinone oxidoreductase (complex I) of respiratory chains, *Quarterly reviews of biophysics 25*, 253-324.

65. Yagi, T., and Matsuno-Yagi, A. (2003) The proton-translocating NADH− quinone oxidoreductase in the respiratory chain: the secret unlocked, *Biochemistry 42*, 2266-2274.

66. Brandt, U. (2006) Energy converting NADH: quinone oxidoreductase (complex I), *Annu. Rev. Biochem. 75*, 69-92.

67. Ohnishi, T. (1998) Iron–sulfur clusters/semiquinones in complex I, *Biochimica et Biophysica Acta (BBA)-Bioenergetics 1364*, 186-206.

68. Sazanov, L. A. (2007) Respiratory complex I: mechanistic and structural insights provided by the crystal structure of the hydrophilic domain, *Biochemistry 46*, 2275-2288.

69. Hirst, J. (2010) Towards the molecular mechanism of respiratory complex I, *Biochemical Journal 425*, 327-339.

70. David, S., and Nicholls, G. (2002) Bioenergetics, Academic Press.

71. Vinogradov, A. D. (1998) Catalytic properties of the mitochondrial NADH–ubiquinone oxidoreductase (complex I) and the pseudo-reversible active/inactive enzyme transition, *Biochimica et Biophysica Acta (BBA)-Bioenergetics 1364*, 169-185.

72. Moparthi, V. K., and Hägerhäll, C. (2011) The evolution of respiratory chain complex I from a smaller last common ancestor consisting of 11 protein subunits, *Journal of molecular evolution 72*, 484-497.

73. Carroll, J., Fearnley, I. M., Skehel, J. M., Shannon, R. J., Hirst, J., and Walker, J. E. (2006) Bovine complex I is a complex of 45 different subunits, *Journal of Biological Chemistry 281*, 32724-32727.

74. Efremov, R. G., and Sazanov, L. A. (2012) The coupling mechanism of respiratory complex I—a structural and evolutionary perspective, *Biochimica et Biophysica Acta (BBA)-Bioenergetics 1817*, 1785-1795.

75. Berrisford, J. M., and Sazanov, L. A. (2009) Structural basis for the mechanism of respiratory complex I, *Journal of Biological Chemistry 284*, 29773-29783.

76. Verkhovskaya, M. L., Belevich, N., Euro, L., Wikström, M., and Verkhovsky, M. I. (2008) Real-time electron transfer in respiratory complex I, *Proceedings of the National Academy of Sciences 105*, 3763-3767.

77. Bridges, H. R., Bill, E., and Hirst, J. (2011) Mossbauer spectroscopy on respiratory complex I: the iron–sulfur cluster ensemble in the NADH-reduced enzyme is partially oxidized, *Biochemistry 51*, 149-158.

78. Page, C. C., Moser, C. C., Chen, X., and Dutton, P. L. (1999) Natural engineering principles of electron tunnelling in biological oxidation–reduction, *Nature 402*, 47-52.

79. Sazanov, L. A., and Hinchliffe, P. (2006) Structure of the hydrophilic domain of respiratory complex I from Thermus thermophilus, *science 311*, 1430-1436.

80. Smith, M. A., Finel, M., Korolik, V., and Mendz, G. L. (2000) Characteristics of the aerobic respiratory chains of the microaerophiles Campylobacter jejuni and Helicobacter pylori, *Archives of microbiology 174*, 1-10.

81. Efremov, R. G., Baradaran, R., and Sazanov, L. A. (2010) The architecture of respiratory complex I, *Nature 465*, 441-445.

82. Efremov, R. G., and Sazanov, L. A. (2011) Structure of the membrane domain of respiratory complex I, *Nature 476*, 414-420.

83. Roessler, M. M., King, M. S., Robinson, A. J., Armstrong, F. A., Harmer, J., and Hirst, J. (2010) Direct assignment of EPR spectra to structurally defined iron-sulfur clusters in

complex I by double electron–electron resonance, *Proceedings of the National Academy of Sciences 107*, 1930-1935.

84. Kashani-Poor, N., Zwicker, K., Kerscher, S., and Brandt, U. (2001) A central functional role for the 49-kDa subunit within the catalytic core of mitochondrial complex I, *Journal of Biological Chemistry 276*, 24082-24087.

85. Sled, V. D., Rudnitzky, N. I., Hatefi, Y., and Ohnishi, T. (1994) Thermodynamic analysis of flavin in mitochondrial NADH: ubiquinone oxidoreductase (complex I), *Biochemistry 33*, 10069-10075.

86. Birrell, J. A., King, M. S., and Hirst, J. (2011) A ternary mechanism for NADH oxidation by positively charged electron acceptors, catalyzed at the flavin site in respiratory complex I, *FEBS letters 585*, 2318-2322.

87. Vinothkumar, K. R., and Henderson, R. (2010) Structures of membrane proteins, *Quarterly reviews of biophysics 43*, 65-158.

88. Hayashi, T., and Stuchebrukhov, A. A. (2010) Electron tunneling in respiratory complex I, *Proceedings of the National Academy of Sciences 107*, 19157-19162.

89. Wu, D.-Y., Li, J.-F., Ren, B., and Tian, Z.-Q. (2008) Electrochemical surface-enhanced Raman spectroscopy of nanostructures, *Chemical Society Reviews 37*, 1025-1041.

90. Fleischmann, M., Hendra, P. J., and McQuillan, A. J. (1974) Raman spectra of pyridine adsorbed at a silver electrode, *Chemical Physics Letters 26*, 163-166.

91. Albrecht, M. G., and Creighton, J. A. (1977) Anomalously intense Raman spectra of pyridine at a silver electrode, *Journal of the american chemical society 99*, 5215-5217.

92. Tian, Z.-Q., Ren, B., Li, J.-F., and Yang, Z.-L. (2007) Expanding generality of surface-enhanced Raman spectroscopy with borrowing SERS activity strategy, *Chemical Communications*, 3514-3534.

93. Schlücker, S. (2014) Surface-Enhanced raman spectroscopy: Concepts and chemical applications, *Angewandte Chemie International Edition 53*, 4756-4795.

94. Li, J. F., Huang, Y. F., Ding, Y., Yang, Z. L., Li, S. B., Zhou, X. S., Fan, F. R., Zhang, W., Zhou, Z. Y., and Ren, B. (2010) Shell-isolated nanoparticle-enhanced Raman spectroscopy, *nature 464*, 392-395.

95. Anema, J. R., Li, J.-F., Yang, Z.-L., Ren, B., and Tian, Z.-Q. (2011) Shell-isolated nanoparticle-enhanced Raman spectroscopy: expanding the versatility of surface-enhanced Raman scattering, *Annual Review of Analytical Chemistry 4*, 129-150.

96. Jensen, T. R., Malinsky, M. D., Haynes, C. L., and Van Duyne, R. P. (2000) Nanosphere lithography: tunable localized surface plasmon resonance spectra of silver nanoparticles, *The Journal of Physical Chemistry B 104*, 10549-10556.

97. Haynes, C. L., and Van Duyne, R. P. (2001) Nanosphere lithography: a versatile nanofabrication tool for studies of size-dependent nanoparticle optics, ACS Publications.

98. Mahajan, S., Baumberg, J. J., Russell, A. E., and Bartlett, P. N. (2007) Reproducible SERRS from structured gold surfaces, *Physical Chemistry Chemical Physics 9*, 6016-6020.

99. Sole, M. J. (1994) Electroforming: Methods, materials, and merchandise, *JOM Journal of the Minerals, Metals and Materials Society 46*, 29-35.

100. McGeough, J., Leu, M., Rajurkar, K., De Silva, A., and Liu, Q. (2001) Electroforming process and application to micro/macro manufacturing, *CIRP Annals-Manufacturing Technology 50*, 499-514.

101. Ismail, M. (1979) Periodic reverse current electroplating and surface finishing, *Journal of applied electrochemistry 9*, 407-410.

102. Ulman, A. (1996) Formation and structure of self-assembled monolayers, *Chemical reviews 96*, 1533-1554.

103. Siebert, F., and Hildebrandt, P. (2008) Experimental Techniques, In *Vibrational Spectroscopy in Life Science*, pp 99-153, Wiley-VCH Verlag GmbH & Co. KGaA.

104. Yuan, T., Le Thi Ngoc, L., van Nieuwkasteele, J., Odijk, M., van den Berg, A., Permentier, H., Bischoff, R., and Carlen, E. T. (2015) In situ surface-enhanced raman spectroelectrochemical analysis system with a hemin modified nanostructured gold surface, *Analytical chemistry 87*, 2588-2592.

105. Messerschmidt, A. (2001) *Handbook of metalloproteins*, Wiley.

106. Ignarro, L. (2002) Nitric oxide as a unique signaling molecule in the, *Journal of physiology and pharmacology 53*, 503-514.

107. Jiang, X., and Wang, X. (2004) Cytochrome C-mediated apoptosis, *Annual review of biochemistry 73*.

108. Siebert, F., and Hildebrandt, P. (2008) Heme Proteins, In *Vibrational Spectroscopy in Life Science*, pp 227-282, Wiley-VCH Verlag GmbH & Co. KGaA.

109. Mauk, A. G., Mauk, M. R., Moore, G. R., and Northrup, S. H. (1995) Experimental and theoretical analysis of the interaction between cytochromec and cytochromeb 5, *Journal of bioenergetics and biomembranes 27*, 311-330.

110. Scott, R. A., and Mauk, A. G. (1996) *Cytochrome c: a multidisciplinary approach*, Univ Science Books.

111. Cantor, C. R., and Schimmel, P. R. (1980) *Biophysical chemistry: Part III: the behavior of biological macromolecules*, Macmillan.

112. Spiro, T. G., and Strekas, T. C. (1974) Resonance Raman spectra of heme proteins. Effects of oxidation and spin state, *Journal of the American Chemical Society 96*, 338-345.

113. Rousseau, D., and Ondrias, M. (1983) Resonance Raman scattering studies of the quaternary structure transition in hemoglobin, *Annual review of biophysics and bioengineering 12*, 357-380.

114. Spiro, T. G. (1985) Resonance Raman spectroscopy as a probe of heme protein structure and dynamics, *Advances in protein chemistry 37*, 111-159.

115. Pereira, M. M., Santana, M., and Teixeira, M. (2001) A novel scenario for the evolution of haem–copper oxygen reductases, *Biochimica et Biophysica Acta (BBA)-Bioenergetics 1505*, 185-208.

116. Pitcher, R. S., and Watmough, N. J. (2004) The bacterial cytochrome cbb 3 oxidases, *Biochimica et Biophysica Acta (BBA)-Bioenergetics 1655*, 388-399.

117. Buschmann, S., Warkentin, E., Xie, H., Langer, J. D., Ermler, U., and Michel, H. (2010) The structure of cbb3 cytochrome oxidase provides insights into proton pumping, *Science 329*, 327-330.

118. Richter, O.-M., and Ludwig, B. (2003) Cytochrome c oxidase—structure, function, and physiology of a redox-driven molecular machine, In *Reviews of physiology, biochemistry and pharmacology*, pp 47-74, Springer.

119. Wikström, M. (1989) Identification of the electron transfers in cytochrome oxidase that are coupled to proton-pumping, *Nature 338*, 776-778.

120. Kitagawa, T., and Ogura, T. (1998) Time-resolved resonance Raman investigation of oxygen reduction mechanism of bovine cytochrome c oxidase, *Journal of bioenergetics and biomembranes 30*, 71-79.

121. Rich, P., Jünemann, S., and Meunier, B. (1998) Protonmotive mechanism of heme-copper oxidases, *Journal of bioenergetics and biomembranes 30*, 131-138.

122. Michel, H. (1998) The mechanism of proton pumping by cytochrome c oxidase, *Proceedings of the National Academy of Sciences 95*, 12819-12824.

123. Michel, H. (1999) Cytochrome c oxidase: catalytic cycle and mechanisms of proton pumping-a discussion, *Biochemistry 38*, 15129-15140.

124. Lee, H. J., Gennis, R. B., and Ädelroth, P. (2011) Entrance of the proton pathway in cbb3-type heme-copper oxidases, *Proceedings of the National Academy of Sciences 108*, 17661-17666.

II. MATERIALS AND METHODS

List of figures in chapter 2

List of tables in chapter 2

1. Techniques

In the present work different experimental spectroscopic techniques were used: infrared, Raman and UV-Visible spectroscopies.

1.1 Spectroscopy

The light-matter interaction may result in absorption, emission or diffusion of the light. The wavelength and frequency of the electromagnetic wave are related by the expression presented below:

$$c = \lambda\nu \qquad \text{Equation 1}$$

where c is the speed of light in vacuum (3×10^{8} m.s^{-1}), λ is the wavelength (in m), and ν is the frequency (in Hz).

According to the quantum theory light waves transfer energy to matter and vice-versa in discrete bundles called photons. The energy of a photon is related to the frequency by the following expression:

$$E = h\nu \qquad \text{Equation 2}$$

where ν is the frequency in Hz and h is Planck's constant (6.626×10^{-34} J.s).

Figure 1 represents a diagram of the electromagnetic spectrum. The energy of light decreases with wavelength; therefore, energy decreases from top to bottom in the figure.

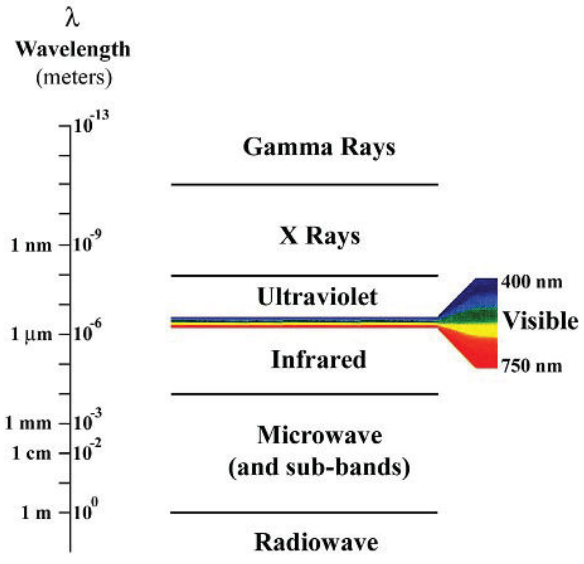

Figure 1: Electromagnetic spectrum[(1)]

The most familiar classifications of wavebands are indicated by regions that span a portion of the spectrum, the radiowave, microwave, infrared, visible, ultraviolet, x-ray and gamma-ray wave bands.[1]

1.2 UV/Visible spectroscopy

The interaction of light in the visible and ultraviolet region of the spectrum with molecules results in the electronic transitions between their allowed energy levels. Some of the radiation is absorbed by the sample when it is illuminated by the light. This absorption can result in the heating of the sample, emission of the photons or in photochemical reactions. The electronic transitions are detected in the near ultraviolet (200 – 400 nm) and in the visible spectral regions (400 – 800 nm).

The quantity of absorbed light by a sample can be determined using the Beer-Lambert law, that relates the light intensity entering the solution (I_0) with the light intensity leaving the solution, I:

$$A = \log (I_0/I) = \varepsilon C l \qquad \text{Equation 3}$$

Here A is the absorbance, ε is the extinction coefficient ($mol^{-1}.L.cm^{-1}$), C is the concentration of the sample ($mol.L^{-1}$), and l is the thickness of the sample through which the light passes (cm).

In the visible-ultraviolet spectrophotometers, visible or ultraviolet light is passed through the sample solution placed into a cuvette of calibrated dimensions. The intensity of the light before and after passing through the solution is determined through different detectors, such as photodiodes and photomultipliers. The extinction coefficient is characteristic of the molecule and depends on the wavelength.

Deviations from the Beer-Lambert law can be observed. For example, the sample might be inhomogeneous, the light might not be monochromatic, scattering of the light may occur, the photodetectors might exhibit nonlinear behavior, etc. These are instrumental and sample artifacts. But the deviations also occur due to the molecular properties of the sample: for example, sample aggregation or complex formation while changing the concentration. In this case, the deviations can be used to study these properties.

An important property of light absorbed by solutions is that if there are multiple absorbing species in the sample. The total absorbance is the sum of the absorbance of the individual species. Thus, for example, for species X and Y, the absorbance is

$$A_\lambda = A_\lambda^X + A_\lambda^Y = \varepsilon_\lambda^X \, l \, C_X + \varepsilon_\lambda^Y \, l \, C_Y \qquad \text{Equation 4}$$

It is possible to determine the concentrations of the individual species if the extinction coefficients are known and if the measurements are made at two different wavelengths where the extinction coefficients are sufficiently different.[(2)]

In the present study UV/Visible spectroscopy was used to determine sample concentration as well as the size of gold nanoparticles (Au NPs).

1.3 Infrared absorption spectroscopy

At the beginning of the last century, IR radiation was widely used to measure interactions with matter, thereby producing the first vibrational spectra.[(3)]

IR spectroscopy measures the transitions between molecular vibrational energy levels followed by the absorption of the IR radiation. This interaction between light and matter is a resonance condition that involves the electric dipole mediated transition between vibrational energy levels.

IR frequencies include three spectral regions: the near-IR (14000 – 4000 cm^{-1}), the mid-IR (4000 – 400 cm^{-1}) and the far-IR regions (400 – 10 cm^{-1}). The IR spectrum is the plot of the intensity (of absorbance or transmittance) versus the wavenumber, that is proportional to the energy difference between the ground and the excited vibrational states.[(4)]

The periodic oscillations of atoms within a molecule are probed by vibrational spectroscopy. This can be understood by taking into account that the N-atomic molecule has 3N degrees of freedom, of which three refer to translations and three (two) are related to the rotations in the case of a nonlinear (linear) molecule structure. The remaining degrees of freedom represent 3N – 6 (3N – 5) vibrations of a nonlinear (linear) molecule, the so-called normal modes. Vibrational modes are active in the IR only when the dipole moment of the molecule is changed during vibration. However, the frequency depends on the forces acting on the individual atoms and on the respective masses. These forces do not depend only on the chemical bonds connecting the individual atoms but also they include contributions from nonbonding interactions within the molecule and with the molecular environment. Therefore, the frequencies of the normal modes represent a characteristic signature of the structure, chemical constitution and electron density distribution of the molecule in a given chemical environment.[(3)]

The important parameters: wavelength (λ), frequency (ν), wavenumber ($\tilde{\nu}$) (number of waves per unit length) and refractive index of the medium (n) are related by the following expression:

$$\tilde{\nu} = \frac{\nu}{c/n} = \frac{1}{\lambda} \qquad \text{Equation 6}$$

It is useful to consider a simple model derived from classical mechanics in order to better understand the molecular vibrations responsible for the characteristic bands observed in infrared and Raman spectra (Figure 2).

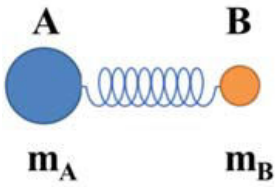

Figure 2: Simple model from classical mechanics to represent the harmonic oscillator

The classical vibrational frequency for a diatomic molecule is:

$$\nu = \frac{1}{2\pi}\sqrt{k(\frac{1}{m_A} + \frac{1}{m_B})} \qquad \text{Equation 7}$$

where k is the force constant in N.m^{-1} and m_A and m_B are the masses in kg. This expression also uses the reduced mass where

$$\frac{1}{\mu} = \frac{1}{m_A} + \frac{1}{m_B} \text{ or } \mu = \frac{m_A m_B}{m_A + m_B} \qquad \text{Equation 8}$$

This simple expression shows that the observed frequency of a diatomic oscillator is depending on the atomic masses of the two atoms involved in the vibration and on the bond energy.[(4)]

Different types of vibrational normal modes are observed in IR spectroscopy; elongation vibrations are associated with the change of the bond length and deformation vibrations correspond to the change of the angle between the bonds. Diverse types of vibrational normal modes are shown in Figure 3.

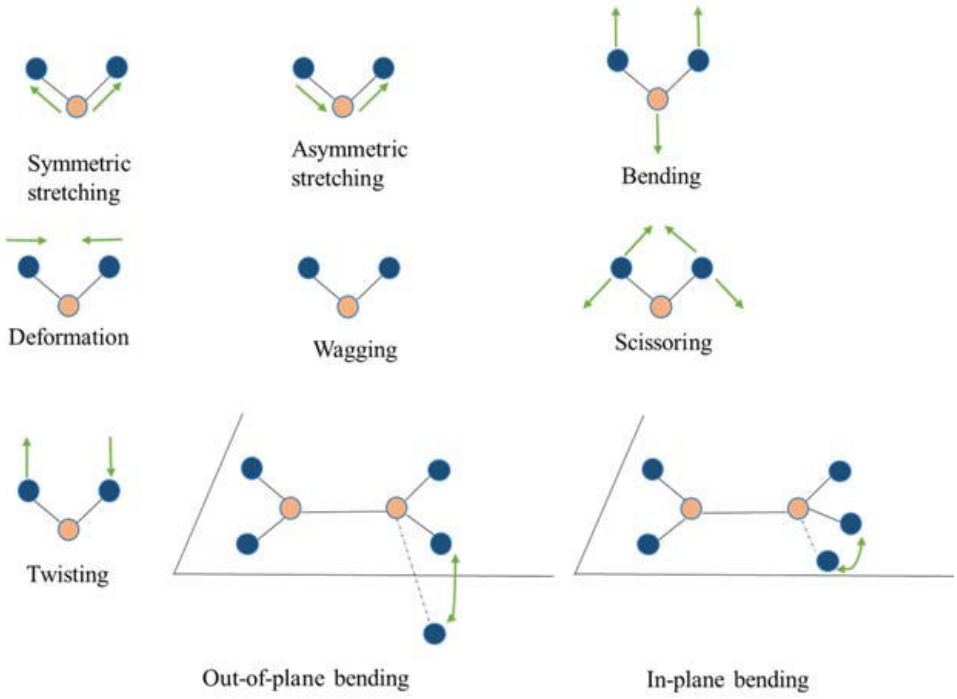

Figure 3: Different normal vibrational modes[5]

1.4 Fourier transform infrared spectroscopy (FTIR)

Today modern IR spectrometers comprise an optical setup that consists of a polychromatic source, a detector and a Michelson interferometer. Michelson interferometer is shown schematically in Figure 4.[6] It is named after Albert Abraham Michelson (1852–1931) who constructed the interferometer in the 1880s.[7] Normally the interferometer comprises two plane mirrors that are oriented perpendicularly to each other and a beamsplitter, which ideally transmits 50% of the incoming radiation to one of the mirrors and reflects 50% to the other mirror. One of the mirrors is movable that can change the optical pathlength in one arm of the interferometer. The beams that are reflected by the two mirrors are recombined *via* the beamsplitter, which also divides the combined beam into two parts: one is leaving the interferometer into the direction of the incoming beam, the other into the exit port of the interferometer.[6]

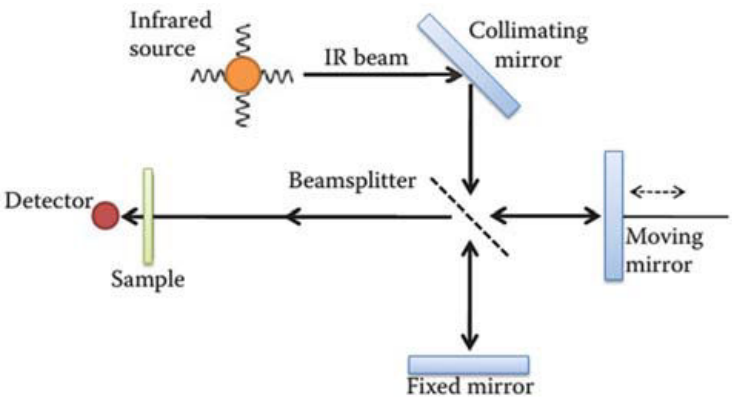

Figure 4: Representation of a Michelson interferometer[7]

When the waves are superposed they will interfere with each other. This means that their amplitudes add together to form a single wave. In the Michelson interferometer the light beams reflected from the fixed and moving mirrors interfere as follows:

$$A_f = A_1 + A_2 \qquad \text{Equation 9}$$

where A_f – final amplitude, A_1 – the amplitude of the fixed mirror beam, A_2 – the amplitude of the moving mirror beam.

If A_f is greater than A_1 or A_2 than two beams undergo *constructive* interference. If A_f is less than A_1 or A_2 then *destructive* interference takes place.
The two light beams interfere constructively with each other when their optical path difference is a multiple of their wavelength, as follows:

$$\delta = n\lambda \qquad \text{Equation 10}$$

where δ – optical path difference, λ - wavelength, n = 0, 1, 2…

The destructive interference takes place when the two beams are some number of cycles plus a half out of phase with each other. Thus, for destructive interference:

$$\delta = (n + \tfrac{1}{2})\lambda \qquad \text{Equation 11}$$

Interferogram (that means "interference writing"), is a plot of light intensity versus optical path difference. In order to register an interferogram using a Michelson interferometer the mirror must be moved back and forth once. This is called a *scan*. The interferograms that are measured while scanning are Fourier transformed, hence the term *Fourier Transform Infrared (FTIR) spectroscopy* (Figure 5).[7]

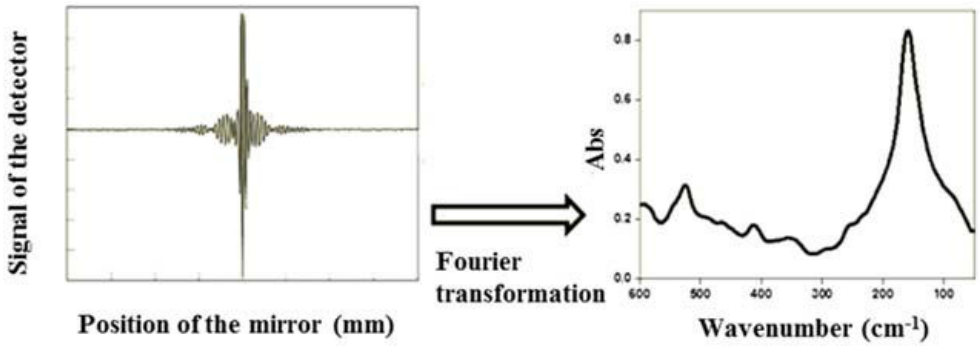

Figure 5: Interferogram (left) and absorption spectrum (right) obtained after Fourier transformation[(4)]

The important equations for the Fourier transformation are:

$$I(\delta) = \int_0^{\infty} B(\tilde{\nu}) \cos(2\pi\delta\tilde{\nu})\, d\tilde{\nu} \qquad \text{Equation 12}$$

$$B(\tilde{\nu}) = \int_{-\infty}^{+\infty} I(\delta) \cos(2\pi\delta\tilde{\nu})\, d\delta \qquad \text{Equation 13}$$

where $\tilde{\nu}$ – wavenumber (cm^{-1}), I – intensity of the interferogram, δ – optical path difference of two beams and $B(\tilde{\nu})$ – spectral power density. These equations are interconvertible and are solved with the help of computers by an algorithm.[(8),(9)]

1.5 Infrared spectroscopy of proteins

Proteins are macromolecules that consist of amino acid residues linked *via* the peptide bonds.[(10)] Mid-infrared spectroscopy is widely used to study protein structure and structural changes *via* vibrational resonances that originate from the polypeptide backbone or side chains. Therefore, information about the secondary structure of proteins can be obtained in a label-free fashion. Vibrations of amide groups of the backbone are important for the protein IR spectroscopy, as they are native to all proteins and give information on the conformation and solvation. These bands include the amide I region, between 1700 and 1600 cm^{-1}, that results from C=O stretching vibration, the amide II band, related to CN stretch and NH in-plane bending, the amide III vibration, that results from CN stretching, NH bending, and CO in-plane bending, and, finally, the amide A (NH stretch) band.[(11)] The typical MIR and FIR absorption spectra of the protein are shown on Figure 6A and B, respectively, and assignments of different vibrational modes of amide bonds are presented in the Table 1.

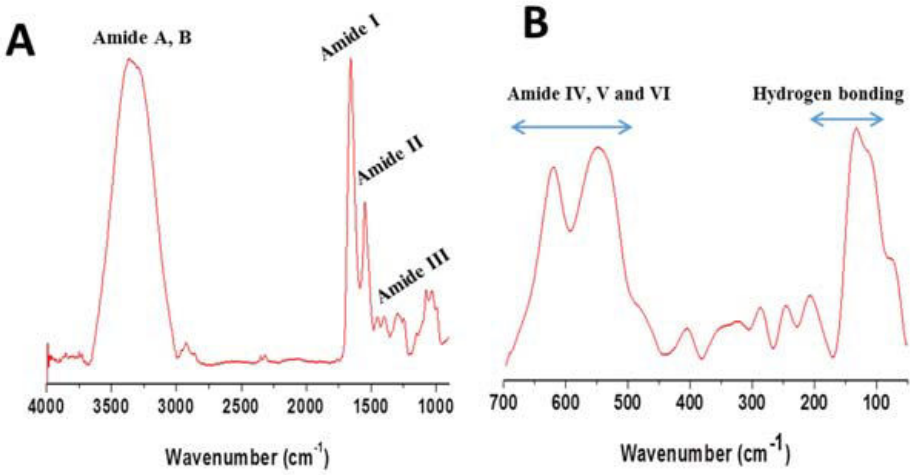

Figure 6: FTIR absorbance spectra of a protein in the mid infrared (A) and far infrared (B) regions

Table 1: Assignment of the polypeptide skeleton amide bands in the mid- and far-infrared[(10),(12),(13)]

Amide bands	Wavenumber (cm^{-1})	Vibrational modes
Amide A	~3300	ν(N-H), ν(O-H)
Amide B	3100-3050	ν(N-H)
Amide I	1700-1600	80% ν(C=O), ν(C-N), δ(N-H)
Amide II	1580-1480	60% δ(N-H), ν(C-N)
Amide III	1400-1200	δ(N-H), δ(C-N), ν(C=O), δ(N-C=O)
Amide IV	780-650	δ(C=O) in-plane, ν(C-C)
Amide V	600-540	δ(C-N) torsion
Amide VI	540-500	δ(C=O) in-plane and out-of-plane
Amide VII	290-250	δ(N-H) out-of-plane

Amide I band is used to estimate proteins secondary structure and it allows following induced conformational changes of the proteins.

1.5.1 Analysis of the secondary structure

In order to estimate the secondary structure of the studied proteins, amide I band was deconvoluted using the program Origin (version 8.5).[(14),(15)] The lineshape of amide I band is sensitive to the different types of secondary structure elements, and is not much influenced by

the side chains. Absorption properties are different for different protein secondary structure elements (e.g., α-helices, β-sheets, random coils, and loops), since they exhibit hydrogen bonding of different strength from one peptide –C=O group to N–H group of a neighboring amino acid. The strength of the hydrogen bond influences the absorption frequency of the C=O vibration. This leads to the regions of resolvable absorptions in the amide I region corresponding to different secondary structure elements of the protein.[11] Second derivative is calculated in order to estimate the number and approximate position of the components of amide I band. Deconvolution is performed using the Gaussian profile of each component and consecutive optimization of the position, amplitude and width at half-height of each band. Afterwards, the area of individual band was used to calculate the relative contribution of each component of the secondary structure of the protein into the total surface area of amide I band. Positions of the different components of amide I band are summarized in the Table 2.

Table 2: Assignment of the positions of different components of amide I band[10],[16],[17]

Secondary structure	H_2O (cm^{-1})	D_2O (cm^{-1})
α- helices	1648-1657	1642-1660
Parallel β-sheets	1623-1641	1615-1638
Antiparallel β-sheets	1674-1695/1615-1627	1672-1694/1613-1625
β-turns	1662-1686	1653-1691
Unordered structure	1642-1657	1639-1654

Deuterated solvents are widely used in the protein infrared spectroscopy since they allow distinguishing between α-helical and random structures. In H_2O these two structures overlap. The frequency of the amide II band decreases by about 100 cm^{-1} upon H/D exchange of amide protons. Therefore, this band is usually used to measure the extent of amide-proton exchange in proteins and peptides.[12]

1.6 Transmission mode

In transmission measurements, first the infrared light passes a cuvette with the sample and then it reaches the detector.[10] In a simple, direct transmission FTIR experiments certain accessories are used. These normally include a liquid sample holder, two infrared-transparent windows (for example, CaF_2 or BaF_2), a spacer which is a thin ring that fits the circumference of the windows.

It is normally made of Teflon or another inert and durable material (the reasonable thickness of the spacer is in the range 5–50 μm).

The strong absorbance of water in the mid-infrared spectral region (near 1645 cm^{-1}) is the drawback of infrared spectroscopy of aqueous solutions since it overlaps the important amide I band of proteins and some side chain bands. In the case when these protein bands are of interest, the strong water absorption requires a short path length for aqueous samples (typically around 5 μm) and relatively high concentrations of the samples. The pathlength can be increased to 50 μm and the concentration lowered when using D_2O since the water band is downshifted to ~1210 cm^{-1}. Typical concentrations for proteins in the infrared spectroscopy are 0.1 to 1 mM and 1 to 100 mM for small molecules.[10]

This experimental setup was used to verify the extraordinary optical transmission (EOT) features of the gold grids used in our laboratory as working electrodes (WE) in the electrochemical cell. EOT is an optical phenomenon in which a structure comprising subwavelength apertures in an opaque screen transmits more light than might be predicted on the basis of either ray optics or even knowledge of the transmission through individual apertures.[18] EOT properties of the gold grids would be promising to further reduce the amount of the studied samples.

1.7 Attenuated Total Reflection (ATR) mode

The principle of this technique is shown in Figure 7. The IR beam enters an IR transparent slab with the high refractive index, such that at its surface the total reflection occurs. If the surfaces are clean without any adsorbed molecules then the IR beam leaves the slab without attenuation. But in the case when one of the surfaces is in contact with material that can absorb in the IR region, the IR beam is attenuated at the frequencies of the absorption bands.

Upon the total reflection of the beam an evanescent wave penetrates into the optically rarer or less dense medium (i.e., possessing a lower refractive index) with an amplitude that exponentially decays in the direction normal to the surface (i.e., in z-direction), and carrying no energy.

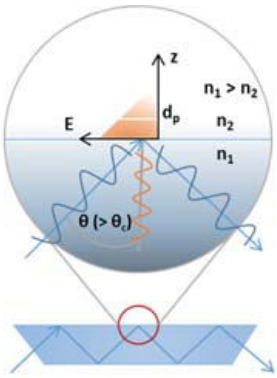

Figure 7: Schematic representation of the ATR principle. The ATR crystal is represented by blue trapezoid and the reflected IR beam by the blue arrows. The decreasing of the intensity of the evanescence wave is represented by the orange curve[19]

When the absorbing sample is placed onto the surface, it couples with the electric field and energy is drawn out of the radiation, i.e., the total reflection is attenuated. The exponentially decaying field amplitude can be determined by the following equation

$$E = E_0 \exp(-\frac{z}{d_p}) \qquad \text{Equation 14}$$

This field amplitude is characterized by the penetration depth d_p

$$d_p = \frac{\lambda_1}{2\pi\sqrt{sin^2\theta - {n_{21}}^2}} \qquad \text{Equation 15}$$

Here λ_1 is the wavelength of the radiation in the optically denser medium with refractive index n_1, θ is the angle of incidence in the denser medium, and n_{21} is the ratio of the refractive indices n_2/n_1 where the index "2" is related to the rarer medium. It is evident that the penetration depth becomes infinite when θ approaches the critical angle arcsin(n_{21}) when light begins to be transmitted into the medium of lower refractivity. The minimum penetration depth will be at the grazing incidence, i.e., at $\theta = 90^0$.[20] d_p can be defined as the distance where the amplitude of the electric field is 1/e of E_0, which is a function of n_1, n_2, θ and the wavelength of the radiation, λ.[21]

The penetration depth for ZnSe crystal varies between 0.83 and 1.66 µm in the range between 5 and 10 µm (2000–1000 cm^{-1}). Only a very low attenuation is obtained with a single reflection with such penetration depth. That is why a multireflection element is normally used.

It is possible to overlay the biological sample with an extended aqueous layer of water, i.e., the bulk phase of the aqueous solution since the thickness of the biological sample in the z-direction can be arbitrarily larger than the penetration depth without affecting the attenuation. This

provides a full hydration of the sample. Moreover, ATR is an ideal technique for the probing the effect of ligand binding to a receptor. The only one prerequisite is that the sample must be firmly immobilized on the surface of the ATR crystal.

FTIR instruments usually include a circular aperture. In order to allow a perpendicular entrance of the IR beam for 45^0 total reflection the entrance and exit faces must be inclined by 45^0. Importantly, only the flat mirrors are required to reflect the IR beam into the element and to collect the radiation from the exit face.

Nowadays, many ATR devices are available as flow cells. They allow either the measurement of liquid samples or the change of the buffer solution in experiments while the sample is immobilized on the surface of the crystal. The ATR technique is the method that is widely used in many biological applications since it avoids not desired structural distortions due to extensive dehydration, and moreover it allows flexible control of the environmental parameters (such as buffer, pH, ionic strength) and probing molecular processes induced by binding of the ligands.[20]

1.7.1 Polarized ATR FTIR spectroscopy

Information about the orientation of the molecules can be obtained from polarized IR spectra of oriented samples. This is possible due to the fact that the absorbance is proportional to the square of the product of the transition dipole moment, *M*, and the projection of the electric field, *E*, of the polarized IR beam on *M*, i.e. $|ME|^2 cos^2\zeta$, where ζ f is the angle between the directions of *M* and *E*. That is why the corresponding parameter for optical orientation measurements, the dichroic ratio,

$R = \frac{A_{\parallel}}{A_{\perp}} = \frac{\int A_{\parallel}(\nu)d\nu}{\int A_{\perp}(\nu)d\nu} = \frac{cos^2\zeta_{\parallel}}{cos^2\zeta_{\perp}}$ is largest for *M* which is parallel to $E_{//}$ and smallest for *M* parallel to $E_{\perp}$. $A_{//,\perp}$, $\int A_{//,\perp}(\nu)d\nu$, and $\zeta_{//,\perp}$ in the equation represent the peak absorbances, the absorbances that are integrated through an entire absorbance band, and the respective angles for parallel (p) and perpendicular (s) polarized incident light, respectively.[12]

In the present study polarized ATR FTIR spectroscopy was used for the estimation of the major helical orientation of lactose permease on the modified gold surface.

1.7.2 ATR-FTIR coupled to perfusion cell

Perfusion of a reagent in an attenuated total reflection cell is an approach suitable for FTIR difference spectroscopy of membrane protein. This was successfully developed for the

investigation of the ligand-induced IR changes of the nicotinic acetycholine receptor[22]. As was mentioned before, in the ATR measurement, the IR beam penetrates the internal total reflection prism on which the sample film is attached[21] and which is enclosed in a specially designed liquid flow cell (Figure 8).

The evanescent wave propagates through the sample film which is exposed to a flow of different perfusion solutions. That is why, this extension of the ATR FTIR technique is very important since it allows difference spectra to be recorded between two states of the protein that can be obtained by changing the composition of the perfusion solutions. Moreover, it allows precise control of the ionic composition and pH of the solution in a fully hydrated sample with no influence from the strong absorption bands of water encountered in transmission measurements. The ligand-induced ATR-FTIR absorption experiments were extended to the study of pH- and ion-induced changes as well as to the study of the interactions between the proteins.

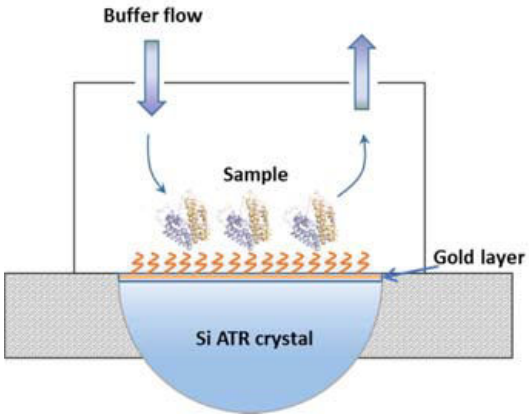

Figure 8: Representation of the perfusion ATR cell

Interestingly, for the important class of redox active proteins for which studies that include perfusion of solutions poised at different redox potentials have appeared only very recently. Probably this is due to the experimental difficulties met in achieving the high sensitivity that is necessary in such measurements or in obtaining protein films that remain sufficiently stable under the flow conditions.[23]

In order to obtain a stable protein film under continuous flow conditions silicon ATR crystal was first modified with the gold film and afterwards with the Nickel-nitrilotriacetic acid (Ni-NTA) self-assembled monolayer (SAM) (see sections 3.3.1 and 3.3.2).

1.7.2.1 FTIR difference spectroscopy

FTIR difference spectroscopy was developed and widely used as the technique to investigate the molecular changes that occur at the active site of many membrane proteins that are involved in the transport of ions or solutes, respiration, proton pumping or signal transduction. The idea of this technique is to record IR spectra for two different states of the protein that are obtained before and after applying of the external perturbation that triggers the transition between different states. In the registered difference spectrum, only the vibrational modes that are influenced by this transition will be detected, because the bulk of the IR signals are not perturbed by the reaction. Therefore, this method is effective in probing even minute structural alterations between two states that differ by, e.g. hydrogen bonding, protonation, ionization.[23] In many cases, negative bands in a difference spectrum are associated with the state before the reaction and positive bands with that after the reaction (Figure 9).[10]

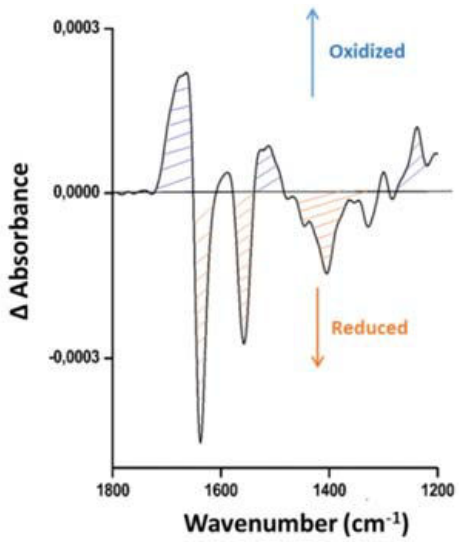

Figure 9: Representation of a difference spectrum between the fully oxidized and the fully reduced state of the protein

Here, the main method used to displace proteins from equilibrium is perfusion with buffers of different pH, oxidation-reduction capabilities and of different composition.

In the difference spectra conformational changes of the studied proteins were detected in the spectral region of Amide I and Amide II. Protonation and deprotonation of acidic residues like Glutamic and Aspartic acids can be monitored through spectral changes in between 1750 and 1700 cm^{-1}.

1.8 Raman spectroscopy

Raman spectroscopy is a branch of vibrational spectroscopy that allows a highly sensitive structural identification of trace amounts of the samples on the basis of their unique vibrational characteristics. Raman scattering was first predicted theoretically by Smekal in 1923 and experimentally by Raman and Krishnan in 1928. The basis of Raman spectroscopy is inelastic scattering of radiation in the visible or near-infrared region by the sample. There are two types of light scattering: the elastic and inelastic scattering. The elastic scattering occurs when the photon frequency is not shifted. Most of the scattered light (Rayleigh scatter) has the same wavelength as that of laser source light. Another type is inelastic scattering that forms the basis of Raman spectroscopy. The frequency shift can be used to get information about the molecular structure of the sample.

Raman spectroscopy measures the frequency shift of the inelastic scattered light from the sample. The outcoming scattered light can be a photon with the higher frequency which is known as anti-Stokes Raman scattering or with a lower frequency than the original photon and in that case, it is known as stokes Raman scattering. In the first case, the photon will get energy from the molecule which is initially in the excited vibrational state. The diagram explaining the origin of Raman signals is shown on Figure 10.

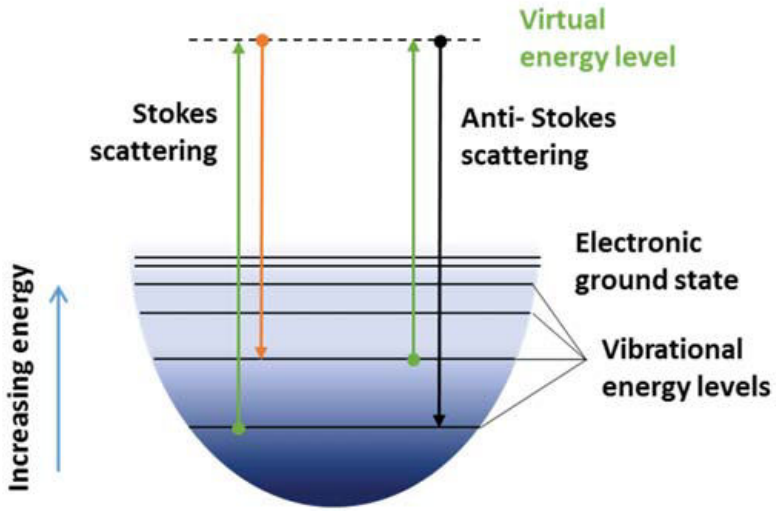

Figure 10: Energy-level diagram showing the states involved in Raman spectra

The shift in wavelength of the scattered light is depending on the chemical composition of the molecules involved in the scattering. The intensity of Raman scattering is proportional to the magnitude of the change in the molecular polarization. According to Raman selection rule, the

displacement of the constituent atoms from the equilibrium positions as the result of the molecular vibrations will change the molecular polarizability.

A Raman spectrometer consists of a light source, monochromator, sample holder, notch filter, mirrors, grating, amplifier and a detector. Several types of lasers can be used as the excitation source, for example krypton ion (530.9 and 647.1 nm), He-Ne (632.8 nm), Nd:YAG (1064 nm and 532 nm), argon ion (488.0 and 514.5 nm) and diode laser (630 and 780 nm). A major challenge in Raman spectroscopic analysis of organic and biological samples is fluorescence. Use of 1064 nm near-IR (NIR) excitation laser results in a lower fluorescent effect comparing to the visible wavelength lasers. Schematic representation of Raman spectrometer is shown on Figure 11.[24]

Rayleigh scattering is more intense than Raman scattering (~10^7 times). The magnitude of Raman scattering is small therefore stimulation is needed to enhance it. Scattered light is filtered and only Raman scattering passes through the filter. Afterwards, the Raman scattering is diffracted by a grating to a detector and a spectrum is registered with the information about molecular bonding.

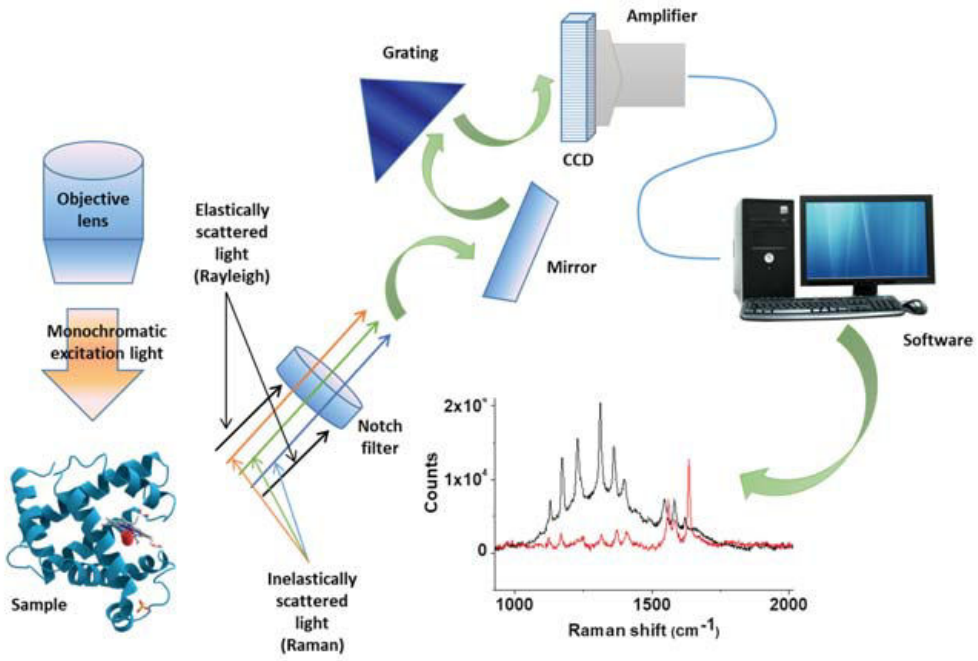

Figure 11: Representation of a Raman spectrometer

Normally a photo-detector, such as a charged couple device (CCD), records the intensity of inelastic scattering in arbitrary units by wavelength.[25]

1.9 Surface enhancement effects in Raman and IR spectroscopies

During the last decades surface-enhanced Raman scattering became a mature vibrational spectroscopic technique with the increasing number of applications in the chemical, material, and in particular life sciences.

In comparison to normal Raman spectroscopy, SERS also requires the presence of metal nanostructures. In order to understand SERS, one must consider not only the interaction between light and sample, but also that between light and metal nanostructures. The central topic of plasmonics is the optical properties of metal nanostructures. The term plasmonics indicates the coupling of photons to charge density oscillations of the conduction electrons in metals.[(26)]

Surface-enhanced IR absorption spectroscopy (SEIRAS) was discovered in 1980th after SERS by Harstein *et al.* They reported that absorption of the molecules adsorbed at the nanostructured noble metal films may be enhanced by a factor of 10–1000 in magnitude.

The electromagnetic (EM) and chemical mechanisms are two different mechanisms that are supposed to contribute to the total enhancement in the case of SERS and SEIRAS.[(27)]

Electromagnetic enhancement. In the classic harmonic oscillator model, the eigenfrequency $\omega = (\frac{k}{\mu})^{1/2}$ of the oscillator is determined by the force constant k and the reduced mass μ of the system. In analogy, the laser light as an electromagnetic wave (which is an external driving force) can also resonantly excite the delocalized conduction electrons in a metal (so called plasma oscillations). The resonance frequency ω_{max} of the plasma oscillations (plasmons) in the metal nanostructure is depending on the dielectric functions of the surrounding medium $\varepsilon_m(\omega)$ and the metal $\varepsilon_{metal}(\omega)$. Plasmon peaks for colloidal silver (yellowish) and gold (reddish color) are observed in the visible region and therefore can be excited at optical frequencies (ca. 10^{14} – 10^{15} Hz). The oscillating electric field of the incoming laser radiation with angular frequency ω_{inc} and amplitude E_0 upon resonant excitation drives an oscillation of the conduction electrons, (Figure 12A) and results in a charge separation.

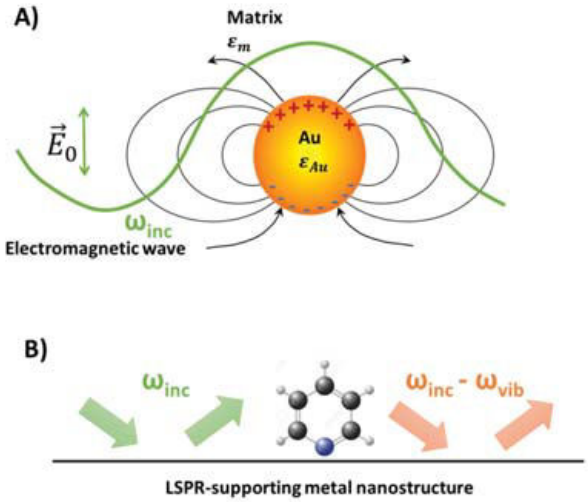

Figure 12: Electromagnetic enhancement in SERS. A) A gold nanoparticle acts as a nanoantenna upon excitation. B) Both the "incoming" field ($\boldsymbol{\omega}_{inc}$, green) and the "outgoing" field ($\boldsymbol{\omega}_{inc} - \boldsymbol{\omega}_{vib}$, orange) are enhanced by elastic light scattering off the plasmonic metal nanostructure

This type of resonance is called dipolar localized surface plasmon resonance (LSPR). The magnitude of the induced dipole $\mu_{ind(metal)}$ is determined by the incident electric field strength $E_0(\omega_{inc})$ and the polarizability of the metal sphere α_{metal}: and $\mu_{ind} = \alpha_{metal} E_0(\omega_{inc})$. In general, a Hertzian dipole (electric field lines in Figure 12A) on the nanoscale, i.e., a nanoantenna, is generated, that is able to emit radiation at the same frequency ω_{inc} (green color in Figure 12A and B). In other words: resonant elastic light scattering off a metal sphere leads to an increased local electric field $E_{loc}(\omega_{inc})$ in the vicinity of the metal particle relative to the incident electric field $E_0(\omega_{inc})$.

It is also important to consider the interaction of the local electric field $E_{loc}(\omega_{inc})$ with a molecule near the surface of the metal sphere (Figure 12B). In analogy to a dipole induced in the metal sphere, dipoles in molecules can also be induced: $\mu_{ind} = \alpha_{molecule} E_{loc}(\omega_{inc})$. Classical theory can explain the inelastic light scattering in terms of a modulation of the incident electric field $E_{loc}(\omega_{inc})$ by a vibrating molecule with angular eigenfrequency ω_{vib}.

Further, since the electric field strength of dipolar radiation scales with $E(r) \sim \frac{1}{r^3} = r^{-3}$, a SERS distance dependence of $I_{SERS} \sim \frac{1}{r^{12}} = r^{-12}$ is expected by theory and observed experimentally. In other words: SERS is a truly surface-selective effect. The orientation of the molecule relative to the surface normal is also important and can be detected: flat versus tilted versus perpendicular orientations give rise to distinct SERS signatures because the various vibrational bands of the adsorbed molecule are differently enhanced.

Discussed above electromagnetic enhancement is the dominant enhancement mechanism for SERS and it includes only the metal nanostructure and photons. The most important message here is that very high local electric fields causes the significantly increased signal strength observed in SERS relative to normal Raman scattering. An increase of $E_{loc}/E_{inc} = 100 = 10^2$, for example, results in an overall increase of the SERS intensity by a factor of $(E_{loc}/E_{inc})^4 = (10^2)^4 = 10^8$ or one hundred million. In other words: moderate increases of E_{loc}/E_{inc} results in a huge SERS enhancement. The number 10^8 in this example is called the SERS enhancement factor (EF). Determination of SERS EFs requires measurements of the signal intensity of the adsorbed molecule on the metal surface, relative to the normal Raman signal intensity of the same "free" molecule in solution. Both signal intensities must be normalized to the corresponding number of molecules on the surface (SERS) and in solution (conventional Raman), respectively.

"Chemical" and Resonance Raman contributions. "Chemical" enhancement (CE) mechanism corresponds to the electronic features of the adsorbate and it acts by means of the increasing of the electronic polarizability $\alpha_{molecule@metal}$ of the adsorbed molecule on the induced dipole μ_{ind}. CE is of the order of one to three orders of magnitude which is significantly smaller than the EM contribution. Charge transfer (CT) between the molecule in the ground state and the metal can result in the change of polarizability of the molecule, causing a change of the Raman scattering cross-section of the molecule. Moreover, the energy levels of the adsorbate molecule usually are different comparing to those of the molecule in its unbound or "free" state.

It can happen that the laser excitation wavelength does not coincide with an electronic absorption band of the "free" molecule, but coincides with one of the adsorbed molecule. The resonant excitations of electronic transitions in the molecules are called resonance Raman (RR) scattering.[26]

In this study SEIRAS (ATR mode) was combined with perfusion cell (see section 1.7.2) in order to monitor different states in proteins upon changing different perfusion solutions. And SERS was coupled to electrochemical cell to develop a combined electrochemical and surface enhanced Raman spectroscopic approach using gold grids as working electrodes and SERS active substrates.

1.9.1 Electrochemical Surface Enhanced Raman Scattering (EC-SERS)

The electrochemical surface-enhanced Raman scattering (EC-SERS) system normally consists of the nanostructured electrode and electrolyte.[28]

Here, in order to develop combined electrochemical-Raman approach an optically transparent thin layer electrochemical cell was used.[29] It consists of a solid polyvinyl chloride (PVC) cell body with four inlets, three of them serve to connect a three electrode system: working electrode (WE, gold grid), counter electrode (platinum sheet) and reference electrode (Ag/AgCl 3M KCl) (+208 mV *vs.* SHE). The fourth one used to fill the cell with buffer solution (Figure 13A).
Electrochemical cell was placed in the PVC body between two CaF_2 windows and two joints were used to ensure the sealing of the system. Afterwards, assembled cell was placed between two steel plates that were squeezed together creating a very short optical path-length of 10 µm (Figure 13 B). Then, the system was placed into the Raman spectrometer, connected to the potentiostat *via* three electrodes and kept at the constant temperature (5 °C) by the connection to the thermostat (Huber, Offenburg) through the inlets for thermostatisation.

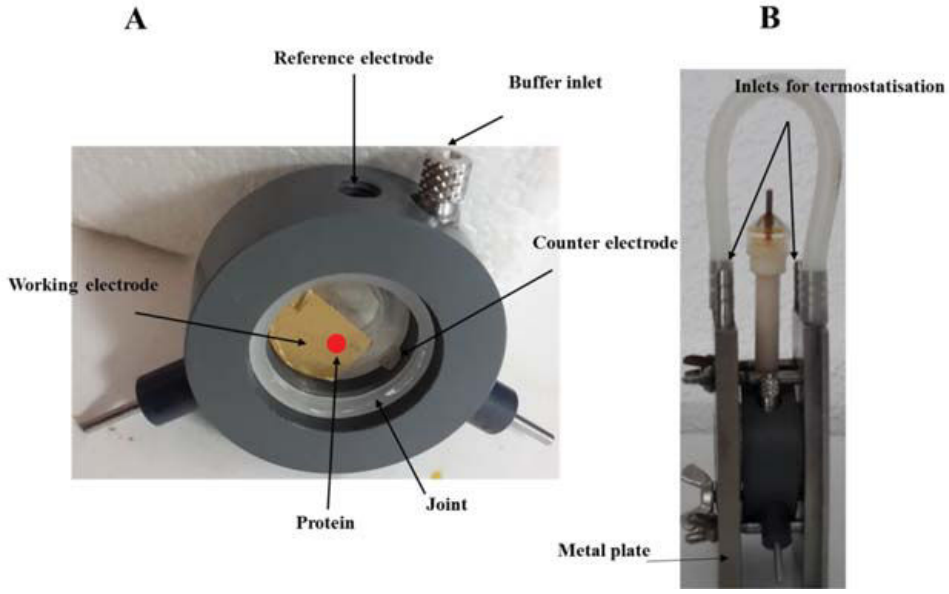

Figure 13: Representation of the thin layer electrochemical cell before (A) and after (B) assembly

The gold grid working electrode was modified with the self-assembled monolayers of thiols in order to avoid denaturation of the proteins (Figure 14).

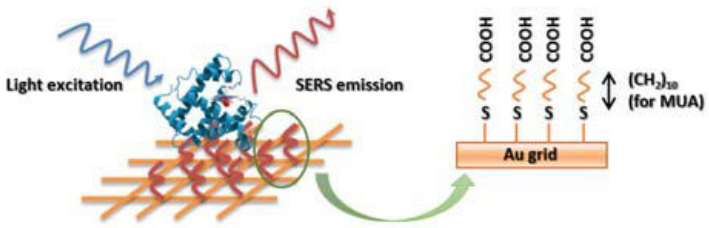

Figure 14: 11-MUA SAM formed on the gold grid

First, well studied model heme proteins like cytochrome *c* (Cyt *c*), hemoglobin (Hb) and myoglobin (Mb) were tested in order to validate experimental setup. Afterwards, cytochrome cbb_3 oxidase was used to check the validity of the setup to study proteins that contain several hemes in their structure.

1.10 Focused ion beam (FIB) imaging

Focused ion beam (FIB) is a widely used technique for the imaging of the samples of interest. In this work FIB was used for the estimation of the physical parameters and morphology of the surface of the gold grids.

FIB imaging of the gold grids was performed by the members of the Nanostructures Laboratory - Dr. Jino George and Dr. Eloïse Devaux at the Institute de Science et d'Ingénierie Supramoléculaires (ISIS, Strasbourg).

Schematic representation of the principle of FIB imaging is shown below (Figure 15).

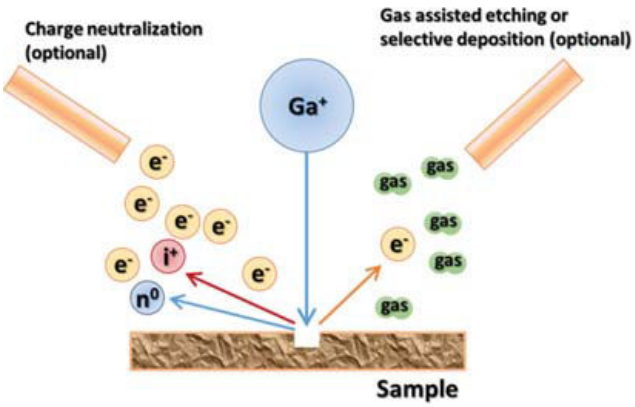

Figure 15: Representation of the principle of FIB imaging

The gallium (Ga^+) primary ion beam hits the sample surface and sputters a small amount of material, that leaves afterwards the surface as either secondary ions (i^+ or i^-) or neutral atoms (n^0). The primary beam produces secondary electrons (e^-) as well. When the primary beam rasters on the sample surface, the signal from the sputtered ions or secondary electrons is collected to create an image of this surface.[30]

2. Sample preparation

2.1 Thiols

11-Mercaptoundecanoic acid (11-MUA) (95%), cysteamine (2-aminoethanethiol hydrochloride) (95%), 6-mercapto-1-hexanol (97%) and 1-hexanethiol (95%) were purchased from Sigma-Aldrich (France). 20 mM solutions of 11-MUA and cysteamine were prepared by dissolving of the powders in ethanol. An equimolar solution of 6-mercapto-1-hexanol and 1-hexanethiol (1/1 M) was prepared by dissolving of corresponding volumes of the thiols in ethanol.

2.2 Heme proteins

Bovine heart cytochrome *c* (≥ 95% purity), bovine blood hemoglobin and equine heart myoglobin (≥ 90% purity) were purchased from Sigma-Aldrich (France). 2 mM solutions were prepared by dissolving the proteins in 10 mM KPi at pH 8.0 and KCl was added only in the buffer solutions used in electrochemical cell to a final concentration of 50 mM; proteins dissolved in 10 mM KPi without KCl were used for the adsorption on the modified gold surface. Salts for the preparation of buffers (KPi and KCl) were purchased from Sigma-Aldrich (France).

P. stutzeri ZoBell cells were cultured under microaerobic conditions and harvested according to the previously published procedures[31] at Max Planck Institute of Biophysics, Department of Molecular Membrane Biology, Frankfurt/Main, Germany. Membrane preparation and solubilization as well as the purification of the homologously expressed *P. stutzeri* cbb_3 (cbb_3 *PS*) oxidase were performed as published previously.[32] Briefly, two chromatographic steps were applied for protein purification: A Strep-Tactin affinity column followed by ion exchange on Q Sepharose high performance column. The purified proteins were washed and concentrated in 20 mM Tris/pH 7.5, 100 mM NaCl and 0.02 % (w/v) n-dodecyl-β-D-maltoside (DDM). Before the experiments cbb_3 *PS* samples were conditioned in the 50 mM KPi, 0.01 % DDM (pH 7.5).

2.3 Gold grids

Gold grids were purchased from the manufacturer Precision Eforming (Cortland, New York). Two types of gold grids have been used with the size of the square holes of 11 µm and 40 µm. These gold grids were fabricated by means of electroforming.

2.4 Synthesis of gold nanoparticles

Gold nanoparticles were prepared following the procedure proposed initially by Turkevich and refined by Frens. Solution of $HAuCl_4$ (55 mg) was boiled in Milli-Q water (140 mL), and subsequently an aqueous solution of sodium citrate (160 mg in 13 mL of water) was added. The mixture was boiled during 15 min and then it was allowed to cool down to room temperature. This stock solution was centrifuged at 10 g for 30 min to obtain concentrated solution of gold nanoparticles.[33]

2.5 Materials for the preparation of Lactose Permease and its mutants

Oligonucleotides were synthesized by Integrated DNA Technologies, Inc. Restriction enzymes were purchased from New England Biolabs. The QuikChange II kit was purchased from Stratagene. NPG was from Sigma. Talon superflow resin was purchased from BD Clontech. Dodecyl-β-D-maltopyranoside (DDM) and octyl-β-D-glucoside (OG) were from Affimetrix. Synthetic phospholipids 1-palmitoyl-2-oleoyl-sn-glycero-3-phosphoethanolamine (POPE) and 1-palmitoyl-2-oleoyl-sn-glycero-3-phospho-(1-rac-glycerol) (POPG) were from Avanti Polar Lipids, Inc. All other materials were of reagent grade obtained from commercial sources.

2.6 Construction of Mutants, Purification of LacY, and Reconstitution into Proteoliposomes

Construction of mutants, expression in *E. coli*, and purification of LacY were performed as described[34] at the University of California in Los Angeles, USA. All constructs contained a C-terminal 6His-tag that was used for affinity purification with Talon resin. Purified proteins (3–12.5 mg/mL) in 50 mM sodium phosphate (NaPi/0.02% DDM; pH 7.5) were frozen in liquid nitrogen and stored at -80 °C until use. Reconstitution into proteoliposomes was carried out with synthetic phospholipids (POPE/POPG ratio 3:1) by using the dilution method.[35] Briefly, purified LacY in 0.02% DDM (wt/vol) was mixed with phospholipids dissolved in 1.2% OG maintaining a lipid-to-protein ratio of 5 (wt/wt). The mixture was kept on ice for 20 min and then quickly diluted 50 times in 50 mM NaPi buffer (pH 7.5). The proteoliposomes (PLs) were harvested by centrifugation for 1h at 100,000 g, suspended in the same buffer, and subjected to two cycles of freeze/thaw/sonication. Flash-frozen PLs were stored at -80 °C. Before use, the PLs were subjected to an additional two cycles of freeze/thaw/sonication.

2.7 Preparation of wild type complex I from *E. coli*

Preparation of complex I was performed according to a well-established protocol in Pr. Dr. T. Friedrich's group at the Albert-Ludwigs University Freiburg. This preparation was done in cooperation with a PhD student Johannes Schimpf.

Cells (30 – 40 g) were resuspended in a 6-fold volume of 50 mM MES/50 mM NaCl/0.1 % DDM (pH 6.0) with PMSF (30 µL per 100 mL of buffer) and 10 µg/mL DNAse using "teflon-in-glass" homogenizer at 4^0C. Resuspended cells were disrupted by a triple pass through a French pressure cell at 1000 – 1500 MPa. Cell walls and not disrupted cells were separated by a low-speed centrifugation (Rotor A 8.24, 4^0C, 14500 rpm, 20 min), supernatant was collected for further preparation. Afterwards, cytoplasm and membranes were separated by high speed centrifugation (Rotor 50.2Ti, 4^0C, 42000 rpm, 70 min) and membranes were collected.

Separated membranes were homogenized with 50 mM MES/50 mM NaCl/5 mM $MgCl_2$ (pH 6.0) and PMSF [1:1000] (1 mL of buffer per 1 g of membranes). 100 µL of the sample were collected for the oxidoreductase activity measurements.

For the extraction by detergent 10 % DDM was added dropwise to the membrane homogenized solution to a final concentration of 1 %. This solution was incubated with DDM during 15 min. Afterwards, 100 mL of buffer (50 mM MES/50 mM NaCl/5 mM $MgCl_2$ (pH 6.0)) with 100 µL of PMSF were added to the prepared mixture and further high speed centrifugation (Rotor 60Ti, 4^0C, 50000 rpm, 15 min) was performed in order to separate soluble proteins and lipids. 300 µL of the sample were collected for the oxidoreductase activity measurements.

The supernatant was applied to a 60 mL anion exchange column (Fractogel, Merk) equilibrated with 50 mM MES/50 mM NaCl/5 mM $MgCl_2$/0.1 % DDM (pH 6.0). The column was first washed with the same buffer until the absorbance at 280 nm decreased. Protein was eluted with a linear salt gradient from 50 to 350 mM NaCl in 50 mM MES/5 mM $MgCl_2$/0.1 % DDM (pH 6.0). Anion exchange column was regenerated by washing first with 0.5 M NaOH and then with 2 M NaCl.

Afterwards, imidazole was added to a final concentration of 20 mM to the collected fractions exhibiting NADH/ferricyanide oxidoreductase activity. Then, this solution was applied to an affinity chromatography column previously equilibrated with 50 mM MES/500 mM NaCl/5 mM $MgCl_2$/0.1 % DDM/20 mM imidazole (pH 6.3). Column was washed first with 50 mM MES/500 mM NaCl/5 mM $MgCl_2$/0.1 % DDM/20 mM imidazole (pH 6.3) until the absorbance decreased

to 250 mAU. Protein was eluted with a step gradient: 25%, 50%, 100% of elution buffer (50 mM MES/500 mM NaCl/500 mM imidazole (pH 6.3)). Complex I was collected when washing the column with 50 % of elution buffer. The fractions with NADH/ferricyanide oxidoreductase activity were pooled, concentrated by ultrafiltration (100 kDa MWCO Amicon, Millipore), shock frozen in liquid nitrogen and stored at -80 °C for further use.

2.8 NADH/$K_3[Fe(CN)_6]$ oxidoreductase activity measurements

The oxidoreductase activity of the complex I samples was measured by following the reduction of ferricyanide by NADH.[36] This was done by measuring the Absorbance at 410 nm[37] in a cuvette with 1 cm path length at room temperature. The cuvette contained 1 mL of 1 mM $K_3[Fe(CN)_6]$, 20 µL of 10 mM NADH and 5 – 10 µL of the sample.

2.9 Determination of complex I concentration through UV-Visible spectroscopy

To quantify the concentration of the complex I, an UV-Vis spectrum of 2 µL sample diluted in 298 µL buffer (50 mM MES/50 mM NaCl/5 mM $MgCl_2$ (pH 6.0)) was recorded in a 1 cm path length quartz cuvette *via* a Diode-Array UV-Vis Spectrophotometer (TIDAS II, J&M). The spectrum of 300 µL of the buffer was previously recorded as background. To account for absorption by lipids and aromatic amino acids, the absorbance value at 310 nm, where no protein absorption should be present, was subtracted from the absorbance value at 280 nm. The concentration was then calculated according to the Beer Lambert Law using a molar extinction coefficient for complex I (MW 535.4 kDa) of ε_{280} = 781 $mM^{-1}.cm^{-1}$ (calculated according to ref.[38]).

2.10 Determination of total protein content by biuret reaction

To estimate the yield of the complex I purification, the total protein content after the four purification steps (collection of membrane, extraction with detergent, anion exchange chromatography and affinity chromatography) was determined by means of biuret reaction.[39] 1 mL of 6% w/v trichloroacetic acid (TCA) was added in 10 to 60 µL of the sample solutions. The mixtures were then centrifuged for 1 min, 13200 rpm. The supernatant was discarded and the pellets were dried in the oven for 3 min at 57^0C before being resuspended in 1 mL Biuret-reagent. Afterwards, the samples were shaken for 30 min at 1400 rpm at 37°C (Thermomixer Compact, Eppendorf). The absorbance of each solution was measured at 546 nm, which

corresponds to the absorption maximum of the created Protein-Cu(II) complexes (water was measured as background solution). After addition of a small amount of potassium cyanide in order to mask the Protein-Cu(II) complexes, the absorbance was measured again at 546 nm. The last absorbance values serve as a background by taking the absorption of lipids and detergents into account. Protein concentration was then determined taking into account the calculated difference between the two absorbance values and by comparison to a calibration line of 0.1 to 10 mg/mL Bovine Serum Albumin solution.

2.11 SDS-PolyAcrylamid Gel Electrophoresis (SDS-PAGE)

SDS PAGE was used to analyze the purity of complex I. The first section of gel contained 3.9 % of [acrylamid - bisacrylamid 30%] to sample the protein and the second one – to separate the subunits (10 % of [acrylamid - bisacrylamid 30%]). 5 µL of Millipore water and 2 µL of Schägger sample buffer[40] were added to 50-80 µg of each sample and the mixtures were shaken at 800 rpm for 30 min at 37°C (Thermomixer Compact, Eppendorf). Afterwards, the sample was applied on the gel together with a molecular weight marker (PageRuler Unstained Broad Range Protein Ladder, Fermentas). 40 mA current (500 mV, 100 W) was applied to start electrophoresis and it was stopped when the first marker band reached the end of the plate. Protein spots were colored with hot Coomassie blue solution and the gel was decolored with an acetic acid/ethanol solution.

3. Experimental conditions

3.1 UV-Visible spectroscopy

Absorption spectra of the samples in a 1 cm path length quartz cuvette were recorded in the UV-Visible spectrometer Varian Cary 300. The measurements were performed in order to determine concentration of the samples and the size of gold nanoparticles. To determine sample concentration 1 µL of the sample solution was diluted to a final volume 600 µL with a solvent in which it was prepared. Afterwards, concentrations were calculated according to a Beer-Lambert law (see section 1.2).

To determine the size of gold nanoparticles stock solution was diluted 10-fold in quartz cuvette with Milli-Q water. Ratio of the absorbance of Au NPs at the surface plasma resonance peak (A_{spr}) to the absorbance at 450 nm (A_{450}) was calculated and size of Au NPs was determined as described in ref.[41].

3.2 FTIR spectroscopy

All IR spectra were measured with a Vertex 70 infrared spectrometer from Bruker. The spectrometer was purged with dried air in order to avoid the influence of humidity. Depending on the different studied frequency range different sources, beamsplitters and detectors can be used. In the present study, all experiments were done in the mid-infrared (MIR) (400–4000 cm^{-1}) and far-infrared (FIR) (10 – 400 cm^{-1}) ranges. The appropriate optical elements for each optical range are presented in the Table 3.

Table 3: Equipment used for the infrared measurements depending on the studied spectral range

Optical elements	MIR	FIR
Source	Globar	Mercury vapor lamp
Detector	Liquid nitrogen cooled Mercury-Cadmium-Telluride (LN-MCT)	Deuterated Triglycine Sulfate (DTGS)
Beamspliter	Potassium bromide (KBr)	Silicon

3.3 Perfusion-induced ATR FTIR spectroscopy

A configuration allowing the simultaneous acquisition of FTIR spectra in the ATR mode with perfusion of solutions with given composition was used. As a multireflection ATR unit, we used

silicon crystal with 3-mm surface diameter. All experiments were carried out with a Bruker Vertex 70 FTIR spectrometer (Globar source, KBr Beamsplitter, mercury cadmium telluride detector) at 8-mm aperture and 40-kHz scanner velocity, 256 scans and 4 cm^{-1} resolution. The measurements were carried out at ~7°C. Solutions were kept on ice before use. 5 µL of the proteins were deposited on the modified silicon crystal. For the data presented here, the pump speed was kept constant at a flow rate of 0.2 mL/min. Before each perfusion step, the input tube was carefully washed with water and buffer.

Tethering of the proteins *via* His-tag on the surface of the ATR crystal was performed after its modification with gold layer and nickel nitrilotriacetic acid self-assembled monolayer (see sections 3.3.1. and 3.3.2).

3.3.1 Electroless deposition of the Gold Film on the ATR silicon crystal

First, a gold layer was cast on the surface of a Si ATR crystal by etching the Si with hydrofluoric acid (HF) and reduction of $AuCl_4$ as described previously.[42] Before the deposition of the gold film, the ATR crystal was polished with 0.3 µm alumina, rinsed with copious amounts of Millipore water, acetone and water again. The crystal was then dried under an argon stream and immersed in 40% NH_4F (wt/vol) for 1 min, rinsed and dried again. It was then heated at 65-70 °C for 10 min together with the plating solution. This solution was a 1:1:1 mix (vol/vol/vol) of (i) 15 mM $NaAuCl_4$, (ii) 150 mM Na_2SO_3, 50 mM $Na_2S_2O_3$, and 50 mM NH_4Cl, and (iii) HF 2% (wt/vol; total volume: 1mL). Once the plating temperature was reached, the prism was covered with the solution for 40 s, and the reaction was stopped by washing the plating solution off with water, followed by drying with a stream of argon. The resulting gold film was then tested for electrical conductance with a multimeter (the typical electric resistance of the layer as measured from one corner to another of the crystal should be ~15 Ω for a thickness of 50 nm).

3.3.2 Modification of the gold surface with Ni-NTA SAM and protein immobilization

The experimental procedure for the nickel nitrilotriacetic acid self-assembled monolayer (Ni-NTA SAM) was adapted from refs.[42],[43] First, the gold modified silicon ATR crystal was covered with 1 mg/mL of 3,3′-dithiodipropionic acid di(N-hydroxysuccinimide ester) (DTSP) in dry dimethyl sulfoxide and the monolayer was allowed to self-assemble for 1 h. The excess DTSP was then washed away with dry DMSO and the crystal was dried under an argon stream. Afterward, it was covered with 100 mM $N_{\alpha'}$,$N_{\alpha''}$-bis(carboxymethyl)-L-lysine in 0.5 M K_2CO_3 at

pH 9.8 for 3 h and then rinsed with water. Finally, the surface was incubated in 50 mM $Ni(ClO_4)_2$ for 1 h before being washed one last time with water. For immobilization of the protein, 5 µL of the studied proteins were deposited on the modified gold surface for 1h.

3.3.3 Calculation of the standard deviation

Standard deviation (S) between three measurements performed in perfusion cell was calculated for the peak intensity at 1742 cm^{-1} that corresponds to the protonated carboxyl group (COOH). The standard deviation was calculated according to the follow formula:

$$S = \sqrt{\frac{\sum(x - \bar{x})^2}{n - 1}}$$

The average value of peak intensity $\bar{x}$ was subtracted from each measured peak intensity x and after divided by the total number of performed measurements n.

3.4 pH-induced difference spectra of LacY

To monitor pH-induced difference spectra, we used one perfusion buffer with constant pH value 7.0 (25 mM KPi/100 mM KCl/0.01% DDM) and a second perfusion solution with the same composition but at different pH values ranging from 8.0 to 11.5. At the beginning, the system was equilibrated with the KPi (pH 7.0) for 30 min. Thereafter, the spectrum was recorded as background and the perfusion solution was changed to the second solution (pH range 8.0–11.5). After 20 min (pH 8.0–11.5) minus pH 7.0 difference spectra were recorded. The new state of the protein was recorded as background, and the solution was changed to pH 7.0. Again after 20 min, the pH 7.0 minus (pH 8.0–11.5) difference spectra were obtained. The same procedure was repeated five times and the difference spectra were averaged and smoothed. Baseline correction was done, where necessary. The data were normalized on the basis of the absorbance spectra obtained at the beginning of each experiment, when the data from different samples had to be compared.

3.5 pH-induced difference spectra of LacY in the presence of *p*-nitrophenyl-α-D-galactopyranoside

P-nitrophenyl-α-D-galactopyranoside (NPG) was dissolved in 25mM KPi/100 mM KCl/0.01% DDM (pH 7.0) at a final concentration of 80 µM. A second perfusion solution of the same

composition at pH values ranging from 9.0 to 11.5 was also prepared. The experiments have then been performed in analogy to the data obtained in the absence of NPG.

3.6 Perfusion-induced difference spectra of complex I

To monitor redox-induced difference spectra, we used one perfusion buffer containing reducing agent (50 µM of Nicotinamide Adenine Dinucleotide (NADH)) and a second perfusion solution containing 50 µM of one of the following oxidizing agents: ubiquinone-2 (Q-2), ubiquinone-10 (Q-10) or potassium hexacyanoferrate (III) ($K_3[Fe(CN)_6]$). Reducing and oxidizing agents were dissolved in 50 mM MES, 50 mM NaCl, 0.01% DDM (pH 6.0). First, the system was equilibrated with buffer containing NADH for 30 min. Afterwards, the spectrum was recorded as background and the perfusion solution was changed to the second solution containing oxidizing agent. After 20 min oxidized minus reduced difference spectra were recorded. The new oxidized state of complex I was recorded as background, and the solution was changed to the buffer containing NADH. Again after 20 min, the reduced minus oxidized difference spectra were obtained. This procedure was repeated five times and the difference spectra were averaged and smoothed. Baseline correction was done, where necessary. The data were normalized on the basis of the absorbance spectra obtained at the beginning of each experiment, when the data from different samples had to be compared.

3.7 Perfusion-induced difference spectra of IM 30

To record perfusion-induced spectra of IM 30, we used perfusion buffer 20 mM HEPES (pH 7.6) containing Mg^{2+} ions (90 mM final concentrations) and another buffer solution without Mg^{2+} ions. The experiments have then been performed in analogy to the perfusion procedures described above.

3.8 Raman spectroscopy

Raman spectra were obtained with an InVia Renishaw spectrometer using an excitation wavelength of 514 nm with laser power below 1 mW measured at the output of the microscope objective. Spectrometer is equipped with CCD (charge coupled device) detector. Raman spectra were recorded in the spectral region from 100 to 3200 cm^{-1} at 1 cm^{-1} resolution with exposition time 10s and with gratings 1200 lines/mm. To obtain spectra with optimal resolution of the signals 20 accumulations were done. Laser beam was focalized on the sample *via* microscope objective 20x. All Raman spectra were calibrated using silicon window as a reference.

In order to obtain the Raman spectra of the proteins in solution a simple liquid cell made of two CaF_2 windows and with a defined path was used (see section 1.9.1). The principle of this cell consisted in the deposition of 5 µl of 2 mM protein solution on the beveled calcium fluoride (CaF_2) window that was covered with another one. Afterwards, these windows were placed in the metallic support and connected to the thermostatic bath that cooled down the system to 4^0C.

3.8.1 Raman spectroscopy coupled to electrochemistry

To obtain Raman spectra of redox proteins electrochemical cell described before (see section 1.9.1) was used. Modified gold grid was used as the working electrode. It was modified with self-assembled monolayers created by immersion in the solutions of the thiols and keeping overnight at +4°C. Three types of thiols were tested: 20 mM negatively charged 11-mercaptoundecanoic acid (11-MUA), 20 mM positively charged cysteamine and neutral mixture of 1 mM 6-mercapto-1-hexanol with 1 mM 1-hexanethiol. Before adsorption of the proteins, the modified Au grids were washed with pure ethanol (≥99.8% grade) in order to remove physically adsorbed molecules. Then 8 µL of 2 mM proteins were put on the modified surface of the grids and kept at +4°C during 4 h. Not adsorbed proteins were rinsed from the surface with Milli-Q water.

The gold grid working electrode modified with the adsorbed protein was placed between two CaF_2 windows. The Pt counter electrode and the Ag/AgCl 3M KCl reference electrode (+ 208 mV vs standard hydrogen electrode) were used as previously described (see section 1.9.1). The assembled cell was placed in front of the objective inside Raman spectrometer and connected to the cooling system (Huber, Offenburg) to keep the temperature at +4°C during the experiment. Full oxidation and reduction of each protein was obtained by applying of follow potentials: Cyt *c*: E (Red) = -500 mV, E (Ox) = +500 mV; Hb: E (Red) = -600 mV, E(Ox) = +500 mV; Mb: E (Red) = -500 mV, E(Ox) = +300 mV[(44),(45),(46)] and *cbb₃*: E (Red) = -650 mV, E(Ox) = +400 mV[(47)] with a Ag/AgCl 3 M KCl reference electrode. Baseline correction was done, where necessary.

4. References

1. Richards, A. (2011) *Alien Vision: Exploring the Electromagnetic Spectrum with Imaging Technology*, Society of Photo Optical.

2. Hammes, G. G. (2005) *Spectroscopy for the Biological Sciences*, Wiley.

3. Siebert, F., and Hildebrandt, P. (2008) Introduction, In *Vibrational Spectroscopy in Life Science*, pp 1-10, Wiley-VCH Verlag GmbH & Co. KGaA.

4. Larkin, P. (2011) *Infrared and Raman Spectroscopy: Principles and Spectral Interpretation*, Elsevier.

5. Ma, G., and Allen, H. C. (2004) Handbook of Spectroscopy, Volumes 1 and 2 Edited by Günter Gauglitz (University of Tübingen) and Tuan Vo-Dinh (Oak Ridge National Laboratory). Wiley-VCH Verlag GmbH & Co. KGaA: Weinheim. 2003. 1168 pp. ISBN: 3-527-29782-0, *126*, 8859-8860.

6. Siebert, F., and Hildebrandt, P. (2008) Instrumentation, In *Vibrational Spectroscopy in Life Science*, pp 63-97, Wiley-VCH Verlag GmbH & Co. KGaA.

7. Smith, B. C. (2011) *Fundamentals of Fourier Transform Infrared Spectroscopy, Second Edition*, CRC Press.

8. Stuart, B. H. (2004) *Infrared Spectroscopy: Fundamentals and Applications*, Wiley.

9. Smith, G. D., and Palmer, R. A. (2002) Fast Time-Resolved Mid-Infrared Spectroscopy Using an Interferometer, *Handbook of vibrational spectroscopy*.

10. Barth, A. (2007) Infrared spectroscopy of proteins, *Biochimica et Biophysica Acta (BBA)-Bioenergetics 1767*, 1073-1101.

11. López-Lorente, Á. I., and Mizaikoff, B. (2016) Mid-infrared spectroscopy for protein analysis: potential and challenges, *Analytical and bioanalytical chemistry 408*, 2875-2889.

12. Tamm, L. K., and Tatulian, S. A. (1997) Infrared spectroscopy of proteins and peptides in lipid bilayers, *Quarterly reviews of biophysics 30*, 365-429.

13. Kong, J., and Yu, S. (2007) Fourier transform infrared spectroscopic analysis of protein secondary structures, *Acta biochimica et biophysica Sinica 39*, 549-559.

14. Byler, D. M., and Susi, H. (1986) Examination of the secondary structure of proteins by deconvolved FTIR spectra, *Biopolymers 25*, 469-487.

15. Surewicz, W. K., Mantsch, H. H., and Chapman, D. (1993) Determination of protein secondary structure by Fourier transform infrared spectroscopy: a critical assessment, *Biochemistry 32*, 389-394.

16. Goormaghtigh, E., Cabiaux, V., and Ruysschaert, J.-M. (1994) Determination of soluble and membrane protein structure by Fourier transform infrared spectroscopy, In *Physicochemical methods in the study of biomembranes*, pp 405-450, Springer.
17. Tatulian, S. A. (2013) Structural characterization of membrane proteins and peptides by FTIR and ATR-FTIR spectroscopy, *Lipid-Protein Interactions: Methods and Protocols*, 177-218.

18. Garcia-Vidal, F. J., Martin-Moreno, L., Ebbesen, T., and Kuipers, L. (2010) Light passing through subwavelength apertures, *Reviews of Modern Physics 82*, 729.
19. Chalmers, J. M., and Griffiths, P. R. (2002) *Handbook of Vibrational Spectroscopy*, Wiley.

20. Siebert, F., and Hildebrandt, P. (2008) Experimental Techniques, In *Vibrational Spectroscopy in Life Science*, pp 99-153, Wiley-VCH Verlag GmbH & Co. KGaA.

21. Goormaghtigh, E., Raussens, V., and Ruysschaert, J.-M. (1999) Attenuated total reflection infrared spectroscopy of proteins and lipids in biological membranes, *Biochimica et Biophysica Acta (BBA)-Reviews on Biomembranes 1422*, 105-185.

22. Baenziger, J. E., Miller, K. W., and Rothschild, K. J. (1993) Fourier transform infrared difference spectroscopy of the nicotinic acetylcholine receptor: evidence for specific protein structural changes upon desensitization, *Biochemistry 32*, 5448-5454.

23. Iwaki, M., Andrianambinintsoa, S., Rich, P., and Breton, J. (2002) Attenuated total reflection Fourier transform infrared spectroscopy of redox transitions in photosynthetic reaction centers: comparison of perfusion-and light-induced difference spectra, *Spectrochimica Acta Part A: Molecular and Biomolecular Spectroscopy 58*, 1523-1533.

24. Rostron, P., Gaber, S., and Gaber, D. Raman Spectroscopy, Review, *laser 21*, 24.

25. Crawford, A., Silva, E., York, K., and Li, C. Raman spectroscopy: a comprehensive review, *Department of Textile Engineering, Chemistry and Science, North Carolina State University*.
26. Schlücker, S. (2014) Surface-Enhanced raman spectroscopy: Concepts and chemical applications, *Angewandte Chemie International Edition 53*, 4756-4795.

27. Osawa, M. (2001) Surface-enhanced infrared absorption, In *Near-Field Optics and Surface Plasmon Polaritons*, pp 163-187, Springer.

28. Wu, D.-Y., Li, J.-F., Ren, B., and Tian, Z.-Q. (2008) Electrochemical surface-enhanced Raman spectroscopy of nanostructures, *Chemical Society Reviews 37*, 1025-1041.

29. Moss, D., Nabedryk, E., Breton, J., and Mantele, W. (1990) Redox-linked conformational changes in proteins detected by a combination of infrared spectroscopy and protein electrochemistry, *European Journal of Biochemistry 187*, 565-572.

30. Fukuda, T., Fumihito, A., and Nakajima, M. (2013) *Micro-Nanorobotic Manipulation Systems and Their Applications*, Springer Berlin Heidelberg.

31. Urbani, A., Gemeinhardt, S., Warne, A., and Saraste, M. (2001) Properties of the detergent solubilised cytochrome c oxidase (cytochrome cbb 3) purified from Pseudomonas stutzeri, *FEBS letters 508*, 29-35.

32. Xie, H., Buschmann, S., Langer, J. D., Ludwig, B., and Michel, H. (2014) Biochemical and biophysical characterization of the two isoforms of cbb3-type cytochrome c oxidase from Pseudomonas stutzeri, *Journal of bacteriology 196*, 472-482.

33. Meyer, T., Melin, F., Richter, O.-M., Ludwig, B., Kannt, A., Müller, H., Michel, H., and Hellwig, P. (2015) Electrochemistry suggests proton access from the exit site to the binuclear center in Paracoccus denitrificans cytochrome c oxidase pathway variants, *FEBS letters 589*, 565-568.

34. Smirnova, I., Kasho, V., Choe, J.-Y., Altenbach, C., Hubbell, W. L., and Kaback, H. R. (2007) Sugar binding induces an outward facing conformation of LacY, *Proceedings of the National Academy of Sciences 104*, 16504-16509.

35. Viitanen, P., Newman, M. J., Foster, D. L., Wilson, T. H., and Kaback, H. R. (1986) [32] Purification, reconstitution, and characterization of the lac permease of Escherichia coli, *Methods in enzymology 125*, 429-452.

36. Friedrich, T., Hofhaus, G., Ise, W., Nehls, U., Schmitz, B., and Weiss, H. (1989) A small isoform of NADH: ubiquinone oxidoreductase (complex I) without mitochondrially encoded subunits is made in chloramphenicol-treated Neurospora crassa, *The FEBS Journal 180*, 173-180.

37. Cohen, S. R., and Plane, R. A. (1957) The Association of Ferrocyanide Ions with Various Cations, *The Journal of Physical Chemistry 61*, 1096-1100.

38. Gill, S. C., and Von Hippel, P. H. (1989) Calculation of protein extinction coefficients from amino acid sequence data, *Analytical biochemistry 182*, 319-326.

39. Gornall, A. G., Bardawill, C. J., and David, M. M. (1949) Determination of serum proteins by means of the biuret reaction, *Journal of biological chemistry 177*, 751-766.

40. Schägger, H., and Von Jagow, G. (1987) Tricine-sodium dodecyl sulfate-polyacrylamide gel electrophoresis for the separation of proteins in the range from 1 to 100 kDa, *Analytical biochemistry 166*, 368-379.

41. Haiss, W., Thanh, N. T., Aveyard, J., and Fernig, D. G. (2007) Determination of size and concentration of gold nanoparticles from UV− Vis spectra, *Analytical chemistry 79*, 4215-4221.

42. Kriegel, S. b., Uchida, T., Osawa, M., Friedrich, T., and Hellwig, P. (2014) Biomimetic environment to study E. coli complex I through surface-enhanced IR absorption spectroscopy, *Biochemistry 53*, 6340-6347.

43. Ataka, K., and Heberle, J. (2006) Use of surface enhanced infrared absorption spectroscopy (SEIRA) to probe the functionality of a protein monolayer, *Biopolymers 82*, 415-419.

44. Collinson, M., Bowden, E. F., and Tarlov, M. J. (1992) Voltammetry of covalently immobilized cytochrome c on self-assembled monolayer electrodes, *Langmuir 8*, 1247-1250.
45. Zhang, L., Jiang, X., Wang, E., and Dong, S. (2005) Attachment of gold nanoparticles to glassy carbon electrode and its application for the direct electrochemistry and electrocatalytic behavior of hemoglobin, *Biosensors and Bioelectronics 21*, 337-345.

46. Nassar, A.-E. F., Willis, W. S., and Rusling, J. F. (1995) Electron transfer from electrodes to myoglobin: facilitated in surfactant films and blocked by adsorbed biomacromolecules, *Analytical chemistry 67*, 2386-2392.

47. Melin, F., Xie, H., Meyer, T., Ahn, Y. O., Gennis, R. B., Michel, H., and Hellwig, P. (2016) The unusual redox properties of C-type oxidases, *Biochimica et Biophysica Acta (BBA)-Bioenergetics 1857*, 1892-1899.

III. COMBINED PERFUSION AND SEIRAS APPROACH TO DETERMINE THE PK_A OF AN ACIDIC RESIDUE IN LACTOSE PERMEASE

List of figures in chapter 3

List of tables in chapter 3

Combined perfusion-SEIRAS approach

In this section a combined perfusion-SEIRAS approach to study membrane transport protein Lactose Permease (LacY) and its mutants is described.

1. Deposition and modification of the gold surface

Electroless deposition of the gold film on the surface of Si ATR crystal was performed according to the oxidoreduction equation shown below and the process is described in details in the section 3.3.1:

$$3\ Si\ (s) + 18\ F^-\ (aq) + 4\ AuCl_4^-\ (aq) \rightarrow 3\ SiF_6^{2-}\ (aq) + 4\ Au\ (s) + 16\ Cl^-\ (aq)$$

Modification of the deposited gold surface with Ni-NTA SAM was established previously[1, 2] and described in the section 3.3.2 in Materials and methods. Here, each step of the formation of Ni-NTA SAM was followed by FTIR spectroscopy.
First, the gold surface was covered with 10 mM 3,3'-dithiodipropionic acid di(N-hydroxysuccinimide ester) (DTSP) in dry DMSO and the monolayer was allowed to self-assemble during 1 h (see reaction in Figure 1A). Corresponding IR spectrum is shown in Figure 2A.

After the addition of DTSP, three bands appear at 1811, 1782, and 1737 cm^{-1}, which increase in intensity over time. The frequency of these bands corresponds to the C=O stretching modes of the succinimidyl ester of TSP. On the basis of DFT calculations the bands at 1737 and 1782 cm^{-1} are assigned to the asymmetric (ν_{as}) and symmetric (ν_s) stretching vibrations, respectively, of two C=O groups of the succinimidyl ring (see Figure 1A).[3] The band at 1811 cm^{-1} is attributed to the ν(C=O) of the ester group of TSP.

The surface-bound succinimidylester moiety of TSP was used to react with the primary amine of ANTA (see Figure 1B). This reaction yields the NTA surface which is used afterwards to finally ligate a Ni^{2+} ion.

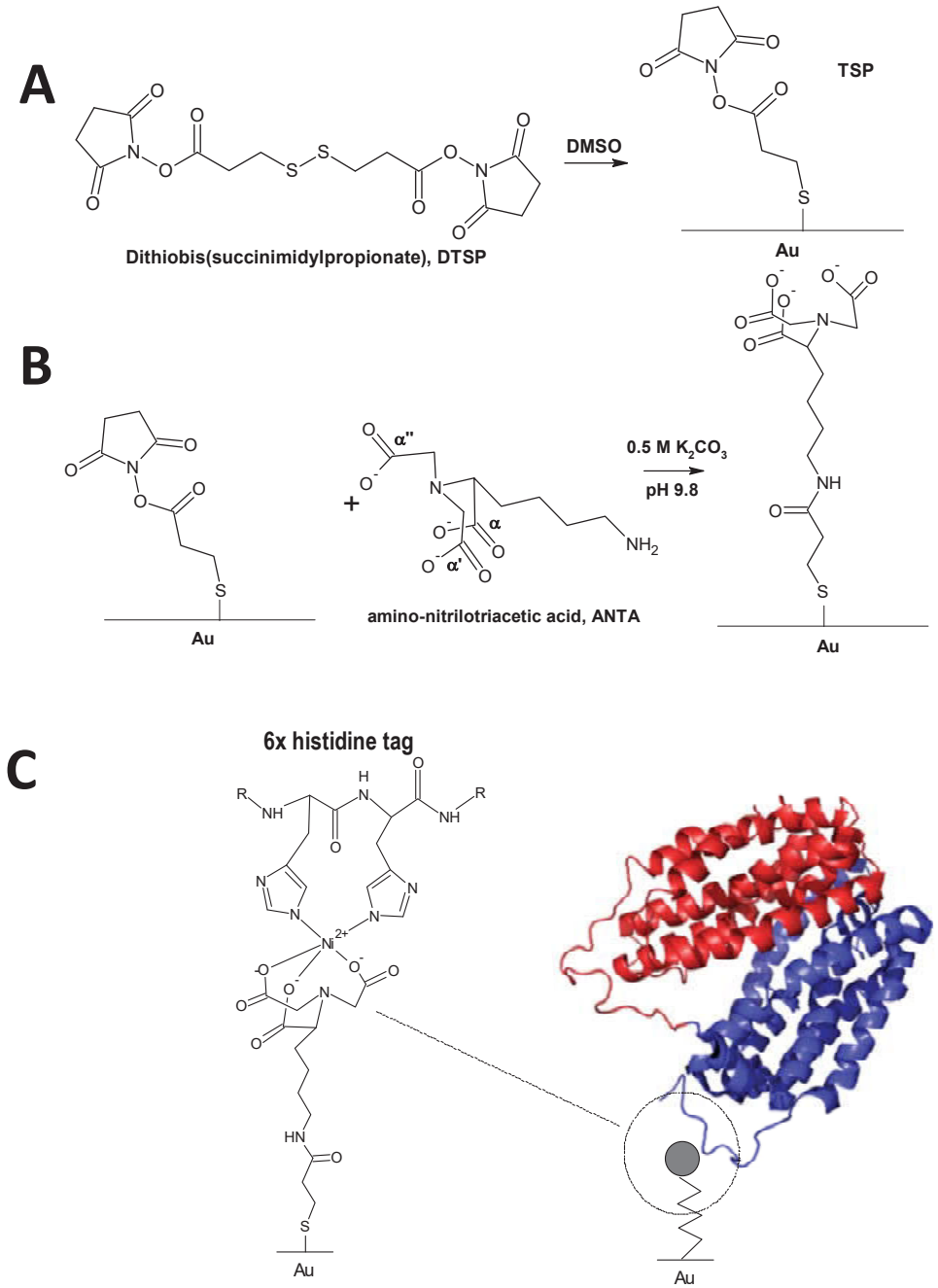

Figure 1: Illustration of the surface modification process. (A) Self-assembly of the TSP monolayer on the bare Au surface by spontaneous splitting of the disulfide bond of DTSP. (B) Cross-linking of ANTA with the TSP monolayer. (C) Immobilization of the protein onto the Ni-NTA SAM *via* His-tag

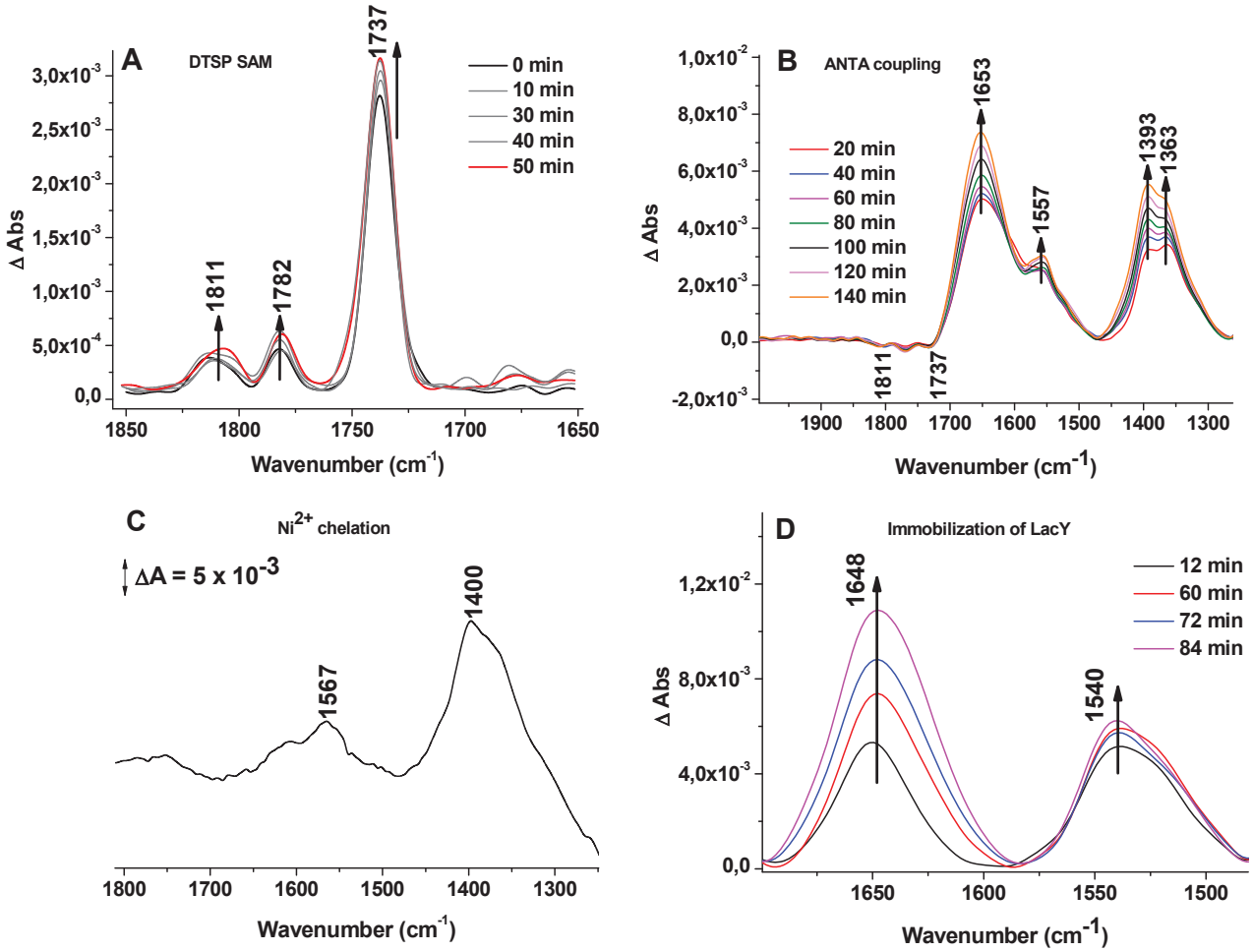

Figure 2: Creation of the Ni-NTA SAM followed by FTIR difference spectroscopy. A. Temporal evolution of DTSP SAM adsorption on Au layer. Reference spectrum: bare gold layer covered with DMSO; B. Coupling process of ANTA with the surface-bound TSP monolayer. Reference spectrum: DTSP SAM in K_2CO_3 0.5 M, pH 9.8; C. Chelation of Ni^{2+}. Reference spectrum: TSP-NTA SAM covered with water; D. Adsorption of LacY on the Ni-NTA SAM. Reference spectrum: Ni-NTA modified gold layer with water

The negative bands in the difference spectra (Figure 2B) are assigned to the vibrations of the reactant at the surface (TSP), while positive bands represent the product species (NTA). Two negative bands are observed at 1811 and 1737 cm^{-1}. Since these bands were assigned to the succinimidylester vibrations of TSP, this provides the evidence for the reaction of the succinimidylester.

Two intense bands appear at 1653 and 1557 cm^{-1} concomitant with the appearance of the negative bands of DTSP. These bands are assigned to the amide I and the amide II modes of the carboxamide (-CONH-) linkage, respectively.[4] The presence of these bands provides the evidence for the presence of the cross-link between ANTA and TSP.

The bands at around 1400 cm^{-1} region are attributed to the corresponding symmetric stretching modes of the three carboxylate groups of NTA. Here, two peaks are resolved at 1393 and 1363 cm^{-1}. The detailed assignment of the symmetric carboxylate vibrations is hampered by the strong coupling to the C-H in-plane bending and the C-N stretching modes of the molecule.[3]

Figure 2C represents the difference spectrum of surface-bound NTA before and after the addition of 50 mM $Ni(ClO_4)_2$. Complexation of Ni^{2+} leads to the appearance two bands at 1567 and 1400 cm^{-1} in the IR spectrum. These bands are assigned to the asymmetric and the symmetric stretching mode of the terminal carboxylate groups of NTA that get deprotonated during complexation of the Ni^{2+} ion.[3]

Formation of Ni-NTA SAM took around 5h.

Afterwards, LacY was immobilized on this surface through the affinity of the genetically introduced His-tag for the Ni-NTA layer (Figure 1C). Adsorption of LacY was monitored by SEIRAS. As shown in Figure 2D, bands appear at 1648 and 1540 cm^{-1}. These two bands are readily assigned to the amide I and the amide II modes of the protein backbone vibrations of LacY, respectively.

The increase of the band intensities in the course of incubation reflects the accumulation of LacY onto the Ni-NTA surface. During the immobilization of LacY the shape, position and intensity ratio of amide I and amide II bands varied. This might be explained by the different orientation of the protein with respect to the surface. LacY is quite tightly adsorbed on the Ni-NTA modified surface, as the amide signals persisted after perfusion experiments.
Polarized FTIR spectroscopy was used to give insight into the orientation of LacY on the Ni-NTA modified surface (see Appendix).
Thus, after immobilization of the protein on the surface of Si ATR crystal perfusion experiments were carried out. The results are described below.

2. Perfusion-induced IR Spectroscopy of Lactose Permease

In this study, Glu325 is identified *in situ*, and the pK_a of this residue is determined by monitoring pH-induced changes in purified LacY by infrared spectroscopy.

2.1 pH- and substrate-dependent conformational changes in a monolayer of immobilized LacY

Reaction-induced IR spectroscopy is an established technique for studying protonation changes in proteins. It has been used successfully to identify several important residues in the proton path of membrane proteins[5, 6], as well as water molecules.[7] For example, Zscherp *et al*.[8] determined the pK_a value of Asp96 in bacteriorhodopsin, and the protonation state of the central glutamic acid residue in cytochrome *c* oxidase was also identified by means of IR.[9] Here we investigated the pH- and substrate-dependent conformational changes in a monolayer of immobilized Lactose Permease on the modified gold layer by surface enhanced IR spectroscopy in an ATR perfusion cell. Experimental conditions are described in detail in the sections 3.3, 3.4 and 3.5 in Materials and methods.

Figure 3 represents the reversible perfusion-induced IR difference spectra obtained from pH 9 – 10.5 and back with LacY WT in the presence of NPG (*p*-nitrophenyl-α-D-galactopyranoside). A broad peak which is centered at 1695 cm^{-1} and 1675 cm^{-1} is observed in the amide I region, that ranges from 1700 cm^{-1} to 1600 cm^{-1} and comprises conformational changes in the C=O groups of the protein backbone. Signals at ∼1650 – 1660 cm^{-1} are expected for a typical α-helical structure[10] (see, for example, absorption spectra in Figure 8). Nevertheless, conformational changes in helices can markedly shift these vibrational modes because both dipole-dipole coupling and the hydrogen bonding environment may be perturbed.[10] Thus, changes in the amide I spectral range are informative with respect to conformational rearrangements.

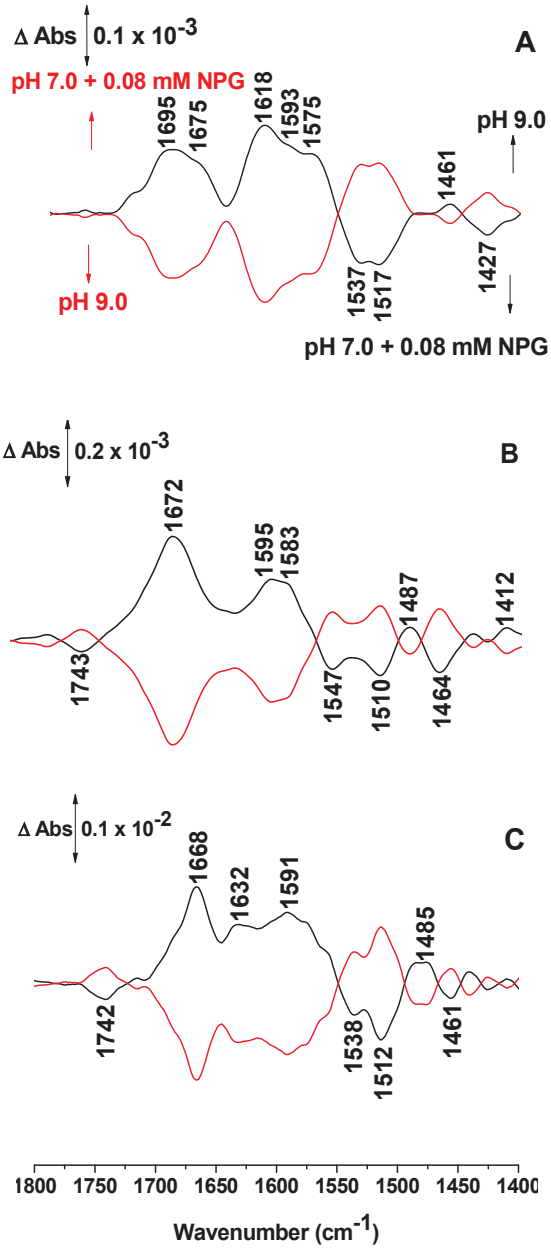

Figure 3: Perfusion-induced FTIR difference spectra of LacY WT obtained from the sample equilibrated at pH 7 in the presence of NPG and subtracted from the sample equilibrated at pH 9 (A), 10 (B), and 10.5 (C), respectively (black line) and reverse (red line)

Comparing the spectra obtained stepwise at pHs up to 10.5 (Figure 3A–C), it is possible to notice that the broad amide I absorbance becomes sharper with increasing pH, and at pH 10.5 it is centered

at 1668 cm^{-1} with a shoulder at 1632 cm^{-1}, pointing toward a conformational change related to the increase in pH.

The amide II spectral range (between 1590 cm^{-1} and 1450 cm^{-1}) comprises coupled CN/NH vibrational modes of the protein backbone,[10] together with the contributions from individual amino acids reorganizing or changing their protonation states with the alkaline pH shift. Marked shifts and increases in intensity are also observed when increasing the pH.

An interesting change when increasing the pH is observed at 1742 cm^{-1}. Signals in this spectral region are characteristic of protonated Asp or Glu residues in a hydrophobic environment as was shown in the IR spectra of model compounds and in the IR difference spectra that were obtained with a number of membrane proteins.[11] A negative signal which is observed here reflects deprotonation of carboxylic group. As can be seen, the signal is absent at pH 9 (Figure 4A), starts to appear at pH 10 (Figure 4B), and increases in intensity at pH 10.5 (Figure 4C), clearly pointing toward the deprotonation of an acidic side chain(s). Protonation and deprotonation are absolutely reversible and correlate with reorganization of the protein backbone. Although signals corresponding deprotonated acidic side chains are expected to be at around 1575 cm^{-1} and 1400 cm^{-1},[12, 13] these signals overlap with the amide II band, and they are difficult to assign unambiguously.

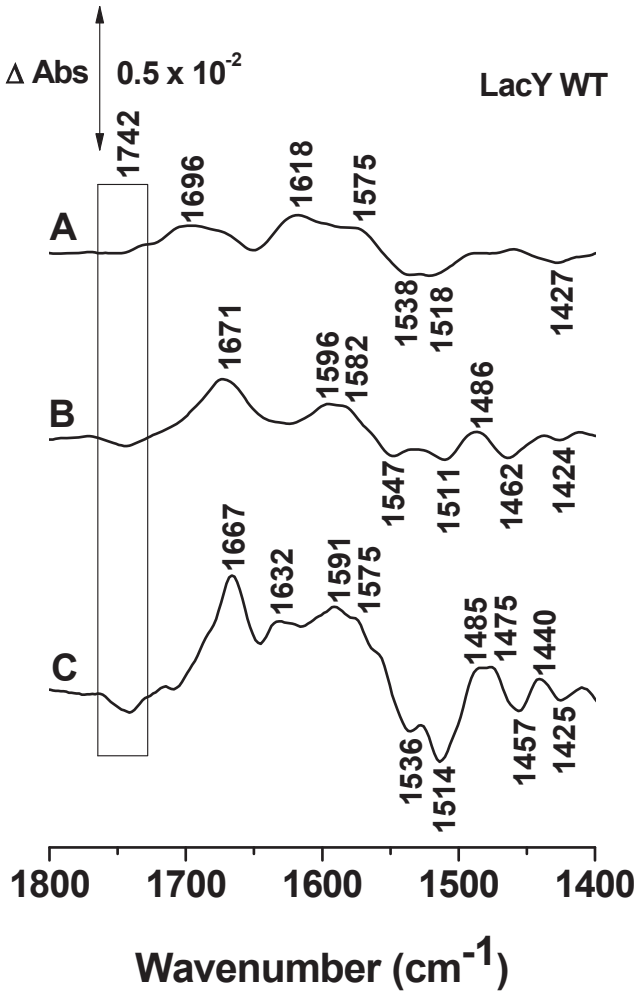

Figure 4: Perfusion-induced FTIR difference spectra of LacY wild type equilibrated in the presence of 0.08 mM NPG at pH 7 and subtracted from the sample equilibrated at pH 9.0 (A), 10.0 (B), and 10.5 (C), respectively

2.1.1 An alkali-stable double-Trp mutant LacY G46W/G262W

Galactoside binding by LacY WT becomes unstable at highly alkaline pH (>11).[14-16] Since the studies presented here require exposure of the protein to high pH, the alkali stability of LacY WT was compared with that of the double-Trp mutant G46W/G262W ($LacY_{ww}$), which is more stable than LacY WT, but exhibits the identical pK^{app} for sugar binding.[17] In this mutant Gly46 (helix II) and Gly262 (helix VIII) which connect the N- and C-terminal six-helix domains on the periplasmic

side of LacY are replaced with bulky Trp residues (Figure 5). $LacY_{ww}$ exists in an outward-open conformation (open to periplasm).

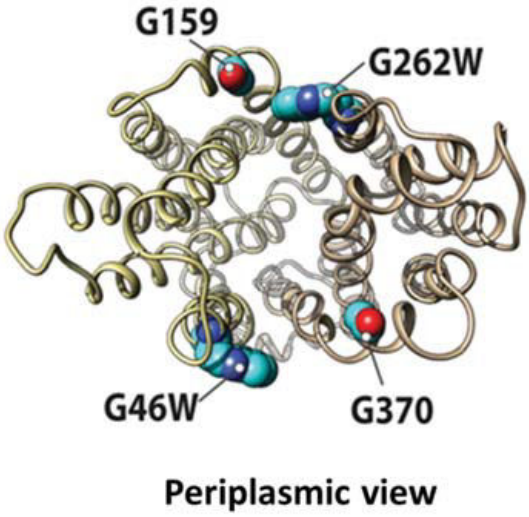

Figure 5: Trp replacements in two pairs of Gly-Gly residues that connect the N- and C-terminal six-helix domains on the periplasmic side of LacY[18]

Stability of LacY WT and 46W/262W mutant at pH 10.5 was studied by Irina Smirnova from the research group of Pr. Dr. Ronald Kaback (Los-Angeles, USA). Sugar binding was measured as Trp151-NPG Förster resonance energy transfer[19] after pre-incubation of reconstituted proteoliposomes (PLs) with 14 mM protein at a lipid-to-protein ratio of 5 (wt/wt) in 50 mM CAPS pH 10.5 for given time at room temperature (see Figure 6A-D).

Trp fluorescence intensity (excitation at 295 nm) increases following the displacement of bound *p*-nitrophenyl-α-D-galactopyranoside (NPG) (0.1 mM) by excess of β-D-galactopyranosyl-1-thio-β-D-galactopyranoside (TDG) (6 mM) measured at pH 7.5 in 50 mM NaPi with 0.4 mM LacY. As can be seen in Figure 6A the Trp151 fluorescence in LacY WT is restored by 23% following NPG displacement after incubation at pH 10.5 during 1 min. At the same conditions Trp151 fluorescence in the mutant is restored by 37% (Figure 6C). Moreover, when the time of incubation of $LacY_{ww}$ at pH 10.5 was increased up to 4.5h the Trp151 fluorescence is restored by 35% (Figure 6D) while in the case of LacY WT this number is only 10% (Figure 6B) despite less time of incubation (4h).

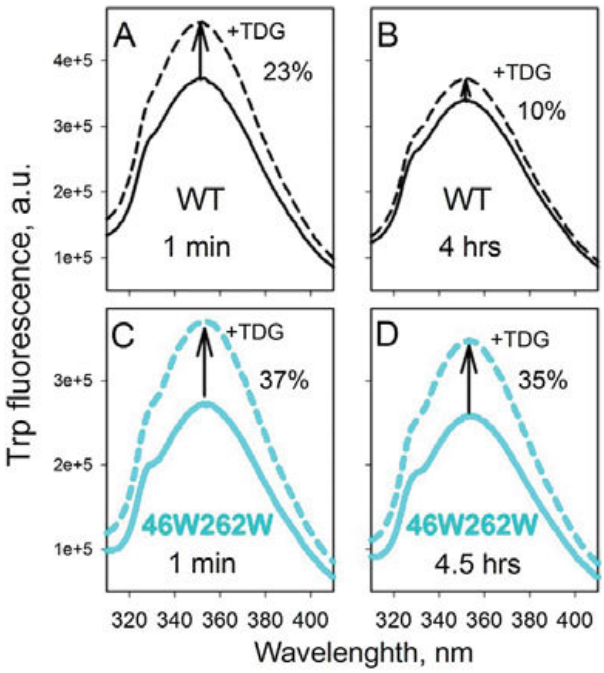

Figure 6: Trp151-NPG Förster resonance energy transfer after preincubation of reconstituted PLs at pH 10.5 for given time at room temperature. Spectra of LacY WT are illustrated in black (A and B) and of $LacY_{ww}$ – in light blue (C and D)[20]

The time course of LacY WT and the mutant inactivation at pH 10.5 is illustrated in Figure 7.

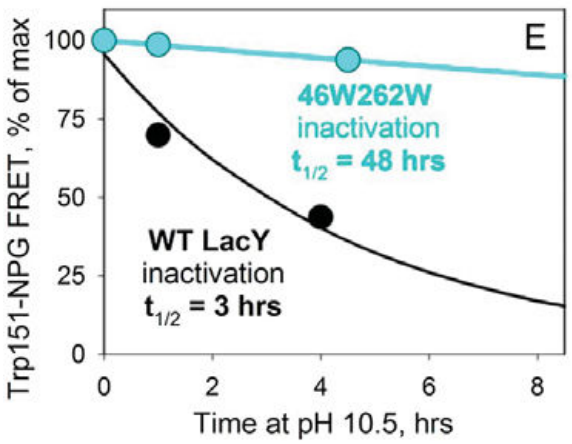

Figure 7: The time course of LacY inactivation at pH 10.5[20]

Thus, LacY WT exhibits a half-life ($t_{1/2}$) with respect to NPG binding of 3 h at pH 10.5, whereas the $t_{1/2}$ for $LacY_{ww}$ is 48 h (Figure 7). These results clearly indicate that $LacY_{ww}$ has higher stability at alkaline pH values compared to LacY WT.

Stability of some mutants of LacY was studied by means of FTIR as well. The results are described in the next sections.

2.2 Determination of the secondary structure of LacY G46W/G262W, LacY G46W/G262W/E325A and LacY WT

Since perfusion experiments had to be carried out at different pH values it was important to check the changes in secondary structure upon variation of pH and thus verify the stability of the protein structure. Moreover, an interesting point was to monitor if the amino acid mutations will lead to the changes in the secondary structure.

Thereby, absorption spectra of the initial purified samples of LacY G46W/G262W and LacY G46W/G262W/E325A as well as the spectra of the same samples equilibrated at pH 7.5 and 11.5 were recorded. Deconvolutions of amide I bands were performed to determine the secondary structure of the proteins. The results are presented below (Figure 8) and compared to the secondary structure of wild-type protein (Figure 9).

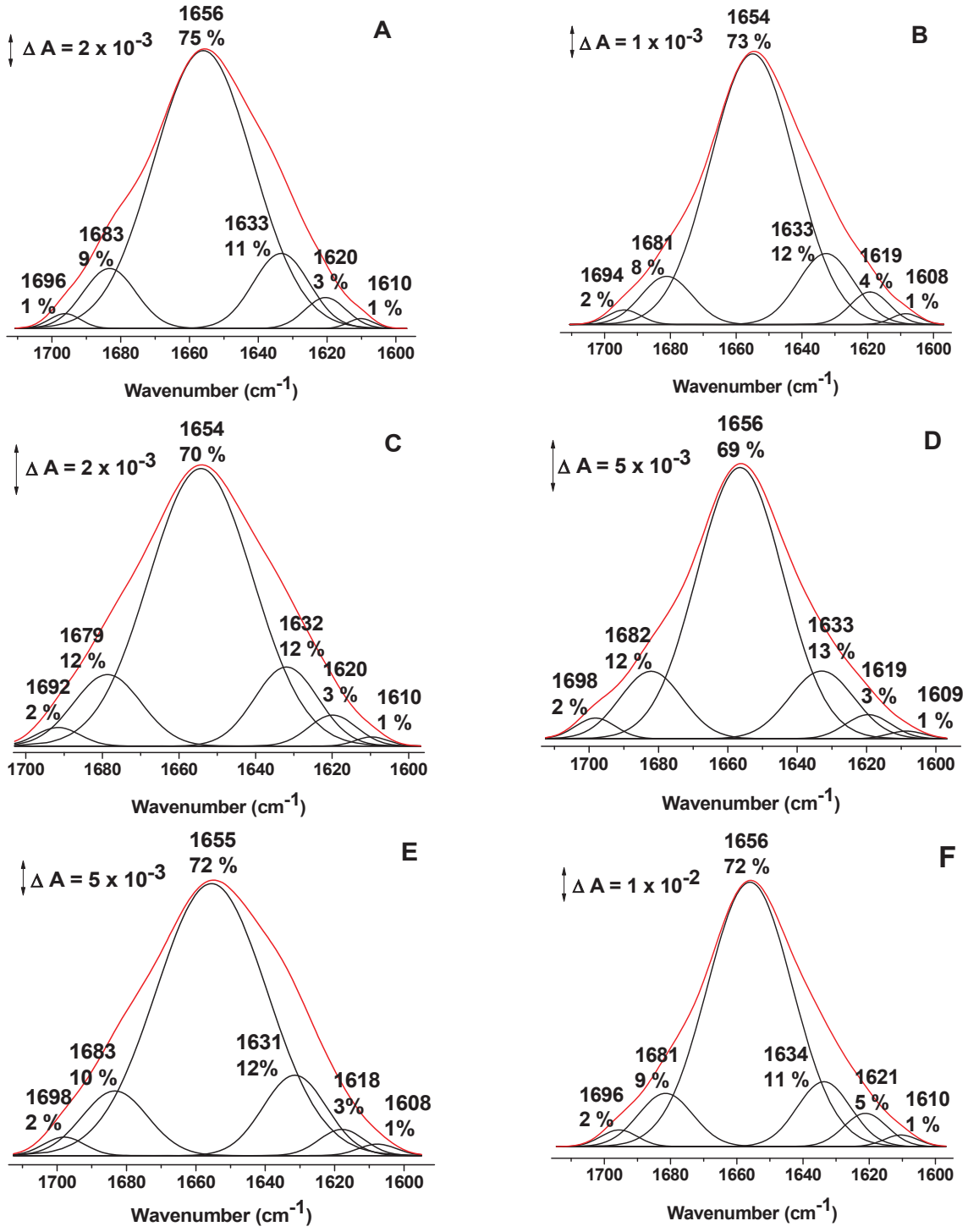

Figure 8: Deconvolution of amide I bands of initial purified samples of LacY G46W/G262W and LacY G46W/G262W/E325A prepared in 50 mM NaPi/0.02% DDM (pH 7.5) (A and B, respectively), of the same samples equilibrated at pH 11.5 (C and D, respectively) and pH 7.5 (E and F, respectively)

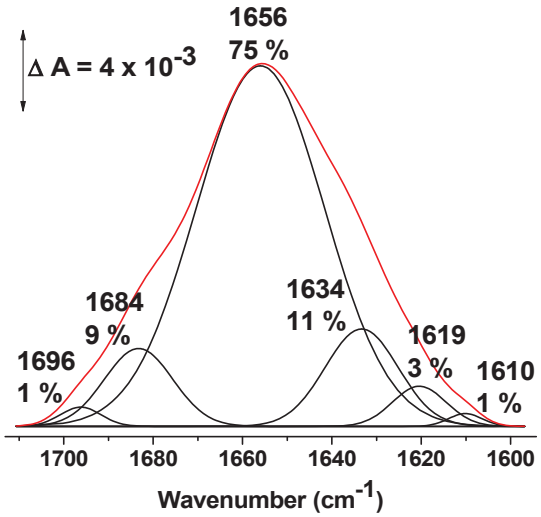

Figure 9: Deconvolution of amide I band of initial purified sample of LacY WT prepared in 50 mM NaPi/0.02% DDM

The amide I band centered at 1654 – 1656 cm^{-1} corresponds to the sum of contributions of several components. Six bands at around 1695, 1680, 1655, 1633, 1620 and 1610 cm^{-1} were used to deconvolute the amide I band. These components are assigned to the different elements of secondary structure.

Table 1 summarizes the assignment of different components of amide I bands of LacY WT, LacY G46W/G262W and LacY G46W/G262W/E325A at different pH values and represents the percentage of different elements of secondary structure.

Table 1: Secondary structure of initial purified samples of LacY WT, LacY G46W/G262W and LacY G46W/G262W/E325A prepared in 50 mM NaPi/0.02% DDM (pH 7.5), of the same samples of double-Trp mutants equilibrated at pH 11.5 and pH 7.5

Secondary structure	Position of amide I and estimated percentage						
	LacY WT initial	$LacY_{ww}$ initial	$LacY_{ww}$ E325A initial	$LacY_{ww}$ pH 11.5	$LacY_{ww}$ E325A pH 11.5	$LacY_{ww}$ pH 7.5	$LacY_{ww}$ E325A pH 7.5
α-helices + disordered structures	1656 (75 %)	1656 (75 %)	1654 (73 %)	1654 (70 %)	1656 (69 %)	1655 (72 %)	1656 (72 %)
Parallel β-sheets	1634 (11%)	1633 (11 %)	1633 (12 %)	1632 (12 %)	1633 (13 %)	1631 (12 %)	1634 (11 %)
Parallel β-sheets	1619 (3 %)	1620 (3 %)	1619 (4 %)	1620 (3 %)	1619 (3 %)	1618 (3 %)	1621 (5 %)
Antiparallel β-sheets	1696 + 1610 (2 %)	1696 + 1610 (2 %)	1694 + 1608 (3 %)	1692 + 1610 (3 %)	1698 + 1609 (3 %)	1698 + 1608 (3 %)	1696 + 1610 (3 %)
β-turns	1684 (9 %)	1683 (9 %)	1681 (8 %)	1679 (12 %)	1682 (12 %)	1683 (10 %)	1681 (9 %)

The results show that at different pH values the major secondary structures of LacY WT and double-tryptophan mutants of LacY are α-helices. Our results coincide well with the crystal structure of LacY solved with the resolution 3.6 Å (PDB 2V8N) showing that the protein has predominantly helical structure. The percentage of α-helices and non-organized structures at pH 11.5 is little lower when comparing to the samples equilibrated at pH 7.5 (in the initial buffer 50 mM NaPi/0.02% DDM and in the perfusion buffer 25 mM KPi/100 mM KCl/0.01% DDM). The percentage of other elements of secondary structure is almost identical. Observed differences can be due to the errors of deconvolution (around ± 3.5%).

These results demonstrate high stability of double-tryptophan mutants at alkaline pH and clearly show that mutation of Glu325 with Ala as well as double-Trp mutation do not change the secondary structure of the proteins. Thus, perfusion experiments at alkaline pH values can be carried out without denaturation of the samples.

2.3 Perfusion-induced conformational changes in a monolayer of immobilized $LacY_{ww}$

Since $LacY_{ww}$ was shown to be stable at alkaline pH values perfusion measurements were performed up to pH 11.5.

Difference spectra obtained from this mutant clearly show the same signal as LacY WT at 1742 cm^{-1} (Figure 10). As was mentioned before, signals at this position are characteristic of protonated Asp or Glu residues in a hydrophobic environment.[11] A negative signal observed in the Figure 10 at 1742 cm^{-1} reflects deprotonation. As shown, the signal is absent at pH 9 (Figure 10A), begins to appear at pH 10 (Figure 10B), and increases in intensity at pH 10.5 (Figure 10C) reaching the plateau at pH 10.9 and 11.5 (Figure 10D-E, respectively), clearly indicating deprotonation of an acidic side chain(s). Protonation and deprotonation are absolutely reversible and correlate with reorganization of the polypeptide backbone.

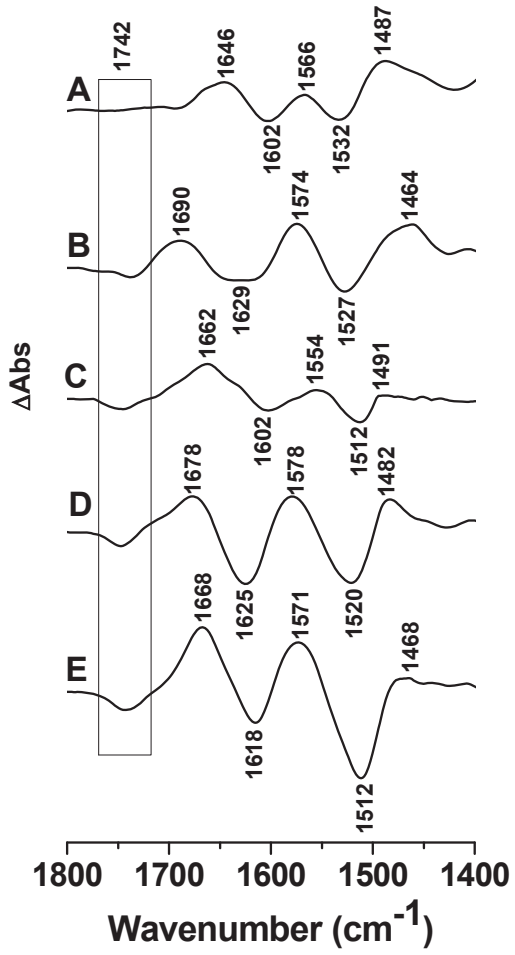

Figure 10: Perfusion-induced FTIR difference spectra of LacY G46W/G262W in the presence of 0.08 mM NPG in both perfusion solutions. The sample equilibrated at pH 7.0 was subtracted from the sample equilibrated at 9.0 (A), 10.0 (B), 10.5 (C), 10.9 (D) and 11.5 (E), respectively

2.4 Identification of Glu325

The same kind of experiments was performed with $LacY_{ww}$ and with $LacY_{ww}$ carrying the E325A mutation in the absence of NPG. Both mutants are more stable at high pH comparing to LacY WT. The difference signal at 1742 cm^{-1} becomes markedly stronger in $LacY_{ww}$ when pH increases from 10.5 to 10.9 – 11.5 (Figure 11A). Nevertheless, in the perfusion-induced IR difference spectra of the $LacY_{ww}$/E325A and the E325A mutants, the signal at 1742 cm^{-1} is totally absent (Figure 11B and C, respectively).

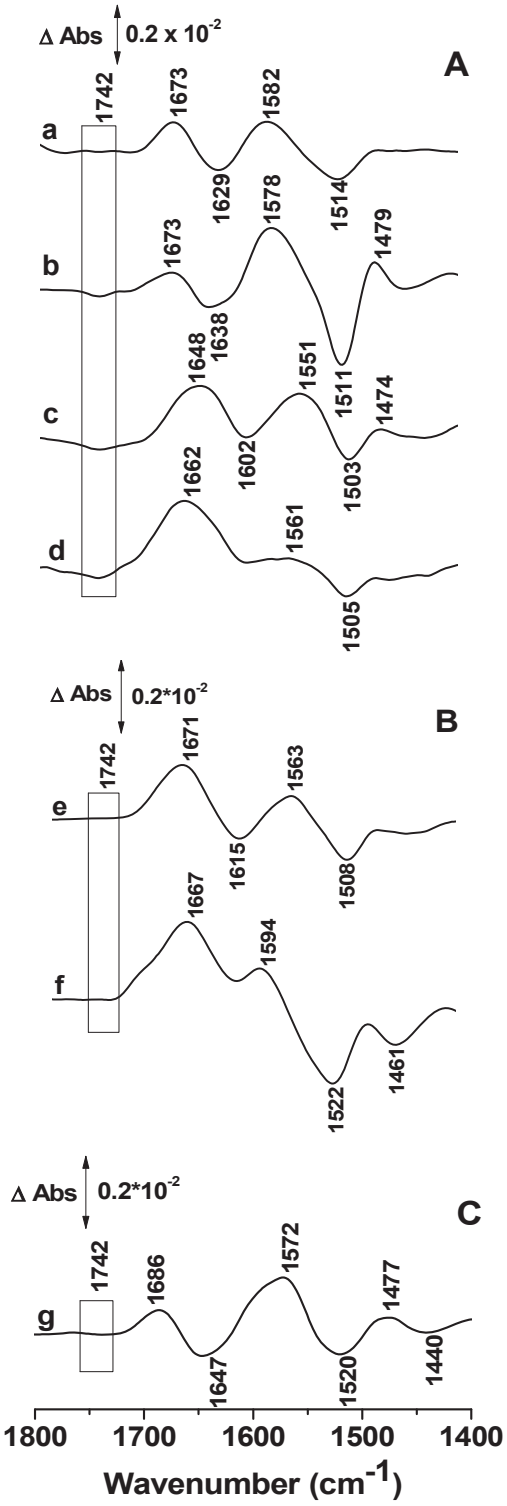

Figure 11: Perfusion-induced FTIR difference spectra of LacY G46W/G262W in the absence of 0.08 mM NPG obtained from samples equilibrated at pH 7 and subtracted from the samples equilibrated at pH 8.0 (A,a), 10.5 (A, b), 10.9 (A, c), and 11.5 (A, d), respectively. Difference spectra of the mutant LacY G46W/G262W/E325A for the step

from pH 7.0 to pH 11.5 (B, e) and 10.9 (B, f), and for the simple LacY E325A mutant for the step from pH 6.0 to pH 10.0 (C, g)

Glu325, which is clearly involved in the coupling between H^+ and galactoside translocation,[18] is localized within the membrane bilayer in helix X and surrounded by hydrophobic side chains as can be seen in Figure 12.

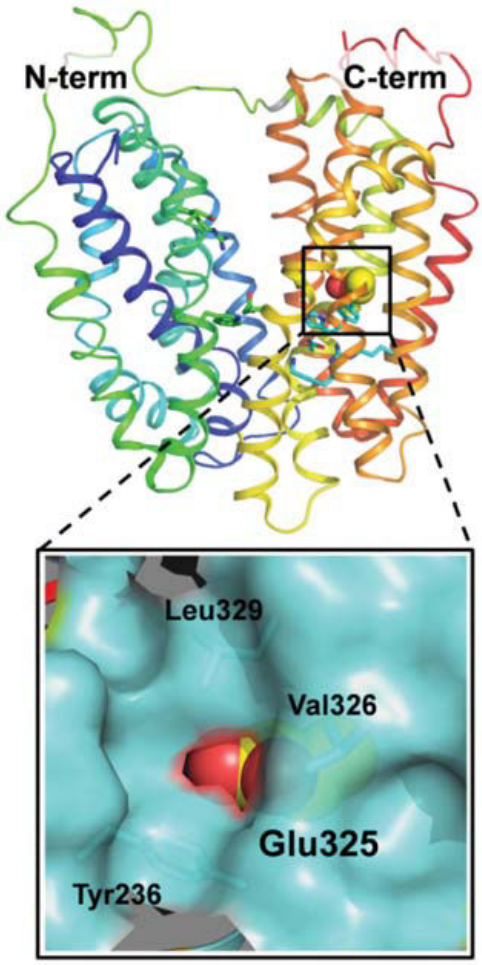

Figure 12: Position of Glu325 in the C-terminus of LacY WT (PDB code 2V8N). LacY is represented as a rainbow-colored backbone (from blue to red for helices 1–12) with hydrophilic cavity open to the cytoplasm. Side chain of Glu325 is localized in helix X and is shown in the figure as spheres. The area surrounding Glu325 is enlarged with hydrophobic environment which is displayed as a space-filled cartoon (cyan)[20]

Previous observations demonstrated that this side chain has a pK^{app} of around 10.5 based on the pH titrations of galactoside affinity.[14-16] During these titration experiments dissociation constants for sugar binding (K_d) were determined as the ratio of rate constants (k_{off}/k_{on}) measured by stopped flow (Figure 13). The current results unequivocally confirm that Glu325 is responsible for the band centered at 1742 cm^{-1}. The pK_a of Glu325 was determined by plotting the Δ Absorbance at 1742 cm^{-1} versus pH (Figure 13). From the observed fit (red), Glu325 has a pK_a of 10.5 ± 0.1, a value that agrees very well with the pK^{app}s obtained previously for either LacY WT (green)[14, 16] or mutant $LacY_{ww}$ (cyan).[15] Although the LacY E325A mutant binds galactoside with high affinity over the entire measured pH range, essentially no value for Δ Absorbance is observed (open circles).

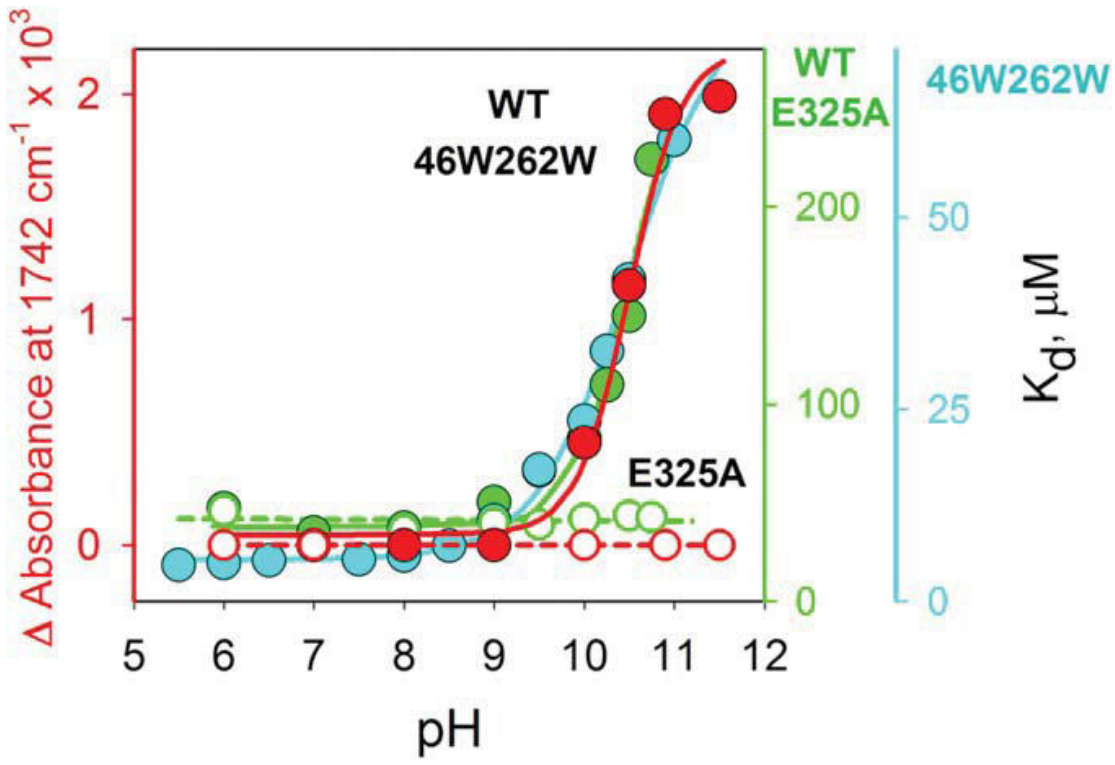

Figure 13: pH dependence of Δ Absorbance intensity change at 1742 cm^{-1} measured with $LacY_{ww}$ in the absence or presence of 0.08 mM NPG (filled red circles) or LacY E325A (open red circles), and K_d values for NPG binding to LacY WT (filled green circles), LacY E325A (open green circles), or $LacY_{ww}$ (filled cyan circles). K_d values were determined by stopped flow[14, 17]

2.5 Effect of NPG and discussion

The signal at 1742 cm^{-1} in the FTIR difference spectra exhibits no significant difference in the absence or presence of 0.08 mM NPG at pH 10.5, 10.9 or 11.5 with either LacY WT or the $LacY_{ww}$ mutant. Moreover, the pH titration is not affected by the absence or presence of the galactoside as can be seen in Figure 13.

Presented studies provide convincing evidence that Glu325 in LacY, which plays a central role in galactoside/H^+ symport, has a pK_a of 10.5, as was suggested previously by studies on the effect of pH on the galactopyranoside binding. Glu325 plays an essential role in the coupling mechanism in LacY, since its protonation or deprotonation determines whether or not galactoside binds effectively. Therefore, this demonstrates an important aspect of coupling, which initiates the transport mechanism. Importantly, other symporters with a carboxyl group that has the same behavior as Glu325 with respect to transport have also been described recently for FucP,[21] and XylE[22] and GlcPSe.[23]

Protonated form of Glu325 is stabilized probably due to the hydrophobic microenvironment within transmembrane helix X (Figure 12). Nevertheless, deprotonation is also important for the turnover, and with an apparent pK_a of 10.5, how does deprotonation occur? It is possible that the pK_a of Glu325 may decrease by becoming more accessible to water. In opposite, however, Arg302 may be important in this process.[24, 25] Similarly to the neutral replacements for Glu325, certain neutral replacements for Arg302 are also defective in the symport of lactose and H^+, but catalyze equilibrium exchange.[24] Possibly, the positively charged guanidinium group at position 302 facilitates deprotonation of Glu325 after dissociation of galactoside. Although Arg302 and Glu325 are relatively far from each other with the hydroxyl group of Tyr236 in between in the current structure, the double-mutant R302C/E325C demonstrates excimer fluorescence when labeled with pyrene maleimide[26] and the double-mutant R302H/E325H binds Mn(II) with micromolar affinity.[27] Thus, Arg302 and Glu325 might be in a closer proximity in another conformation of LacY.

Some examples of the residues with perturbed pK_as in important mechanistic positions were described for several membrane proteins, as reviewed by Harris and Turner for example.[28] The evidence was given that the pK_a is often modulated by a combination of several types of interactions

such as long-range and local electrostatic effects. An interesting example is residue D96 in bacteriorhodopsin. A high pK_a is also observed for cytochrome *c* oxidase, where residue E278 (*Paracoccus denitrificans* numbering), which is localized in the membrane part, was found to have a pK_a higher than 11.[29] Electrochemically induced FTIR difference spectra illustrated a signal at 1748 cm^{-1}, at a position very close to that observed in this study for E325 in LacY. A similar hydrogen-bonding environment is thus expected.

One important result observed in the current work is that the titration of Glu325 is not changed by binding of NPG. This is unexpected since protonation of Glu325 is related to the increased affinity for galactoside. In a straightforward thermodynamic model, the H^+ and sugar affinities should demonstrate reciprocity, (i.e., if H^+ binding increases sugar affinity by 100-fold, then sugar binding should also increase the affinity of the H^+ by 100-fold). Nevertheless, in addition to the obtained IR results, binding of sugar to LacY does not induce any change in ambient pH, as discussed previously.[15]

2.6 pH-dependent changes in LacY WT and LacY G46W/G262W observed in the FIR spectral region

The basic information about the protein dynamics that gives rise to major conformational changes within the protein can be obtained from the spectroscopic characterization of the collective low frequency modes. Thus, studies in FIR spectral region were carried out in order to gain insight into the pH-induced conformational changes of LacY WT and LacY G46W/G262W that were already observed in the MIR region (in the region of amide I and amide II on the difference spectra).

The pH stable $LacY_{ww}$ mutant as well as LacY WT were equilibrated at different pH values and FIR measurements were performed (Figure 14).

Amide IV (C=O in plane, C-C stretch), amide V (C-N torsion) and amide VI (C=O out of plane, C-N torsion) bands are observed at 700 – 500 cm^{-1}.[30] The amide VII band (N-H out of plane) appears at around 285 cm^{-1}. An intense peak at around 133 - 135 cm^{-1} can be attributed to the hydrogen bonding collective motions.[31]

The peak centered at around 133 - 135 cm^{-1} comprises the contributions from intra- and intermolecular hydrogen bonding within the protein or with water molecules. This peak represents an overall breathing mode of the protein and is therefore a marker of conformation of the protein. Figure 14 shows this relatively intense and broad signature for the samples of LacY WT and $LacY_{ww}$ equilibrated at different pHs. Interestingly, for $LacY_{ww}$ upon pH change from pH 7.5 to pH 10.9 (blue and grey lines on Figure 14 in the left, respectively) this signature shifts from 133 cm^{-1} to 122 cm^{-1}. In LacY WT this peak shifts from 135 cm^{-1} to 129 cm^{-1} when increasing pH from 7.5 to 10.5 (blue and violet lines on Figure 14 in the right, respectively). These observations indicate that conformational changes take place within the proteins and that the hydrogen bonding at alkaline pH becomes weaker.

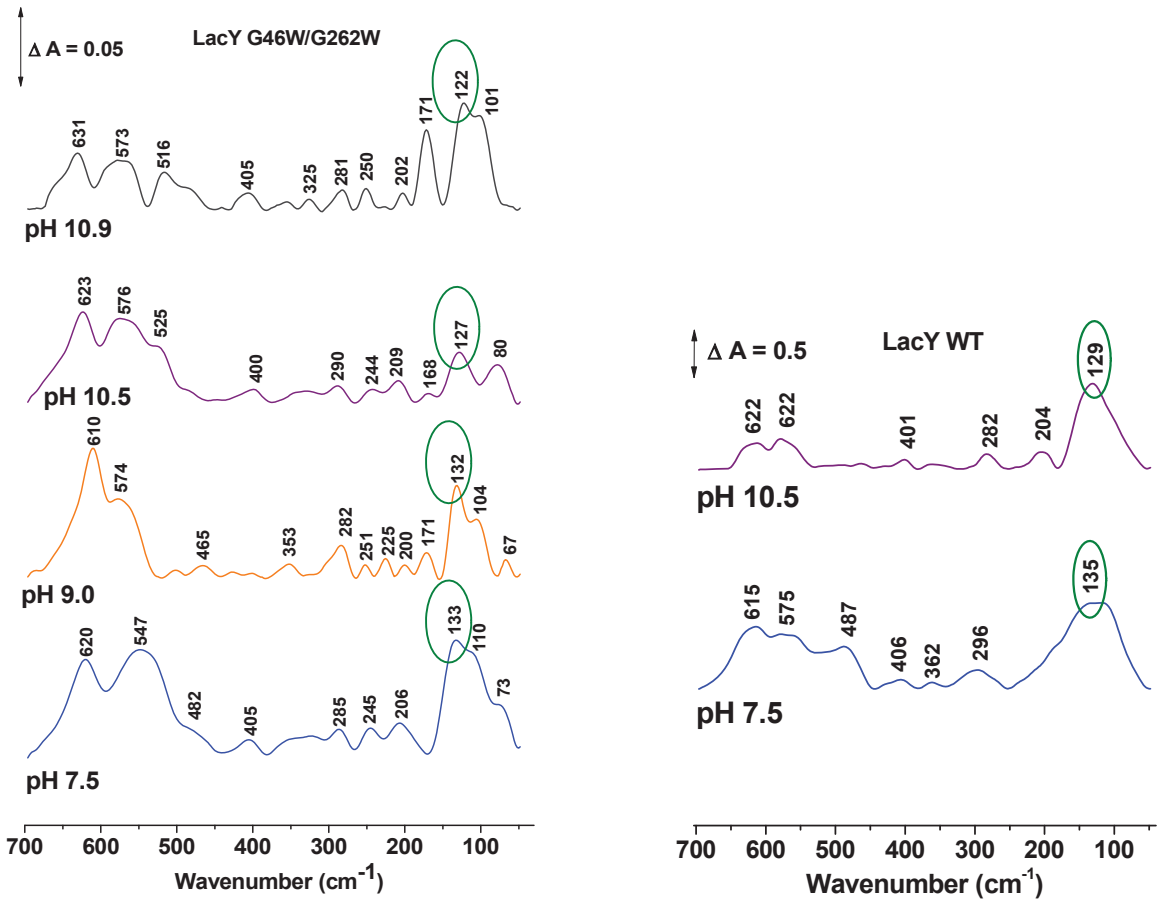

Figure 14: FIR ATR absorbance spectra of the films from $LacY_{ww}$ equilibrated at pH 7.5 (blue), 9.0 (orange), 10.5 (violet) and 10.9 (grey) in the left and from LacY WT equilibrated at pH 7.5 (blue) and 10.5 (violet) in the right

Contribution from β-sheets is observed at around 547 cm^{-1} while α-helical contribution can be seen at around 525 cm^{-1}. The spectral profiles of LacY WT and $LacY_{ww}$ in the region of amide IV, amide V and amide VI change upon variation of pH. These spectral changes indicate that the proteins undergo large pH-dependent conformational changes. In addition, narrowing of the peaks upon increasing of pH can be explained by the decrease of the conformational degrees of freedom of the proteins. Obtained results correlate with the major pH-induced conformational changes observed on the difference spectra in MID IR at the region of amide I and amide II bands.

2.7 Determination of pK_a value of Glu325 residue in the active site in mutants of Lactose Permease

Functional analysis of mutants at virtually every position has led to the following three observations.[32-34] (*a*) Only six side chains are irreplaceable with respect to active transport: Glu126 (helix IV) and Arg144 (helix V), which are crucial for substrate binding; Glu269 (helix VIII), which is likely involved in both substrate binding and H^+ translocation; and Arg302 (helix IX), His322 (helix X), and Glu325 (helix X), which play irreplaceable roles in H^+ translocation. (*b*) Residues such as Trp151 and Tyr236 are important, but not irreplaceable. (*c*) Substrate-induced changes in the reactivity of side chains with various chemical modification reagents, site-directed fluorescence, and spin labeling suggest widespread conformational changes during turnover.

In this study the mutants at positions of Glu325, Arg302 and His322 were examined. As reported previously[33] none of these mutants can catalyze active transport. It is possible that active transport is not possible due to the perturbation of the hydrogen bonging in the active center. Changes in hydrogen bonding can lead to the changes in the pK_a of the critical residue involved in the active transport. Therefore, it was important to check if the single point mutations of Glu325, Arg302 and His322 can change the pK_a value of carboxyl group at position 325.

2.7.1 pK_a of Glu325 in the mutant LacY E325D

In the present study, attention was focused on the mutant LacY E325D in which the essential carboxylate is retained but the side chain is one methylene group shorter relative to wild-type. In wild-type permease, the electrostatic interaction between Glu325 (helix X) and Arg302 (helix IX) is sufficiently strong. In contrast, with Asp at position 325, the electrostatic interaction is broken.[35]

The carboxylic acid is essential at position 325 and it was important to check if the change of the length of acid chain will result in the pK_a shift of carboxylic group at this position. Thus, combined perfusion-SEIRAS approach was applied to register pH-induced difference spectra of LacY E325D in the presence and absence of NPG to determine the pK_a value as described before (see sections 3.4 and 3.5 in Materials and methods part). But first of all deconvolution of amide I band of LacY E325D was done in order to check if the single amino acid mutation changes the secondary structure of the mutant.

2.7.1.1 Secondary structure of LacY E325D

Absorption spectrum of the purified sample of LacY E325D was recorded and deconvolution of amide I band was done. The result is presented below in Figure 15.

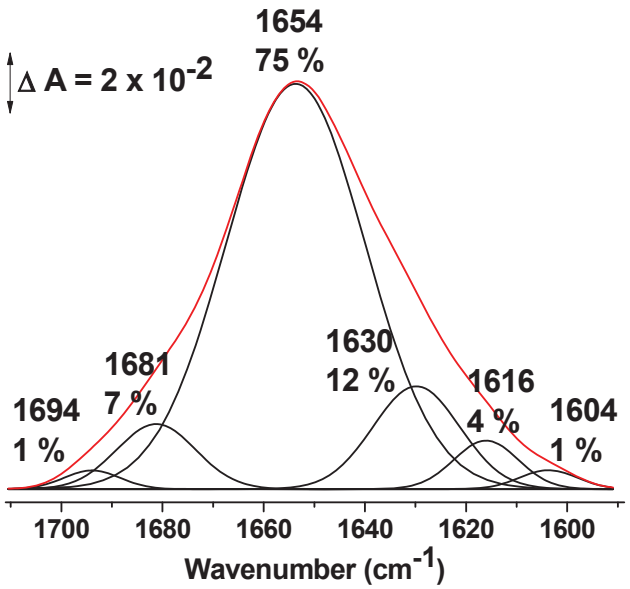

Figure 15: Deconvolution of amide I band of LacY E325D

As mentioned in the section 2.2, the amide I band is centered at 1654 – 1656 cm^{-1} and corresponds to the sum of contributions of few components. Six bands at around 1695, 1680, 1655, 1633, 1620 and 1610 cm^{-1} were used to do the deconvolution of amide I band of LacY E325D.

Table 2 summarizes the assignment of different components of amide I band of LacY E325D and represents the percentage of different elements of secondary structure.

Table 2: Secondary structure of the purified sample of LacY E325D

Secondary structure	Position of amide I and estimated percentage
α-helices + disordered structures	1654 (75 %)
Parallel β-sheets	1630 (12 %)
Parallel β-sheets	1616 (4 %)
Antiparallel β-sheets	1694 + 1604 (2 %)
β-turns	1681 (7 %)

These results clearly demonstrate that the major secondary structures of LacY E325D are α-helices. The percentage of all the elements of secondary structure of LacY E325D comparing to LacY WT is almost identical. The differences can be due to the errors of deconvolution (± 3.5 %).

It is also evident that single mutation of Glu325 with Asp does not change the secondary structure of the proteins. Thus, at the next step of the work perfusion measurements were done in order to determine the pK_a of carboxylic group at position 325 in the mutant LacY E325D.

2.7.1.2 Perfusion-induced conformational changes in a monolayer of immobilized LacY E325D

Perfusion-induced FTIR difference spectra of LacY E325D were registered first in the absence of NPG. The results are presented below in Figure 16.

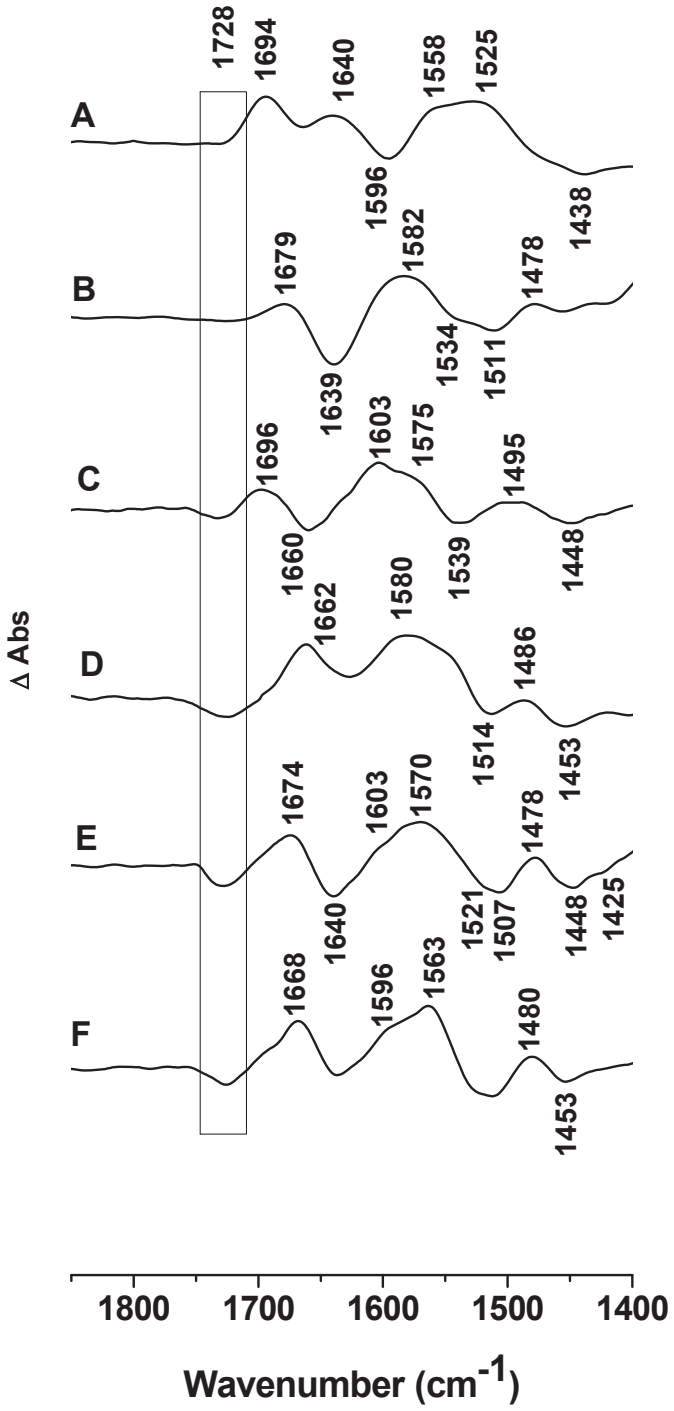

Figure 16: Perfusion-induced FTIR difference spectra of LacY E325D in the absence of NPG. The sample equilibrated at pH 7.0 (6.0 and 6.5 in A and B, respectively) was subtracted from the sample equilibrated at 7.0 (A), 7.5 (B), 8.0 (C), 8.5 (D), 9.0 (E) and 9.5 (F), respectively

An interesting change with increasing pH is observed at 1728 cm^{-1}. A negative signal observed here reflects deprotonation of Asp325. Frequency shift of carboxylic group at position 325 from 1742 cm^{-1} (in LacY WT and $LacY_{ww}$) to 1728 cm^{-1} (in LacY E325D) can be explained by the change of the environment of this group due to the different length of acid chain.

As shown, the signal is absent at pH 7 and 7.5 (Figure 16A and B, respectively) and it increases in intensity at pH 8 – 9.5 (Figure 16C-F), clearly indicating deprotonation of an acidic side chain. Protonation and deprotonation are fully reversible and correlate with reorganization of the polypeptide backbone.

The pK_a of Asp325 was determined by plotting the Δ Absorbance at 1728 cm^{-1} versus pH (Figure 17). From the observed fit (red), Asp325 has a pK_a of 8.3 ± 0.1, a value that agrees remarkably well with the pK^{app} for the exchange obtained previously for LacY E325D[35] but differ from pK^{app} for TDG binding.[14]

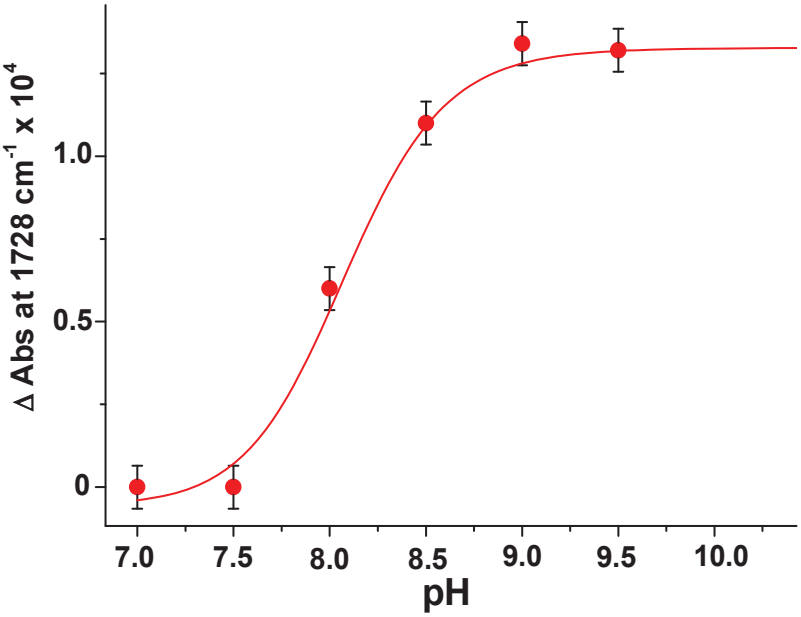

Figure 17: pH dependence of Δ Absorbance change at 1728 cm^{-1} measured with LacY E325D in the absence of NPG

Remarkably, it was not possible to register reversible pH-induced FTIR difference spectra of LacY E325D in the presence of NPG. Probably, it is related to the instability of the mutant with the bound substrate.

2.7.2 pK_a of Glu325 in the mutant LacY H322Q

As was mentioned before His322 is one of the relatively small number of amino acid chains that are irreplaceable with respect to the active transport.[32] H^+ translocation involves residues primarily in the C-terminal six-helix bundle, which are positioned across the cavity from the sugar-binding site (Figure 18, cyan sticks). Arg302 (helix IX), His322 (helix X), Tyr236 (helix VII), Glu325 (helix X), Asp240 (helix VII), and Lys319 (helix X) form a H-bond/salt bridge network between helices VII, IX, and X (Figure 19). Arg302, Tyr236, His322, and Asp240 are within 3Å of each other, and Glu325 and Lys319 flank the network from the cytoplasmic and periplasmic sides, respectively. A charge pair between Asp237 and Lys358 connects helices VII and XI and is important for membrane insertion and stability of LacY but not for sugar/H^+ symport.[27, 36, 37] Any single replacement of Arg302, Tyr236, His322, and Asp240 results in a marked decrease in the affinity for sugar.

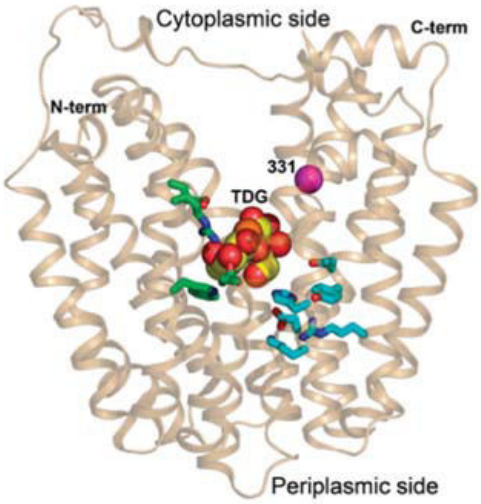

Figure 18: X-ray structure model of LacY. Side view of overall structure (PDB ID 1PV7) with TDG molecule (shown as spheres) bound at the apex of the cytoplasmic cavity. Amino acid residues implicated in sugar binding and H+ translocation are shown as green or cyan sticks, respectively. The Cα atom at position 331, where the Cys residue introduced was labeled with fluorophore, is shown as a magenta sphere[14]

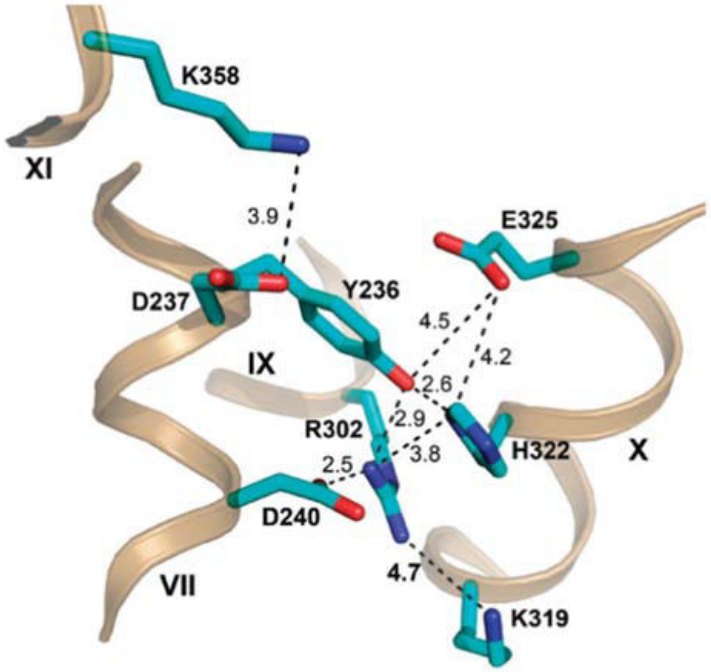

Figure 19: Side view from the cytoplasmic cavity toward the proton translocation site (PDB ID 2CFQ). The network of hydrogen bond/salt bridge interactions is shown with only the shortest distances displayed as dashed lines (in Å)[14]

In this section the results on the mutant H322Q in which the residue His322 was substituted with Gln will be presented. It is important to check how mutation of this residue influences pK_a value of Glu325 since changes in pK_a are related to the changes in H-bond/salt bridge network.

Thus, the perfusion-SEIRAS approach was applied to register pH-induced FTIR difference spectra of LacY H322Q in the absence of NPG to determine the pK_a value of Glu325 following the same procedure as described before (see section 3.4 in Materials and methods part). The experiments were carried out in the absence of NPG since it was shown before that the presence of sugar did not have any effect on the pK_a of Glu325 (see Figure 13 and section 2.5) or it was not possible to register reversible difference spectra in the presence of NPG (see section 2.7.1.2).

The results are presented below in Figure 20.

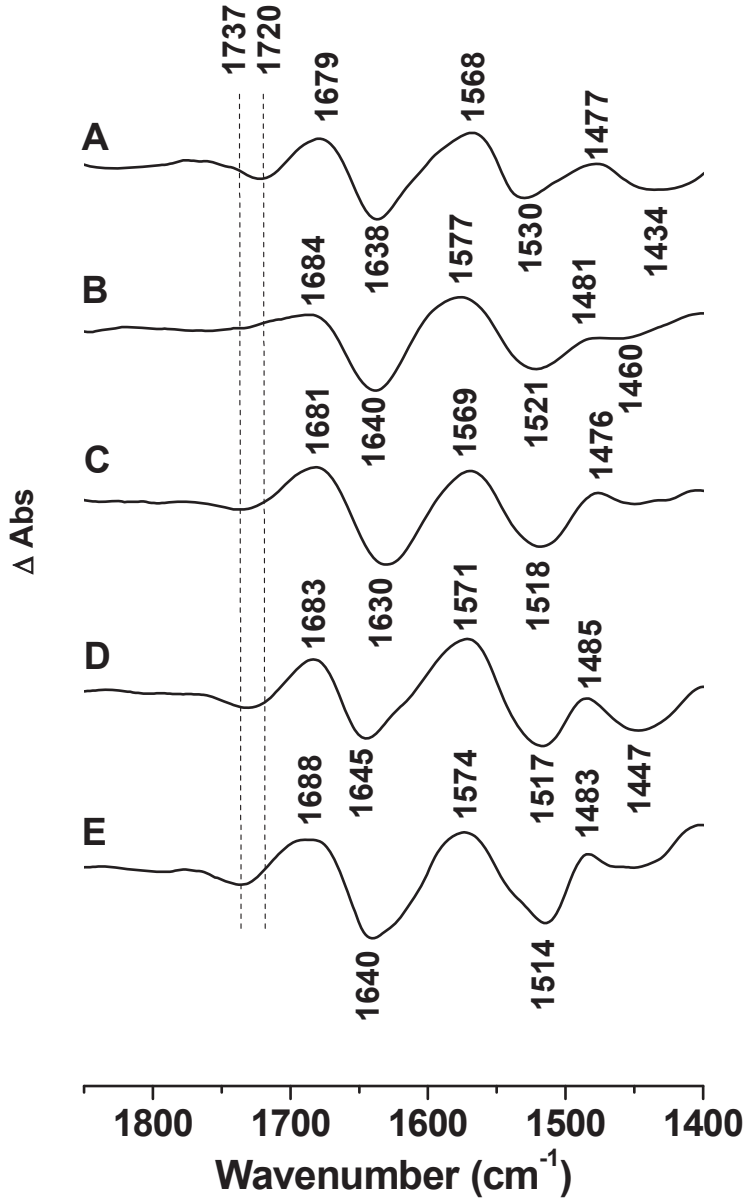

Figure 20: Perfusion-induced FTIR difference spectra of LacY H322Q in the absence of NPG. The sample equilibrated at pH 7.0 (6.0 in A) was subtracted from the sample equilibrated at 7.0 (A), 9.5 (B), 10.0 (C), 10.5 (D) and 10.9 (E), respectively

The change with increasing pH is observed at 1737 cm^{-1}. A negative signal which is observed here reflects deprotonation of Glu325. Frequency shift of carboxylic group at position 325 from 1742 cm^{-1} (in LacY WT and $LacY_{ww}$) to 1737 cm^{-1} (in LacY H322Q) can be explained by the changing of the

surrounding environment and possible perturbation of the geometry of H^+ translocation cluster following the substitution of His322 with Gln.

It can be seen that the signal is absent at pH 9.5 (Figure 20B) and it increases in intensity at pH 10 – 10.9 (Figure 20C-E), clearly indicating deprotonation of an acidic side chain. An interesting negative peak at 1720 cm^{-1} is observed at pH 7 (Figure 20A). Position 1720 cm^{-1} is typical for carboxylic groups in a less hydrophobic environment. Thus, this peak might be explained by the deprotonation of some carboxylic group(s) with the pK_a between pH 6 and 7. Protonation and deprotonation are fully reversible and correlate with reorganization of the polypeptide backbone.

The pK_a of Glu325 was determined as before by plotting the Δ Absorbance at 1737 cm^{-1} versus pH (Figure 21). From the observed fit (blue), Glu325 has a pK_a of 10.1 ± 0.1. To the best of our knowledge pK^{app} of the studied mutant for TDG binding was not determined yet.

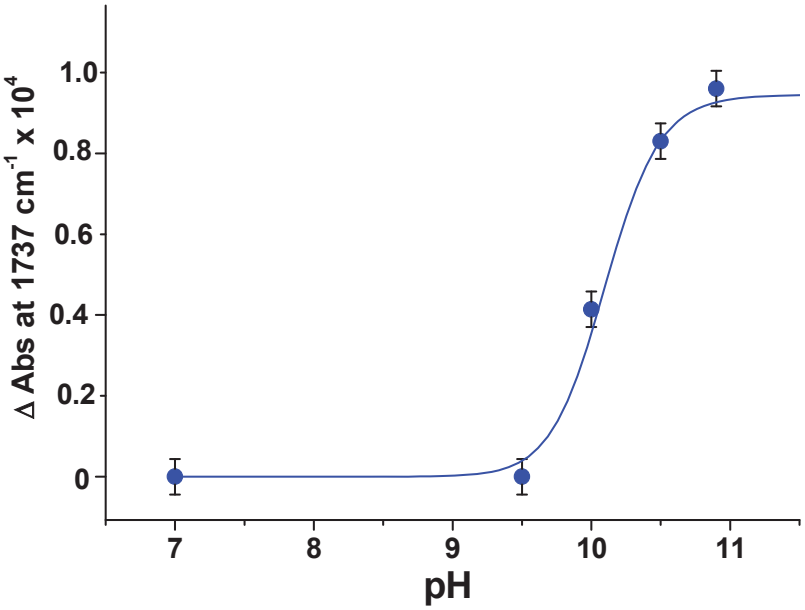

Figure 21: pH dependence of Δ Absorbance change at 1737 cm^{-1} measured with LacY H322Q in the absence of NPG

2.7.3 pK_a of Glu325 in the mutants with substituted Arg302

As was mentioned before Arg302 is an important irreplaceable residue with respect to the active transport. As well as His322, Arg302 is involved in the formation of H-bond/salt bridge network between helices VII, IX, and X (Figure 19). It has been suggested that Arg302 could interact with Glu325 to drive deprotonation.[24] On the one hand, in the published structure, the side chain of Arg302 is ~7 Å away from Glu325, suggesting that a large conformational rearrangement may occur. On the other hand, LacY with two Cys residues at positions 302 and 325 exhibits excimer fluorescence,[26] and with two His residues, an Mn(II)-binding site is observed.[27]

Any disturbance in the central core of the H^+ translocation site decreases sugar affinity by affecting H^+ binding. Thus, any replacement of Arg302 residue which does not make direct contact with the galactopyranosyl ring[38] results in a marked decrease in the affinity for sugar and also a concomitant change in the pH dependence of K_d^{app}.[14]

In this work two mutants R302K and R302A were studied.

2.7.3.1 pK_a of Glu325 in the R302K mutant

Combined perfusion-SEIRAS approach was applied to register pH-induced FTIR difference spectra of LacY R302K in the absence of NPG following the same procedure as described before (see section 3.4 in Materials and methods part) in order to check whether substitution of R302 with Lys will affect the pK_a of Glu325.

It was possible to register perfusion-induced FTIR spectra only for the samples equilibrated at pH values 8.5 and 9.0. No reversible and reproducible spectra were obtained below pH 8.5 or higher than pH 9.0.

The results are presented below in Figure 22.

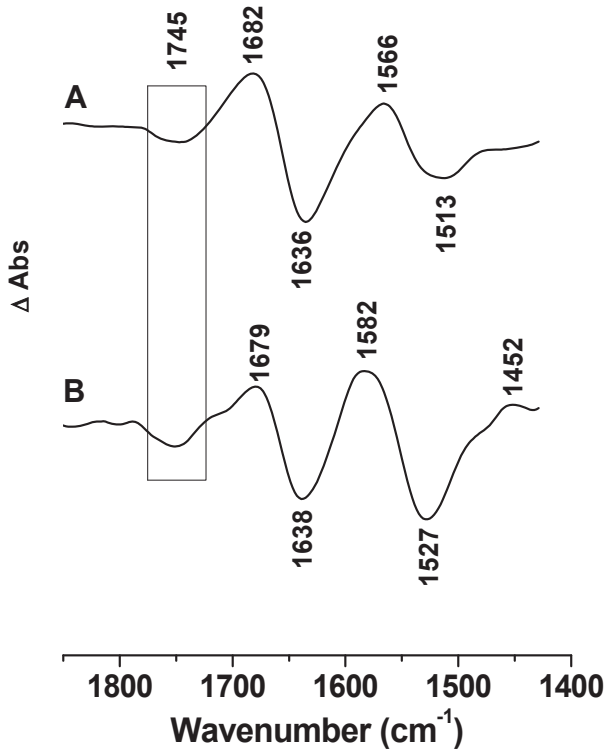

Figure 22: Perfusion-induced FTIR difference spectra of LacY R302K in the absence of NPG. The sample equilibrated at pH 7.0 was subtracted from the sample equilibrated at 8.5 (A) and 9.0 (B), respectively

The change with increasing pH is observed at 1745 cm^{-1}. A negative signal that is observed here reflects as mentioned before deprotonation of Glu325. Frequency shift of carboxylic group at position 325 from 1742 cm^{-1} (in LacY WT and $LacY_{ww}$) to 1745 cm^{-1} (in LacY R302K) might be because of the change of the surrounding environment and subsequent change of the interactions with other amino acids. In the case of mutant LacY R302K the possible perturbation of the geometry of H^+ translocation cluster might be due to the change of charge distribution when guanidinium group of Arg302 is substituted with primary amino group of Lys (see comparison of two amino acids below on Figure 23).

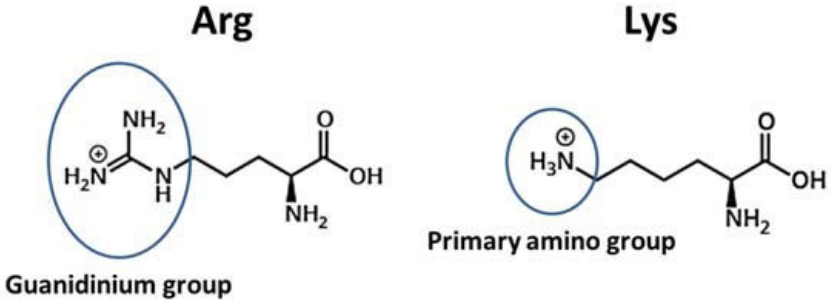

Figure 23: Representation of structure formulas of Arg and Lys amino acids

The negative signal at 1745 cm^{-1} is clearly observed at pH 8.5 and 9 (Figure 22A and B, respectively), indicating deprotonation of Glu325 amino acid. Protonation and deprotonation are fully reversible and correlate with reorganization of the polypeptide backbone.

Since the negative signal is already observed at pH 8.5 it is very probable that pK_a of Glu325 in LacY R302K is lower comparing to the wild-type protein.

2.7.3.1.1 pK_a of Glu325 in the alkali-stable LacY G46W/G262W R302K mutant

Since LacY R302K was not stable another alkali-stable double-Trp mutant carrying the same R302K mutation was constructed.

The perfusion-SEIRAS approach was applied to register the pH-induced FTIR difference spectra of $LacY_{ww}$ R302K in the absence of NPG to determine the pK_a value of Glu325 according to the same procedure described before (see section 3.4 in Materials and methods part). The experiments were carried out in the absence of NPG since before it was shown before that the presence of sugar did not have any effect on the pK_a of Glu325 (see Figure 13 and section 2.5) or it was not possible to register reversible difference spectra in the presence of NPG (see section 2.7.1.2).

The results are presented below in Figure 24.

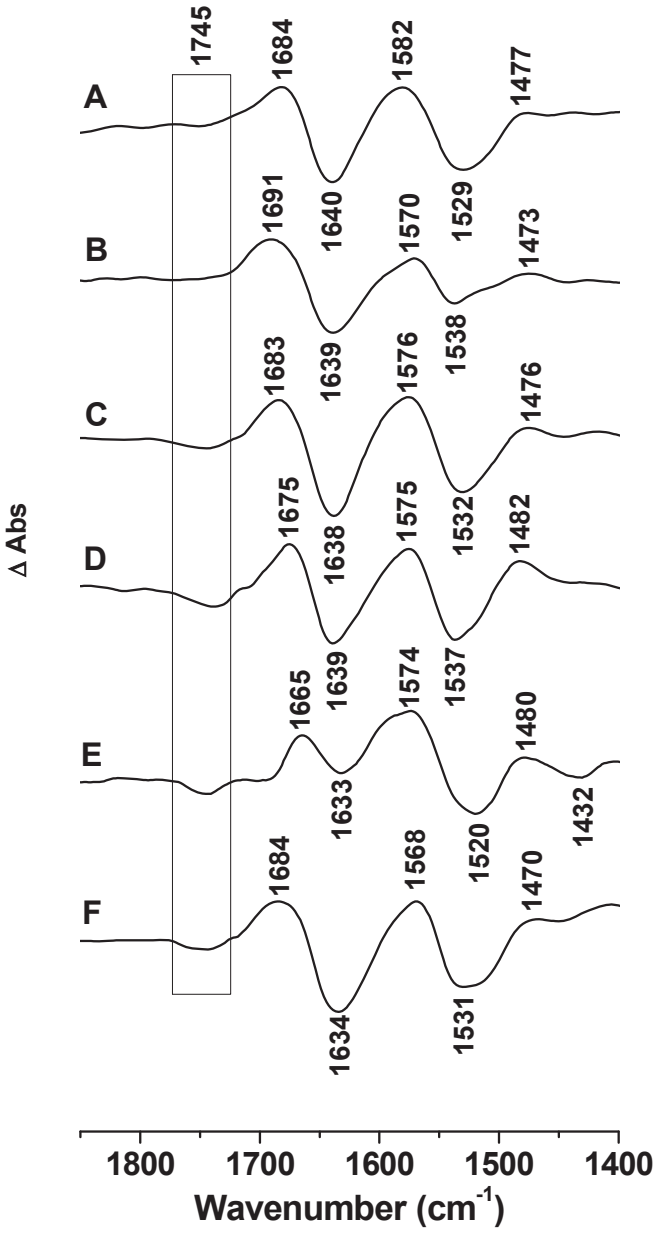

Figure 24: Perfusion-induced FTIR difference spectra of $LacY_{ww}$ R302K in the absence of NPG. The sample equilibrated at pH 7.0 was subtracted from the sample equilibrated at 7.5 (A), 8.0 (B), 8.5 (C), 9.0 (D), 10.0 (E) and 10.9 (F), respectively

The change with increasing pH is observed at 1745 cm^{-1}.

It can be seen that the signal is absent at pHs 7.5 and 8.0 (Figure 24A and B, respectively) and it increases in intensity at pH 8.5 – 10.9 (Figure 24C-F), clearly indicating deprotonation of an acidic side chain. Protonation and deprotonation are reversible and correlate with reorganization of the polypeptide backbone.

The pK_a of Glu325 was determined as usually by plotting the Δ Absorbance at 1745 cm^{-1} versus pH (Figure 25). From the observed fit (orange), Glu325 has a pK_a of 8.4 ± 0.1. It was reported previously[14] that Glu325 in R302K mutant has pK^{app} for TDG binding equal 8.4.

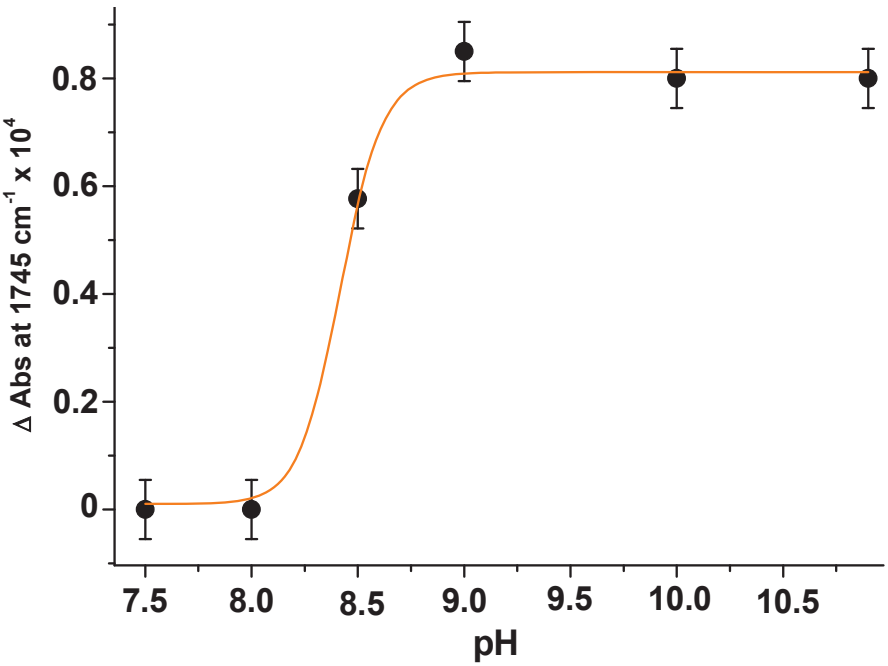

Figure 25: pH dependence of Δ Absorbance change at 1745 cm^{-1} measured with $LacY_{ww}$ R302K in the absence of NPG

2.7.3.2 pK_a of Glu325 in the R302A mutant

It is very interesting to understand why Glu325 in LacY R302K deprotonates at lower pH values comparing to the wild-type protein. In order to check the hypothesis that in LacY R302K it is the positive charge from Lys302 that causes the change in the pK_a of Glu325 we studied another mutant LacY R302A in which Arg302 was substituted with not charged Ala.

Therefore, the same perfusion-SEIRAS approach was applied to register pH-induced FTIR difference spectra of LacY R302A in the absence of NPG.

The difference spectra are presented below in Figure 26.

The change with increasing pH is observed at 1742 cm^{-1}. Interestingly, the peak position corresponding deprotonation of Glu325 in the mutant LacY R302A is the same as in wild-type protein.

It can be seen from the Figure 26 that the signal is absent at pH 8 and 9 (Figure 26A and B, respectively) and it continuously increases in intensity from pH 10 to 11 (Figure 26C-E), clearly indicating deprotonation Glu325. Protonation and deprotonation are fully reversible and correlate with reorganization of the polypeptide backbone.

The pK_a of Glu325 was determined as usually by plotting the Δ Absorbance at 1742 cm^{-1} versus pH (Figure 27). From the observed fit (black), it can be seen that plateau is still not reached even at pH 11. Unfortunately, it was not possible to register difference spectra at pH values higher than 11 because of the denaturation of the mutant. Thus, we could suppose that Glu325 has a pK_a of 10.5 or even more ± 0.1. To the best of our knowledge pK^{app} of the studied mutant for TDG binding was not determined yet but it was mentioned about suppression of the effect of alkaline pH on sugar affinity with LacY R302A.

In order to perform perfusion measurements at alkaline pH and to determine the pK_a of Glu325 in the R302A mutant an alkali-stable double-Trp mutant $LacY_{ww}$ R302A was used. The results are described in the next section.

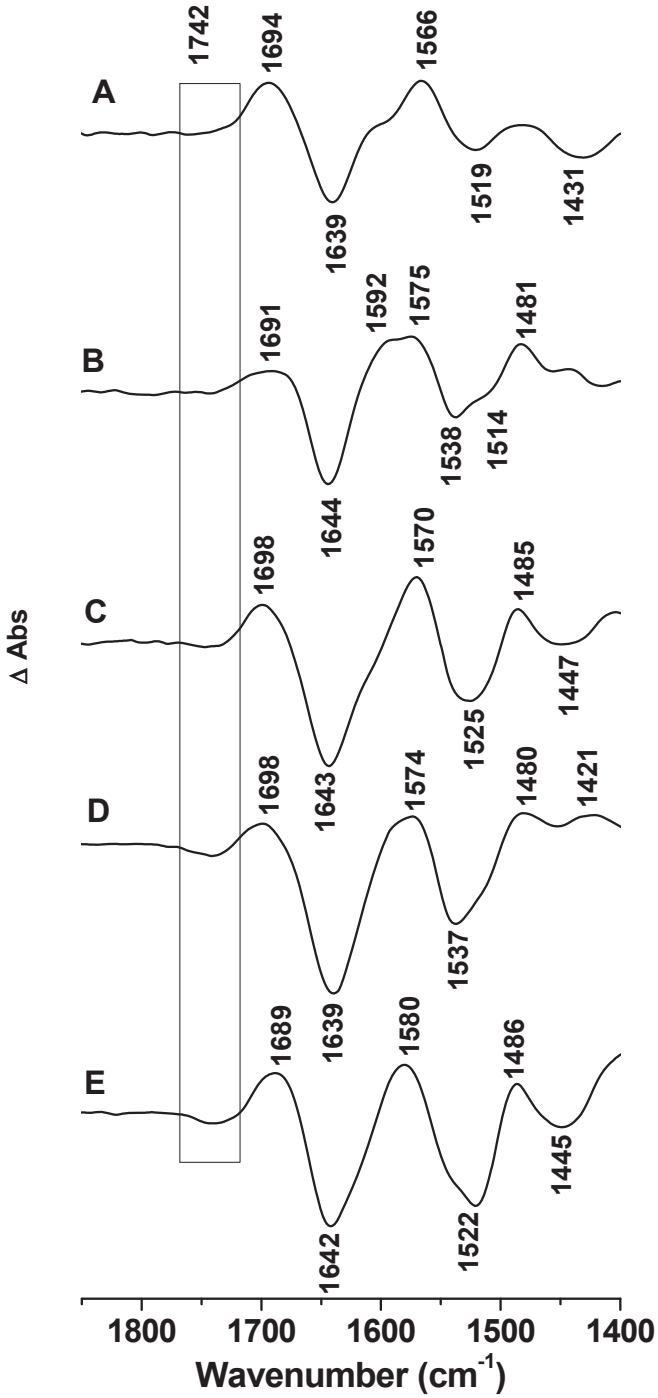

Figure 26: Perfusion-induced FTIR difference spectra of LacY R302A in the absence of NPG. The sample equilibrated at pH 7.0 was subtracted from the sample equilibrated at 8.0 (A), 9.0 (B), 10.0 (C), 10.5 (D) and 11.0 (E), respectively

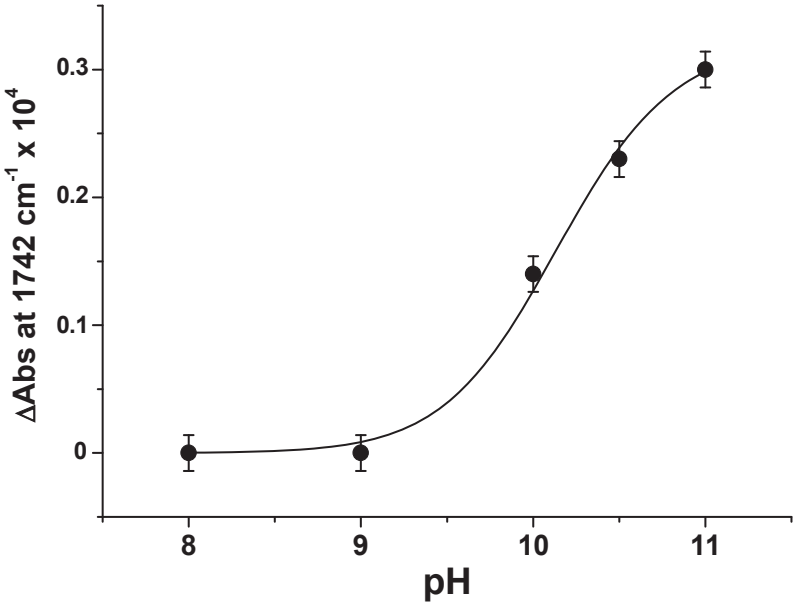

Figure 27: pH dependence of Δ Absorbance at 1742 cm^{-1} measured with LacY R302A in the absence of NPG

2.7.3.2.1 pK_a of Glu325 in the alkali-stable LacY G46W/G262W R302A mutant

An alkali-stable mutant $LacY_{ww}$ R302A was used to register pH-induced difference spectra and to determine the pK_a of Glu325 in the absence of sugar by means of perfusion-SEIRAS approach according to the procedure described before (see section 3.4 in Materials and methods part). The experiments were performed in the absence of NPG because the presence of sugar did not have any effect on the pK_a of Glu325 (see Figure 13 and section 2.5) or it was not possible to register reversible difference spectra in the presence of NPG (see section 2.7.1.2).

The results are presented below in Figure 28.

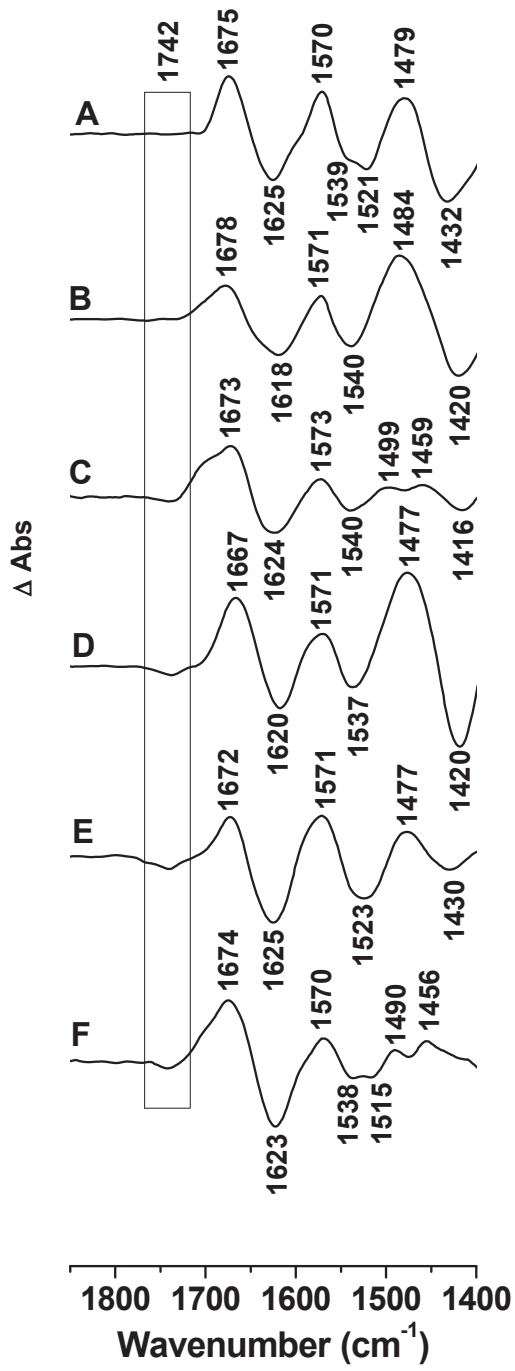

Figure 28: Perfusion-induced FTIR difference spectra of $LacY_{ww}$ R302A in the absence of NPG. The sample equilibrated at pH 7.0 was subtracted from the sample equilibrated at 8.0 (A), 9.0 (B), 10.0 (C), 10.5 (D), 11.0 (E) and 11.5 (F), respectively

Here, the change with increasing pH is observed at 1742 cm^{-1}. The observed negative signal points toward deprotonation of Glu325.

It can be noticed that the signal is absent at pHs 8.0 and 9.0 (Figure 28A and B, respectively) and it increases in intensity at pH 10.0 – 11.5 (Figure 28C-F), clearly indicating deprotonation of an acidic side chain. Protonation and deprotonation are reversible and correlate with reorganization of the polypeptide backbone. It is important to mention that perfusion-induced difference spectra of alkali-stable mutant LacY G46W/G262W R302A (Figure 28A-F) are shifted toward the lower wavenumbers comparing to the difference spectra of LacY R302A (Figure 26A-E) pointing toward different pH-induced conformational changes. This is in accordance with the previous observations that indicate that double-Trp mutant is conformationally restricted because of the bulky Trp residues.*(17, 18)*

The pK_a of Glu325 was determined by plotting the Δ Absorbance at 1742 cm^{-1} versus pH (Figure 29). From the observed fit (dark cyan), Glu325 has a pK_a of 10.3 ± 0.1. As was mentioned before in the previous section, to the best of our knowledge pK^{app} of the studied R302A mutant for TDG binding has not been determined yet.

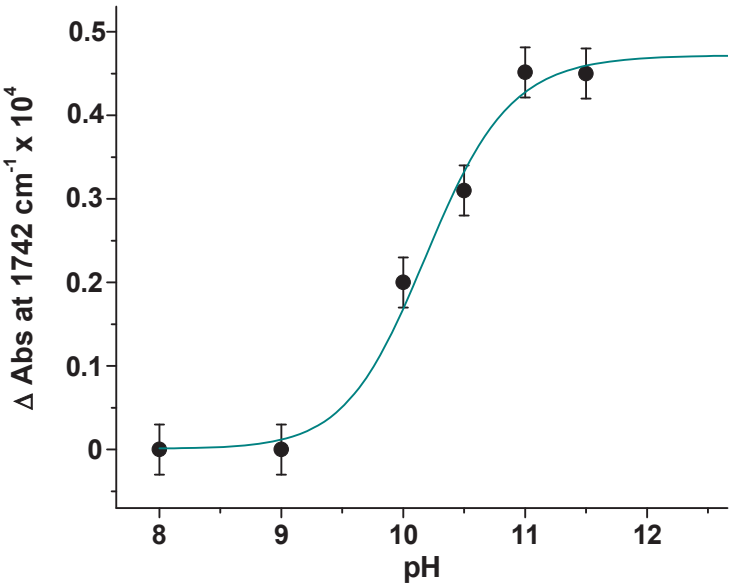

Figure 29: pH dependence of Δ Absorbance at 1742 cm^{-1} measured with $LacY_{ww}$ R302A in the absence of NPG

2.7.3.3 pH-dependent changes in LacY R302A observed in the FIR spectral region

FIR measurements were also performed for the mutant LacY R302A that exhibit different activity toward active transport comparing to LacY WT. Thus, that sample of LacY R302A was equilibrated at pH 7.5 and 10.5 and FIR spectra were recorded. The results are shown on Figure 30.

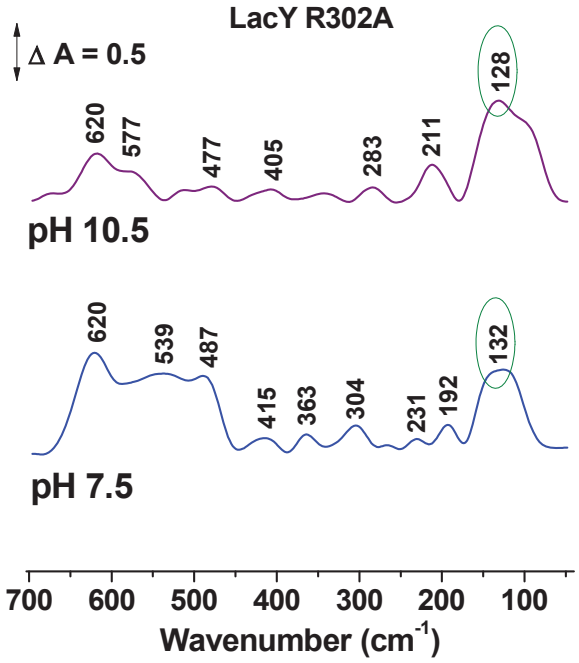

Figure 30: FIR ATR absorbance spectra of the films from LacY R302A at pH 10.5 (violet) and pH 7.5 (blue)

The intense and broad band corresponding to hydrogen bonding shifts toward lower frequencies from 132 cm^{-1} to 128 cm^{-1} (Figure 30 blue and violet lines, respectively) upon change of the pH form 7.5 to 10.5. This observation points toward large conformational changes taking place within the proteins upon variation of pH. Moreover, shifting toward lower frequencies indicates weakening of hydrogen bonding at alkaline pH values. This behavior is the same as in the case of LacY WT and $LacY_{ww}$ described above. The spectral profile in the region from 700 cm^{-1} to 500 cm^{-1} corresponding to amide IV, amide V and amide VI bands is different. On the basis of these results it can be concluded that variation of pH induces large conformational changes and results in the

change of hydrogen bonding within the protein. Moreover, the mutant LacY R302A and LacY WT that demonstrate different transport activity probably exist in different conformational states at the same pH values. This might be due to the perturbation of the active site of the protein upon mutation of the critical amino acid which leads to the different population of lowest energy conformations at given pH values.

2.8 Summarized results and discussion

The summarized results on the titration of Glu325 in different mutants are represented in Figure 31.

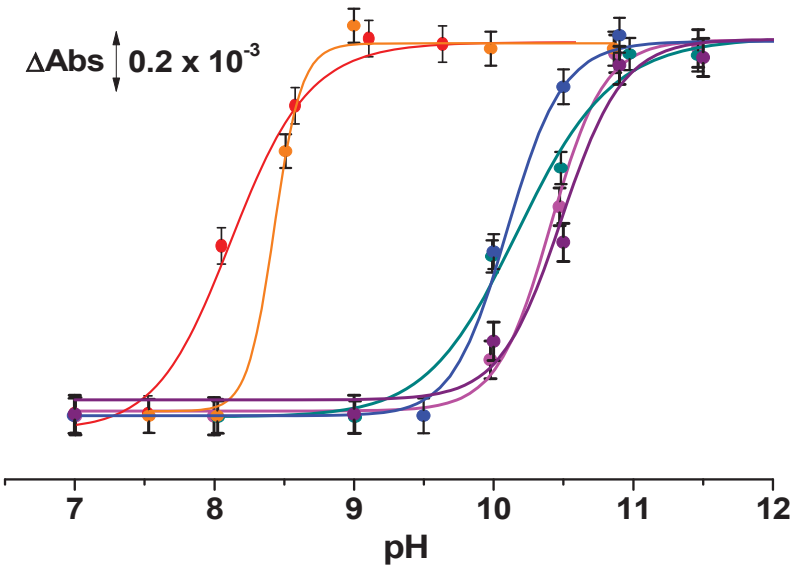

Figure 31: pH dependence of Δ Absorbance measured with $LacY_{ww}$ in the absence (magenta) and presence of sugar (purple), LacY E325D (red), LacY H322Q (blue), $LacY_{ww}$ R302K (orange) and $LacY_{ww}$ R302A (dark cyan)

The data described in this chapter is summarized in the Table 3.

Table 3: Correlation between pK_a of Glu325 and activity[14, 18, 35, 39]

Mutant	Activity	pK_a	Peak position/cm^{-1}
LacY WT	active transport	10.5	1742
$LacY_{ww}$	no active transport	10.5	1742
$LacY_{ww}$ E325A/LacY E325A	no active transport	titration abolished	
LacY E325D	active transport at a low rate (15% of WT)	8.3	1728
LacY H322Q	no active transport	10.1	1737
$LacY_{ww}$ R302K	no active transport	8.4	1745
$LacY_{ww}$ R302A		10.3	1742

The pK_a of Glu325 in $LacY_{ww}$ is the same as in LacY WT nevertheless transport activity in $LacY_{ww}$ is abrogated with little or no effect on galactoside affinity.[18]

Mutations of the residues involved in the H^+ translocation change the pK_a value of carboxylic group at position 325 indicating perturbation of the hydrogen bonding in the H-bond/salt bridge network between helices VII, IX, and X. Thus, substitution of Glu325 with Asp325 which has shorter chain length (difference between two amino acids in 1 methylene group) results in the shift of pK_a from 10.5 to 8.3. In this mutant probably interaction of Asp325 with Arg302 is broken and this causes pK_a shift. Mutant exhibits transport activity at a low rate – 15% of the activity of LacY WT.[35]

In the mutant LacY H322Q substitution of His322 which has partially protonated imidazole at physiological pH with not charged Gln leads to very slight downshift of pK_a. This might indicate that such mutation does not perturb significantly the hydrogen bonding in the H-bond/salt bridge network. Nevertheless, this mutant LacY H322Q exhibits no transport activity.[14, 40, 41]

Interestingly, Glu325 in LacY R302K deprotonates at lower pH comparing to the LacY WT clearly indicating that carboxyl group at position 325 in the mutant has downshifted pK_a compared to LacY WT. Measurements with alkali-stable mutant $LacY_{ww}$ R302K showed that Glu325 has a pK_a equal to 8.4. From the other hand, it can be seen that pK_a of Glu325 in LacY R302A is either 10.5 as in

LacY WT or even higher. Nevertheless, measurements performed with the alkali-stable mutant $LacY_{ww}$ R302A demonstrated that pK_a of Glu325 is 10.3, which is very close to the pK_a of this residue in the wild-type protein. Thus, these findings might indicate that it is the different positive charge distribution in the H^+ translocation cluster of R302K mutant comparing to LacY WT that causes change in the pK_a of Glu325. In the mutant R302A the pK_a value of Glu325, however, is very close to that of wild-type LacY but it is specifically defective in translocation reactions that involve H^+ translocation – accumulation of lactose against a concentration gradient, as well as efflux – but it binds ligand and catalyzes equilibrium exchange.[18]

Thus, it is possible to conclude that there is no direct correlation between transport activity and pK_a value of Glu325.

3. Conclusions

The findings provide direct experimental evidence that Glu325 in LacY has a pK_a of 10.5, a value that coincides precisely with the variation of the affinity of LacY for galactoside as a function of pH. The conclusion provides strong confirmation for the critical role of this residue in the reaction mechanism postulated for LacY.[18]

Mutations of the amino acid residues in the active center that are involved in the H^+ translocation change the pK_a value of carboxylic group at position 325 indicating perturbation of the hydrogen bonding in the H-bond/salt bridge network.

FIR measurements confirmed pH-induced large conformational changes of Lactose Permease and its different mutants.

Taken together, developed perfusion-SEIRAS approach was shown to be a powerful method to study important functional aspects of the proteins. In the next chapter this approach will be applied for the studies of a large membrane protein from the respiration chain – complex I.

4. References

1. Kriegel, S. b., Uchida, T., Osawa, M., Friedrich, T., and Hellwig, P. (2014) Biomimetic environment to study E. coli complex I through surface-enhanced IR absorption spectroscopy, *Biochemistry 53*, 6340-6347.

2. Ataka, K., and Heberle, J. (2006) Use of surface enhanced infrared absorption spectroscopy (SEIRA) to probe the functionality of a protein monolayer, *Biopolymers 82*, 415-419.

3. Ataka, K., Giess, F., Knoll, W., Naumann, R., Haber-Pohlmeier, S., Richter, B., and Heberle, J. (2004) Oriented attachment and membrane reconstitution of His-tagged cytochrome c oxidase to a gold electrode: in situ monitoring by surface-enhanced infrared absorption spectroscopy, *Journal of the American Chemical Society 126*, 16199-16206.

4. Venyaminov, S. Y., and Kalnin, N. (1990) Quantitative IR spectrophotometry of peptide compounds in water (H2O) solutions. II. Amide absorption bands of polypeptides and fibrous proteins in α-, β-, and random coil conformations, *Biopolymers 30*, 1259-1271.

5. Iwaki, M., Giotta, L., Akinsiku, A. O., Schägger, H., Fisher, N., Breton, J., and Rich, P. R. (2003) Redox-induced transitions in bovine cytochrome bc 1 complex studied by perfusion-induced ATR-FTIR spectroscopy, *Biochemistry 42*, 11109-11119.

6. Siebert, F., Mäntele, W., and Gerwert, K. (1983) Fourier-transform infrared spectroscopy applied to rhodopsin, *The FEBS Journal 136*, 119-127.

7. Wolf, S., Freier, E., Cui, Q., and Gerwert, K. (2014) Infrared spectral marker bands characterizing a transient water wire inside a hydrophobic membrane protein, *The Journal of chemical physics 141*, 12B625_621.

8. Zscherp, C., Schlesinger, R., Tittor, J., Oesterhelt, D., and Heberle, J. (1999) In situ determination of transient pKa changes of internal amino acids of bacteriorhodopsin by using time-resolved attenuated total reflection Fourier-transform infrared spectroscopy, *Proceedings of the National Academy of Sciences 96*, 5498-5503.

9. Hellwig, P., Behr, J., Ostermeier, C., Richter, O.-M. H., Pfitzner, U., Odenwald, A., Ludwig, B., Michel, H., and Mäntele, W. (1998) Involvement of glutamic acid 278 in the redox reaction of the cytochrome c oxidase from Paracoccus denitrificans investigated by FTIR spectroscopy, *Biochemistry 37*, 7390-7399.

10. Barth, A. (2007) Infrared spectroscopy of proteins, *Biochimica et Biophysica Acta (BBA)-Bioenergetics 1767*, 1073-1101.

11. Yang, K., Zhang, J., Vakkasoglu, A. S., Hielscher, R., Osborne, J. P., Hemp, J., Miyoshi, H., Hellwig, P., and Gennis, R. B. (2007) Glutamate 107 in subunit I of the cytochrome bd quinol oxidase from Escherichia coli is protonated and near the heme d/heme b 595 binuclear center, *Biochemistry 46*, 3270-3278.

12. Barth, A. (2000) The infrared absorption of amino acid side chains, *Progress in biophysics and molecular biology 74*, 141-173.

13. Wolpert, M., and Hellwig, P. (2006) Infrared spectra and molar absorption coefficients of the 20 alpha amino acids in aqueous solutions in the spectral range from 1800 to 500cm− 1, *Spectrochimica Acta Part A: Molecular and Biomolecular Spectroscopy 64*, 987-1001.

14. Smirnova, I., Kasho, V., Sugihara, J., Choe, J.-Y., and Kaback, H. R. (2009) Residues in the H+ translocation site define the p K a for sugar binding to LacY, *Biochemistry 48*, 8852-8860.

15. Smirnova, I., Kasho, V., Sugihara, J., Vázquez-Ibar, J. L., and Kaback, H. R. (2012) Role of protons in sugar binding to LacY, *Proceedings of the National Academy of Sciences 109*, 16835-16840.

16. Smirnova, I. N., Kasho, V., and Kaback, H. R. (2008) Protonation and sugar binding to LacY, *Proceedings of the National Academy of Sciences 105*, 8896-8901.

17. Smirnova, I., Kasho, V., Sugihara, J., and Kaback, H. R. (2013) Trp replacements for tightly interacting Gly–Gly pairs in LacY stabilize an outward-facing conformation, *Proceedings of the National Academy of Sciences 110*, 8876-8881.

18. Kaback, H. R. (2015) A chemiosmotic mechanism of symport, *Proceedings of the National Academy of Sciences 112*, 1259-1264.

19. Smirnova, I. N., Kasho, V. N., and Kaback, H. R. (2006) Direct sugar binding to LacY measured by resonance energy transfer, *Biochemistry 45*, 15279-15287.

20. Grytsyk, N., Sugihara, J., Kaback, H. R., and Hellwig, P. (2017) pKa of Glu325 in LacY, *Proceedings of the National Academy of Sciences 114*, 1530-1535.

21. Dang, S., Sun, L., Huang, Y., Lu, F., Liu, Y., Gong, H., Wang, J., and Yan, N. (2010) Structure of a fucose transporter in an outward-open conformation, *Nature 467*, 734.

22. Sun, L., Zeng, X., Yan, C., Sun, X., Gong, X., Rao, Y., and Yan, N. (2012) Crystal structure of a bacterial homologue of glucose transporters GLUT1-4, *Nature 490*, 361.

23. Iancu, C. V., Zamoon, J., Woo, S. B., Aleshin, A., and Choe, J.-y. (2013) Crystal structure of a glucose/H+ symporter and its mechanism of action, *Proceedings of the National Academy of Sciences 110*, 17862-17867.

24. Sahin-Tóth, M., and Kaback, H. R. (2001) Arg-302 facilitates deprotonation of Glu-325 in the transport mechanism of the lactose permease from Escherichia coli, *Proceedings of the National Academy of Sciences 98*, 6068-6073.

25. Andersson, M., Bondar, A.-N., Freites, J. A., Tobias, D. J., Kaback, H. R., and White, S. H. (2012) Proton-coupled dynamics in lactose permease, *Structure 20*, 1893-1904.

26. Jung, K., Jung, H., Wu, J., Prive, G. G., and Kaback, H. R. (1993) Use of site-directed fluorescence labeling to study proximity relationships in the lactose permease of Escherichia coli, *Biochemistry 32*, 12273-12278.

27. He, M. M., Voss, J., Hubbell, W. L., and Kaback, H. R. (1995) Use of designed metal-binding sites to study helix proximity in the lactose permease of Escherichia coli. 2. Proximity of helix IX (Arg302) with helix X (His322 and Glu325), *Biochemistry 34*, 15667-15670.

28. Harris, T. K., and Turner, G. J. (2002) Structural basis of perturbed pKa values of catalytic groups in enzyme active sites, *IUBMB life 53*, 85-98.

29. Brändén, G., Pawate, A. S., Gennis, R. B., and Brzezinski, P. (2006) Controlled uncoupling and recoupling of proton pumping in cytochrome c oxidase, *Proceedings of the National Academy of Sciences of the United States of America 103*, 317-322.

30. Bandekar, J. (1992) Amide modes and protein conformation, *Biochimica et Biophysica Acta (BBA)-Protein Structure and Molecular Enzymology 1120*, 123-143.

31. Falconer, R. J., Zakaria, H. A., Fan, Y. Y., Bradley, A. P., and Middelberg, A. P. (2010) Far-infrared spectroscopy of protein higher-order structures, *Applied spectroscopy 64*, 1259-1264.

32. Frillingos, S., Sahin-tóth, M., Wu, J., and Kaback, H. R. (1998) Cys-scanning mutagenesis: a novel approach to structure–function relationships in polytopic membrane proteins, *The FASEB Journal 12*, 1281-1299.

33. Kaback, H. R., Sahin-Tóth, M., and Weinglass, A. B. (2001) The kamikaze approach to membrane transport, *Nature reviews. Molecular cell biology 2*, 610.

34. Roepe, P. D., and Kaback, H. R. (1989) Site-directed mutagenesis of tyrosine residues in the lac permease of Escherichia coli, *Biochemistry 28*, 6127-6132.

35. Frillingos, S., and Kaback, H. R. (1996) Monoclonal Antibody 4B1 Alters the p K a of a Carboxylic Acid at Position 325 (Helix X) of the Lactose Permease of Escherichia coli, *Biochemistry 35*, 10166-10171.

36. Dunten, R. L., Sahin-Toth, M., and Kaback, H. R. (1993) Role of the charge pair aspartic acid-237-lysine-358 in the lactose permease of Escherichia coli, *Biochemistry 32*, 3139-3145.

37. Frillingos, S., Sahin-Toth, M., Lengeler, J. W., and Kaback, H. R. (1995) Helix packing in the sucrose permease of Escherichia coli: properties of engineered charge pairs between helixes VII and XI, *Biochemistry 34*, 9368-9373.

38. Abramson, J., Smirnova, I., Kasho, V., Verner, G., Kaback, H. R., and Iwata, S. (2003) Structure and mechanism of the lactose permease of Escherichia coli, *Science 301*, 610-615.

39. Guan, L., and Kaback, H. R. (2006) Lessons from lactose permease, *Annu. Rev. Biophys. Biomol. Struct. 35*, 67-91.

40. Padan, E., Sarkar, H. K., Viitanen, P. V., Poonian, M. S., and Kaback, H. R. (1985) Site-specific mutagenesis of histidine residues in the lac permease of Escherichia coli, *Proceedings of the National Academy of Sciences 82*, 6765-6768.

41. Puettner, I. B., Sarkar, H. K., Poonian, M. S., and Kaback, H. R. (1986) Lac permease of Escherichia coli: histidine-205 and histidine-322 play different roles in lactose/protein symport, *Biochemistry 25*, 4483-4485.

IV. THE STUDY OF COMPLEX I BY PERFUSION-SEIRAS APPROACH

List of figures in chapter 4

List of tables in chapter 4

1. Immobilization of complex I on the ATR crystal

The spectrum of complex I immobilized on the Ni-NTA SAM is illustrated in Figure 1.

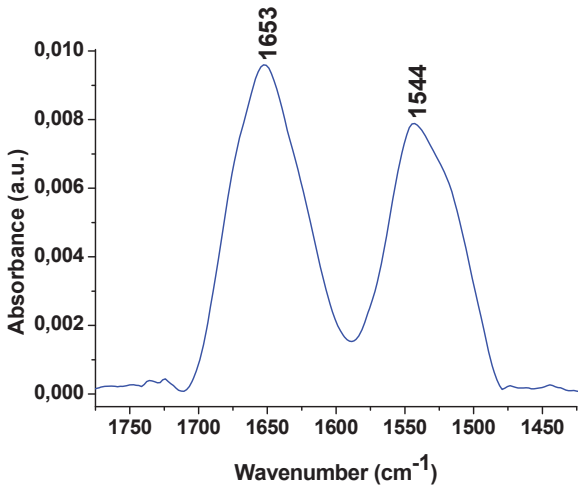

Figure 1: ATR FTIR absorbance spectrum of complex I from *E. coli*. MES buffer was taken as a background

The dominant amide I band is observed in the range from 1700 to 1600 cm^{-1} and the amide II band at 1544 cm^{-1}. Maximum of the amide I band appears at 1653 cm^{-1} indicating that complex I has predominantly α-helical structure. This observation correlates with the crystal structure of complex I solved at the resolution of 3.3 Å.[(1)]

Thus, after immobilization of the complex I on the surface of Si ATR crystal perfusion experiments can be carried out. The results are described below in the next section.

2. Perfusion-induced IR Spectroscopy of complex I

In this section, the combined perfusion-SEIRAS approach was used to investigate conformational changes in a monolayer of immobilized complex I upon oxidation and reduction which are natural processes. Experimental conditions are described in detail in the section 3.6 in Materials and methods. Figure 2 shows

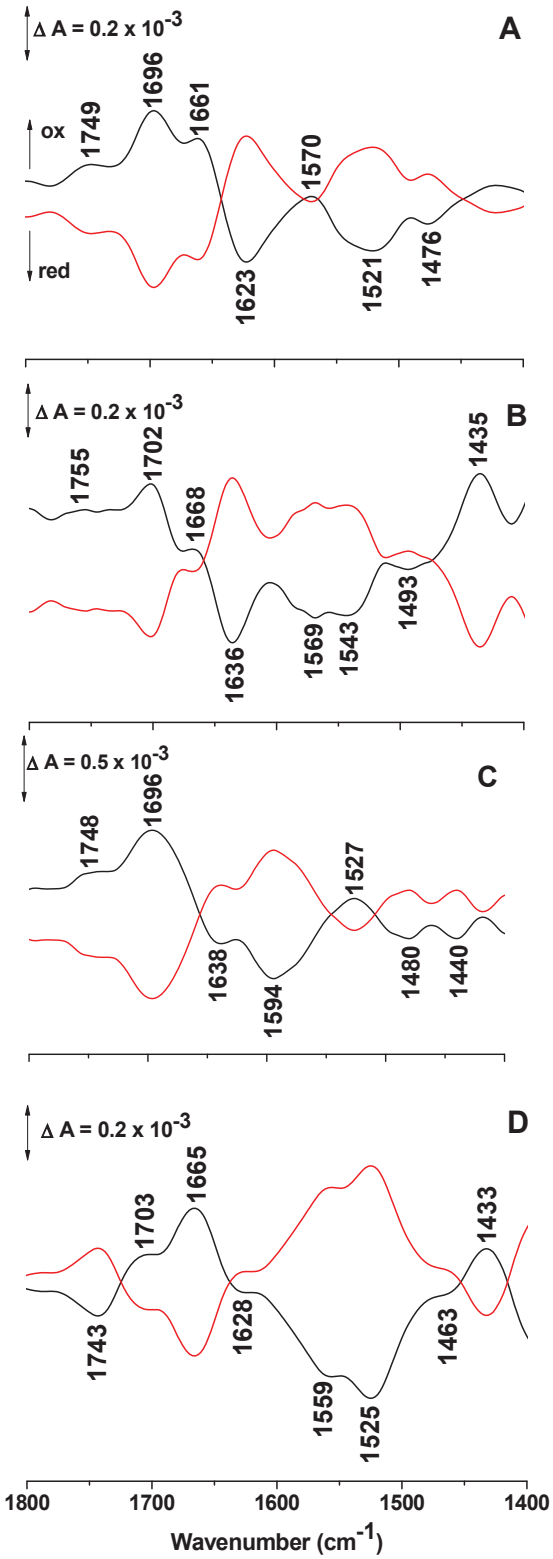

Figure 2: Perfusion-induced FTIR difference spectra of complex I obtained from the sample equilibrated with the oxidizing agent: ubiquinone-2 (A), ubiquinone-10 (B), $K_3[Fe(CN)_6]$ (C) or with MES buffer (D), respectively, and subtracted from the sample equilibrated with NADH (oxidized *minus* reduced, black line) and reverse (red line)

reversible perfusion-induced IR difference spectra obtained from the samples equilibrated with different oxidizing agents (ubiquinone-2 (Q-2) (E'_0 = 65 mV[2]), ubiquinone-10 (Q-10) (E'_0 = 68 mV[3]), potassium hexacyanoferrate (III) ($K_3[Fe(CN)_6]$) (E'_0 = 436 mV[4]) or with MES buffer without oxidizing agents but containing only solubilized oxygen (E'_0 = 815 mV[5])) and subtracted from the sample equilibrated with reducing agent NADH and vice versa (black and red lines in Figure 2, respectively).

The peaks observed in the difference spectra above can be attributed to the reorganization of secondary structure elements, individual amino acid side chains as well as flavinmononucleotide (FMN) which is involved in the electron transfer and proton translocation. Strong signals are observed in the amide I region ranging from 1700 cm^{-1} to 1600 cm^{-1}. These signals originate from the conformational changes in the C=O groups in the protein backbone. Thus, the signals at 1623 – 1641 cm^{-1} are characteristic of parallel β-sheets contributions.[6-8] Since complex I contains many α-helices in the structure the signals at ∼1650 – 1660 cm^{-1} are expected.[6] Nevertheless, these vibrational modes can be strongly shifted following the conformational changes in the parts of a helix because of the perturbation of both dipole-dipole coupling and the hydrogen bonding environment.[6] Moreover, the ν(C=O) vibrations of individual amino acid side chains like Asn, Gln or Arg might also contribute to the spectral region from 1700 cm^{-1} to 1600 cm^{-1}. The ν(C=O) vibrational modes of the protonated aspartic and glutamic acid side chains are expected at 1710 – 1750 cm^{-1}.[8, 9] In addition, a clear shoulder can be observed in the electrochemical redox spectra at 1710 cm^{-1} which is attributed to the ν(C=O) mode of the FMN.[10] In Figure 2 strong signals are observed in the amide II range (between 1590 cm^{-1} and 1450 cm^{-1}) that involves coupled CN/NH vibrational modes of the protein backbone,[6] as well as contributions from individual amino acids reorganizing or changing protonation states upon oxidation and reduction. Signals coming from FMN appear between 1650 – 1500 cm^{-1} and at 1548 cm^{-1}.[10] Moreover, ring vibrations of tyrosine around can be observed at around 1516 cm^{-1} and small contributions from other amino acid side chains can appear in the spectral region from 1450 to 1300 cm^{-1}.

To compare the difference spectra obtained by oxidation with different oxidizing agents the oxidized *minus* reduced spectra (black lines in Figure 2) are shown together in Figure 3.

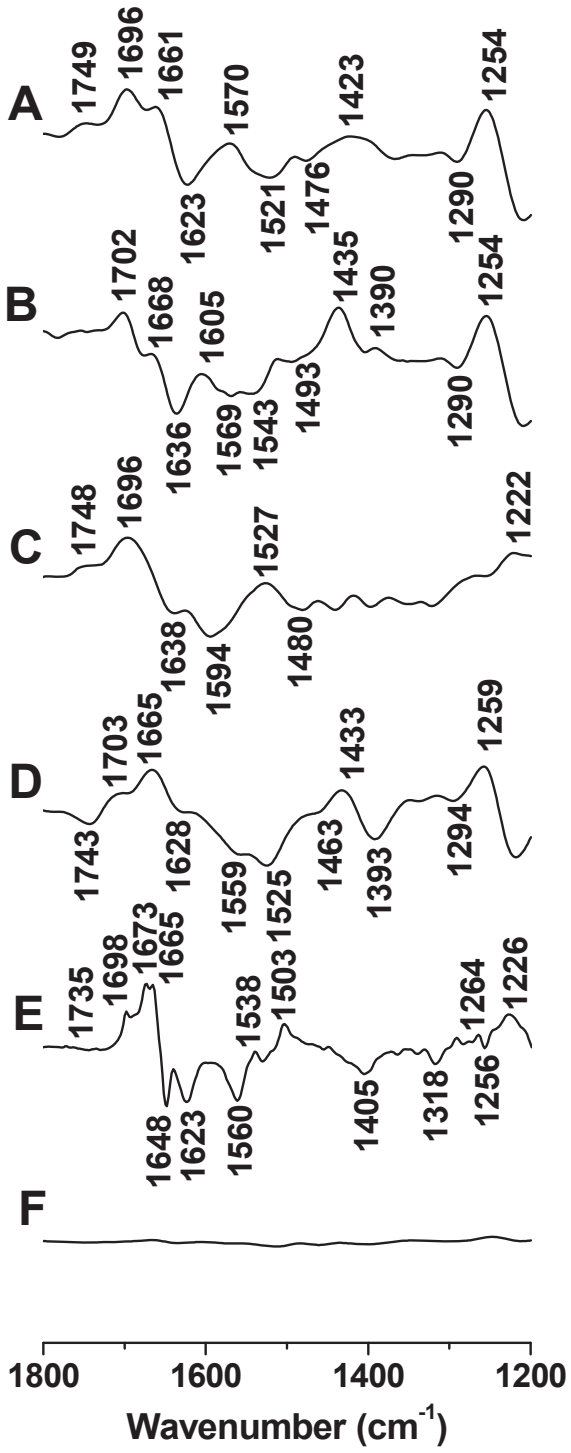

Figure 3: Perfusion-induced FTIR difference spectra of complex I obtained from the sample equilibrated with the oxidizing agent: ubiquinone-2 (A), ubiquinone-10 (B), $K_3[Fe(CN)_6]$ (C) or with MES buffer containing O_2 (D), respectively, and subtracted from the sample equilibrated with NADH. Line E represents electrochemically-induced oxidized *minus* reduced spectrum.[10] Control difference spectrum in the absence of immobilized complex I (F)

The signals at 1259 – 1254 cm^{-1} cannot be assigned to the $\delta(C\text{-}OCH_3)$ contributions of the methoxy side chain of ubiquinone since the corresponding signal should appear at around 1264 – 1266 cm^{-1}. In perspective, it would be interesting to use the labeled ubiquinone in order to attribute the corresponding signals precisely. The signals from ubiquinone might contribute to the difference spectra of complex I at 1662 – 1609 cm^{-1}. These bands clearly appear among other bands in the absorption spectrum of ubiquinone (Figure 4).[11-14] Nevertheless, the content of ubiquinone in the perfusion solutions is very small.

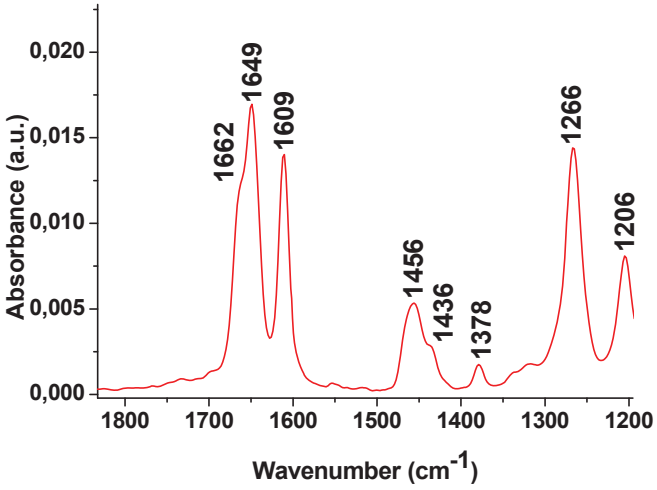

Figure 4: MID IR spectrum of the dry film of ubiquinone-10

The tentative assignments of ubiquinone-10 vibrational modes are given in the Table 1.

Table 1: Tentative assignments of ubiquinone-10 vibrations. Positions are given in cm^{-1}[15]

band position	tentative assignments
1662	ν(C=O)
1649	ν(C=O)
1609	ν(C=C)
1456	CH_2
1378	CH_3
1266	$\delta(C\text{-}OCH_3)$

Finally, contributions from NADH can be expected in the range of amide I between 1690 and 1590 cm^{-1} (see ATR FTIR absorbance spectrum of the powder of NADH in Figure 5 below).

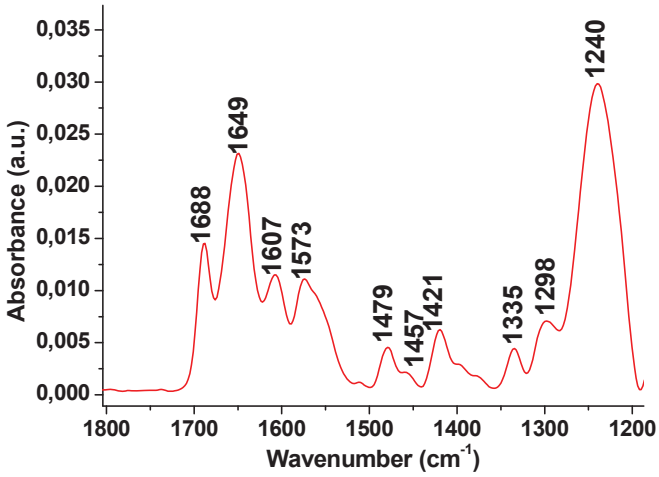

Figure 5: ATR FTIR absorbance spectrum of the powder of NADH

The tentative assignments of NADH vibrational modes are given in the Table 2.

Table 2: Tentative assignments of NADH vibrations. Positions are given in cm^{-1} *(16)*

band position	tentative assignments
1688	ν(C=O) carbonyl carboxamide
1649	adenine ring
1607	adenine ring
1573	adenine ring
1479	adenine ring
1421	nicotinamide ν(C-N)
1335	adenine ring

Iron-sulfur modes are not expected to be observed at frequencies above 800 cm^{-1}. Thus, all signals in difference spectra should arise from protein, FMN, ubiquinone, and possibly not known for the moment redox groups.*(17)*

The tentative assignments of the signals observed in the Figure 3 are summarized in the Table 3.

Table 3: Tentative assignments of perfusion-induced FTIR difference spectra of complex I. Positions are given in cm^{-1}. The negative signals arise from the protein in reduced state, whereas positive signals arise from change in the protein upon oxidation. ν: stretching, δ: deformation, ω: wagging[9, 10, 18-20]

Q-2/ NADH	Q-10/ NADH	$K_3[Fe(CN)_6]$/ NADH	MES buffer/ NADH	tentative assignments
1749 (+)		1748 (+)	1743 (-)	$\nu(C=O)_{asp,\ glu}$
1696 (+)	1702 (+)	1696 (+)	1703 (+)	amide I
1661 (+)	1668 (+)		1665 (+)	amide I, $\nu(C=O)_{asn,\ gln}$, $\nu(C=O)_{UQ}$
	1636 (-)	1638 (-)		amide I
1623 (-)			1628 (-)	β-sheet, $\nu_{as}(CN_3H_5^+)_{arg}$
	1605 (+)			amide I
		1594 (-)		amide II
1570 (+)	1569 (-)			amide II (ν (C=N)), $\nu_s(CN_3H_5^+)_{arg}$
			1559 (-)	
	1543 (-)			$\nu(C=C)_{FMN}$, $\nu_{as}(COO^-)_{asp,\ glu}$
1521 (-)		1527 (+)	1525 (-)	ring-OH_{tyr}
	1493 (-)			amide II, ring modes in reduced UQ
1476 (-)		1480 (-)		amide II, ring modes in reduced UQ
			1463 (-)	
	1435 (+)		1433 (+)	amino acid side chains
1423 (+)				
	1390 (+)		1393 (-)	$\nu_s(COO^-)_{asp,\ glu}$
1290 (-)	1290 (-)		1294 (-)	
1254 (+)	1254 (+)		1259 (+)	
		1222 (+)		ν (S=O) MES buffer

Differences in the spectra in Figure 3 can be explained by not the same degree of oxidation of complex I when using different oxidizing agents. For example, it is expected that more complete oxidation of complex I will occur when using ubiquinone-2 (Figure 3A) compared to ubiquinone-10 (Figure 3B). This can be explained by the fact that Q-2 has only two isoprenyl subunits in its tail and it is more soluble while Q-10 has ten isoprenyl subunits and it is less soluble. Moreover, Q-2 can

easily enter to the quinone binding site of complex I and oxidize it faster. Anyway, electron and proton transfers by complex I are expected when using either Q-2 or Q-10 together with NADH.

The profile of the oxidized *minus* reduced spectrum in the Figure 3C obtained when using $K_3[Fe(CN)_6]$ as the oxidizing agent is almost identical to the ones illustrated in Figure 3A-B when using Q-2 and Q-10, respectively, in the spectral region from 1800 cm^{-1} to 1638 cm^{-1}. In the region from 1638 cm^{-1} to 1200 cm^{-1} the spectrum in Figure 3C is quite different comparing to the ones in Figure 3A-B. This observation might be explained by the fact that only electron transfer is possible when using $K_3[Fe(CN)_6]$. Therefore, corresponding conformational changes will differ from those when the protein transfers both electrons and protons. This is an important observation since this perfusion-SEIRAS approach can be further used to control whether the mutants of complex I can transfer only electrons or both electrons and protons. Moreover, the binding site of $K_3[Fe(CN)_6]$ in complex I is not identified yet and as was suggested in the literature[21] the binding of the quinone in the quinone binding site is necessary for the appropriate conformational changes of the protein allowing proton pumping.

Spectrum in the Figure 3D corresponds to the oxidation of complex I with the MES buffer solution containing only naturally dissolved oxygen under normal atmospheric conditions without addition of oxidizing agents as in the previous cases. As can be seen the overall profile of the spectrum is very similar to the ones observed when complex I was oxidized with Q-2, Q-10 and $K_3[Fe(CN)_6]$ (Figure 3A-C, respectively). Nevertheless, the curve is shifted toward the lower wavenumbers. This shift can be explained by the fact that complex I is not completely but partially oxidized by the oxygen naturally dissolved in the MES buffer solution. The partial oxidation of complex I by dissolved oxygen might be explained by the slow oxidation kinetics. Moreover, as in the case of $K_3[Fe(CN)_6]$ the binding site of the oxygen in complex I is not identified yet and observed spectral differences (Figure 3D vs Figure 3A-B) can be explained by the different mechanism of conformational changes.

Obtained oxidized *minus* reduced perfusion-induced difference spectra of complex I are highly comparable with electrochemically induced ones (see Figure 3E).[10]

In order to check the contributions from perfusion buffers as well as from Ni-NTA SAM in the difference spectra of complex I the control experiments were necessary. To perform these

measurements Si ATR crystal was first modified with gold layer and then with Ni-NTA SAM as described in sections 3.3.1 and 3.3.2 in Materials and methods but at the last step of modification complex I was not immobilized on the surface. Figure 3F shows the control difference spectrum obtained when using two perfusion solutions $K_3[Fe(CN)_6]$ and NADH but in the absence of immobilized complex I.

From the comparison of the difference spectra shown in Figure 3A-D with the one shown in Figure 3F it is evident that there is no contribution from the perfusion buffers in the obtained spectra. Therefore, the signals in the difference spectra illustrated in Figure 3A-D arise from the immobilized complex I as the result of perfusion-induced conformational changes. The same control experiments were performed to check the contribution of perfusion solutions in the difference spectra of LacY (data not shown). These control experiments also confirmed that signals in the difference spectra arise from the immobilized protein.

3. Conclusions

In conclusion, the developed SEIRAS-perfusion approach was successfully applied to study conformational changes in complex I upon oxidation with different oxidizing agents and reduction with NADH.

The findings demonstrate that complex I undergoes different conformational changes depending on whether it is fully oxidized or partially. Eventually, the higher degree of the oxidation of protein can be obtained when using ubiquinones. Oxygen naturally dissolved in the MES buffer has the lowest ability to oxidize complex I and corresponding difference spectrum (Figure 3D) is noticeably shifted to the lower wavenumbers comparing to the other difference spectra obtained from complex I when it is equilibrated with other oxidizing agents (Figure 3A-C). The summarizing diagram is shown below.

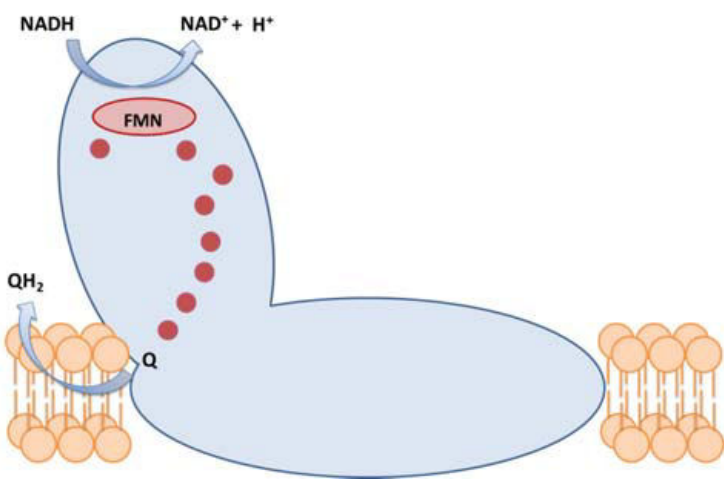

- ✓ **Electrochemically → oxidize all**
- ✓ **NADH/UQ → do not oxidize all; electron transport and H^+ pumping**
- ✓ **NADH/no UQ → do not oxidize all; electron transport and no H^+ pumping**

As perspective, the combined perfusion-SEIRAS approach can be further applied to study different mutants of complex I and reveal if they can transfer only electrons or both electrons and protons since corresponding difference spectra are not identical.

The results presented in this chapter confirm that oxidation and reduction of complex I induce long range global conformational changes that are eventually linked to the mechanism of the enzyme functioning however presence of UQ is necessary. It is widely accepted that energy released from

the electron transfer is converted into the global conformational movements of the protein allowing proton translocation.[21-26]

The perfusion-SEIRAS approach was also used to study conformational changes in the protein IM30 upon interaction with Mg^{2+}. Some results are shown in the Appendix.

4. References

1. Baradaran, R., Berrisford, J. M., Minhas, G. S., and Sazanov, L. A. (2013) Crystal structure of the entire respiratory complex I, *Nature 494*, 443.

2. Urban, P., and Klingenberg, M. (1969) On the redox potentials of ubiquinone and cytochrome b in the respiratory chain, *The FEBS Journal 9*, 519-525.

3. Lemmer, C., Bouvet, M., and Meunier-Prest, R. (2011) Proton coupled electron transfer of ubiquinone Q 2 incorporated in a self-assembled monolayer, *Physical Chemistry Chemical Physics 13*, 13327-13332.

4. Pandurangachar, M., Swamy, B. K., Chandrashekar, B., Gilbert, O., Reddy, S., and Sherigara, B. (2010) Electrochemical investigations of potassium ferricyanide and dopamine by 1-butyl-4-methylpyridinium tetrafluoro borate modified carbon paste electrode: A cyclic voltammetric study, *Int J Electrochem Sci 5*, 1187-1202.

5. Wood, P. M. (1988) The potential diagram for oxygen at pH 7, *Biochemical Journal 253*, 287-289.

6. Barth, A. (2007) Infrared spectroscopy of proteins, *Biochimica et Biophysica Acta (BBA)-Bioenergetics 1767*, 1073-1101.

7. Goormaghtigh, E., Cabiaux, V., and Ruysschaert, J.-M. (1994) Determination of soluble and membrane protein structure by Fourier transform infrared spectroscopy, In *Physicochemical methods in the study of biomembranes*, pp 405-450, Springer.

8. Tatulian, S. A. (2013) Structural characterization of membrane proteins and peptides by FTIR and ATR-FTIR spectroscopy, *Lipid-Protein Interactions: Methods and Protocols*, 177-218.

9. Venyaminov, S. Y., and Kalnin, N. (1990) Quantitative IR spectrophotometry of peptide compounds in water (H2O) solutions. II. Amide absorption bands of polypeptides and fibrous proteins in α-, β-, and random coil conformations, *Biopolymers 30*, 1259-1271.

10. Hellwig, P., Scheide, D., Bungert, S., Mäntele, W., and Friedrich, T. (2000) FT-IR spectroscopic characterization of NADH: ubiquinone oxidoreductase (complex I) from Escherichia coli: oxidation of FeS cluster N2 is coupled with the protonation of an aspartate or glutamate side chain, *Biochemistry 39*, 10884-10891.

11. Bauscher, M., and Mäntele, W. (1992) Electrochemical and infrared-spectroscopic characterization of redox reactions of p-quinones, *The Journal of Physical Chemistry 96*, 11101-11108.

12. Hellwig, P., Mogi, T., Tomson, F. L., Gennis, R. B., Iwata, J., Miyoshi, H., and Mäntele, W. (1999) Vibrational Modes of Ubiquinone in Cytochrome bo 3 from Escherichia coli Identified by Fourier Transform Infrared Difference Spectroscopy and Specific 13C Labeling, *Biochemistry 38*, 14683-14689.

13. Burie, J.-R., Boussac, A., Boullais, C., Berger, G., Mattioli, T., Mioskowski, C., Nabedryk, E., and Breton, J. (1995) FTIR spectroscopy of UV-generated quinone radicals: evidence for an intramolecular hydrogen atom transfer in ubiquinone, naphthoquinone, and plastoquinone, *The Journal of Physical Chemistry 99*, 4059-4070.

14. Bauscher, M., Nabedryk, E., Bagley, K., Breton, J., and Mäntele, W. (1990) Investigation of models for photosynthetic electron acceptors: Infrared spectroelectrochemistry of ubiquinone and its anions, *FEBS letters 261*, 191-195.

15. Breton, J., Boullais, C., Burie, J.-R., Nabedryk, E., and Mioskowski, C. (1994) Binding sites of quinones in photosynthetic bacterial reaction centers investigated by light-induced FTIR difference spectroscopy: assignment of the interactions of each carbonyl of QA in Rhodobacter sphaeroides using site-specific 13C-labeled ubiquinone, *Biochemistry 33*, 14378-14386.

16. Hielscher, R. G. (2009) The role of lipids and nucleotides in the catalytic mechanism of proteins from the respiratory chain: an electrochemical and infrared spectroscopic approach, Freiburg (Breisgau), Univ., Diss. und Université de Strasbourg, Diss., 2009.

17. Friedrich, T., Brors, B., Hellwig, P., Kintscher, L., Rasmussen, T., Scheide, D., Schulte, U., Mäntele, W., and Weiss, H. (2000) Characterization of two novel redox groups in the respiratory NADH: ubiquinone oxidoreductase (complex I), *Biochimica et Biophysica Acta (BBA)-Bioenergetics 1459*, 305-309.

18. Venyaminov, S. Y., and Kalnin, N. (1990) Quantitative IR spectrophotometry of peptide compounds in water (H2O) solutions. I. Spectral parameters of amino acid residue absorption bands, *Biopolymers 30*, 1243-1257.

19. Wolpert, M., and Hellwig, P. (2006) Infrared spectra and molar absorption coefficients of the 20 alpha amino acids in aqueous solutions in the spectral range from 1800 to 500cm− 1, *Spectrochimica Acta Part A: Molecular and Biomolecular Spectroscopy 64*, 987-1001.

20. Barth, A. (2000) The infrared absorption of amino acid side chains, *Progress in biophysics and molecular biology 74*, 141-173.

21. Efremov, R. G., and Sazanov, L. A. (2012) The coupling mechanism of respiratory complex I—a structural and evolutionary perspective, *Biochimica et Biophysica Acta (BBA)-Bioenergetics 1817*, 1785-1795.

22. Sazanov, L. A. (2015) A giant molecular proton pump: structure and mechanism of respiratory complex I, *Nature Reviews Molecular Cell Biology 16*, 375-388.

23. Berrisford, J. M., and Sazanov, L. A. (2009) Structural basis for the mechanism of respiratory complex I, *Journal of Biological Chemistry 284*, 29773-29783.

24. Hellwig, P., Kriegel, S., and Friedrich, T. (2016) Infrared spectroscopic studies on reaction induced conformational changes in the NADH ubiquinone oxidoreductase (complex I), *Biochimica et Biophysica Acta (BBA)-Bioenergetics 1857*, 922-927.

25. Brandt, U. (2006) Energy converting NADH: quinone oxidoreductase (complex I), *Annu. Rev. Biochem. 75*, 69-92.

26. Hirst, J. (2010) Towards the molecular mechanism of respiratory complex I, *Biochemical Journal 425*, 327-339.

V. PROBING GOLD GRIDS FOR A COMBINED ELECTROCHEMICAL AND SURFACE-ENHANCED RAMAN SPECTROSCOPIC APPROACH

List of figures in chapter 5

List of tables in chapter 5

Combined SERS-electrochemical approach

The second axis of this PhD work is related to the development of a combined surface-enhanced Raman spectroscopic (SERS) and electrochemical approach.

Modification of the gold grids, immobilization of heme proteins as well as experimental conditions of SERS-electrochemical measurements are described in detail in the sections 3.8 and 3.8.1 in Materials and methods.

1. SERS signals of Cyt *c* on the gold grids

The adsorption of the molecules on the surface is a crucial parameter for successful SERS experiments. Chemisorption of alkanethiols is known to be the most efficient method for functionalization of gold surfaces, since they form self-assembled monolayers on these surfaces.[1] Three types of thiols have been tested for the adsorption of Cyt *c* on both gold grids (hole size 35 µm and 8 µm): negatively charged 11-mercaptoundecanoic acid (11-MUA), positively charged cysteamine and neutral mixture of 6-mercapto-1-hexanol with 1-hexanethiol. COOH-terminated SAMs have been reported to have excellent binding properties to Cyt *c* due to the strong electrostatic interaction between positively charged lateral chains of Lys and Arg of the protein and acidic groups of SAM of ω-carboxylalkanethiols.[2]

Figure 1A and B show a typical SERS spectrum of Cyt *c*. The tentative assignments are summarized in Table 1. [3-6]

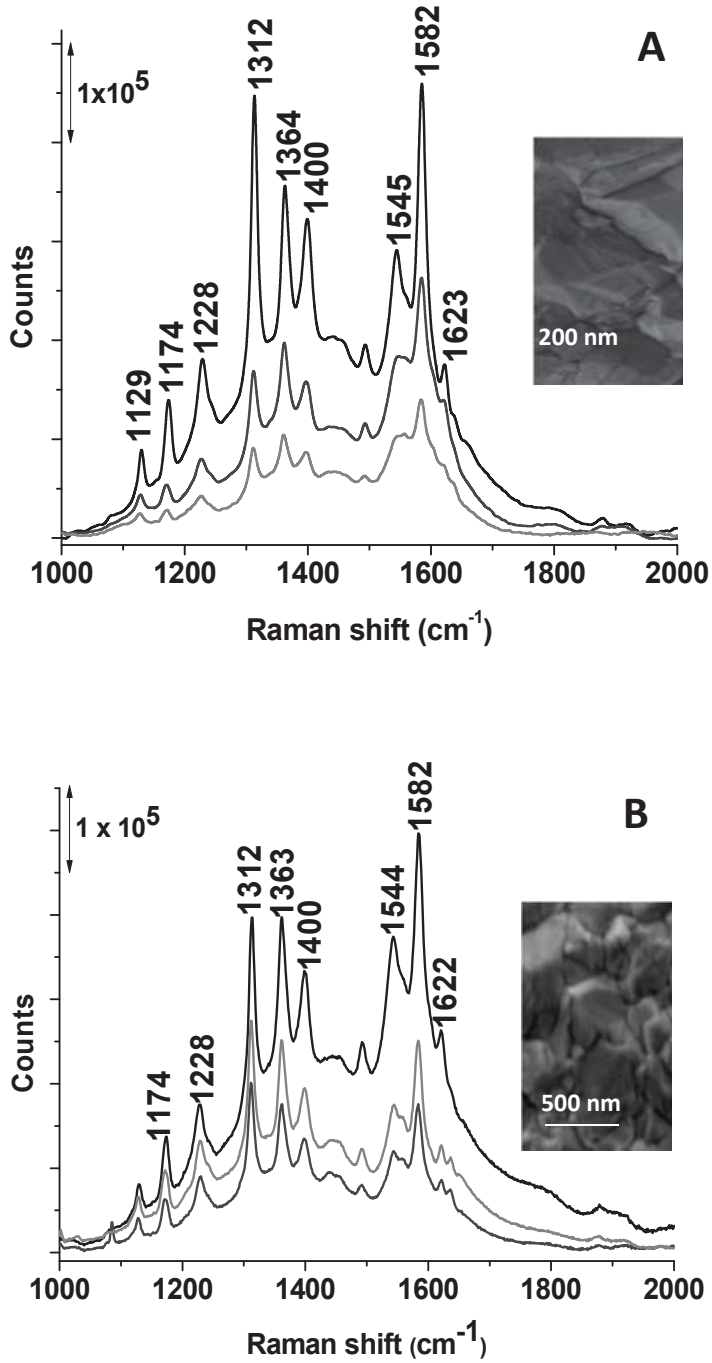

Figure 1: SERS spectra of Cyt *c* adsorbed on the corresponding gold grids surfaces with a hole size of 35 µm (A) and 8 µm (B) modified with different thiols: 11-mercaptoundecanoic acid (black), cysteamine (dark grey) and with mixture of 6-mercapto-1-hexanol with 1-hexanethiol (grey). Laser excitation wavelength is 514 nm, laser power less than 1 mW. The insets show the FIB images of the gold surfaces of the grids

Table 1: Surface-enhanced Raman frequencies of Cyt *c*, Hb and Mb adsorbed on 11-MUA modified gold grid, resonance Raman scattering (RRS) of Cyt *c*, Hb, Mb and their normal mode assignment.[3-6] The frequencies are given in cm^{-1}

Local coordinate and mode assignment	Cyt *c*		Hb		Mb	
	RRS	Raman shift (experiment)	RRS	Raman shift (experiment)	RRS	Raman shift (experiment)
ν_{45} (ν (C_bC_1)$_{as}$), Phe aromatic ring breathing	-	-	1002	1001	1007	1004
ν_{22}, ν_{14} ($\nu(C_\alpha N)$)	1131	1127	1130	1127	1130	1131
ν_{30} (ν (NC_α)$_{as}$, ν (py half-ring)$_{as}$)	1174	1171	1166	1168	1169	1173
ν_{23} ($\delta(=C_bH_2)_{as}$)	-	-	1089	1086	-	-
ν_{13} ($\delta(C_mH)$), prop CH_2 twisting, ν_{42} ($\delta(C_mH)$)	1230	1228	1226	1231	1231	1230
ν_{21} ($\delta(C_mH)$, $\delta(C_\alpha H=)$)	-	-	1305	1304	-	-
ν_4 ($\delta(C_RH)$), ν_{21} (ν ($C_\alpha C_\beta$))	1313	1312	1312	1309	1312	1312
$\delta(=C_bH_2)_s$, ν_{41} (ν (py half-ring)$_s$)	-	-	1341	1335	1341	1338
ν_4 (Fe^{2+}) (ν (py half-ring)$_s$)	1358	1361	1355	1355	1355	1355
ν_4 (Fe^{3+}) (ν (py half-ring)$_s$)	1373	1369	1378	1376	1371	1372
ν_{40} (ν (py quarter-ring)	-	-	-	-	1396	1400
ν_{29} (ν (pyr quarter-ring), ν ($C_\alpha C_\beta$)$_{as}$), $\nu(COO^-)$	1400	1399	1399	1400	1404	1402
ν_2 ($\delta(=C_bH_2)_s$)	-	-	1433	1435	-	-
ν_{28} (ν ($C_\alpha C_m$)$_s$)	-	-	-	-	1426	1428
ν_3 (ν ($C_\alpha C_m$)$_s$)	-	-	1502	1505	-	-
ν_{11} (ν (C_bC_b))	1548	1545	-	-	1544	1543
ν_{19} (Fe^{3+}) (ν ($C_\alpha C_m$))	1559	1562	-	-	-	-
ν_{19} (Fe^{2+}) (ν ($C_\alpha C_m$)$_{as}$)	-	-	1555	1547	-	-
ν_2 (ν (C_bC_b)), ν_{19} (ν ($C_\alpha C_m$)$_{as}$)	-	-	1560	1563	1563	1562
ν_{19} (Fe^{2+}) (ν ($C_\alpha C_m$)$_{as}$)	1585	1582	-	-	-	-
ν_{19} (Fe^{3+}), ν_{37} (ν ($C_\alpha C_m$)$_{as}$) ν ($C_\alpha C_m$)$_{as}$	-	-	1586	1586	1586-1588	1588
ν_{10} (Fe^{2+}) (ν ($C_\alpha C_m$)$_{as}$)	1623	1621	1605	1605	1605	1605
ν_{10} (Fe^{3+}) (ν ($C_\alpha C_m$)$_{as}$)	1638	1635	1640	1640	1640	1640

The main bands at 1312 and 1582 cm^{-1} are assigned to the characteristic heme vibrational modes (ν_4, $\delta(C_RH)$; ν_{21} ($\nu(C_\alpha C_\beta)$)) and (ν_{19}, $\nu(C_\alpha C_m)_{as}$). The weaker signals at 1174 and 1623 cm^{-1} can be

attributed to pyridine half-ring symmetric stretching vibrations (ν_{30}) and C-C stretching vibrations (ν_{10}, $\nu(C_\alpha C_m)_{as}$), respectively. The bands at 1228, 1364 and 1545 cm^{-1} correspond to the C-H deformation ($\nu_{13,}$ ν_{42} $\delta(C_mH)$), pyridine half-ring symmetric stretching vibration (ν_4) and C-C stretching vibration (ν_{11}, $\nu(C_bC_b)$), respectively. For better understanding of the atom labelling of pyrrole rings and methine bridges, the structural formula of heme *c* is shown below in Figure 2 (R indicates the peripheral heme substituents)[(7)]:

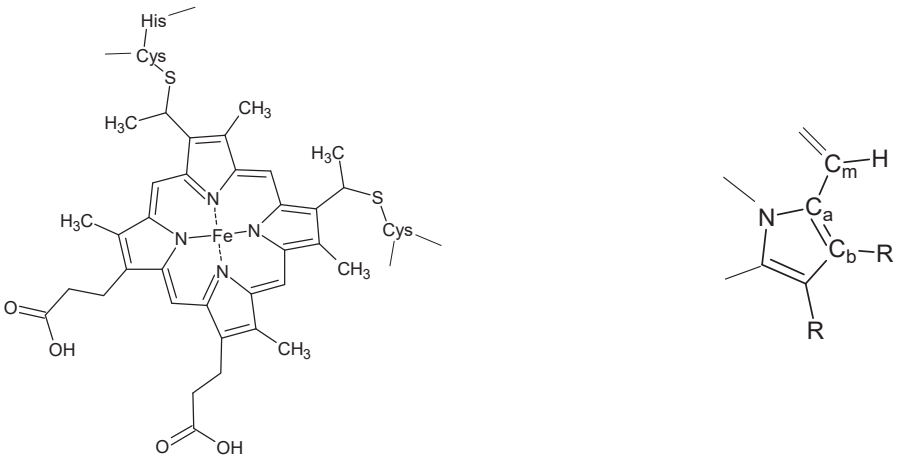

Figure 2: Structural formula of heme *c*

The bands frequencies are assigned on the basis of a large body of experimental data and correspond mostly to the resonance Raman frequencies of Cyt *c*.[(3)] The used immobilization procedure allows maintaining the native conformation of the protein on the modified gold grid, which is in line with previous studies.[(8-10)]

Figure 1 shows that the spectra of Cyt *c* obtained at the different thiol modified gold grids are highly comparable. The SERS spectra of Cyt *c* obtained at the gold grid surfaces modified with negatively charged 11-MUA (black lines on Figure 1A-B) are more intense compared to the ones obtained at the gold grid surfaces modified with cysteamine or with a mixture of thiols (dark grey and grey lines on Figure 1A-B, respectively). The difference in the alkane backbone chain length of the used SAMs of thiols will lead to a different SAMs thickness on the gold grid surface. Thus, the variation of signals intensities of Cyt *c* adsorbed on modified gold grids can be explained by the distance effects. However, Cyt *c* adsorbed on the gold grid modified with negatively charged 11-MUA containing 10 CH_2-groups in the chain exhibited the highest signal enhancement. Therefore,

probably COOH-terminated SAMs provide better adsorption of the protein resulting in the more intense signals. This thiol was thus used for the modifications in the experiments shown hereafter.

Importantly, the band intensities of the Cyt *c* adsorbed at 11-MUA modified surfaces of both gold grids (with hole size 8 µm and 35 µm) are quite similar (order of magnitude $x10^5$) (black lines on Figure 1A-B). Hence, there is no influence of the size of the holes on the enhancement of the Raman signals. The signal enhancement seen in our data is thus arising from the roughness of the surface of gold grids and from the resonant charge transfer in heme group adsorbed on the gold surfaces. However, different enhancement of the bands intensities of Cyt *c* adsorbed on gold grid can be explained by the possible different surfaces roughness, self-assembly of thiols monolayers and orientation of the protein.

2. SERS signals of Cyt *c* on the Au NPs-coated gold grid

To probe if the enhancement of the signals can be further improved, the effect of the addition of gold nanoparticles (Au NPs) to a gold grid was examined. Au NPs are widely used in SERS for the detection of proteins.[11]

Figure 3A (dark grey line) shows the SERS spectrum obtained from Cyt *c* at the modified surface of the gold grid coated with 10 nm Au NPs in direct comparison to the data obtained without nanoparticles (Figure 3A, black line). It can be seen that both SERS spectra display the same Raman features of the studied Cyt *c* but an important loss of intensity can be noticed in case when the protein is adsorbed at the Au NPs-coated gold grid surface (from the order of magnitude $x10^5$ to $x10^4$). No additional enhancement of the SERS signals of Cyt *c* is observed in the presence of Au NPs aggregates at the surface of gold grid. The FIB image shown in Figure 3B reveals that the roughness of the gold grid surface with Au NPs is diminished when compared to the initial surface of the gold grid (Figure 1A).

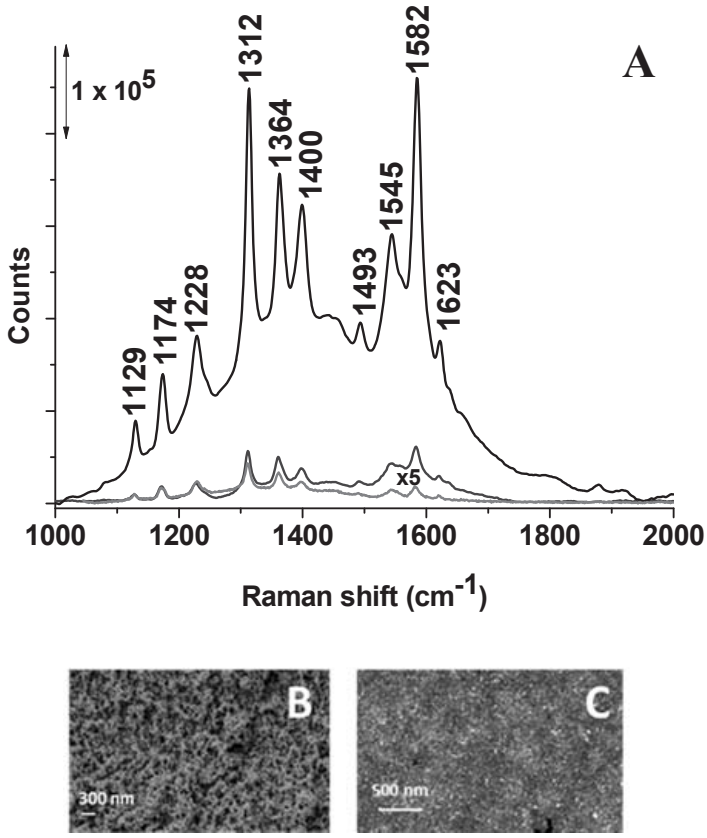

Figure 3: Raman spectra of Cyt *c* on the gold grid without Au NPs (black), on the Au NPs-coated gold grid (dark grey) and on the chemically deposited gold surface (grey) (A). A grey spectrum was multiplied by factor 5 for better visualization. Laser excitation wavelength is 514 nm, laser power less than 1 mW. FIB images of gold grid (35 µm) with gold nanoparticles (B) and chemically deposited gold layer on the silicon surface (C)

The gold nanoparticles are densely arranged and form multi-layers on the grid surface (Figure 3B). The decrease of the band intensities of Cyt *c* adsorbed on the Au NPs-coated gold grid can be explained by the reduced number of hot spots which is related to the reduced surface roughness.

For comparison, we also tested a chemically deposited gold layer on the silicon crystal as an example of simple substrate with probable SERS activity. It was previously demonstrated that other gold substrate such as gold nanostructures fabricated using electro-plating and electron-beam lithography were used in SERS to investigate the structural changes of different proteins.[(12)] FIB imaging of the chemically deposited gold substrate shows a perfect continuous island structure surface (Figure 3C). However, the intensities of the bands of Cyt *c* adsorbed on this chemically

created Au film (Figure 3A, grey line) are one order of magnitude less intense when compared to those observed on Au NPs-coated gold grid (Figure 3A, dark grey line), and two orders of magnitude less intense when compared to the gold grid without Au NPs (Figure 3A, black line). This can be explained by the reduced surface roughness of the chemically deposited gold film when compared to the gold grid surfaces with and without Au NPs. Thus, the ideal electrode for the SERS experiments is the SAMs modified gold grid alone without Au NPs.

3. SERS spectra of heme proteins in the solution and on a gold grid electrode

Figure 4A-C shows the Raman spectra of Cyt *c*, Hb and Mb measured in the solution with a transmission cell without gold grid while Figure 5A-C presents the redox controlled Raman spectra of the same proteins measured with an electrochemical cell in the presence of gold grid electrode.

The proteins in solution are at least partially in the reduced state due to the irradiation by the laser. The mixture of the oxidized and reduced forms is confirmed by the simultaneous presence of the frequency modes at 1370, 1559, 1635 cm^{-1} for oxidized Cyt *c* and at 1360, 1582, 1620 cm^{-1} for reduced Cyt *c* (Figure 4A) as well as the appearance of frequency modes at 1370, 1583, 1639 cm^{-1} for oxidized Hb and at 1358, 1558, 1604 cm^{-1} for reduced Hb (Figure 4B). A similar situation is observed for Mb in solution (Figure 4C).

Raman spectra of the heme proteins in solution obtained in the transmission cell reveal no influence of the adsorption on the proteins integrity. Since most of the bands of the adsorbed proteins (Figure 5A-C) with nearly the same frequencies are observed in Raman spectra of the protein solutions (frequency shift difference is around 3 cm^{-1}) (Figure 4A-C), a stable protein structure in adsorbed form is confirmed. The small frequency shift difference between the adsorbed and not adsorbed proteins is due to the fact that adsorption may lead to the orientation of the molecules at the gold grid surface and not due to a change of protein stability. On the basis of the SERS selection rules, the orientation of the local electromagnetic field is always perpendicular to the surface, thus the SERS effect preferentially enhances vibrations that involve a change in polarizability along an axis perpendicular to the surface.[(13)]

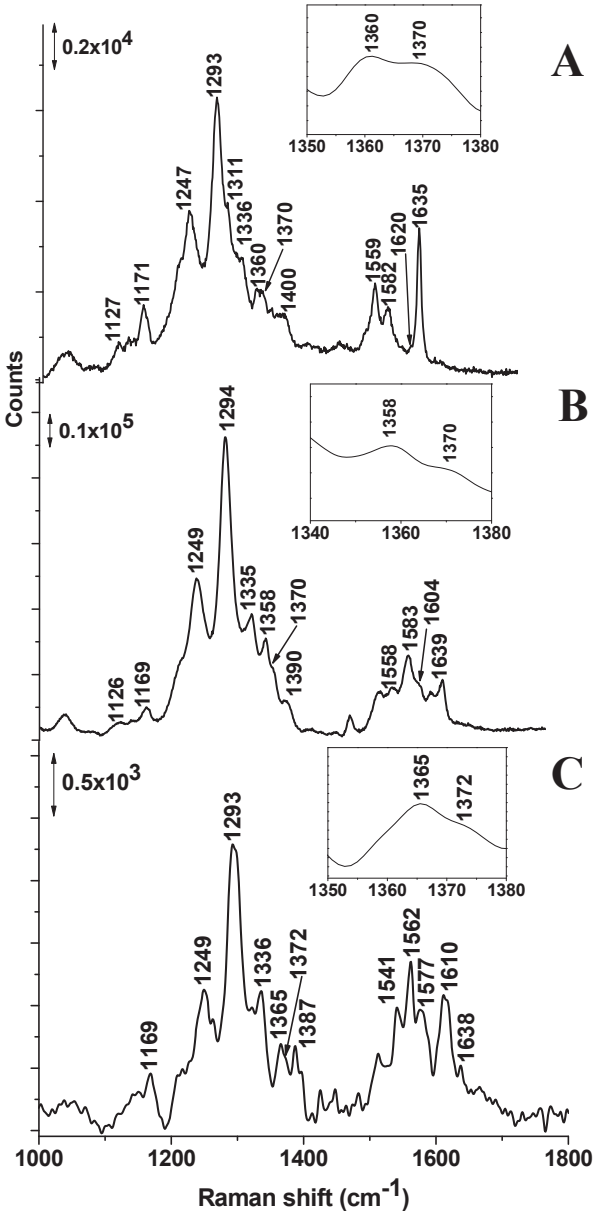

Figure 4: Raman spectra of Cyt *c* (A), Hb (B) and Mb (C) recorded in solution (10 mM KPi at pH 8.0). Excitation wavelength is 514 nm. The insets show the enlarged view of the spectral range from 1340 to 1380 cm^{-1} showing the marker band of ν_4 vibrational mode of the heme proteins

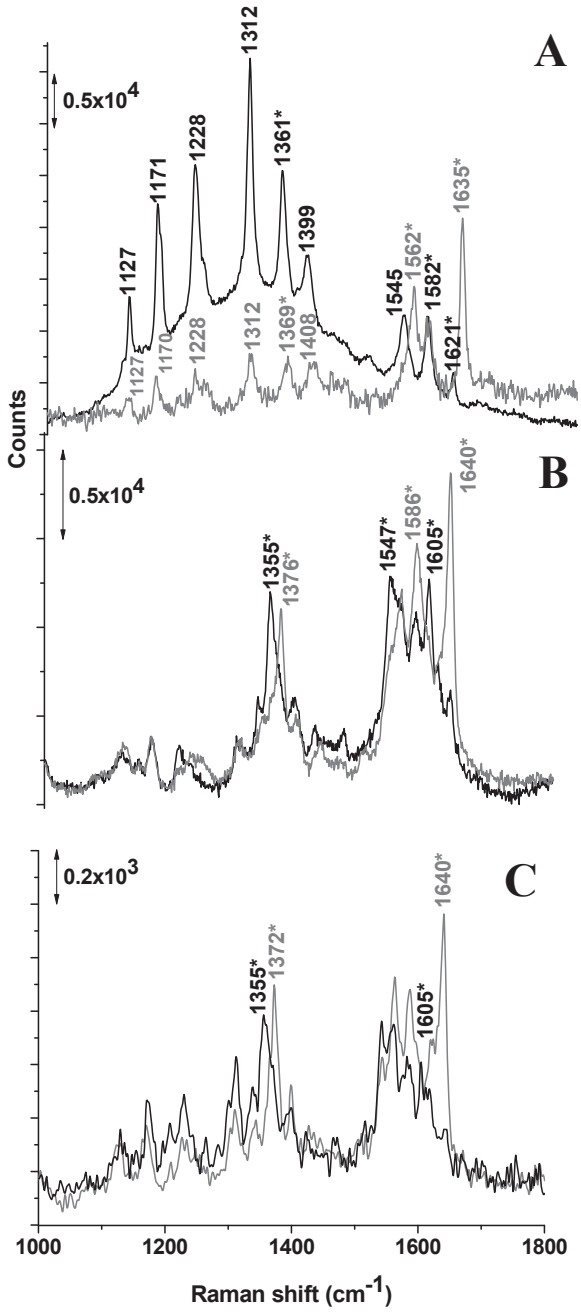

Figure 5: SERS spectra of the reduced (black) and oxidized (grey) forms of the Cyt c (A), Hb (B) and Mb (C) in 10 mM KPi, 50 mM KCl at pH 8.0. The spectrum of oxidized form of Cyt *c* was multiplied by factor 5 for better visualization. Laser excitation wavelength is 514 nm, laser power less than 1 mW

Three additional intense bands at around 1248, 1293 and 1335 cm^{-1} were observed in Raman spectra of the protein solutions as compared to the spectra of the adsorbed proteins (Figure 5A-C). They are assigned to the phosphate buffer used to solubilize the proteins. The control Raman spectrum of the pure phosphate buffer solution is shown in Figure 6.

As previously described,[4-6] oxidation and reduction processes of these heme proteins can be monitored from the frequencies of the ν_4, ν_{10} and ν_{19} sensitive vibrational modes. Upon complete reduction of Cyt *c* using spectroelectrochemical cell, the frequency of the mode ν_{19} is shifted from 1562 to 1582 cm^{-1} and the frequencies of ν_4 and ν_{10} modes downshift from 1369 and 1635 cm^{-1} to 1361 and 1621 cm^{-1}, respectively (Figure 5A). Upon reduction of Hb (Figure 5B), the bands at 1376 (ν_4), 1586 (ν_{19}) and 1640 (ν_{10}) cm^{-1} are entirely shifted to 1355, 1547 and 1605 cm^{-1}, respectively. For the reduced Mb the marker bands, ν_4 and ν_{10} are similarly shifted (Figure 5C).

Frequency shifts of marker bands can be explained by the movement of the iron in the porphyrin pocket. For example, reduction of the heme is associated with the slight movement of the iron out of the porphyrin plane and corresponding oxidation marker bands will be shifted reflecting the increased electron density in the porphyrin ring. Changes in the heme pocket structure caused by reduction or oxidation of iron can be also monitored using vinyl stretching modes (between 1620 and 1635 cm^{-1}) since their frequencies mainly depend on the orientation with respect to the porphyrin.

All values of the observed Raman bands including the redox marker bands correlate with the resonance Raman bands of Cyt *c*, Hb and Mb reported in the literature[4-6] and summarized in the Table 1.

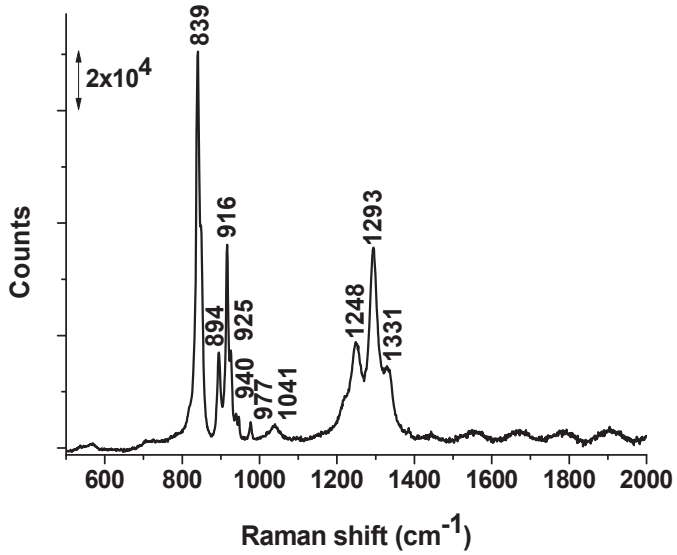

Figure 6: Raman spectrum of dry film of the buffer 10 mM KPi and 50 mM KCl at pH 8.0. Excitation wavelength is 514 nm

Figure 7 shows the Raman spectra of the oxidized (grey line) and the reduced (black line) forms of *cbb₃* oxidase immobilized on the gold grid under precise potential control. It is obvious that there are distinct differences between the oxidized and the reduced form. A shift of the frequencies of the ν_4, ν_2 and ν_{10} sensitive vibrational modes is observed between the oxidized and the reduced forms. The spectrum from the oxidized *cbb₃* oxidase (grey line) has the ν_4 mode at 1372 cm^{-1} indicating that all hemes are in the oxidized state. Moreover, this sensitive mode (ν_4) of the enzyme in the fully reduced state (black line) is at 1359 cm^{-1}, establishing that all hemes are in the reduced state. Table 2 summarizes the marker band frequencies of the *cbb₃* oxidase. A detailed analysis of the Raman data also reveals that these frequencies are in agreement with previously reported resonance Raman (RR) spectra of oxidized and reduced *cbb₃* oxidase (see Table 2).[(14)] Consequently, enhancement of the Raman signals partially arises from the resonant charge transfer in heme groups of the enzyme adsorbed on the gold electrode. All results confirm that full and reversible oxidation and reduction of heme proteins can be obtained with this set up.

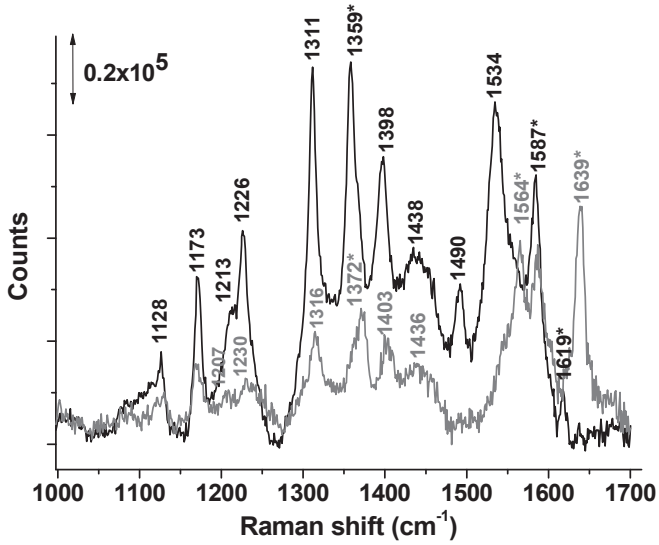

Figure 7: SERS spectra of the reduced (black) and oxidized (grey) forms of cytochrome *cbb*$_3$ oxidase in 10 mM KPi, 50 mM KCl at pH 7.5. The spectrum of oxidized form of *cbb*$_3$ oxidase was multiplied by factor 5 for better visualization. Laser excitation wavelength is 514 nm, laser power less than 1 mW

Table 2: Surface-enhanced Raman frequencies of the markers bands of cytochrome *cbb*$_3$ oxidase adsorbed on the11-MUA modified gold grid, resonance Raman scattering (RRS) of *cbb*$_3$ oxidase and their normal mode assignment.[14] The frequencies are given in cm^{-1}

Mode assignment	Oxidized		Reduced	
	RRS	Raman shift (experiment)	RRS	Raman shift (experiment)
ν_4	1373	1372	1362	1359
ν_2	1561	1564	1592	1587
ν_{10}	1638	1639	1622	1619

Importantly, low laser power (around 0.67 mW) was used in the EC-SERS measurements in order to prevent reduction of the proteins by laser irradiation. In contrary, Raman spectra of the protein solutions in the transmission cell without gold grid were obtained using high laser power (more than 1 mW) in order to register high quality spectra since the peaks on the Raman spectra were not well resolved when using 0.67 mW laser power.

4. Conclusions

The spectroelectrochemical cell adapted here for SERS allowed us to obtain fully and reversibly oxidized and reduced spectra of the adsorbed heme proteins (Cyt *c*, Hb, Mb, cbb_3 oxidase) under precise potential control with very low laser power. Moreover, it is interesting to notice that the adsorption of proteins on the working electrode did not lead to any noticeable shift of the signal (3 cm^{-1}), pointing towards stable proteins structure. The important advantages of this device are the ease of assembly and the small amount of the sample (8µL). Moreover, the good quality of Raman data and their reproducibility demonstrate that this cell can be successfully used for the electrochemical studies of various redox proteins by means of the suitable functionalization of gold grid. No limitation is given by the size of the proteins and even large membrane proteins can be studied.

5. References

1. Love, J. C., Estroff, L. A., Kriebel, J. K., Nuzzo, R. G., and Whitesides, G. M. (2005) Self-assembled monolayers of thiolates on metals as a form of nanotechnology, *Chemical reviews 105*, 1103-1170.

2. Song, S., Clark, R. A., Bowden, E. F., and Tarlov, M. J. (1993) Characterization of cytochrome c/alkanethiolate structures prepared by self-assembly on gold, *The Journal of Physical Chemistry 97*, 6564-6572.

3. Hu, S., Morris, I. K., Singh, J. P., Smith, K. M., and Spiro, T. G. (1993) Complete assignment of cytochrome c resonance Raman spectra via enzymic reconstitution with isotopically labeled hemes, *Journal of the American Chemical Society 115*, 12446-12458.

4. Hu, S., Smith, K. M., and Spiro, T. G. (1996) Assignment of protoheme resonance Raman spectrum by heme labeling in myoglobin, *Journal of the American Chemical Society 118*, 12638-12646.

5. Rygula, A., Majzner, K., Marzec, K. M., Kaczor, A., Pilarczyk, M., and Baranska, M. (2013) Raman spectroscopy of proteins: a review, *Journal of Raman Spectroscopy 44*, 1061-1076.

6. Spiro, T. G., and Strekas, T. C. (1974) Resonance Raman spectra of heme proteins. Effects of oxidation and spin state, *Journal of the American Chemical Society 96*, 338-345.

7. Desbois, A. (1994) Resonance Raman spectroscopy of c-type cytochromes, *Biochimie 76*, 693-707.

8. de Groot, M. T., Evers, T. H., Merkx, M., and Koper, M. T. (2007) Electron Transfer and Ligand Binding to Cytochrome c 'Immobilized on Self-Assembled Monolayers, *Langmuir 23*, 729-736.

9. Hildebrandt, P., and Murgida, D. (2002) Electron transfer dynamics of cytochrome c bound to self-assembled monolayers on silver electrodes, *Bioelectrochemistry 55*, 139-143.

10. Yu, Q., and Golden, G. (2007) Probing the protein orientation on charged self-assembled monolayers on gold nanohole arrays by SERS, *Langmuir 23*, 8659-8662.

11. Jain, P. K., Huang, X., El-Sayed, I. H., and El-Sayad, M. A. (2007) Review of some interesting surface plasmon resonance-enhanced properties of noble metal nanoparticles and their applications to biosystems, *Plasmonics 2*, 107-118.

12. Das, G., Mecarini, F., Gentile, F., De Angelis, F., Kumar, H. M., Candeloro, P., Liberale, C., Cuda, G., and Di Fabrizio, E. (2009) Nano-patterned SERS substrate: application for protein analysis vs. temperature, *Biosensors and Bioelectronics 24*, 1693-1699.

13. Moskovits, M., and Suh, J. (1984) Surface selection rules for surface-enhanced Raman spectroscopy: calculations and application to the surface-enhanced Raman spectrum of phthalazine on silver, *The Journal of Physical Chemistry 88*, 5526-5530.

14. Pinakoulaki, E., and Varotsis, C. (2008) Resonance Raman spectroscopy of nitric oxide reductase and cbb 3 heme-copper oxidase, *The Journal of Physical Chemistry B 112*, 1851-1857.

GENERAL CONCLUSION

This thesis consists of two projects: the first one is focused on the development of the surface-enhanced infrared spectroscopic approach combined with perfusion cell and the second one is related to the development of the electrochemical approach combined with surface-enhanced Raman spectroscopy.

Within the first project different proteins were studied: transporter protein Lactose Permease, protein from the respiration chain complex I and the protein involved in the thylakoid membrane biogenesis and/or maintenance IM30.

The findings provided a strong confirmation that Glu325 in LacY has a very alkaline pK_a equal to 10.5. This value coincides very well with the variation of affinity of LacY for sugar binding as a function of pH. Different mutants of LacY carrying mutations in the proton translocation channel have been studied by the perfusion-SEIRAS approach in order to check the change of pK_a of carboxylic group at position 325: LacY E325D, LacY H322Q, LacY R302K, LacY G46W/G262W R302K, LacY R302A and LacY G46W/G262W R302A. The results demonstrated that pK_as of carboxylic group at position 325 are shifted toward lower values especially in the mutants LacY E325D and LacY R302K (LacY G46W/G262W R302K). These findings indicate that mutation of the residues in the active center of the protein results in the perturbation of the hydrogen bonding in the H-bond/salt bridge network. Moreover, obtained results showed that there is no direct correlation between transport activity and pK_a value of Glu325.

Measurements in the FIR spectral region confirmed large pH-induced conformational changes of LacY and its different mutants.

Developed SEIRAS-perfusion approach was also successfully used to study conformational changes in complex I upon oxidation with various oxidizing agents (Q-2, Q-10, $K_3[Fe(CN)_6]$ or with oxygen which is naturally dissolved in the MES buffer under atmospheric conditions) and reduction with NADH. The findings provided evidence that complex I undergoes different conformational changes when using different oxidizing agents. These conformational changes depend on whether complex I is fully or partially oxidized. It is probable that the protein has higher degree of oxidation when using Q-2. MES buffer containing dissolved oxygen has the lowest ability to oxidize complex I comparing to other tested oxidizing agents and corresponding difference redox spectrum is noticeably shifted to lower wavenumbers as compared to the other difference spectra obtained from complex I when it is equilibrated with other oxidizing agents.

Evidence was given that oxidation and reduction of complex I induce major conformational changes which are related to the mechanism of function of the protein: conversion of the energy released from the electron transfer into global conformational movements allowing proton translocation across the biological membrane.

As perspective, perfusion-SEIRAS approach can be used to study different mutants of complex I in order to study if they can transfer only electrons or both electrons and protons. Moreover, this approach can be used for the further studying of IM30 since in this work only initial results were obtained demonstrating that Mg^{2+} ions induce major conformational changes in the protein.

As was mentioned above the second part of the project is related to the development of a combined SERS-electrochemical approach. The spectroelectrochemical cell allowed obtaining reversible SERS spectra of adsorbed heme proteins (Cyt *c*, Hb, Mb and cbb_3 oxidase). No denaturation took place after adsorption of the proteins on the modified gold grid electrode. The advantages of the electrochemical cell are facility to assemble, reassemble and disassemble it. Moreover, small volumes of the samples are needed (8µL). High quality of SERS spectra demonstrated that this cell can be used to study many other redox active proteins. No limitations are given by the size of the proteins. Thus, even large membrane proteins can be studied using this approach.

VI. APPENDIX

List of figures in the appendix

List of tables in the appendix

1. Determination of the secondary structure of IM30 in the absence and presence of Mg^{2+}

IM30 is approximately 30 kDa protein conserved in chloroplast and cyanobacteria. This protein has been suggested to be involved in thylakoid membrane (TM) biogenesis and/or maintenance. IM30 binds specifically to membranes that contain anionic lipids as an oligomeric ring in a well-defined geometry. Membrane binding triggered by Mg^{2+} eventually results in membrane fusion, and membrane contacts and fusion established by IM30 eventually allow dynamic remodelling of TM liposomes, which probably may permit regulated exchange of proteins and/or lipids between internal membranes in cyanobacteria and chloroplasts.[1]

Since IM30 functions efficiently in the presence of Mg^{2+} ions, SEIRAS-perfusion approach was used to study if Mg^{2+} ions trigger conformational changes of the protein. Before SEIRAS-perfusion measurements secondary structure of IM30 in the absence and in the presence of Mg^{2+} was determined by FTIR spectroscopy. Deconvolutions of amide I bands of the IM30 samples equilibrated in the buffer with and without Mg^{2+} are shown below in Figure S1.

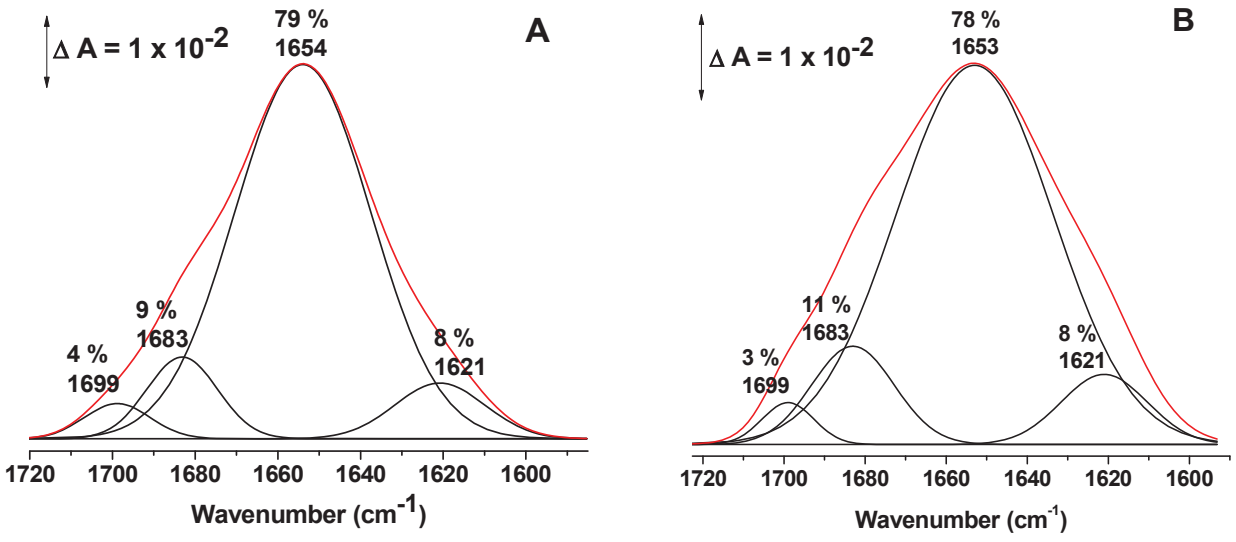

Figure S1: Deconvolution of amide I band of IM30 equilibrated in 20 mM HEPES (pH 7.6) in the absence (A) and presence (B) of 90 mM Mg^{2+}

The amide I band centered at 1653 – 1654 cm^{-1} corresponds to the sum of contributions of several components. Four bands at around 1699, 1683, 1654 and 1621 cm^{-1} were used to decompose the amide I band. These components are assigned to the different elements of secondary structure.

Table S1 summarizes the assignment of different components of amide I bands of IM30 in the absence and presence of Mg^{2+} and represents the percentage of different elements of secondary structure.

Table S1: Secondary structure of IM30 equilibrated in 20 mM HEPES (pH 7.6) in the absence and presence of 90 mM Mg^{2+}

Secondary structure	Position of amide I and estimated percentage	
	Without Mg^{2+}	**With Mg^{2+}**
α-helices + disordered structures	1654 (79 %)	1653 (78 %)
Parallel β-sheets	1621 (8 %)	1621 (8 %)
Antiparallel β-sheets	1699 (4 %)	1699 (3 %)
β-turns	1683 (9 %)	1683 (11 %)

The results show that the major secondary structure of IM30 is α-helical structure. Moreover, interaction of IM30 with Mg^{2+} does not change the secondary structure of the protein. The percentage of different elements of secondary structure is almost identical. Observed differences can be due to the errors of deconvolution.

2. Perfusion-induced conformational changes in a monolayer of immobilized IM30 upon Mg^{2+} binding

The effect of interaction of Mg^{2+} ions with IM30 was monitored by surface enhanced IR spectroscopy in an ATR perfusion cell. Experimental conditions are described in detail in the sections 3.3 and 3.7 in Materials and methods.

Figure S2 displays the perfusion-induced IR difference spectrum obtained from the IM30 sample equilibrated in HEPES with 90 mM Mg^{2+} and subtracted from the sample equilibrated in the same buffer however without Mg^{2+} ions. A broad peak centered at 1669 cm^{-1} and 1638 cm^{-1} is observed in the amide I region that includes conformational changes in the C=O groups of the protein backbone.

Peaks at 1669 cm^{-1} and 1638 cm^{-1} indicate that conformational rearrangements in β-turns and parallel β-sheets take place upon interaction of IM30 with Mg^{2+} ions.

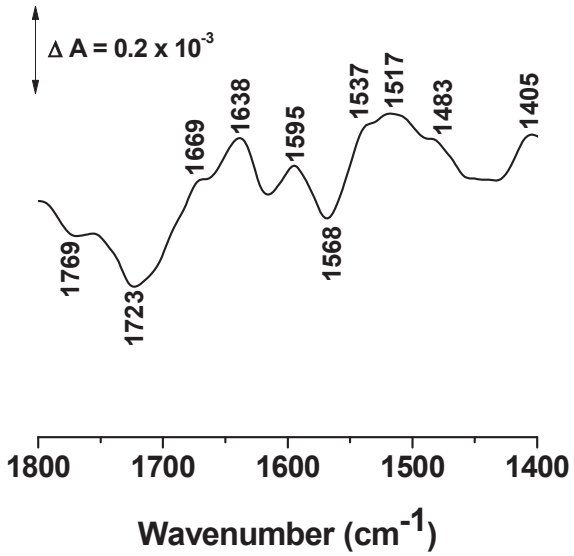

Figure S2: Perfusion-induced FTIR difference spectra of IM30 obtained from the sample equilibrated in 20 mM HEPES with 90 mM Mg^{2+} and subtracted from the sample equilibrated in the same buffer but without Mg^{2+} ions. C (IM30) = 0.67 $mg.mL^{-1}$

The peaks between 1590 cm^{-1} and 1450 cm^{-1} correspond to the amide II range that involves coupled CN/NH vibrational modes of the protein backbone, contributions from individual amino acids reorganizing or changing protonation states.

Contribution from the HEPES buffer in the difference spectrum can be expected at 1451 cm^{-1} since ATR FTIR absorbance spectrum of the powder shows a strong peak at this position (Figure S3). The control experiments (perfusion measurements with the same buffers in the absence of adsorbed IM30 on the modified ATR crystal) provided evidence that the signals observed in Figure S2 arise from the conformational changes of the protein (Figure S4).

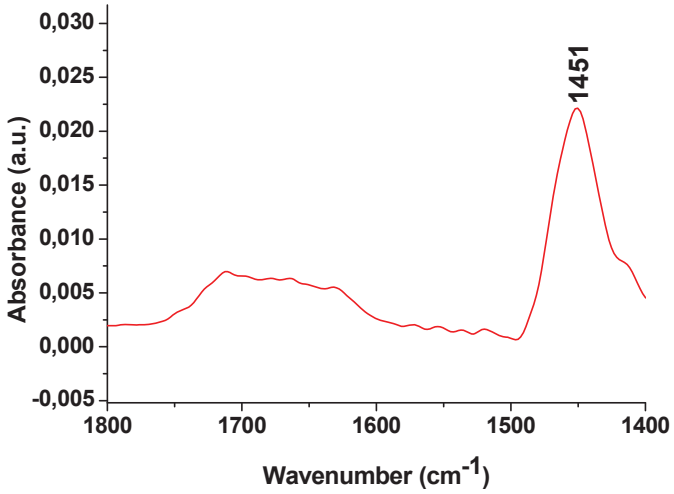

Figure S3: ATR FTIR absorbance spectrum of the HEPES powder

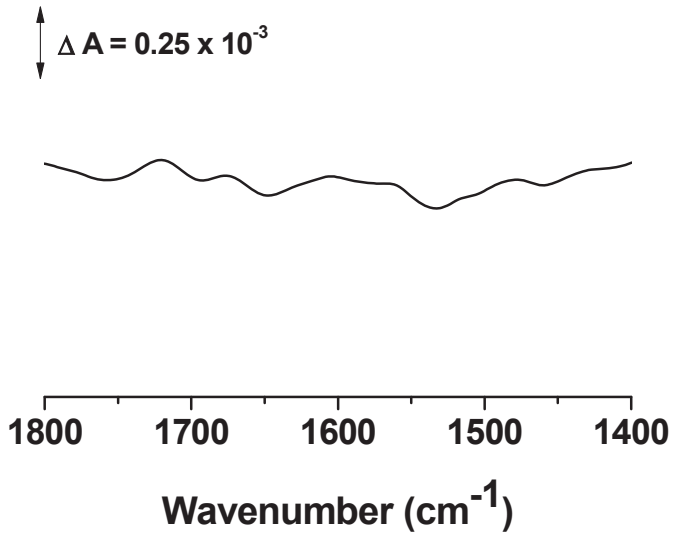

Figure S4: Control difference spectrum in the absence of immobilized IM30 on the modified ATR crystal

Less concentrated solutions of Mg^{2+} (5 mM and 10 mM) also trigger conformational changes in IM30 and corresponding difference spectra (data is not showed) exhibit in general the same spectral profile. Some marked differences between these spectra were observed in the amide II spectral range.

Thus, obtained results clearly demonstrated that Mg^{2+} ions induce conformational changes of IM30 that are eventually important for the mechanism of function of this protein.

3. Infrared absorption spectra of the gold grids

Infrared spectra of the gold grids were recorded in the transmission mode in order to check the enhanced optical transmission properties (extraordinary transmission, EOT). If the gold grids possess this feature then appearance of plasmonic peak in the spectra is expected. This property of the gold grids would be promising to enhance the signals of adsorbed molecules. Figure S5 shows the FIR absorption spectra of the gold grids with hole size 8 µm (periodicity 17 µm) (A) and 35 µm (periodicity 49 µm) (B).

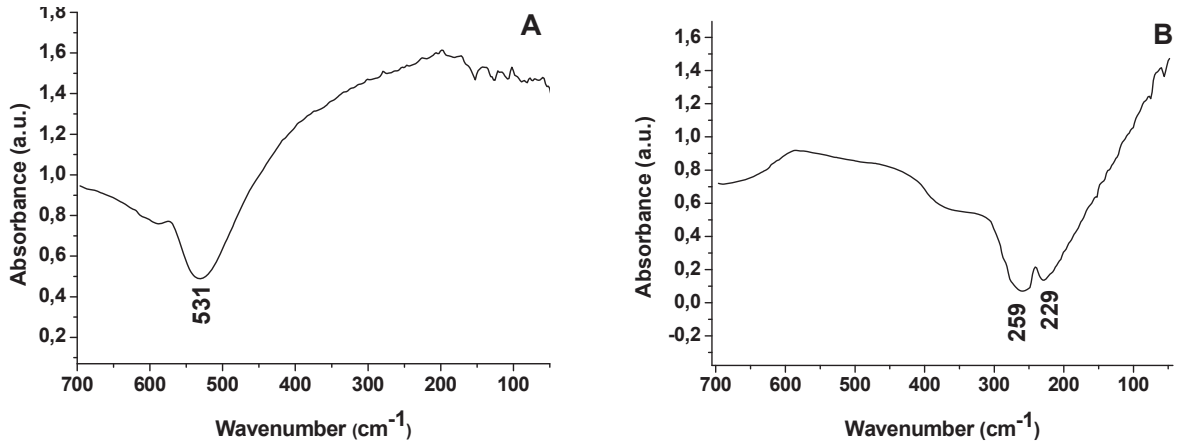

Figure S5: FIR absorption spectra of gold grids with hole size 8 µm (periodicity 17 µm) (A) and 35 µm (periodicity 49 µm) (B)

For the gold grid with periodicity 17 µm a peak at 531 cm^{-1} was observed (Figure S5A) and for the second gold grid with periodicity 49 µm two peaks at 259 µm and 229 µm appeared (Figure S5B).

Plasmonic modes should be proportional to the 1/periodicity.[2, 3] Hence, for the first periodicity (17 µm) the first mode is expected at round 600 cm^{-1} and for the larger period (49 µm) around 200 cm^{-1}. However, the shape of plasmonic peaks should be sharp.

Example of gold grid (hole size 8 µm and periodicity 12 µm) that definitely has plasmonic peak in the absorption spectrum was provided by the Nanostructures Laboratory (ISIS, Strasbourg, France). The IR absorption spectrum is shown in Figure S6.

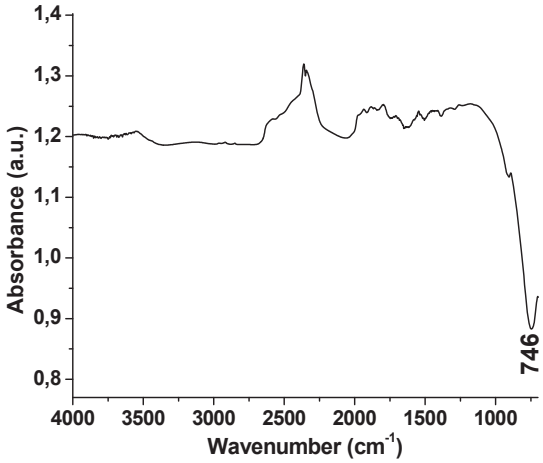

Figure S6: MID IR absorption spectrum of the model grid with the hole size 8 μm and periodicity 12 μm

For this grid plasmonic peak was observed at 746 μm. Importantly, the peak is intense and it has sharp shape.

Thus, it is not evident if our grids (periodicity 17 μm and 49 μm) have plasmonic properties in the IR region. It is known that position of the plasmonic peak depends on the angle of an incident beam.[(2)] Thus, in order to check the plasmonic properties of the grids it would be important to rotate them relative to the incoming IR beam. If they follow the expected dispersion of the plasmon, so this should give more insights.

4. Major helical orientation of LacY adsorbed on the Ni-NTA modified gold surface

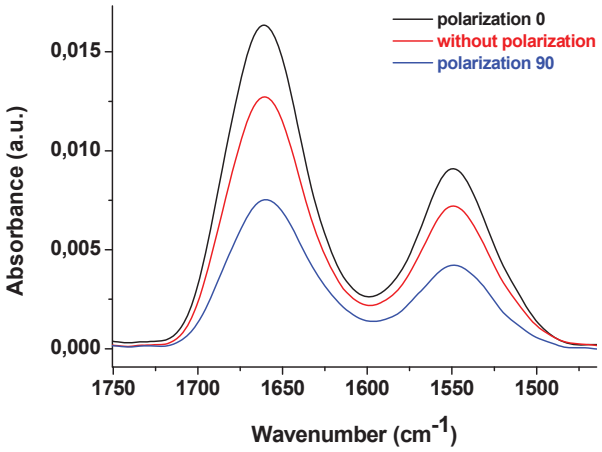

Figure S7: MID IR spectrum of LacY WT recorded with polarization 0° (black), 90° (blue) and without polarization (red)

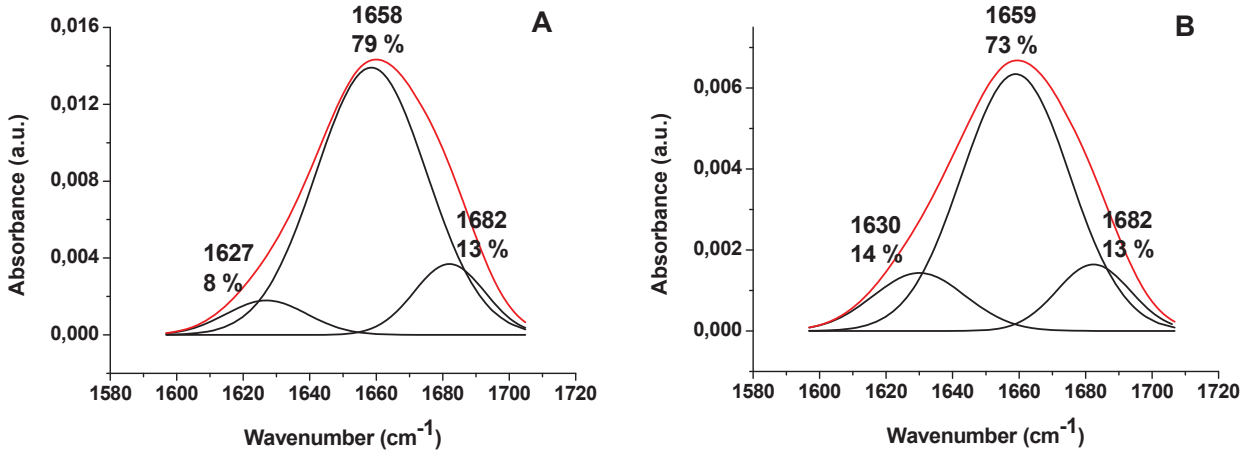

Figure S8: Deconvolutions of amide I bands of LacY WT recorded with polarization 0° (A) and 90° (B)

$$R = \frac{A_{\parallel}(\alpha - helices)}{A_{\perp}(\alpha - helices)} = \frac{0.01391}{0.00634} = 2.19$$

Data gives evidence that LacY WT adsorbed on the Ni-NTA modified gold surface is oriented or partially oriented.

5. References

1. Hennig, R., Heidrich, J., Saur, M., Schmüser, L., Roeters, S. J., Hellmann, N., Woutersen, S., Bonn, M., Weidner, T., and Markl, J. (2015) IM30 triggers membrane fusion in cyanobacteria and chloroplasts, *Nature communications 6*, 7018.

2. Coe, J. V., Williams, S. M., Rodriguez, K. R., Teeters-Kennedy, S., Sudnitsyn, A., and Hrovat, F. (2006) Extraordinary IR transmission with metallic arrays of subwavelength holes, ACS Publications.

3. Williams, S. M., Stafford, A. D., Rogers, T. M., Bishop, S. R., and Coe, J. V. (2004) Extraordinary infrared transmission of Cu-coated arrays with subwavelength apertures: Hole size and the transition from surface plasmonto waveguide transmission, *Applied physics letters 85*, 1472-1474.

Natalia GRYTSYK

Développement d'approches spectroscopiques infrarouge exaltées de surface et Raman couplée à l'électrochimie pour l'étude du mécanisme réactionnel des protéines membranaires

Résumé

Cette thèse concerne le développement d'approches spectroscopiques infarouge et Raman exaltées de surface: la spectroscopie infrarouge exaltée de surface (SEIRAS) combinée avec une cellule de perfusion et la spectroscopie Raman exaltée de surface (SERS) coulplée avec l'électrochimie.
Dans le cadre du premier projet, différentes protéines ont été étudiées: Lactose perméase (LacY), complexe I et IM30. Nous avons déterminé le pK_a de Glu325 dans LacY sauvage et dans différents mutants portant des mutations dans le centre actif de translocation des protons. Sauvage complexe I a été oxydé avec différents agents oxydants et réduit avec NADH. Spectres différentiels correspondants ont été analysés. Des changements conformationnels dans la protéine IM30, induits par la présence des ions Mg^{2+}, ont été observés.
Dans le cadre du deuxième projet, une cellule spectroélectrochimique contenant une grille d'or a été adaptée pour étudier des protéines redox actives. Cette grille d'or sert à la fois de substrat SERS et d'électrode de travail. Cyt *c*, Hb et Mb ont d'abord été utilisés pour valider la configuration, puis l'approche a été étendue pour étudier une protéine membranaire.

Mots-clés: perfusion-SEIRAS, Lactose Perméase, Glu325, complexe I, IM30, SERS-électrochimie, grille d'or, Cyt *c*, Hb, Mb, *cbb*$_3$ oxydase

Résumé en anglais

This thesis concerns the development of surface-enhanced infrared and Raman spectroscopic approaches: surface-enhanced infrared absorption spectroscopy (SEIRAS) combined with perfusion cell and surface-enhanced Raman spectroscopy (SERS) combined with electrochemistry.
Within the first project different proteins were studied: Lactose Permease (LacY), complex I and IM30.The pK_a of Glu325 in LacY WT and in different mutants carrying mutations in the proton translocation active center was determined. WT complex I was oxidized with different oxidizing agents and reduced with NADH. Corresponding redox-induced conformational changes were studied. The evidence was given that Mg^{2+} ions induce conformational changes in the protein IM30.
Within the second project the spectroelectrochemical cell containing gold grid electrode was adopted for the studies of redox active proteins. This gold grid serves both as working electrode and as SERS active substrate. First Cyt *c*, Hb and Mb were used to validate the setup and then the approach was extended to study a membrane protein.

Keywords: perfusion-SEIRAS, Lactose Permease, Glu325, complex I, IM30, SERS-electrochemistry, gold grid, Cyt *c*, Hb, Mb, *cbb*$_3$ oxidase